

**UNIVERSIDADE FEDERAL DE SANTA CATARINA
PÓS-GRADUAÇÃO EM ENGENHARIA ELÉTRICA**

Arturo Fajardo Jaimes

**CONTRIBUTIONS ON THE ENERGY FLOW
MODELING IN A SELF-SUSTAINABLE WIRELESS
ENERGY TRANSFER SYSTEM BASED ON EFFICIENT
INDUCTIVE LINKS**

Florianópolis

2018

Arturo Fajardo Jaimes

CONTRIBUTIONS ON THE ENERGY FLOW MODELING IN A
SELF-SUSTAINABLE WIRELESS ENERGY TRANSFER SYSTEM
BASED ON EFFICIENT INDUCTIVE LINKS

Tese submetida ao Programa de
Pós-Graduação em Engenharia
Elétrica da Universidade Federal
de Santa Catarina para a obtenção
do Grau de Doutor em Engenharia
Elétrica.

Orientador: Prof. Dr.
Fernando Rangel de Sousa

Florianópolis
2018

Ficha de identificação da obra elaborada pelo autor,
através do Programa de Geração Automática da Biblioteca Universitária da UFSC.

FAJARDO, ARTURO

Contributions on the energy flow modeling in a
self-sustainable wireless energy transfer system
based on efficient inductive links / ARTURO FAJARDO
; orientador, Fernando Rangel de Sousa, 2018.
348 p.

Tese (doutorado) - Universidade Federal de Santa
Catarina, Centro Tecnológico, Programa de Pós
Graduação em Engenharia Elétrica, Florianópolis, 2018.

Inclui referências.


1. Engenharia Elétrica. 2. Transferência de
energia sem fio em redes de área corporal sem fio.
3. Modelagem de células fotovoltaicas. 4. Modelagem
de amplificadores de potência. 5. Modelagem de
indutores planares. I. Rangel de Sousa, Fernando.
II. Universidade Federal de Santa Catarina.
Programa de Pós-Graduação em Engenharia Elétrica.
III. Título.

Arturo Fajardo Jaimes

**CONTRIBUTIONS ON THE ENERGY FLOW
MODELING IN A SELF-SUSTAINABLE WIRELESS
ENERGY TRANSFER SYSTEM BASED ON EFFICIENT
INDUCTIVE LINKS**

Esta Tese foi julgada adequada para a obtenção do Título de “Doutor em Engenharia Elétrica”, e aprovada em sua forma final pelo Programa de Pós-Graduação em Engenharia Elétrica da Universidade Federal de Santa Catarina.

Florianópolis, 15 de Março 2018.



Prof. Dr. Coordenador do Programa de Pós-Graduação em
Engenharia Elétrica
Marcelo Lobo Heldwein
Universidade Federal de Santa Catarina

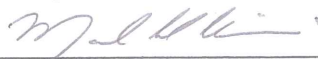


Prof. Dr. Orientador
Fernando Rangel de Sousa
Universidade Federal de Santa Catarina

Banca Examinadora:



Prof. Dr. Valner João Brusamarello
Universidade Federal do Rio Grande do Sul



Prof. Dr. Marcelo Lobo Heldwein
Universidade Federal de Santa Catarina



Prof. Dr. Fabian Cabrera
Universidade Federal de Santa Catarina

A minha família, especialmente a minha mãe, minha esposa e minha filha que me ensinam todo dia o que é amar e ser amado.

AGRADECIMENTOS

Não tenho como agradecer a todas as pessoas que tornaram possível eu desenvolver minha pesquisa, portanto só quero escrever uma lembrança para mim: de não me esquecer de acreditar nas pessoas.

Hoje não sou engenheiro, estudante, projetista, físico, matemático, escritor, e muitas mais coisas que precisei neste programa de doutorado. Ao mundo peço licença para atuar onde quiser. Meu sobrenome é PAPAI, meu nome é ESPOSO FILHO, é meu apelido é AMIGO.

(Arturo Fajardo, 2017)

ABSTRACT

A Wireless Body Area Network is a wireless network that operates in, on, or around the body. This system is capable of interacting with its wearer without any conscious intervention. Therefore, it is a technological tool that can change our perception of the world. However, many social and technical challenges must be solved before its full adoption. In this research, we modeled an autonomous Wireless Power Transfer system composed of a photovoltaic solar cell as the energy source, a DC/RF converter that is based on a power amplifier, and an inductive link that is based on planar inductors. This type of system can be used to provide energy autonomy for biomedical implanted devices avoiding the surgical procedure associated with the recharge or change of the battery of subcutaneous devices. In this document, we summarize the state-of-the-art of the self-sustaining wireless power transfer systems for wireless body area network applications and we present the theoretical background of energy harvesting systems, the solar cell, planar inductors and power amplifier modeling. Furthermore, we discuss the theory using an integrative approach that is based on familiar concepts as well as new ones. The main contributions of this research are: 1) the modeling of energy carriers, harvesters, and conventional energy sources (e.g., commercial energy grid) under the same theoretical framework; 2) a novel model for photovoltaic solar cells under indoor environmental conditions.;3) a novel experimental characterization method for inductors embedded in WPT applications; 4) an innovative design methodology for self-sustaining WPT systems which maximizes the power chain efficiency and extract the maximum available power of the harvester using the power interactions among the subsystems.

Keywords: Photovoltaic modeling, Power amplifier modeling, Inductor modeling, Wireless Body Area Networks, Wireless Power Transfer, Energy Harvesting, Energy Harvester modeling.

RESUMO

Uma rede corporal sem fio é uma rede que opera dentro ou ao redor do corpo. Tal sistema é capaz de interagir com seu usuário sem qualquer intervenção consciente. Portanto, trata-se de uma ferramenta tecnológica que pode mudar nossa percepção do mundo. No entanto, muitos desafios sociais e técnicos devem ser resolvidos antes da sua adoção. Nesta pesquisa, modelamos um sistema autônomo de transferência de energia sem fio, o qual é composto por uma célula solar fotovoltaica como fonte de energia, um conversor DC/RF baseado em um amplificador de potência e um enlace indutivo baseado em indutores planares. Este tipo de sistema pode ser usado para fornecer autonomia energética a implantes biomédicos, evitando os procedimentos cirúrgicos associados à recarga ou à troca da bateria dos dispositivos subcutâneos. Neste documento, resumimos o estado da arte dos sistemas de transferência de energia sem fio autossustentáveis para aplicação em redes corporais sem fio e analisamos os referenciais teóricos dos sistemas de coleta de energia e da célula solar fotovoltaica. Além disso, apresentamos a modelagem do indutor planar e do amplificador de potência e discutimos a teoria usando uma abordagem integrativa baseada em conceitos familiares e novos. Entre as principais contribuições desta pesquisa, destacamos a modelagem dos elementos de transporte e coleta de energia, bem como fontes convencionais de energia. Também enfatizamos a criação de um novo modelo para células solares fotovoltaicas para operação em ambientes internos e um novo método de caracterização experimental para indutores empregados em transferência de potência sem fio. Por fim, propomos uma inovadora metodologia de projeto para sistemas autossustentáveis de transmissão de potência sem fio, a qual maximiza a eficiência e extrai a potência máxima disponível da fonte, focando nas interações de energia entre os subsistemas.

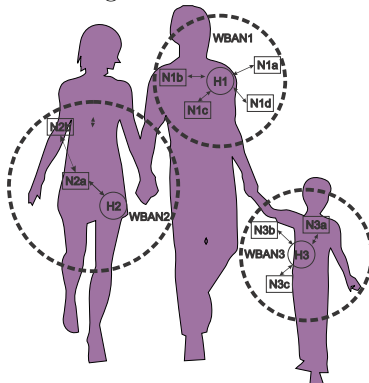
Palavras-chave: Modelagem fotovoltaica, Modelagem de amplificadores de potência, Modelagem de indutores, Redes de área corporal sem fio, Transferência de energia sem fio, Colheita de energia, Modelagem de colheitadeira de energia.

RESUMO EXPANDIDO

TÍTULO DA TESE: Contribuições à modelagem do fluxo de potência nos sistemas de transferência de energia sem fio sustentáveis baseados em links indutivos eficientes.

INTRODUÇÃO E MOTIVAÇÃO: A implementação de uma rede corporal sem fio (WBAN) consiste em instalar nós (N) de ultra baixo consumo de potência no corpo, capazes de estabelecer comunicação com um concentrador (H) também instalado no mesmo corpo, como é mostrado na Figura 1. Os nós e o concentrador são transportados pelo corpo e são capazes de interagir com ele sem uma intervenção consciente da pessoa. A WBAN é uma ferramenta tecnológica que pode mudar nossa percepção do mundo. Esse potencial já é reconhecido pela comunidade científica e industrial, ao ponto de ter se tornado objeto de padronização do IEEE (Instituto de Engenheiros Eletrônicos e Eletricistas). Inúmeras aplicações podem ser vislumbradas, dentre as quais é válido citar próteses auditivas ou de retina, marca-passos ou desfibriladores, monitores de batimentos cardíacos, de pressão ou de glicose, além do tratamento em tempo real de doenças neurológicas, como epilepsia ou mal de Parkinson. No entanto, muitos desafios técnicos e sociais devem ser resolvidos antes da sua plena adoção.

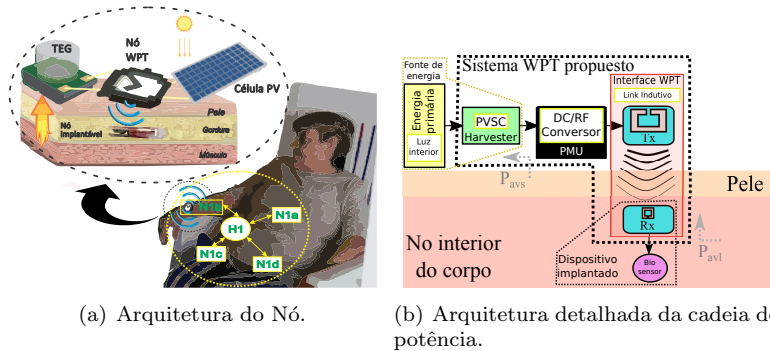
Figure 1 – WBAN.



Fonte: (O autor, 2013)

Pesquisas envolvendo redes de sensores têm sido realizadas desde a década de 1980, mas somente recentemente, com os avanços tecnológicos, especialmente nas áreas de comunicação sem fio e na tecnolo-

Figure 2 – Nó vestível para WPT e conectividade de uma rede WBAN.



Fonte: (O autor, 2014)

gia de circuitos integrados, permitiu-se o desenvolvimento das modernas redes de sensores sem fio (WSN). As WBAN podem ser entendidas como WSN com as suas próprias especificidades. No entanto, elas enfrentam os desafios específicos associados à interação entre a rede e o corpo humano. Por exemplo, se o nó é implantado, cada troca da bateria do nó implica em um procedimento cirúrgico com riscos para a saúde do paciente. Por esse motivo, a autonomia de energia acaba se tornando uma restrição crítica do projeto deste nó.

Em geral, a autonomia energética do nó de uma WBAN pode ser obtida a partir da captação de energia disponível no ambiente, a qual pode ser naturalmente gerada, como a energia térmica radiada pelo corpo, ou artificialmente gerada, como a energia eletromagnética fornecida por uma fonte externa implementada para esse propósito. Com o uso destes tipos de fontes de energia, o tempo de vida da bateria do nó (tempo em que a bateria requer ser trocada) é aumentado e, em algumas vezes, pode superar o tempo em que o nó funciona sem manutenção (tempo de vida do nó).

O Grupo de Pesquisa em Radiofrequência da UFSC tem como um dos seus objetivos a concepção de arquiteturas e metodologias de projeto para nós WBAN miniaturizados com autonomia energética para aplicações biomédicas. Atualmente, está sendo explorada a arquitetura mostrada na Figura 2(a), em que um nó vestível coleta energia das fontes presentes na superfície do corpo humano, como as energias solar e térmica, para dotar de autonomia energética e conectividade um nó implantável miniaturizado.

Esta pesquisa esta focada na análise de um sistema de transferência de potência sem fios (WPT) com autonomia energética. O sistema proposto é composto por uma célula solar fotovoltaica (PVSC), um conversor DC / RF (Amplificador de potência) e um link indutivo baseado em indutores planares, como é mostrado na Figura 2(b).

PERGUNTA DE PESQUISA E OBJETIVOS: Considerando o sistema WPT autônomo mostrado na Figura 2(a).

Pergunta de pesquisa
Como projetar o sistema para maximizar a eficiência de transferência de potência?.

Para responder esta pergunta estabeleceram-se os seguintes objetivos:

Objetivo geral e objetivos específicos
<p>Modelar um sistema de transferência de potência sem fios autônomo com uma célula fotovoltaica como fonte de energia, um amplificador de potência como gerenciador da energia, e um link indutivo como a interface da transferência de energia.</p> <ol style="list-style-type: none">1. Modelar o fluxo de energia nos subsistemas.2. Modelar as interações entre os subsistemas.3. Formular sistematicamente os compromissos no projeto, especialmente aqueles envolvidos no fluxo de energia.4. Avaliar por simulação o sistema proposto.

METODOLOGIA: A metodologia para atingir os objetivos propostos partiu de uma revisão bibliográfica do estado da arte. A partir desta revisão bibliográfica foi possível entender melhor os princípios físicos da operação dos sistemas envolvidos. Após esta etapa, passou-se para o estudo dos sistemas individualmente, usando uma modelagem matemática para cada sistema, o que possibilitou um entendimento aprofundado do funcionamento da cadeia de potência envolvida. Em sequência, passou-se à fase de validação dos modelos. Nesta etapa,

foram projetados e simulados todos os sistemas individualmente. Após verificarmos que estes estavam de acordo com as expectativas teóricas, partiu-se para o desenvolvimento de uma configuração de medição para cada bloco. Com as configurações implementadas, realizaram-se as medições com o objetivo de confirmar o modelo da célula fotovoltaica e do link indutivo.

RESUMO DAS PRINCIPAIS CONTRIBUIÇÕES DESTA PESQUISA:

1. Identificação do estado da arte dos sistemas de transferência de energia sem fio autossustentáveis para aplicação em redes corporais sem fio e analisamos os referenciais teóricos dos sistemas de coleta de energia e da célula solar fotovoltaica. (Apresentado no Capítulo 2)
2. Proposta do conceito de fonte de energia e potencia que permite a modelagem dos elementos de transporte e coleta de energia, bem como fontes convencionais de energia usando o mesmo marco teórico. (Apresentado no Capítulo 2)
3. Proposta um novo modelo para células solares fotovoltaicas para operação em ambientes internos. (Apresentado no Capítulo 3)
4. Proposta de um método de caracterização para indutores empregados em transferência de potência sem fio. (Apresentado no Capítulo 4)
5. Proposta de uma metodologia de modelagem para amplificadores de potência baseada em conceitos simples e novos. (Apresentado no Capítulo 5)
6. Proposta de uma metodologia de projeto para sistemas autossustentáveis de transmissão de potência sem fio, a qual maximiza a eficiência e extrai a potência máxima disponível da fonte, focando nas interações de energia entre os subsistemas. (Apresentado no Capítulo 5)

CONSIDERAÇÕES FINAIS E ARTIGOS PUBLICADOS: Foi possível atingir todos os objetivos propostos para esta pesquisa. Os resultados obtidos permitiram escrever e publicar seis artigos em conferências internacionais e um artigo de revista internacional os quais estão listados no Capítulo 1 deste documento.

LIST OF FIGURES

Figure 1	WBAN.....	
Figure 2	Nó vestível para WPT e conectividade de uma rede WBAN.....	
Figure 3	WBAN.....	39
Figure 4	WPT architecture for powering subcutaneous devices.....	41
Figure 5	WBAN-WPT node concept.....	41
Figure 6	Diagram of SsWPT systems to power an implanted device.....	42
Figure 7	SsWPT architecture for powering subcutaneous devices.....	52
Figure 8	Energy harvesting system concept.....	52
Figure 9	Energy harvesting system general architectures.....	54
Figure 10	Ragone plot of selected energy carriers and sources....	58
Figure 11	Energy power sources.....	59
Figure 12	Conventional HPMU architectures.....	62
Figure 13	Diagram of the energy states of the harvesting system with storage capacity.....	63
Figure 14	Lossless DC voltage EPS	64
Figure 15	Battery model based on lossless DC voltage EPS	64
Figure 16	Diagram of the proposed SsWPT system.....	68
Figure 17	Energy source of the SsWPT system as chapter focus.....	71
Figure 18	The PVSC modeling flow.....	73
Figure 19	Modeling of PVSC devices.....	75
Figure 20	Selected experimental results of the characterization of the PVSC under test.....	83
Figure 21	Experimental setup of the scalar characterization.....	83
Figure 22	Indoor lighting emulator.....	84
Figure 23	Experimental setup of the spectral characterization.....	85
Figure 24	Spectral characterization of the light emulator.....	87
Figure 25	Empirical dataset of the KXOB22-12X1L.....	90
Figure 26	Component values of the circuit model of KXOB22-12X.....	94
Figure 27	Residuals of the fitting process.....	95
Figure 28	Comparison of the math terms of the I_{pv} equation....	95
Figure 29	Predicted I–V characteristics of the PVSC under test.....	96

Figure 30	P_{mp} at the MPP and its error.....	97
Figure 31	Statistics of the absolute error of the e-PVSC models.	98
Figure 32	Current error vs V_{out}/V_{oc} of the PVSC under test.....	99
Figure 33	MAPE of the IN model Vs N. of samples.....	101
Figure 34	Variation of the NI MAPE with respect to the T and n	102
Figure 35	Measured normalized V_{mp}	103
Figure 36	WPT interface of the SsWPT system as chapter focus.	105
Figure 37	Examples of asymmetrical inductive links.....	106
Figure 38	PSOI geometry and electric characteristics.....	112
Figure 39	Results and photograph of the link reported in (CABR-ERA; SOUSA, 2014).	113
Figure 40	Circuit inductor models for WPT applications.	115
Figure 41	Circuit models and the A impact in the WPT system.	118
Figure 42	Diagram of the fixed modeling techniques.....	122
Figure 43	Flowchart of the physics-based RLC extraction process.	123
Figure 44	PSOI example with extracted SRF of 420 MHz.	124
Figure 45	Variations of the fixed model components as a function of the normalized frequency.....	124
Figure 46	Diagram of the scalable modeling techniques.....	125
Figure 47	Broadband model parameters at minimum frequency .	127
Figure 48	Results of the fitting process.....	128
Figure 49	Experimental evaluation of the PSOI Z_e	130
Figure 50	Full-wave EM simulations versus scalable model predictions.	131
Figure 51	Empirical data versus scalable model predictions.....	131
Figure 52	Experimental setup and circuit models.....	134
Figure 53	Theoretical waveforms of the functions e and g	134
Figure 54	Comparison of the experimental data with the simulated and theoretical results.	136
Figure 55	Link model implemented in ADS.....	137
Figure 56	Empirical setup to measure the S-parameters of the link.	138
Figure 57	Results of A and η_{ILPTE}	139
Figure 58	Example of parasitics after test fixture compensation..	141
Figure 59	WPT interface of the SsWPT system as chapter focus.	143

Figure 60	Power chain of the SsWPT system.....	144
Figure 61	Power definitions in a two-port network.....	146
Figure 62	Equivalent circuits of the network with AC energy input.....	148
Figure 63	Linear EPS model and PETO.....	149
Figure 64	PA model based in its port resistors and a controlled power source.....	150
Figure 65	Power source example.....	150
Figure 66	Equivalent DC circuit of a generic PA.....	152
Figure 67	Class-A PA topology.....	153
Figure 68	Class-D PA topology.....	155
Figure 69	Class-E PA with a finite DC-feed inductance.....	157
Figure 70	r_{Lopt} of the ideal class-E amplifier.....	160
Figure 71	Energy flow models of the PA.....	161
Figure 72	SsPA MAE operation and block diagram.....	162
Figure 73	SsPA with ideal impedance matching networks.....	164
Figure 74	Implemented class-A PA.....	166
Figure 75	SsWPT MAE operation and block diagram.....	168
Figure 76	Efficiency versus frequency.....	168
Figure 77	PVSC I-V characteristic and P_{avs}	175
Figure 78	$r_{L_{opt}}$ for the Class-E PA.....	176
Figure 79	Ideal class-E PA with a finite DC-feed inductance.....	178
Figure 80	Approximate waveforms of class-E PA for $D_{SH} = 0.5$	179
Figure 81	Component design set and space for $D_{SH} = 0.5$	181
Figure 82	Simulation setup and PA waveforms for SsWPT system of study case 1.....	182
Figure 83	Component design spaces of SsWPT system for study case 2.....	185
Figure 84	Simulation setup and waveforms of the SsWPT system for study case 2.....	188
Figure 85	Simulation setup of SsWPT system for study case 2... ..	189
Figure 86	Performance metrics of the SsWPT system and SsPA under non-nominal operation.....	192
Figure 87	World's age pyramid. Based on (UNDESA-POPULATION-DIVISION, New York, United Nations Department for Economic and Social Affairs (UN DESA), Working Paper No. ESA/P/WP.	

228, 2013)	202
Figure 88 Self-sustaining implanted device using Energy Harvesting and WTP.....	203
Figure 89 Wireless network comparison.	205
Figure 90 Schematic view of conventional network challenges in WBANs, WSNs and WLANs. Based on (ZASOWSKI, Dept. Elect. Eng, Ph.D. thesis, Federal Institute of Technology (ETH), Zurich,Switzerland, 2007)	206
Figure 91 Simplified architecture of an isolated WBAN	207
Figure 92 Simplified architecture of a medical TI solution based on WBAN.....	207
Figure 93 Proposed WBAN taxonomy.....	209
Figure 94 Typical architecture of a sensor node	214
Figure 95 Consumption and transfer rates of NB, UWB and HBC transceivers	215
Figure 96 General composition of a body implant	216
Figure 97 Schematic representation of WBAN node	218
Figure 98 Combined electrical-circuit based model.....	224
Figure 99 Hydraulic analogy of a loaded EPS.....	226
Figure 100 DC voltage source with limited energy storage capacity	228
Figure 101 Battery model proposed by (CHEN; RINCON-MORA, 2006) using the ideal battery model	230
Figure 102 Thermoelectric generator model and diagram.	236
Figure 103 Circuit model and SoE of an energy EPS composed of an on-body TEG and its HPMU.....	238
Figure 104 SISO HPMU architecture.....	242
Figure 105 Architectures of MISO EH.....	246
Figure 106 Architectures of MIMO EH.....	247
Figure 107 The proposed electrical model of a battery.	254
Figure 108 Voltage discharge curve of Li-ion battery.....	254
Figure 109 Electrical model of supercapacitors.....	256
Figure 110 Concept of P&O in a PV cell.	259
Figure 111 Losses in the switches as a function of the width.	261
Figure 112 Simulated results of the UT9-28-F2-4040-TA-W6 device.	266
Figure 113 PVSC model, I-V curve and diagram.	267
Figure 114 Simulated results of the KXOB22-12X1L	270

Figure 115 Conventional WPT system for powering subcutaneous devices.	277
Figure 116 Analyzed energy flow problem.	284
Figure 117 Norton (nt) and Thevening (th)	286
Figure 118 Real DC voltage source models	286
Figure 119 Ideal battery	286
Figure 120 PETO for lossless source	287
Figure 121 PETO for a source w/o loss of self-consumption	288
Figure 122 PETO for the voltage source	291
Figure 123 η and load power boundaries vs. k	291
Figure 124 Experimental and theoretical results for PETO on an emulated DC voltage source of $k = 90$	292
Figure 125 Energy current sources	293
Figure 126 Battery loaded by a generic load.	294
Figure 127 Block Diagram of the system with DC transformer model for switched DC/DC converter.	298
Figure 128 Block Diagram of the system with DC/DC converter. .	298
Figure 129 Photograph and model of the link optimized in (CABR-ERA; SOUSA, 2014).	319
Figure 130 PVSC model and experimental setup.	321

LIST OF TABLES

Table 1	Specifications of portable electronic equipments.....	57
Table 2	Comparison in-body harvesting sources uniformly distributed.....	67
Table 3	Coefficients of the calibration fitting.....	86
Table 4	Specifications of the KXOB22-12X1L under AM1.5g. ...	86
Table 5	Parameter extraction steps based on (CUBAS; PINDADO; VICTORIA, 2014).	92
Table 6	Parameters of IN model of the KXOB22-12X1L.....	94
Table 7	Summary of the predicted error of the models.....	99
Table 8	SoA of the models for indoor PVSCs.....	100
Table 9	Geometric parameters of the implemented PSOs.....	129
Table 10	Summary of model errors.....	132
Table 11	Geometric parameters of Tx and Rx PSOI.....	137
Table 12	Resulting maximum values of A and $\eta_{ILPTE_{max}}$	138
Table 13	Comparison with the SoA.....	140
Table 14	Design methodology for SsPA systems.....	163
Table 15	$r_{L_{opt}}$ for the analyzed Pas.....	164
Table 16	PA specifications.....	165
Table 17	PA simulation results.....	165
Table 18	PA experimental results.....	166
Table 19	DC/RF converter specifications.....	167
Table 20	SsPA experimental results.....	167
Table 21	Design methodology for SsWPT systems.....	172
Table 23	Design results of the SsWPT system of study case 1.....	174
Table 24	Simulation results of study case 1 for $f = 399\text{MHz}$ and $D_{SH} = 50\%$	183
Table 25	Design results of the SsWPT system of study case 2.....	184
Table 26	Values of circuit elements in the PA optimization.....	186
Table 27	Performance metrics of the PA optimization.....	187
Table 28	Simulation results for study case 2, $f = 399\text{ MHz}$ and $D_{SH} = 50\%$	190
Table 29	Main results of optimized photovoltaic SsWPT systems.....	191
Table 30	Comparison of in-body harvesting sources uniformly dis-	

tributed.....	197
Table 31 EPS taxonomy	225
Table 32 Analogies between variables	226
Table 33 Significant electric battery behaviors.....	229
Table 34 Comparison of the proposed CECBMs.....	231
Table 35 Comparison of the dependencies of the circuit values on the analyzed models.....	232
Table 36 Comparison between low-power PPU's	248
Table 37 Comparison between losses in low-power PPU's	249
Table 38 Performance measures: Rechargeable technologies involved in storage capacity and energy supply	252
Table 39 Measures of efficiency: Rechargeable technologies involved in energy recharge capacity.....	252
Table 40 Specifications of the UT9-28-F2-4040-TA-W6 TEC mod- ule.	265
Table 41 Specifications of the KXOB22-12X1L under AM1.5g light spectrum.....	270
Table 42 Power of the most significant harvesters for W-WBAN ..	275
Table 43 Comparison in-body harvesting sources uniformly dis- tributed.....	278
Table 44 Estimated Runtime with P_o consumption and optimum RL	297
Table 45 Estimated Runtime with P_o consumption and optimum RL	297
Table 46 Optimum Voltage and current results.....	299
Table 47 Geometric parameters of the Link PSOI.....	317
Table 48 Summary of the inductive link model.....	317
Table 49 Summary of the inductive link model parameters.....	318
Table 50 Specifications of the KXOB22-12X1L under AM1.5g. ...	318
Table 51 Summary of PVSC model equations.....	320
Table 52 Model parameters of the PVSC (i.e., KXOB22-12X1L)..	320

LIST OF ABBREVIATIONS AND ACRONYMS

WBAN	Wireless Body Area Network
IEEE	Institute of Electrical and Electronics Engineers
EM	Electromagnetic
RF	Radio Frequency
WPT	Wireless Power Transfer
CMOS	Complementary Metal-Oxide-Semiconductor technology
PVSC	PhotoVoltaic Solar Cell
DC	Direct Current
PMU	Power Manager Unit
SsWPT	Self-sustaining WPT
PA	Power Amplifier
FoM	Figure of Merit
SISO	Single-Input Single-Output
MISO	Multiple-Input Single-Output
LED	Light-Emitting Diode
EPS	Energy Power Source
AC	Alternating Current
MAPE	Mean Absolute Percentage Error
MPP	Maximum Power Point of a EPS
SRF	Self-Resonance Frequency
SoA	State-of-the-Art
PSOI	Planar Square One-turn Inductors
HPMU	Harvesting PMU
ENO	Energy Neutral Operation
SoE	State of Energy
PPU	Power Processing Unit
MPP	Maximum Power Point
MPPT	Maximum Power Point Tracking
e-PVSC	Extended PVSC model
STC	Standard Test Conditions for characterizing an PVSC
FL	FLuorescent
HA	HAlogen

IESNA	Illuminating Engineering Society of North America
2D&2R	2–Diodes /2–Resistors circuit
STD	STandard deviation
NI	Non-Interpolated PVSC model
IN	Interpolated PVSC model
VNA	Vector Network Analyzer
IUT	Inductor Under Test
MAG	Maximum Available (power) Gain
EMPro	Electromagnetic Professional
MATLAB	MATrix LABoratory
MAE	Maximum Available Efficiency
TEG	Thermoelectric Generator
MIMO	Multiple-Input Multiple-Output
ADS	Advanced Design System
1D&2R	1–Diodes /2–Resistors circuit model

LIST OF SYMBOLS

η_W	Efficiency of the WPT system
$\eta_{W_{PTE}}$	Power transfer efficiency of the WPT system.
P_{inW}	Input power of the WPT system
P_{LW}	Power consumed by the load of the WPT system
P_{avs}	Maximum available power of the source
$\eta_{W_{PTEM}}$	Maximum power transfer efficiency of the WPT system.
Q	Electric quality factor
D_J	Energy density
D_W	Power density
P	Electric power
E	Electric energy
E_{st}	Energy storage capacity of an EPS
E_L	Energy consumed by the load
P_L	Power consumed by the load
i_L	Current of the load
v_L	Voltage of the load
η_{eps}	Efficiency of a generic lossy EPS
E_s	Stored energy in the EPS
P_s	Generated power by the EPS
E_0	Initial stored energy of the EPS
E_h	Extracted energy by the HPMU from a harvester
η_h	Efficiency of input PPU of a conventional HPMU
η_s	Efficiency of output PPU of a conventional HPMU
L_v	Illuminance
G_λ	Spectral irradiance
λ	Wavelength of the electromagnetic wave
A_e	Active area of the PVSC
R_λ	Responsivity of the PVSC
h_P	Planck's constant
c_s	Speed of the electromagnetic wave
ϕ_e	Radiant power of the electromagnetic wave
ϕ_v	Luminous radiant power of the electromagnetic wave

A_R	Corresponding area of the surface integral
V_λ	Luminosity function or luminous efficiency
k_m	Maximum spectral luminous efficiency
v_{idc}	Input voltage of the indoor lighting emulator
L_c	Illuminance on the center of the measurement plane of the indoor lighting emulator
$G_{\lambda_{LED}}$	the G_λ produced by the light LED emulator
$\hat{G}_{\lambda_{LED}}$	the $G_{\lambda_{LED}}$ normalized spectral distribution
$G_{v\%}$	percentage value of the G concentrated inside the visual range
PAR_L	Photosynthetically active radiation of the light LED emulator
L_{LED}	Illuminance of the light LED emulator
G_{LED}	Irradiance of the light LED emulator
$E_{lm\%}$	percentage error of L_{lm} produced by the mismatch between the standard incandescent lamp and the light LED emulator
L_{spL}	Illuminance of the light emulator measured by spectroradiometer
L_{lmL}	Illuminance of the light emulator measured by the lux meter
MF_L	Spectral mismatch correction factor of the lux meter for the light emulator
V_{out}	Output voltage
I_{out}	Output current
P_{out}	Output power
R_x	Receiver inductor of the inductive link
T_x	Transmitter inductor of the inductive link
k_{IL}	Magnetic coupling coefficient of the inductive link
d_{IL}	Distance between the Tx and Rx coils of the link
A	Electromagnetic coupling level of the inductive link
Q_1	Quality factor of the transmitter inductor
Q_2	Quality factor of the receiver inductor
$Q_{E_{max}}$	Generally accepted definition of the quality factor in physics and engineering context
W_{max}	Maximum total stored electric and magnetic energy
W_{diss}	dissipated energy per cycle

Q_a	Apparent inductor quality factor
E_Q	Estimation error in a given Q by using Q_a
Z_e	Input impedance of the inductor
t_c	Metal thickness of the planar square one-turn inductor
d_{avg}	Average diameter of the planar square one-turn inductor
w_{ind}	Line width of the planar square one-turn inductor
t_s	Substrate thickness of the planar square one-turn inductor
r	Real part of Z_e
x	Imaginary part of Z_e
f	Electric frequency
L_a	Apparent inductance of the coil
f_{opt}	Optimum frequency
L_s	Equivalent series inductance of the RL inductor model
R_s	Equivalent series resistance of the RL inductor model
L_p	Equivalent inductance of the RLC inductor model
C_p	Equivalent capacitance of the RLC inductor model
R_p	Equivalent resistance of the RLC inductor model
L	Inductance
C	Capacitance
R	Resistance
\bar{W}_M	Average stored magnetic energy
\bar{W}_E	Average stored electrical energy
$Q_{\bar{W}}$	Conventional Q definition based on average stored energies
ω	Electric angular frequency
Z_G	Impedance of the generator
R_G	Resistance of the generator
X_G	Reactance of the generator
Z_L	Impedance of the load
R_L	Resistance of the load
X_L	Reactance of the load
L_1	Inductance of the Tx coil
R_G	Inductance of the Rx coil
M	Mutual inductance between the Tx and Rx coils
η_{IL}	Link efficiency

$P_{in_{IL}}$	Input power of the link
$P_{L_{IL}}$	Power consumed by the load of the link
C_1	Self-capacitors of the Tx coil
C_2	Self-capacitors of the Tx coil
R_1	Resistance of the transmitter inductor
R_2	Resistance of the receiver inductor
$\eta_{IL_{PTE_M}}$	Maximum power transfer efficiency of the link
η_{IL_M}	Maximum efficiency of the link
s_{xy}	S-parameter from port y to port x
Z_0	Characteristic impedance of the VNA, cabling, and connectors
K_γ	Complete elliptic integral of the first kind
E_γ	Complete elliptic integral of the second kind
η_{PTE}	Power transfer efficiency
G_T	Transducer power gain
η_{PTE_M}	Maximum power transfer efficiency
G_A	Available power gain
η	Efficiency
G_P	Power gain
$\eta_{mp_{AC}}$	MPP efficiency of the AC load
$\eta_{mp_{DC}}$	MPP efficiency of the DC load
η_{mp}	MPP efficiency of the load
P_{RF}	Power delivered by the RF port of the PA
P_{DC}	Power consumed by the PA from its DC port
P_{AC}	Power consumed by the PA from its AC port
I_{RF}	Current of the RF port of the PA
I_{DC}	Current of the DC port of the PA
I_{AC}	Current of the DC port of the PA
V_{RF}	Voltage of the RF port of the PA
V_{DC}	Voltage of the DC port of the PA
V_{AC}	Voltage of the DC port of the PA
η_{PA}	Efficiency of the PA
R_{DC}	Impedance imposed by the PA at its DC Port
R_{bias}	Equivalent impedance of the PA bias circuit
R_{PA}	Equivalent impedance of the PA power stage

I_{PA}	Current of the power stage of the PA
I_{Bias}	Current of the bias circuit of the PA
r_L	Load impedance factor of the PA
r_G	Generator impedance factor of the PA
$r_{L_{opt}}$	Optimum load impedance factor of the PA
$r_{G_{opt}}$	Optimum generator impedance factor of the PA
$R_{DC_{opt}}$	Optimum R_{DC}
$R_{L_{opt}}$	Optimum R_L
I_{pv}	Photovoltaic current
I_D	Current predicted by Shockley diode equation
I_0	Saturation current of the diode
ϕ_t	Thermal voltage
q_e	Electron charge
k_B	Boltzmann constant
T	Temperature
n	Ideality constant of the diode
R_{SS}	Series resistance of the PVSC model
R_{SP}	Parallel resistance of the PVSC model
I	Electric current
V	Electric voltage
P_{mp}	Power supplied by the harvester at MPP operation
V_{mp}	Voltage in the MPP
I_{mp}	Current in the MPP
I_{sc}	Short circuit current
V_{oc}	Open circuit voltage
G	Irradiance

CONTENTS

1	INTRODUCTION	39
1.1	MOTIVATION	39
1.2	SCOPE OF WORK	41
1.3	ASSOCIATED PUBLICATIONS	45
1.4	STRUCTURE OF THIS DOCUMENT	48
2	A SURVEY ON ENERGY HARVESTING FOR WBAN APPLICATIONS	51
2.1	ENERGY HARVESTING SYSTEMS	51
2.2	STOCHASTIC NATURE OF HARVESTERS	54
2.3	THEORETICAL FRAMEWORK OF THE ENERGY-NEUTRAL OPERATION	55
2.3.1	Energy demands in WBAN applications	56
2.3.2	Energy and Power Sources	58
2.3.2.1	EPS concept and proposed taxonomy	58
2.3.2.2	Energy flow modeling	60
2.3.2.3	Energy neutral operation	61
2.3.2.4	The battery as EPS example	62
2.3.2.5	Harvester as EPS example	64
2.3.2.6	Maximum power point operation	65
2.4	SELF-SUSTAINING INDUCTIVE COUPLING SYSTEMS FOR POWERING CMOS IMPLANTED DEVICES	66
2.5	CONCLUSIONS AND CONTRIBUTIONS	69
3	ON THE MODELING OF INDOOR PHOTOVOLTAIC SOLAR CELLS FOR WBAN HARVESTING APPLICATIONS	71
3.1	INTRODUCTION	72
3.2	STATE-OF-THE-ART OF THE INDOOR PVSC MODELING	77
3.2.0.1	Small-signal modeling on both L_v (or G) and T .	77
3.2.0.2	Large-signal modeling for L_v (or G) and small-signal modeling for T	77
3.3	THEORETICAL FRAMEWORK	79
3.3.1	1D&2R circuit as PVSC model	79
3.3.2	PVSC as an indoor harvester	80
3.3.3	Indoor spectrum mismatch	80
3.3.4	PVSC modeling based on illuminance	82
3.4	METHODS AND EXPERIMENTS	83

3.4.1	Test Setup	84
3.4.1.1	Scalar characterization of the light emulator	85
3.4.1.2	Spectral characterization of the light emulator	86
3.4.1.3	Commercial PVSC device	88
3.4.1.4	Characterization of the PVSC under test	88
3.4.2	Resulting dataset	89
3.5	PROPOSED MODELING METHODOLOGY AND STUDY CASE	91
3.5.1	Extraction of the 1D&2R circuit values	91
3.5.2	Fitting of the 1D&2R circuit values	92
3.5.3	Estimation of the payload power constraint	93
3.5.4	Study Case: KXOB22-12X1L modeling	93
3.6	DISCUSSION AND FUTURE WORK	99
3.7	CONCLUSIONS AND CONTRIBUTIONS	103
4	ON THE MODELING OF PLANAR SQUARE ONE-TURN INDUCTORS FOR WIRELESS POWER TRANSFER APPLICATIONS	105
4.1	INTRODUCTION	106
4.2	PLANAR SQUARE ONE-TURN INDUCTOR	112
4.2.1	Geometry and frequency response	112
4.2.2	Inductive links based on PSOI devices	112
4.3	THEORETICAL FRAMEWORK	114
4.3.1	Lumped circuit inductor models for WPT applications	114
4.3.1.1	Lumped RL circuit used as an inductor model	114
4.3.1.2	A lumped RLC circuit as an inductor model	115
4.3.1.3	Inductor quality factor	116
4.3.2	The power transfer effectiveness of the inductive link	118
4.3.3	The relationship between A and the S-parameters of the link	120
4.4	MODELING METHODOLOGY	121
4.4.1	Fixed models of the PSOI	121
4.4.2	Scalable compact models of the PSOI	122
4.4.2.1	Set of equations of the compact model	126
4.4.2.2	Adjusting the model's parameters	127
4.4.2.3	Extending the scalable model for an inductive link	128
4.5	EVALUATING THE MODEL	129
4.5.1	Accuracy of the Z_e estimation	129
4.5.1.1	Simulation and experimental setup	129
4.5.1.2	Results	129

4.5.2	Accuracy of the Q estimation	130
4.5.2.1	Measurement methodology	132
4.5.2.2	Simulation and Experimental Setup	134
4.5.2.3	Results	135
4.5.3	Accuracy of the A estimation	136
4.5.3.1	Simulation and experimental setup	136
4.5.3.2	Results	138
4.6	DISCUSSION AND FUTURE WORK	139
4.7	CONCLUSION AND CONTRIBUTIONS	142
5	ON THE MODELING OF SELF-SUSTAINING WPT (SSWPT) SYSTEMS	143
5.1	INTRODUCTION	144
5.2	THEORETICAL FRAMEWORK	146
5.2.1	Gains and efficiencies of the two-port networks	146
5.2.2	Simple power gain expression using equivalent impedances of the system	147
5.2.3	Power-efficiency trade-off in a power EPS	148
5.3	ON THE PA MODELING FOR WIRELESS POWER TRANSFER APPLICATIONS	149
5.3.1	PA Modeling using equivalent impedances in its input power ports	149
5.3.2	Efficiency of the PA	151
5.3.2.1	Example 1: BJT class-A PA	152
5.3.2.2	Example 2: CMOS class-D PA	154
5.3.2.3	Example 3: Ideal class-E PA	156
5.3.3	Power transfer efficiency of the PA	159
5.3.4	Maximum power transfer efficiency of the PA	160
5.4	DESIGN A SELF-SUSTAINING PA (SSPA) FOR MAE	162
5.4.1	Design methodology for SsPA systems	162
5.4.2	PA study case 1: SsPA based on class-A PA	165
5.5	DESIGN FOR MPP OPERATION OF THE SSWPT	167
5.5.1	Optimum frequency of a SsWPT system	167
5.5.2	Design methodology proposed for SsWPT systems	169
5.5.3	Study Case 1: SsWPT system based on an ideal class-E PA	173
5.5.4	Study Case 2: SsWPT system based on a "real" class-E PA	180
5.6	DISCUSSION AND FUTURE WORK	189
5.7	CONCLUSION AND CONTRIBUTIONS	191
6	CONTRIBUTIONS AND FUTURE WORK	193
6.1	CONTRIBUTION	193

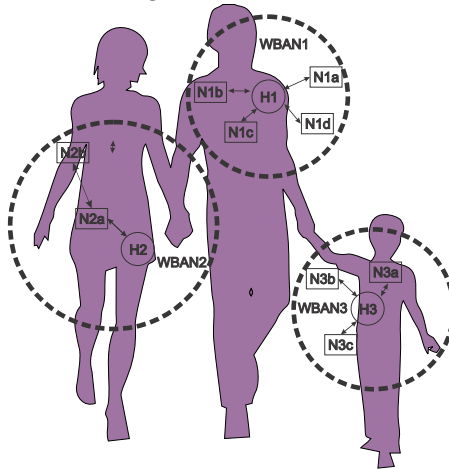
6.2	SPECIFIC CONTRIBUTIONS	193
6.3	FUTURE WORK	194
6.4	ASSOCIATED PUBLICATIONS	195
	APPENDIX A – A brief survey of WBAN.....	201
	APPENDIX B – A survey of typical electric loads and associated power demands for WBANs	213
	APPENDIX C – Using the EPS concept for mod- eling batteries	223
	APPENDIX D – WBAN harvester as Example of Power and Energy EPS.....	235
	APPENDIX E – A survey of power management and processing units for WBAN applications.....	241
	APPENDIX F – MPP examples of linear and non- linear EPS	265
	APPENDIX G – Energy constraints imposed by the harvesting EPSs in WBAN environmental con- ditions	275
	APPENDIX H – The Power–Efficiency Trade-Off on a linear EPS	283
	APPENDIX I – Tutorial of implementation of the ideal class-E model in Maple	303
	APPENDIX J – ADS® models of the link and the indoor PVSC device	317
	References	323

1 INTRODUCTION

1.1 MOTIVATION

A Wireless Body Area Network (WBAN) is a wireless network that operates in, on, or around the body. The implementation of a WBAN consists of placing ultra-low power nodes capable of establishing communication with a concentrator node that is installed in the same body, as shown in Figure 3. The wearer carries these nodes, which are capable of interacting with his body without any conscious intervention. Several applications can be imagined, among them are: (a) medical treatment, monitoring, and diagnosis; (b) remote health/fitness monitoring; (c) safeguarding of uninformed personnel; (d) telemedicine systems; (e) training schedules of professional athletes; (f) consumer electronics; (g) advanced human-computer interfaces; and (h) personal information sharing.

Figure 3 – WBAN.



Source: (The author, 2013)

The WBAN is a technological tool that can change our perception of the world. The scientific and industrial communities already recognize this potential to the extent that the IEEE (Institute of Electrical and Electronics Engineers) has standardized it. However, many social and technical challenges must be solved before its full adoption.

Many researchers have completed projects related to wireless sensor networks since the 1980s. However, their efforts were limited by technological challenges. In particular, the current advances in the areas of wireless communication and integrated circuit technology now make possible the development of modern wireless sensor networks. We can understand the WBAN, with its specifications, as one of these networks, but with particular challenges associated with the interaction between this type of network and the human body.

WBANs have become very common in recent years. The miniaturized wearable or implanted nodes have been commercialized, with a large number of prototypes and solutions available on the market. However, they require coin-cell batteries, which define the form factor and the energy autonomy of the WBAN node. This characteristic becomes very important because the energy autonomy of an implanted node represents a risk to the wearer's health. When the battery's energy runs out, it must either be recharged or changed. In most cases, this means a surgical procedure, which is costly, stressful, and also poses the risk of medical complications.

In general, a portable electronic device could increase its energy autonomy using a harvester to collect ambient energy, which could be naturally or artificially generated. An example of natural energy is heat radiated by the human body. On the other hand, electromagnetic (EM) energy present in the Radio Frequency (RF) band on the radio signals (e.g., TV, Wi-Fi, and cell phone) is an example of artificial energy. Scholarly literature shows that the research on energy-harvesting systems for wearable or implanted WBAN applications is still in its early stages.

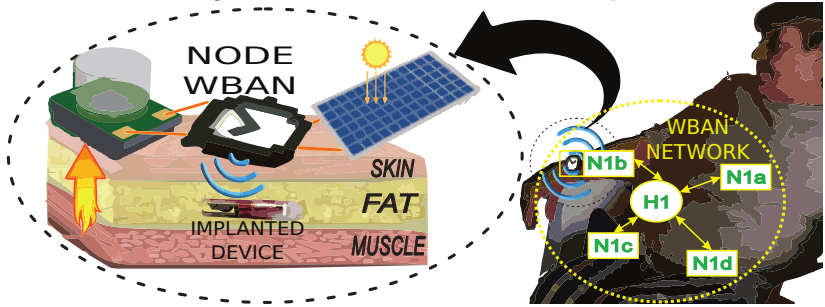
Nowadays, some proofs of concepts of autonomous implants have been designed and tested. They harvest energy from some organs of the body (e.g., kinetic energy from the heart rhythm) or from other natural sources evenly distributed under the human skin (e.g., subcutaneous light). However, there are many parts of the body where there is not enough ambient energy to supply the implant demand. A possible solution is the artificial generation of an in-body energy source using Wireless Power Transfer (WPT) techniques, as shown in Figure 4. The principal drawback to this approach is that the resulting external unit is not wearable or has limited energy autonomy. Moreover, in this architecture, there is a direct correlation between system efficiency and the functionalities of the implanted device. This is because an "optimum" design of the implants allows converting the consumed power into device performance.

Figure 4 – WPT architecture for powering subcutaneous devices.

Source: (The author, 2017)

1.2 SCOPE OF WORK

Figure 5 – WBAN-WPT node concept.

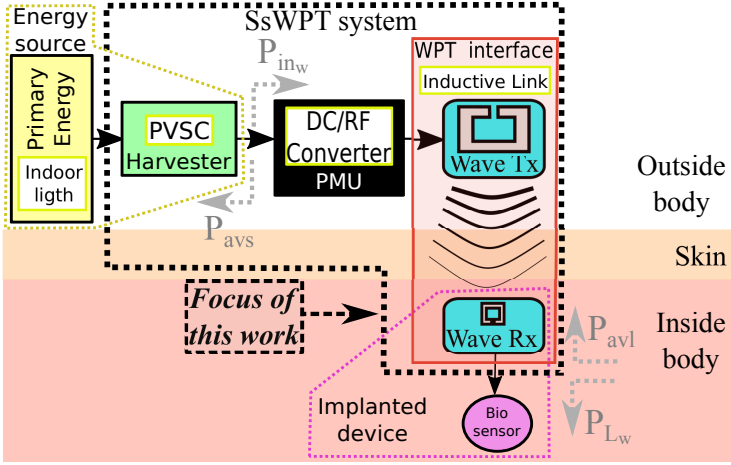


Sources: (The author, 2014)

One of the objectives of our research group is the conception of architectures and design methodologies for implanted WBAN nodes with energy autonomy for biomedical applications. Furthermore, we are currently focused on the transition from the idea to the reality of the WBAN-WPT node, shown in Figure 5. The WBAN-WPT node is an on-body node that collects energy from the sources available on or around the body (e.g., solar or thermal) and provides energy autonomy (and connectivity) to an implanted device fabricated on complementary metal-oxide-semiconductor (CMOS) technology. This work represents one of the first steps in the development of the WBAN-WPT node. More specifically, we modeled a WPT system composed of a photovoltaic solar cell (PVSC), a DC/RF converter, and an inductive link that is based on planar inductors. In Figure 6, we illustrate the diagram of the modeled system.

In this research, we focused in the modeling of autonomous WPT systems composed of a harvester, a power manager unit (PMU), and an EM WPT interface. The architecture of this type of WPT system is shown in Figure 6. In this document, we refer to this type of WPT system as a self-sustaining (Ss) WPT (SsWPT) system. Moreover, we analyze systematically the different trade-offs involved in the system-

Figure 6 – Diagram of SsWPT systems to power an implanted device.



Source: (The author, 2017)

and circuit-level design to answer the following question:

Main research question
How to maximize the available power at the output of an SsWPT system with a harvester as the energy source, a power amplifier (PA) as the PMU, and an inductive link as the WPT interface?

In a conventional WPT system, the power that the system can supply to the payload is limited only by the losses in energy extraction, storage, and transfer. On the other hand, in SsWPT systems, this power is limited both by these losses and by the power constraint imposed by the harvesting source. This power value becomes the main power constraint to its load. For example, although the EM energy of the indoor light can be considered practically infinity, the power that harvests an indoor PVSC is limited by many factors, such as the light spectrum, irradiance, temperature, and its spectral quantum efficiency.

We can calculate the energy transfer effectiveness of the WPT system using two figures of merit (FoMs), its efficiency (η_w), and its

power transfer efficiency ($\eta_{W_{PTE}}$). These FoMs are given by:

$$\eta_W = \frac{P_{L_W}}{P_{in_W}}; \quad (1.1)$$

$$\eta_{W_{PTE}} = \frac{P_{L_W}}{P_{avs}}; \quad (1.2)$$

where P_{in_W} is the input power of the WPT system, P_{L_W} is the power consumed by the load of the WPT system, and P_{avs} is the maximum available power of the source, which is the maximum power that the harvester can supply to the WPT system. We illustrated these powers in the SsWPT system shown in Figure 6.

In this research, we characterize the performance of the SsWPT system using its maximum power transfer efficiency ($\eta_{W_{PTE_M}}$) because it numerically quantifies the system capability to extract the P_{avs} of the harvester (i.e., the PVSC) and to make this power available to the payload (i.e., the Biosensor). This efficiency is given by:

$$\eta_{W_{PTE_M}} = \frac{P_{avl}}{P_{avs}}; \quad (1.3)$$

where P_{avl} is the available power of the WPT system to its output, which is the maximum power that the system can supply to the payload. Considering this context, we reformulated the research question as follows:

Reformulated main research question
<p>Considering an SsWPT system with a harvester as the energy source, a PA as PMU, and an inductive link as the WPT interface, how to design the system to maximize its maximum power transfer efficiency?</p>

In the conventional design approach of WPT systems, the designer reduces the interactions among harvesters, converters, and load to voltage and current specifications between the subsystems. Then each subsystem is individually optimized using the voltage (or current) specifications as constraints in the optimization process. However, following this approach, the output power is only partially maximized, because the designer can decrease the energy losses optimizing the interactions among the subsystems. Therefore, to obtain maximum power

transfer efficiency, the designer must decrease the losses involved in the energy processing (i.e., extraction, storage, and transfer process), and must optimize the interactions between subsystems.

To answer the research question considering this context, we defined the aim of our work as:

Research objectives

Model an SsWPT system with a harvester as the energy source, a PA as PMU, and an inductive link as the WPT interface.

Specifically, the research objectives pursued to answer the research question are:

1. Model the energy flow in the subsystems, which are the harvester, converter, and inductive link.
2. Model the interactions among the subsystems.
3. Formulate the design trade-offs systematically, especially those involved in the energy flow.
4. Evaluate by simulation the SsWPT system that is based on an indoor PVSC, DC/RF converter, and inductive link.

As discussed before, the analyzed system is composed of an indoor PVSC, a DC/RF converter, and an inductive link based on planar inductors. This scheme is a SISO (single-input single-output) WPT system without energy storage capacity. However, the concepts developed in this thesis may also be extended easily to multiple-input single-output (MISO) with or without energy storage devices.

Another common concern in the design of WPT systems is the optimization of the inductive link. This optimization depends on the link (and coil) geometry, sizes (and alignment) of the coils, operation frequency, etc. This subject will not be addressed in this thesis because our methodology maximizes the power transfer efficiency of a WPT system with a preoptimized WPT interface. In this research, we used an optimized inductive link previously reported in the literature. The reference inductive link was optimized, considering that the material around the inductors is air and there the receiver has a size restriction. However, the concepts developed in this thesis may also be used in a future work to maximize by design the power transfer efficiency of a WPT system based on inductive links, which had been optimized with

respect to biological tissues.

A common concern about the modeling of harvesters is their stochastic nature; however, we do not address this topic in the modeling of the indoor PVSC. In our modeling approach, we model the device under warm LED (light-emitting diode) spectrum, illuminance from 177 to 33.3×10^3 lm/m², and room temperature. These test conditions emulate the worst-case conditions at indoors, and the resulting model is advantageous in harvesting applications because it predicts the power constraint imposed by the indoor PVSC device to its load.

There are many DC/RF converter topologies; we focus on the one composed of a PA and an oscillator. However, the modeling techniques proposed and used in this research can be extended easily to other topologies, such as the power oscillator one.

1.3 ASSOCIATED PUBLICATIONS

As a result of the research activities developed during the doctoral program, we published eight papers (six in conferences and two in journals). Here is a summary of those publications.

Paper I. Simple expression for estimating the switch peak voltage on the class-E amplifier with finite DC-feed inductance.(FAJARDO; SOUSA, 2016c)

Conference: 2016 IEEE 7th Latin American Symposium on Circuits Systems (LASCAS).

Abstract: The class-E power amplifier is widely used due to its high efficiency, resulting from switching at zero voltage and zero slope of the switch voltage. This paper presents an analytical expression of the gain between the DC input voltage and the peak switch voltage on an ideal class-E power amplifier with finite DC-feed inductance. This expression is verified by simulations, and it is evaluated by experimental results at a switching frequency of 10.24 MHz. Considering the results (simulated and experimental), the maximum error was 10.2%.

Paper II. A taxonomy for learning, teaching, and assessing wireless body area networks.(FAJARDO; SOUSA, 2016d)

Conference: 2016 IEEE 7th Latin American Symposium on Circuits Systems (LASCAS).

Abstract: Wireless body area networks have recently gained attention, mainly after the IEEE 802.15.6 standard had been proposed. Review-

ing the literature, we easily recognize that several authors use different terminologies for a single concept or a single terminology for different concepts. This generates confusion and blocks fair comparisons between systems. In this paper, we present an overview of wireless body area networks with focus on the applications. Moreover, we propose a detailed taxonomy that could help to disambiguate the confusion regarding current WBAN terminology.

Paper III. Revisiting the power-efficiency trade-off on a DC voltage source.(JAIMES; SOUSA, 2016)

Conference: 2016 IEEE 7th Latin American Symposium on Circuits Systems (LASCAS).

Abstract:When a DC voltage source supplies energy to an electric load, it can operate either for maximum power transfer and low efficiency (50%), or with an acceptable efficiency with less power transferred. In this paper an analytic expression is developed and used to quantify this trade-off. Moreover, this expression is validated by an experimental circuit demonstrator.

Paper IV. Revisiting battery modeling using the energy power supply concept.(FAJARDO; SOUSA, Florianopolis, Brasil. 2016)

Conference: 22nd IBERCHIP (Ibero-American network of microsystem manufacturing services, for industry support and continuous training of microtechnologies experts) Workshop (IBERCHIP2016).

Abstract: Using the concept of an electric source of both energy and power, a source that we refer to as an energy power source (EPS), this paper proposes a DC voltage source with limited energy storage capacity, which models the energy storage capacity of the batteries, the involved energy transfer process, and the constant voltage output behavior when the battery has storage energy. Further, this circuit source is used for understanding the combined electrical circuit-based battery model, which is commonly used for designing of portable electronic devices, hybrid electric vehicles, and smart grid systems.

Paper V. Integrated CMOS class-E power amplifier for self-sustaining wireless power transfer system.(FAJARDO; SOUSA, 2016a)

Conference: 2016 29th Symposium on Integrated Circuits and Systems Design (SBCCI) .

Abstract: In this paper is proposed a methodology for designing a CMOS class-E PA used to drive an inductive link. In order to satisfy the operating conditions imposed by the PA specifications and the available technology, a differential class-E PA with split slab inductor

and high level of integration was both designed and simulated. The proposed methodology uses the analytical solution of the ideal class-E PA equations as the first point of an iterative procedure for solving the optimization of the PA. Further, the proposed design set solves the trade-off between ON-resistance and gate capacitance of the switches, resulting in the optimal choice of the power transistors width for a class-E PA with finite DC-feed inductance. In the post-layout simulation, the power added-efficiency of the PA was 45.7% when 20.7 dBm.

Paper VI. Modeling and design of high-efficiency power amplifiers fed by limited power sources.(FAJARDO; SOUSA, 2016b)

Conference: 2016 29th Symposium on Integrated Circuits and Systems Design (SBCCI) .

Abstract: Recently, non-EM energy sources and wireless power transfer techniques have been used to obtain EM energy sources for providing energy autonomy to electric devices when the energy in the environment is insufficient. Typically, this type of system is composed of a harvester, a DC/RF converter, a WPT interface, and a load. Further, in the power stage of the DC/RF converter, the energy flow is processed using a PA. This paper proposes a design methodology for a generic PA fed by a limited power source. This methodology extracts the maximum available power of the EPS with the maximum PA efficiency using impedance matching and a novel PA modeling based on its impedance ports (DC and AC). Moreover, models of class-A PA and class-D PA were developed as examples. Furthermore, a Class-A PA was designed using its impedance ports model and the proposed methodology as a proof of concept. The results reflect that the designed PA extracts the maximum available power of the source with its maximum efficiency.

Paper VII. Simple modeling of photovoltaic solar cells for indoor harvesting applications.(JAIMES; SOUSA, 2017)

Journal: Solar Energy, the official journal of the International Solar Energy Society.

Abstract: In this paper, using an extended version of the 1-diode/2-resistors circuit model, we propose a methodology suitable for modeling photovoltaic solar cells operating in indoor environments. With low-cost equipment and low-complexity procedures, this methodology finds an equivalent circuit that reproduces the worst-case performance of a harvester based on indoor PVSCs for a continuous illuminance range at room temperature. This methodology is validated using a commercial indoor PVSC that has been tested at several illuminance levels, at room

temperature, and in warm white LED spectrum. The extracted model achieves a mean absolute percentage error (MAPE) of 4.85% for an illuminance ranging from 177 to 33.3×10^3 lm/m². Furthermore, this model achieves a MAPE of 0.57% at maximum power point (MPP), and a MAPE of 2.07% around the MPP.

Paper VIII. On the characterization of high- Q planar inductors up to its self-resonance frequency for wireless power transfer applications. [Submitted under journal review]

Journal: IEEE Microwave and Wireless Components Letters.

Abstract: The main figure of merit of an inductor is its quality factor (Q). Furthermore, the Q characterization is useful for estimating its performance embedded in a wireless power transfer system. When it operates near its Self-Resonance Frequency (SRF), and it has a high Q value, its characterization is challenging, especially because the test instrument must be able to measure a large reactance and a very small resistance at a frequency where it partially radiates. In this paper, we present a novel method suitable for characterizing high- Q inductors up to its SRF. The method is applied to a transmitter coil of a previously reported inductive link. The empirical results are consistent with the theoretical model and the full-wave simulation.

1.4 STRUCTURE OF THIS DOCUMENT

We organized the rest of the text as follows.

Chapter 2. We summarize the state-of-the-art (SoA) of Ss-WPT systems for WBAN applications, and we present the theoretical background of energy harvesting systems. Furthermore, we discuss the theory using an integrative approach that is based on well-known concepts as well as new ones. The resulting circuit approach is useful for the natural understanding of the harvesting theory for electrical engineers. At the end of this chapter, we detail and discuss the architecture of the modeled WPT system. The main contribution of this chapter is the EPS concept that allows modeling energy carriers, harvesters, and conventional energy sources (e.g., commercial energy grid) under the same theoretical framework.

Chapter 3. We recap the SoA of the modeling of PVSC devices operating in indoor environments, and we propose a novel mod-

eling methodology for harvesting applications that predicts the power constraints imposed by the indoor PVSC on its payload. This chapter ends with the validation of the proposed modeling methodology, using a commercial PVSC and an indoor light emulator. The main contribution of this chapter is the new vision of indoor PVSC modeling, as using illuminance instead of irradiance, or using worst-case modeling instead of the nominal case one. These ideas are especially useful when the PVSC is used as a harvester.

Chapter 4. We present the SoA of an inductive link with miniaturized CMOS receivers. Next, we discuss and evaluate a lumped circuit model of Planar Square One turn Inductors inductors (PSOI). This inductor geometry allows optimizing the link efficiency when it is based on planar coils. Moreover, we propose a novel procedure for the experimental characterization of high- Q inductors up to its self-resonance frequency. This approach is instrumental in evaluating the performance of the planar inductor when it is embedded in an inductive link. Finally, we assess the lumped model with full-wave EM simulation and experimental results. The main contribution of this chapter is to show that a lumped model can be used to design the inductive link instead of EM simulation, thus decreasing the optimization complexity with a low impact on the results accuracy.

Chapter 5. We propose a design methodology to maximize the power transfer efficiency of an SsWPT system using the novel EPS concept introduced in Chapter 2 and the models proposed in Chapters 3 and 4. The main contribution of this chapter is to model the energy flow of the SsWPT system. Thus the power chain efficiency can be maximized with respect to the power interactions among the subsystems.

Chapter 6. We discuss some limitations and contributions of this research, so as to prompt future research.

2 A SURVEY ON ENERGY HARVESTING FOR WBAN APPLICATIONS

In this chapter, we introduce the theoretical fundamentals of energy harvesting systems along with the state-of-the-art (SoA) of wireless power transfer (WPT) systems for wireless body area network (WBAN) applications. Moreover, we use the conventional harvesting concepts together with new ones for achieving an integrative approach. In addition, we propose a self-sustaining WPT (SsWPT) system composed of an indoor photovoltaic solar cell (PVSC), a power amplifier (PA) and an inductive link based on planar inductors. This method could be used to generate energy for powering subcutaneous complementary metal-oxide semiconductor (CMOS) implants, in parts of the body where in-body sources are not available and avoiding the use of batteries. We will use the concepts introduced in this chapter for modeling the subsystems of this SsWPT system in subsequent chapters of this document.

We summarize in Figure 7 the focus of this chapter. This figure shows the architecture of a generic hybrid SsWPT system for powering implanted devices proposed in (COLOMER-FARRARONS et al., 2011). This system is composed of an implanted receiver and a wearable transmitter, both with energy autonomy.

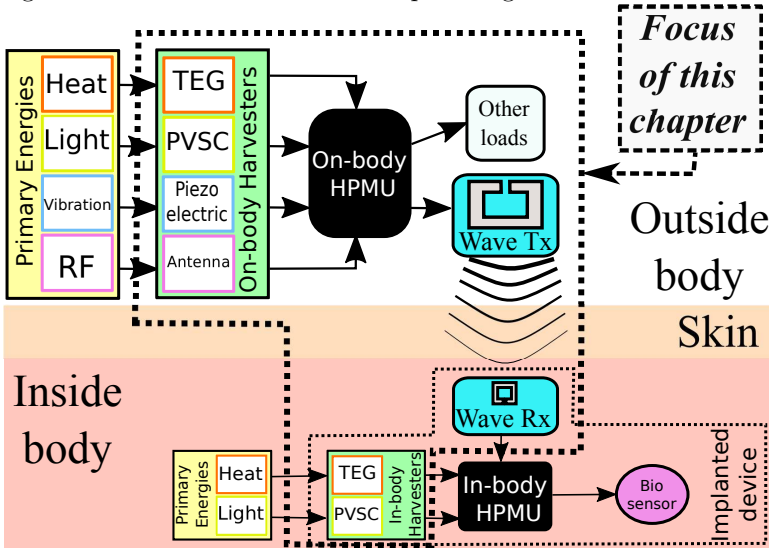
We organize the rest of this chapter as follows. In Section 2.1, we introduce the energy harvesting systems using a brief literature review. In Section 2.2, we discuss the intrinsically stochastic nature of the harvesters. In Section 2.3, we focus on the theoretical basis for modeling neutral energy operation, which is necessary for implementing self-sustaining harvesting systems. In Section 2.4, we detail and justify the architecture of the SsWPT systems that we will use in the rest of this document. Finally, in Section 2.5, we state the conclusions and contributions that have been made by this chapter.

2.1 ENERGY HARVESTING SYSTEMS

An energy harvesting system is explicitly designed to supply energy to a time-variant load from a time-variant energy source. Furthermore, the supplied-instantaneous power could differ from the consumed-instantaneous power (KANSAL et al., 2007), as is shown in Figure 8. These systems are composed of three units (KANSAL et al., 2007):

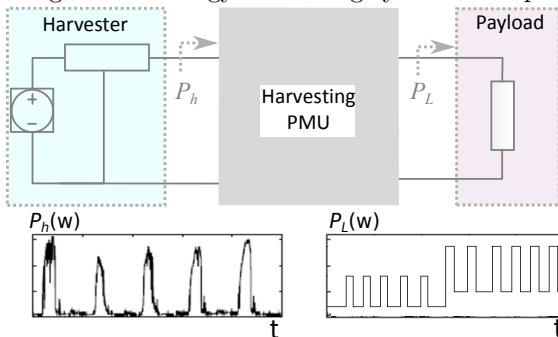
- Harvester: a transducer used for collecting ambient energy, such as solar cells, wind turbines, and piezoelectric actuators. The harvested energy varies with time and depends on environmental conditions.
- Harvesting power manager unit (HPMU) : a system designed

Figure 7 – SsWPT architecture for powering subcutaneous devices.



Source: (The author, 2017)

Figure 8 – Energy harvesting system concept.



Source: (The author, 2014)

specifically for managing the energy collected by a harvester and meeting the energy demands of the payload.

- Payload: a device that consumes the power supplied by the HPMU.

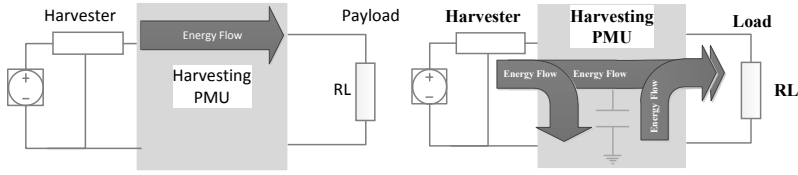
Contrary to the devices powered by batteries, the systems based on energy harvesting can work permanently (KANSAL et al., 2007; SUDEVVALAYAM; KULKARNI, 2011). In this mode, the design goals are:

- The harvester must maximize its energy conversion efficiency.
- The HPMU must:
 - Be capable of extracting the maximum energy from the harvester.
 - Be capable of storage and processing and supply energy to the load without losses.
 - Guarantee Energy Neutral Operation (ENO), which means, the energy consumed by the payload must always be less than or equal to the ambient one converted by the harvester into electrical energy (KANSAL et al., 2007).
- The payload must convert consumed power into application performance. For instance, in conventional autonomous wireless sensor networks, the media access control layer can support individual duty cycles for each node (FAFOUTIS; DRAGONI, 2011). Therefore, each network node can increase its performance (i.e., its energy consumption) up to a level where the system operates in a state that is energetically sustainable (LI; PANDHARIPANDE, 2015; FAFOUTIS; DRAGONI, 2011).

In general, the energy harvesting systems can be divided into two architectures (SUDEVVALAYAM; KULKARNI, 2011; KANSAL et al., 2007):

- Without storage capacity. In this approach, the energy is collected by the harvester and is immediately supplied to the payload, as depicted in Figure 9.
- With storage capacity. In this architecture, the HPMU stores the energy collected by the harvester to provide it in the future to the payload without restrictions regarding instantaneous power, as illustrated in Figure 9.

Figure 9 – Energy harvesting system general architectures.



(a) Harvesting without storage capacity. (b) Harvesting with storage capacity.

Source: (The author, 2014)

In practice, none of these architectures alone is sufficient to allow meeting the load requirements reliably from a time-variant source. Indeed, the losses in the storing, extracting, and processing of the energy limit the efficiency and performance of the architecture with storage (KANSAL et al., 2007). On the other hand, when the designer implements an HPMU without storage element, he must design an optimal payload that must change according to the instantaneous power availability (KANSAL et al., 2007).

2.2 STOCHASTIC NATURE OF HARVESTERS

Energy harvesting is a promising approach to address the energy supply problem. However, the more attractive ambient sources are dynamic and random. In (KANSAL et al., 2007), the authors proposed a taxonomy for learning, teaching, and assessing harvesting sources, as follows:

Noncontrollable but predictable: *“Such an energy source cannot be controlled to yield energy at desired times, but its behavior can be modeled to predict the expected availability at a given time within some error margin”.* For example, a solar cell installed on the body of a cow, which remains approximately in the same place all year, is a noncontrollable but predictable harvesting source. That is because there are models of the harvester and solar energy dependent on seasonal and daily cycles, thus we can predict the expected energy value that the solar cell can harvest from the sunlight.

Noncontrollable and unpredictable : *“Such an energy source cannot be controlled to generate energy when desired, and it yields energy at times which are not easy to predict using commonly available modeling techniques or the when the prediction model is too complex*

for implementation in an embedded system". For example, a solar cell installed on the human body exposed to the sun and the person with ordinary movement routines.

Fully controllable: *"Energy can be generated when desired"*. For example, a kinetic harvester, installed in the leg of a person, that transforms waste vibration into electricity; it is an entirely controllable harvesting source because the wearer can agitate his leg and thus generate power if/when he wants.

Partially controllable: *"Energy generation may be influenced by system designers or users, but the resultant behavior is not fully deterministic"*. An example of a partially controllable harvesting source is a radio-frequency (RF) WPT system fed by a fully controllable energy source, where the energy captured by the receiver depends on the RF-propagation characteristics within the environment, which cannot be controlled.

Typically, the engineer designs the HPMU without a stochastic model of the harvester, ignoring the possibility that the harvested energy could exceed the storage capacity of the system. Such an approach leads to overdesigned systems because the HPMU discards the excess energy when the storage element is full. Hence, we cannot study the efficiency of an HPMU without a statistical model of the harvester. However, the stochastic modeling of the harvesting sources is still in its beginning stages, and it is an open challenge for WBAN applications, as only a few papers have been focused on this topic. As an example, in (ZHANG; SEYEDI, 2013), the authors proposed a Markovian model for modeling the energy harvested by a velocity-damped resonant generator from human motion. The model was developed based on empirical measurements of acceleration at four body locations from 20 subjects.

2.3 THEORETICAL FRAMEWORK OF THE ENERGY-NEUTRAL OPERATION

When the electronic devices consume energy from the distribution grid, we can define the energy source as the system formed by the commercial electrical grid and an AC/DC converter. This source has almost inexhaustible energy, and it can supply power up to a maximum value, which is typically defined by the converter losses and the primary source. Nowadays, several electronic devices are portable and powered by batteries. Recently, the circuit designers increased the energetic autonomy of these types of equipment using harvesters. Furthermore, if

the implemented device achieves the ENO constraints, the apparatus is capable of working perpetually.

In this section, we discuss the ENO operation using the EPS concept. In addition, we summarized the harvested energy sources available in WBAN¹ environments and the power constraints that they impose on its loads.

2.3.1 Energy demands in WBAN applications








To exemplify the challenges imposed by the WBAN loads to the energy sources, we compare, in Table 1, a few requirements of selected electronic devices. We included as WBAN devices a wearable medical device, which uses the narrowband channel defined in the IEEE 802.15.6 standard, and a generic pacemaker. As shown in the table, these WBAN loads lead the ranking of the energy demands considering energy densities. Furthermore, the pacemaker is the leader on this item. In fact, even with the best battery on the market, operational life of the pacemaker is from 7 to 15 years (HAEBERLIN et al., 2014), and the operational life of an on-body WBAN sensor system for wireless body telemetry is short, often on the order of days (PRIYA; INMAN, 2009). Moreover, the instantaneous power demands of a WBAN node can vary suddenly from low to high consumption level (i.e., nW to mW).

In summary, the electric loads, in WBAN applications, demand an energy source with very high density of energy and power, especially the implanted loads². As we will discuss in the next subsections, the harvester can supply the energy demand of the WBAN loads because it can harvest a high amount of energy from the WBAN environment; however, they cannot transfer the energy at the demanded energy rate, per unit time, of this load (PRIYA; INMAN, 2009). In Figure 10, we illustrate this fact with a comparison between energy and power density (D_J and D_W respectively) of some energy sources and carriers commonly used in WBAN applications. In the ragone plane, the better energy devices have both higher energy and greater power density. Hence, this plot is a straightforward way to judge an energy power source by its location on the ragone plot.

¹If the reader is not acquainted with WBAN, it is advisable to read the Appendix A, where we present a brief review of WBAN.

²If the reader wants to understand further the energy demand of the current wearable WBAN loads, it is advisable to read the Appendix B, where we present a brief survey of this topic.

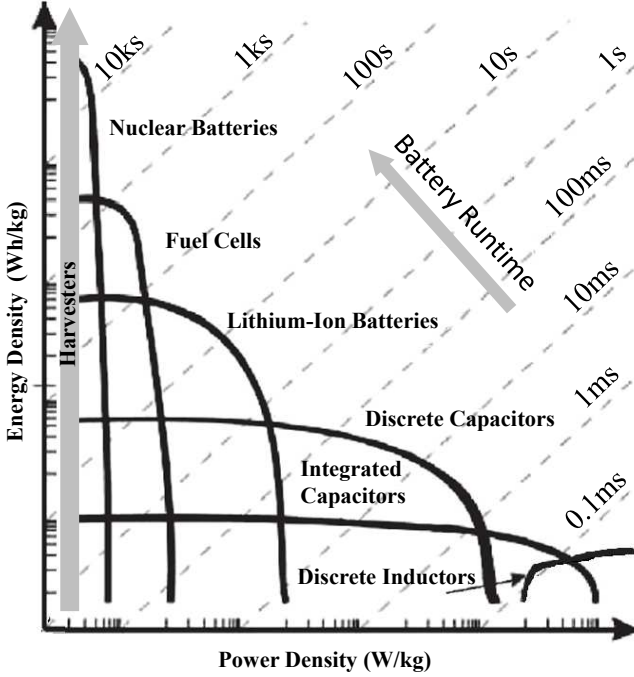
Table 1 – Specifications of portable electronic equipments

Device	Device specifications	Typ. value	Position regarding demand in			
			P	E	D_J	D_W
 cell phone	E(Wh):	5.00				
	P_{avg} (W):	1.00				
	P_{max} (W):	5.00				
	t_{life} (hours):	5.00	1	3	4	1
	Weight(g):	250				
	D_J (mWh/g):	20.0				
	D_W_{max} (mW/g):	20.0				
 MP4	E(Wh):	1.20				
	P_{avg} (mW):	50.0				
	P_{max} (mW):	50.0				
	t_{life} (hours):	24.0	2	5	5	4
	Weight(g):	60.0				
	D_J (mWh/g):	20.0				
	D_W_{max} (mW/g):	0.83				
 WSN node	E(Wh):	51.84				
	P_{avg} (mW):	2.00				
	P_{max} (mW):	200				
	t_{life} (years):	3.00	3	1	3	2
	Weight(g):	500				
	D_J (mWh/g):	100				
	D_W_{max} (mW/g):	0.40				
 MP3	E(Wh):	0.24				
	P_{avg} (mW):	1.00				
	P_{max} (mW):	1.00				
	t_{life} (days):	10.0	4	6	6	5
	Weight(g):	30.0				
	D_J (mWh/g):	8.0				
	D_W_{max} (mW/g):	0.03				
 W-MWBAN node	E(Wh):	4.32				
	P_{avg} (μ W):	100				
	P_{max} (mW):	20				
	t_{life} (years):	5.00	5	4	2	3
	Weight(g):	20				
	D_J (mWh/g):	216				
	D_W_{max} (mW/g):	0.1				
 Pacemaker	E(Wh):	21.9				
	P_{avg} (μ W):	50.0				
	P_{max} (μ W):	50.0				
	t_{life} (years):	15.0	6	2	1	6
	Weight(g):	30				
	D_J (mWh/g):	730				
	D_W_{max} (mW/g):	0.002				
 Wristwatch	E(Wh):	0.043				
	P_{avg} (μ W):	1.00				
	P_{max} (μ W):	1.00				
	t_{life} (years):	5.00	7	7	7	7
	Weight(g):	20				
	D_J (mWh/g):	2.16				
	D_W_{max} (mW/g):	0.001				

Where X_{avg} and X_{max} are the average and maximum value of the X variable.

Source: (Based on (VULLERS et al., 2010) and The author 2014)

Figure 10 – Ragone plot of selected energy carriers and sources.



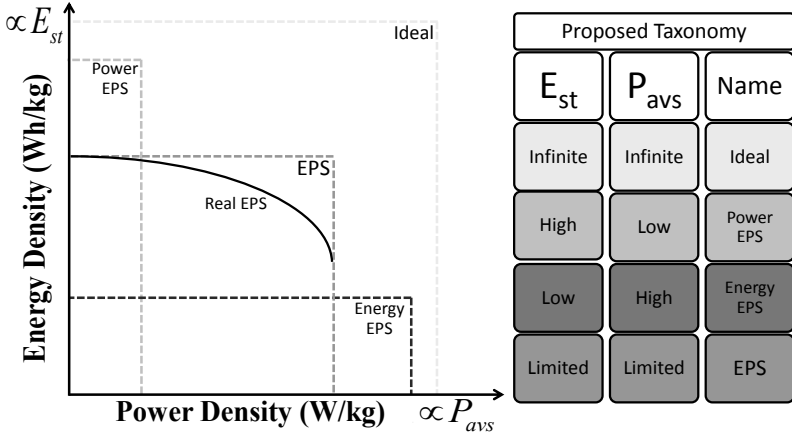
Source: (Taken from (BHASKARAN; SRIRAM; INIEWSKI, 2013))

2.3.2 Energy and Power Sources

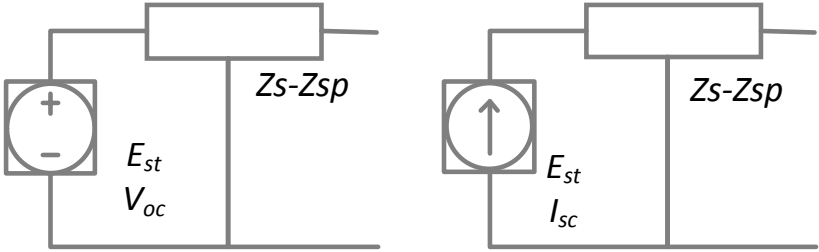
2.3.2.1 EPS concept and proposed taxonomy

The energy and power available from any electricity source are limited. Furthermore, its maximum available power (i.e., its P_{avs}) can be extracted only under the so-called maximum power transfer condition (DORF; SVOBODA, 2010). Besides, its maximum available energy can be limited by its storage or replacement capacities if the electricity is from an energy carrier or a primary energy source respectively. For instance, a battery can supply at most its energy storage capacity (E_{st}). On the other hand, a harvester can convert a high amount of electricity from the ambient energy, which is inexhaustible either because of the enormous amount of energy that it contains or because they are capable of regenerating by natural means.

Figure 11 – Energy power sources



(a) EPS taxonomy



(b) EPS symbols

Source: (The author, 2013)

We define a source of both energy and power as an electric circuit that models the energy and power constraints (at least E_{st} and P_{avs}) imposed by the electrical source on its load. We refer to this type of electrical source as EPS in this document. We use the E_{st} and P_{avs} relative values to propose a simple taxonomy, which is summarized and illustrated in Figure 11(a). An EPS works ideally when its energy and power limits are higher than the energy and power demands of its load. An EPS works as a power EPS when the EPS imposes a power constraint lower than the payload demand. Thus it restricts the payload performance. Finally, an EPS works as an energy EPS when its energy is not enough for supplying the payload demand. Thus it limits the system runtime. Moreover, we propose two EPS symbols,

which are shown in Figure 11(b). The square (that circumscribes the voltage or energy circuit source) and series-parallel impedance denote the energy and the power constraints imposed on the load, respectively.

This modeling approach, regarding energy as well as power, is typical in complex energy generation and distribution systems (LI et al., 2012). However, it is unknown to electronics designers. In subsequent sections, we illustrate the use of this taxonomy with examples, which allow understanding of the limitations of some electric sources from their implicit energy and power nature.

2.3.2.2 Energy flow modeling

The electrical energy consumed by the load (E_L) is given by:

$$E_L(t) = \int_0^t P_L(\tau) \cdot d\tau = \int_0^t v_L(\tau) i_L(\tau) \cdot d\tau; \quad (2.1)$$

where P_L is the power dissipated by the load, i_L and v_L are the load current and voltage, respectively. Assuming an EPS with losses, which can be characterized by a time-invariant efficiency η_{eps} , the expressions of the stored energy (E_s) and generated power (P_s) of the EPS are given by:

$$E_s(t) = \begin{cases} E_0 - \frac{E_L(t)}{\eta_{eps}} & ; E_0 > \frac{E_L(t)}{\eta_{eps}} \\ 0 & ; E_0 \leq \frac{E_L(t)}{\eta_{eps}} \end{cases}; \quad (2.2)$$

$$P_s(t) = -\frac{d}{dt} \left(\frac{E_L(t)}{\eta_{eps}} \right) = -\frac{P_L(t)}{\eta_{eps}}; \quad (2.3)$$

where E_0 is the initial stored energy of the EPS. We normalize (2.2) for simplifying the analysis of the energy flow problem. Thus, it can be rewritten as:

$$SoE = \frac{E_s(t)}{E_{st}} = \begin{cases} SoE_0 - \frac{E_L(t)}{E_{st}\eta_{eps}} & ; E_0 > \frac{E_L(t)}{\eta_{eps}} \\ 0 & ; E_0 \leq \frac{E_L(t)}{\eta_{eps}} \end{cases}; \quad (2.4)$$

where SoE is the State of Energy of the EPS, which is an indicator of the amount of energy stored by the EPS. For example, when the EPS is fully charged ($E_s = E_{st}$) the SoE equals 1 (i.e., $SoE\% = 100\%$).

A conventional harvesting EPS with storage capacity is composed of a harvester and an HPMU with storage element and two power

processing units (PPUs), as shown in Figure 12(a). These units typically are DC/DC, AC/DC, AC/AC converters, or an array of them. Furthermore, for this type of EPS, the (2.2) and (2.4) can be rewritten as:

$$E_s(t) = \begin{cases} E_0 - \frac{E_L(t)}{\eta_s} + \eta_h \cdot E_h(t) & ; E_0 > \frac{E_L(t)}{\eta_s} - \eta_h \cdot E_h(t) \\ 0 & ; E_0 \leq \frac{E_L(t)}{\eta_s} - \eta_h \cdot E_h(t) \end{cases} ; \quad (2.5)$$

$$SoE = \frac{E_s(t)}{E_{st}} = \begin{cases} SoE_0 - \frac{E_L(t)}{E_{st}\eta_s} + \frac{\eta_h \cdot E_h(t)}{E_{st}} & ; E_0 > \frac{E_L(t)}{\eta_s} - \frac{\eta_h \cdot E_h(t)}{E_{st}} \\ 0 & ; E_0 \leq \frac{E_L(t)}{\eta_s} - \frac{\eta_h \cdot E_h(t)}{E_{st}} \end{cases} \quad (2.6)$$

where E_h is the energy extracted by the HPMU, η_h and η_s are the efficiencies of input and output PPUs, respectively. These units could be DC/DC, AC/DC, or DC/AC converters. Moreover, the input PPU is designed to extract the P_{avs} of the harvester and the output PPU to regulate the payload voltage.

When the EPS is based on a harvester and HPMU without storage element, the system HPMU is composed of only one PPU (i.e., one DC/DC, AC/DC, or AC/AC converter), as we illustrate in Figure 12(b). Under this architecture, the extracted and consumed energy are related by:

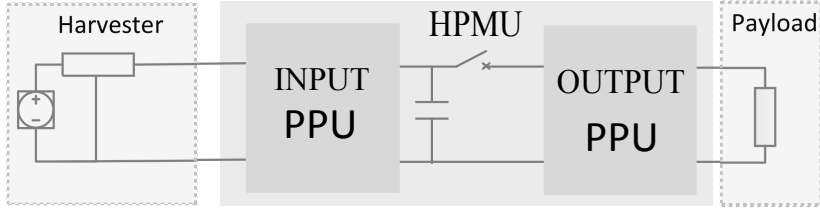
$$E_h = \frac{E_L}{\eta_s}; P_h = \frac{P_L}{\eta_s}. \quad (2.7)$$

Moreover, the PPU must be designed to extract the P_{avs} of the harvester and to regulate the payload voltage. However, in practice the unit achieves these goals only under specific payload and environmental conditions.

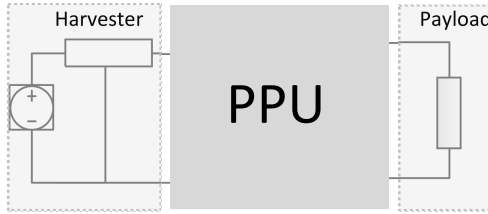
2.3.2.3 Energy neutral operation

The concept of ENO relates to a state where the energy consumed by the payload is always less than or equal to the energy collected by the harvester ($E_L(t)/\eta_s \leq \eta_h E_h(t)$). Moreover, if the harvesting system operates in the ENO state and there is no hardware failure, the harvester guarantees the total energy autonomy of the device (KANSAL et al., 2007). The “optimal” energy operation of a harvesting system is the maximum ENO state ($E_L(t)/\eta_s = \eta_h E_h(t)$) because the load consumes all the harvested energy, thus the system converts all the ambient energy in device performance (VIGORITO; GANESAN; BARTO,

Figure 12 – Conventional HPMU architectures.



(a) HPMU with storage element.



(b) Harvesting without storage capacity.

Source: (The author, 2016)

2007). We illustrate these concepts in Figure 13. However, it is hard to design a system to work in this state all the time, since the dynamics of the ambient energy must be modeled and the harvester load (i.e., the HPMU and payload) must be dynamically adapted to them (KANSAL et al., 2005).

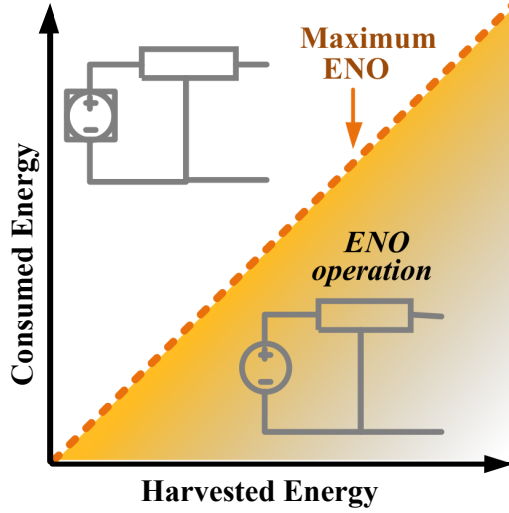
Conventionally, the electronic designer overcomes the unmodeled dynamics of the ambient energy using an HPMU with storage capacity and energy regulation at the load (KANSAL et al., 2007). However, the resulting HPMU can lose more energy in its operation than the energy gain produced by achieving the maximum ENO state, especially when the power density of the harvester is too low.

2.3.2.4 The battery as EPS example

We define an ideal battery as a device that imposes a constant electric potential across its terminals ($v_{s,i}$) whenever its stored energy is greater than zero. Therefore, its output voltage can be written as:

$$v_{s,i}(t) = \begin{cases} V_b & SoE_b(t) > 0 \\ 0 & SoE_b(t) = 0 \end{cases}; \quad (2.8)$$

Figure 13 – Diagram of the energy states of the harvesting system with storage capacity.



Source: (The author, 2014)

where V_b is the constant electric potential established by the ideal battery and SoE_b is the SoE of the battery. Using (2.4) and (2.8), we can describe the energy flow of this source as a charge flow given by:

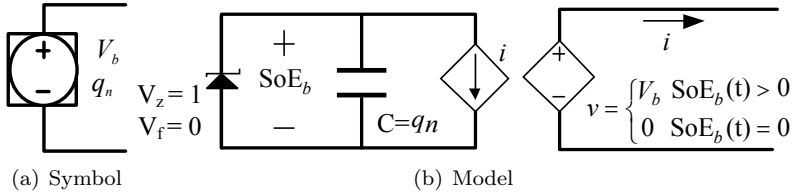
$$SoE_b = \begin{cases} SoE_{0b} - \frac{1}{q_n} \int_0^t i_L(\tau) d\tau & 1 > SoE_{0b} > \frac{1}{q_n} \int_0^t -i_L(\tau) d\tau \\ 0 & SoE_{0b} \leq \frac{1}{q_n} \int_0^t -i_L(\tau) d\tau \end{cases}; \quad (2.9)$$

where SoE_{0b} is the initial value of SoE_b , i_L is the charge current supplied by it, and q_n is its charge storage capacity, which is given by:

$$q_n = \frac{E_{st,b}}{V_b}; \quad (2.10)$$

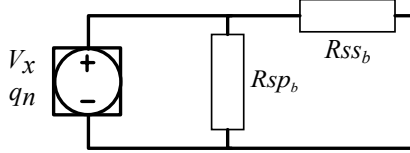
where $E_{st,b}$ is the energy storage capacity of the battery. The electrical behavior described by equations (2.9) and (2.8) can be represented by the circuit shown in Figure 14. Adding resistors to the lossless model, as shown in Figure 15, the resulting circuit can model a battery with

Figure 14 – Lossless DC voltage EPS



Source: (The author, 2014)

Figure 15 – Battery model based on lossless DC voltage EPS



Source: (The author, 2014)

limited power and energy³.

2.3.2.5 Harvester as EPS example

In general, a harvesting system could operate as a power EPS, an energy EPS, or an ideal EPS. The system composed of a harvester and an HPMU without storage operates as a power EPS because the payload cannot consume more than the P_{avs} of the harvester. Furthermore, this system guarantees the total energy autonomy of the payload because the system works at an implicit maximum ENO state and the resulting system is self-sustaining. On the other hand, the system composed of a harvester and an HPMU with storage element that operates at the ENO state is regarded as an ideal EPS. That is because the resulting EPS can supply the energy demand of the payload up to a high power value, which is limited by the equivalent impedance at short circuit condition of the output PPU. In general, this maximum power value is higher than the payload demand. Furthermore, the resulting harvesting system is self-sustaining. In contrast, when the harvester energy is lower than the payload demand, the resulting EPS is regarded as

³If the reader is interested in knowing the use of the EPS concept for modeling real batteries, we recommend reading the Appendix C

an energy EPS because it supplies the payload demand until its storage energy becomes zero ⁴.

2.3.2.6 Maximum power point operation

The maximum available power of the harvester (i.e., its P_{avs}) is supplied for a specific load value (PRIYA; INMAN, 2009; NAGAYOSHI; KAJIKAWA; SUGIYAMA, 2002; ROUNDY et al., 2004). However, the absolute value of the P_{avs} and this “optimum” load depend of the environmental conditions. When the harvester supplies its P_{avs} , it operates at its maximum power point (MPP). Moreover, if the environmental conditions change, then the MPP changes too. Therefore, to guarantee the MPP operation of the harvester, the HPMU imposes a new optimum load value on the harvester (ESRAM; CHAPMAN, 2007). This kind of control strategy is known as MPP tracking (MPPT)⁵.

Assuming a harvester that could be modeled using linear elements as an on-body TEG, its P_{avs} is extracted only when the load of the harvester is equal to its internal resistance (BANDYOPADHYAY; CHANDRAKASAN, 2012; DORF; SVOBODA, 2010). On the other hand, when a model of the harvester is nonlinear, such as PVSCs, the theorem of maximum power transfer is not valid (JEONG; JIANG; CULLER, 2008) ⁶.

Generally, the autonomous systems extract the P_{avs} of harvester to seize as much environmental energy as possible. That is especially because the P_{avs} of the harvesters are very low and impose hard power constraints on its load. Therefore, the first step in a design of autonomous devices is the harvester characterization under the environmental conditions in which it will operate. This characterization allows determining the power constraints that the harvester imposes on the design of the payload ⁷.

⁴If the reader wants to understand better the reason why a harvester could be an energy EPS or a power EPS, we recommend reading the Appendix D. In this Appendix we discuss the on-body TEG as an example.

⁵If the reader is interested in knowing the SoA of the MPPT for WBAN applications, see the Appendix E, where we present a brief review of the topic.

⁶As an example of these facts, we estimate the I-V curves under some environmental conditions of two harvesters in the Appendix F.

⁷If the reader wants to gain numerical insight into the energy constraints imposed by the harvesting EPSs in WBAN environmental conditions, we recommend reading the Appendix G.

2.4 SELF-SUSTAINING INDUCTIVE COUPLING SYSTEMS FOR POWERING CMOS IMPLANTED DEVICES

The natural in-body energy sources are not uniformly distributed in the human body. Thus, there are some parts that do not have enough ambient energy to feed an implanted device. The conventional solution to that problem is the artificial generation of in-body energy sources using WPT techniques. In Table 2, we summarize the power constraints imposed by some in-body harvesters that harvest energy from artificial and natural sources. This table shows that the artificial WPT systems based on inductive coupling in near- and mid-field links provide the highest power density. Furthermore, it shows that there is a trade-off between size and power of the implant. The designer solves this trade-off by using systems based on mid-field electromagnetism (EM), which achieves a good compromise between power and size (this table is discussed further in the Appendix G).

The principal drawback of artificial WPT systems that are based on inductive coupling is that the resulting system is not wearable or has insufficient energy autonomy. That is because the external unit needs to be plugged into the commercial energy grid or because its form factor restrictions limit the energy storage capacity of the battery. In (COLOMER-FARRARONS et al., 2011), the pioneering work in SsWPT systems for WBAN applications, the authors propose to overcome this problem using an autonomous WPT system composed of an on-body harvesting unit and an EM WPT interface. More specifically, they introduce the architecture shown in Figure 7. However, the proof-of-concept of the harvesting unit cannot extract enough energy from the on-body harvesters (i.e., around 6.4 mW) to supply the energy demands of the payload (i.e., an inductive link interface loaded with a commercial biosensor), which was 200 mW. In fact, they were unsuccessful in proving this concept for several reasons, but primarily because of the low efficiency of both the hybrid PMU and the WPT interface. The low efficiency of the interface can be explained because they used a commercial inductive link instead of a custom one where the coil geometries and operation frequency can be optimized. Moreover, the low efficiency of the hybrid HPMU can be partially explained by the fact that they designed the power processing units using linear regulators instead of switching converters.

The concept of a self-sustaining, on-body WPT system for powering implanted devices is an excellent but unexplored idea. However, the efforts made by the researchers have been limited due to techno-

Table 2 – Comparison in-body harvesting sources uniformly distributed.

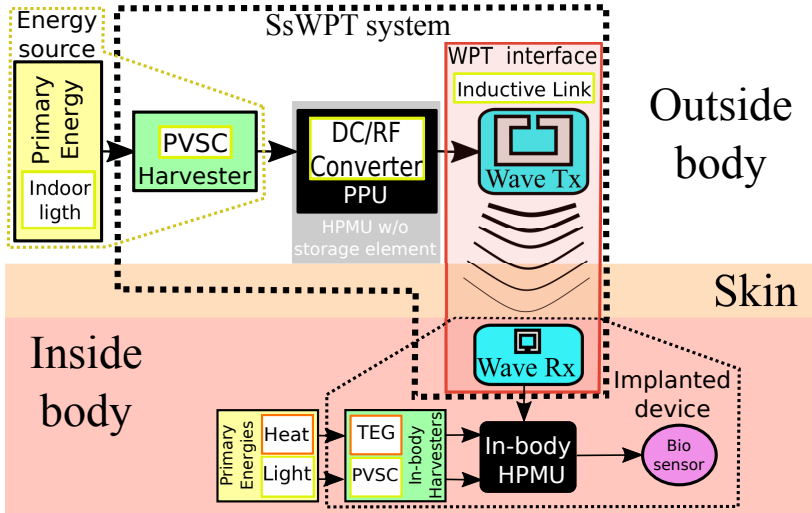
References	(GHOVANLOO; ATLURI, 2007)	(GABRERA; SOUSA, 2016)	(LIU et al., 2014)	(GOTO et al., 2001)
WPT technique	Near-field inductive coupling	EM mid-field	EM far-field	Optical powering
Type of source	Artificial	Artificial	Artificial	Artificial
Frequency or wavelength	1 MHz	986 MHz	2.45 GHz	735 nm
Implanted size	10 cm ²	2.25 mm ²	32mm ²	0.6cm ²
Distance $T_x - R_x$	10 mm	15 mm	20 cm	10 mm
Medium	Air	Air	Liquid skin	Chicken skin
Energy source	External AC	External RF	External Antenna	External Laser
Harvested P	-	0.4 mW	25.1 μ W	-
Harvested D_W	800 μ W/mm ²	180 μ W/mm ²	0.78 μ W/mm ²	10 μ W/mm ²
Harvester	Inductor	Inductor	Antenna	PVSC

References	(VENKATASUBRAMANIAN et al., 2007)	(BEREUTER et al., 2017)	(OZERI; SHMILOVITZ, 2010)
	2007	2017	2010
WPT technique	Thermal	Light	Ultrasonic powering
Type of source	Natural	Natural	Artificial
Frequency or wavelength	-	0-3000 nm	673 kHz
Implanted size	138 mm ²	3.53 cm ²	3.54cm ²
Distance $T_x - R_x$	-	-	5 mm
Medium	-	Skin optical emulator	water
Energy source	Gradient (2 K)	Indoor H.L.	Outdoor H.L.
Harvested P	-	45 μ W	164 μ W
Harvested D_W	10 μ W/mm ²	0.13 μ W/mm ²	0.47 μ W/mm ²
Harvester	TEG	PVSC	PVSC

Source: (The author, 2017)

logical challenges. In particular, the current advances in the areas of power converters, WPT, and integrated circuits technology make it possible to increase the power constraints of the payload and to de-

Figure 16 – Diagram of the proposed SsWPT system.



crease the payload demand. Therefore, these techniques enable the possible development of a proof-of-concept that operates in the ENO region. We found evidence of this fact in some recent works (CABRERA; SOUSA, 2016; BANDYOPADHYAY; CHANDRAKASAN, 2012). In (CABRERA; SOUSA, 2016), the reported WPT interface loaded by the payload has a power demand of less than 10 mW for full operation. The authors proposed an asymmetrical inductive link that is based on a Planar Square One-turn inductor (PSOI) and loaded with a fully integrated receiver. They measured a link efficiency of -25.4 dB (0.285%) at a frequency of 986 MHz. In (BANDYOPADHYAY; CHANDRAKASAN, 2012), the reported HPMU imposed a power constraint of 2.5 mW on its load under indoor illumination. The authors proposed a hybrid-integrated HPMU using CMOS switching techniques. They measured a converter efficiency of 83%. Moreover, we must face many challenges before a SsWPT system to power CMOS implants becomes reality.

In SsWPT systems, the power chain begins with the power collected by the harvester and finishes in the available power that the payload (i.e., the biosensor or bioactuator) can consume. Low efficiency characterizes this chain, and its losses are concentrated in the WPT interface. Perhaps the main challenges are to increase the functionalities of the payload subject to the energy constraints and the maximization of the power transfer efficiency of the chain.

This work represents one of the first attempts to model SsWPT systems for in-body WBAN applications. We modeled an autonomous WPT system composed of an indoor PVSC, an HPMU without storage capacity, and an asymmetrical inductive link that is based on PSOI devices. The block diagram of this system was presented in Chapter 1 and is shown again in Figure 16. We define this architecture because of several reasons:

- The HPMU without storage element is more efficient.
- Considering the harvesting energy sources indoors, the ambient light has the highest power density and is partially controllable. That is because the indoor designer defines the visual power according to illumination standards. Besides, the involved harvester technology (i.e., indoor PVSC) is the most mature at the moment of writing this thesis. Therefore, we consider the light power as the most consistently available energy source around the human body when indoors.
- There are two advantages of the inductive link based on PSOI coils regarding the other EM interfaces. The receiver coil can be easily integrated into standard CMOS technology and coil geometry partially maximizes the power transfer efficiency of the WPT interface.

Moreover, given the choice of these technologies, the power transfer efficiency maximization is influenced by the accuracy of the models and the design methodology.

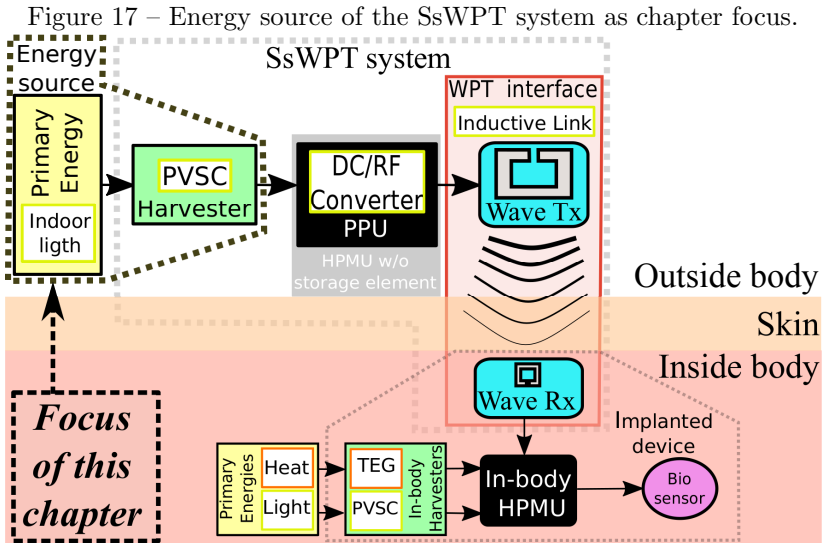
2.5 CONCLUSIONS AND CONTRIBUTIONS

In this chapter and its appendixes, we introduced the theoretical fundamentals of energy harvesting systems along with the SoA of WPT systems for WBAN applications. In addition, we proposed the EPS concept, and we used it to model with circuits the energy flow in a harvesting system. As minor contributions that were developed in the appendice D, we presented the ENO using a comprehensive and straightforward method for electrical engineers based on the circuit modeling of the energy flow in WBAN harvesting systems.

3 ON THE MODELING OF INDOOR PHOTOVOLTAIC SOLAR CELLS FOR WBAN HARVESTING APPLICATIONS

In this chapter, we propose an extended version of the one diode and two resistors (1D&2R) model for PVSC devices operating in indoor environments (so-called indoor PVSC). We have validated the proposed modeling methodology using a commercial PVSC and an indoor light emulator. As we show in this chapter, the resulting model can be used to estimate the worst-case performance of the indoor PVSC as a harvester in real indoor conditions. Hence, it is very useful in harvesting applications because it can predict the power constraint that is imposed by the PVSC on the payload. In Chapter 5, we use the proposed model to maximize the power transfer efficiency of a SsWPT system that is composed of an indoor PVSC, a DC/RF converter and an inductive link that is based on planar inductors. We summarize in Figure 17 the focus of this chapter.

The rest of this chapter is organized as follows. In Section 3.1, we discuss the context of PVSC modeling using a broad literature review. We conclude that the modeling of indoor PVSCs is just beginning and,



Source: (The author, 2017)

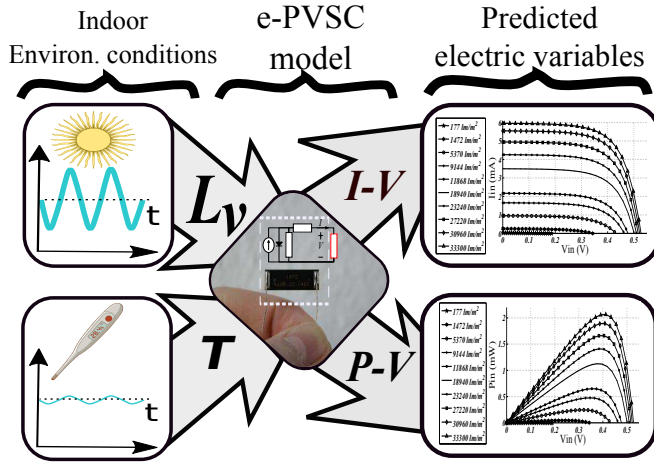
therefore, in this chapter we on the indoor spectrum and its impact on the electrical response of the PVSCs. In addition, a graphical abstract of this chapter is shown in Figure 18(a), and we also add complementary information and some “basic” figures to achieve an integrative approach to the problem. In Section 3.2, we discuss the SoA of indoor PVSC modeling. In Section 3.3, we focus on the theoretical basis for modeling the indoor PVSC for harvesting applications. We will then describe the experimental setup and methods used in this chapter in Section 3.4. Next, Section 3.5 focuses on the proposed methodology and it presents the study case. In Section 3.6, we compare the results with the SoA, and discuss some limitations of this work. Finally, in Section 3.7 we highlight the conclusions and the contributions that have been made by this chapter.

3.1 INTRODUCTION

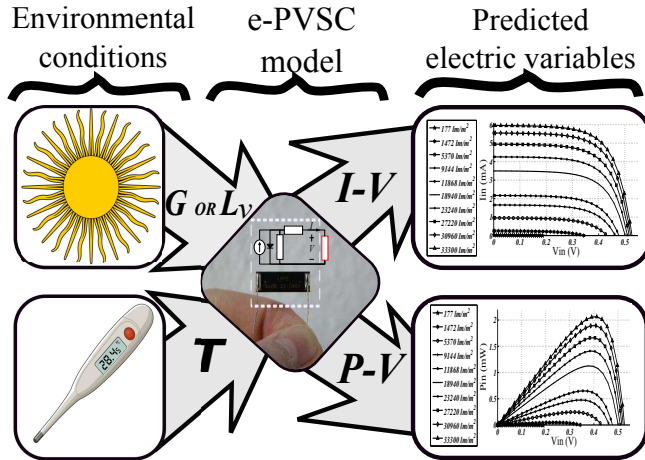
As we discussed in Chapter 2, there is currently an increasing level of interest in providing energy autonomy to electronic devices that are used for implementing WBAN applications. Energy-harvesting systems allow us to achieve this autonomy by collecting energy from primary sources (e.g. solar) and converting it to electric power using a harvester (e.g. PVSC). Autonomous implants have been proposed with WPT systems for healthcare applications. These systems are composed of an external unit and a resonance-based inductive link (HANNAN et al., 2014; AMAR; KOUKI; CAO, 2015). Generally, this unit is either powered by batteries or must be directly plugged into the electrical network. In a pioneering work (COLOMER-FARRARONS et al., 2011), the authors propose harvesting energy from sources that are present around or on the human body to generate an artificial RF energy source in the dermis, which can be used to power subcutaneous implants. As we discuss in chapter 2, we consider the light power as the most consistently available energy source around the human body under indoors conditions. Furthermore, self-sustaining systems powered by PVSC are not rare nowadays (LIU; SANCHEZ-SINENCIO, 2015; TOH et al., 2014). For instance, in (LIU; SANCHEZ-SINENCIO, 2015), the authors proposed a self-sustaining voltage source with low-power operation and a high efficiency for powering sensor nodes with Internet connectivity, which was based on PVSC for harvesting the solar energy. In another example, in (TOH et al., 2014), the authors use a PVSC to power a WBAN node that senses the temperature of the wearer and transmits this in-

formation to the network coordinator-node. The process of designing these electronic payloads generally involves the use of circuit simulators and, therefore, the designers require circuit models that represent the physics of the PVSCs (VILLALVA; GAZOLI; FILHO, 2009).

Figure 18 – The PVSC modeling flow.



(a) Indoor flow.



(b) General flow.

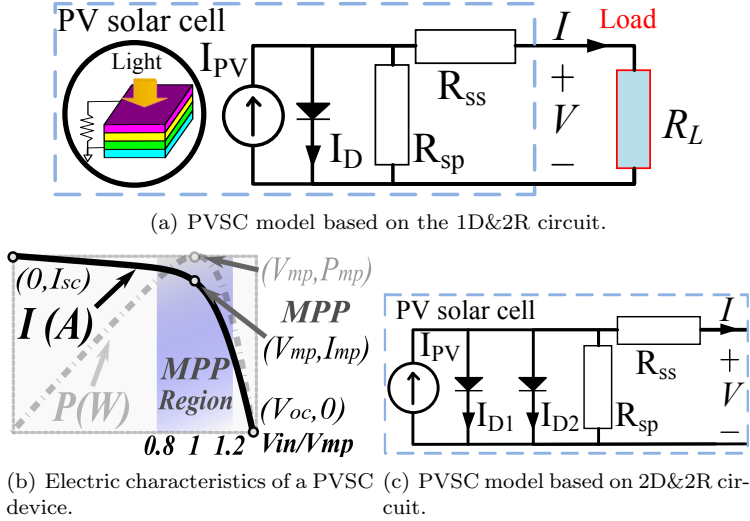
Source: (The author, 2016)

There are several circuit models in the literature that can be used to describe the operation of the PVSCs under defined environmental conditions (JORDEHI, 2016). Furthermore, they predict the electric variables (i.e., I , V , and P) from the environmental-condition inputs, which are irradiance (G) or illuminance (L_v), and temperature (T); as illustrated in Figure 18(b) (CUBAS; PINDADO; MANUEL, 2014; JORDEHI, 2016; HUMADA et al., 2016; CIULLA et al., 2014). In this chapter, we refer to this type of model as an extended PVSC model (e-PVSC). Most of the available information and data about PVSC theory and their models have been developed under Standard Test Conditions (STC). Furthermore, the conventional PVSC models are based on parameters that depend on the environmental conditions, which are extracted by assuming STC conditions or simplifications that are valid in outdoor operation. Hence, they are inaccurate for a PVSC that operates indoors. The modeling of an indoor PVSC is still at an early stage, and there is a discussion about which outdoor practices are directly applicable and which should be suitable for modeling indoor PVSCs. However, the 1D&2R circuit is currently the most common electric model for PVSCs operating in both indoor and outdoor environments.

Figure 19(a) outlines the 1D&2R model. This model is generally used to estimate electric variables under defined environmental conditions (i.e., spectral irradiance G_λ and T) (JORDEHI, 2016) because it is simple and can accurately describe the I–V characteristic of the PVSC around the MPP (CUBAS; PINDADO; VICTORIA, 2014; CIULLA et al., 2014). In Figure 19(b), we highlight the MPP in the I–V characteristic of the PVSC. In several practical cases, the effect of the incident light on the PVSC can be captured using G instead of G_λ (CIULLA et al., 2014; CUBAS; PINDADO; MANUEL, 2014; JORDEHI, 2016; HUMADA et al., 2016). Furthermore, as we discussed in Section 3.3.4, the L_v can be used instead of G when the G_λ is concentrated on the visual range.

An e-PVSC model is composed of a circuit topology (e.g. 1D&2R), and its associated circuit values (e.g. I_{pv} , I_D , R_{SS} and R_{SP}) are related to the captured environmental conditions (i.e., G or L_v , T). Generally, the e-PVSC model parameters are the circuit values organized into some type of data structure on a database (CIULLA et al., 2014). However, these parameters can also be the fitted values of a math function that is used to express the circuit components in terms of the environmental conditions (MASOUDINEJAD et al., 2015). Often, the model's parameters are found from the experimental data or from the device datasheet using a procedure that is particular for each model (CIULLA et al., 2014), which is commonly referred to as PVSC model parameter

Figure 19 – Modeling of PVSC devices.



Source: (The author, 2016)

estimation problem (JORDEHI, 2016). Although PVSC modeling has been extensively explored, it is still an open research problem (HUMADA et al., 2016).

The modeling research of PVSC devices operating outdoors is focused on two topics: first, the trade-off between the accuracy and the complexity of the models under STC (JORDEHI, 2016; HUMADA et al., 2016); and second, the effects of the real operating conditions on the PVSC behaviors (PSARROS; BATZELIS; PAPATHANASSIOU, 2015; ZEGAOUI et al., 2016; SIAW; CHONG, 2012; CHONG et al., 2016; WONG; CHONG, 2016). On the other hand, for the PVSCs operating indoors, or so-called indoor PVSC, The modeling research is focused on determining the appropriate test conditions for the indoor PVSC characterization, perhaps because the standardization is still in its infancy (MINNAERT; VEELAERT, 2014; RANDALL; JACOT, 2003; LI et al., 2015). The few reported indoor e-PVSC models use large-signal modeling for G and small-signal modeling for T (TAN; PANDA, 2011; MASOUDINEJAD et al., 2015), because the temperature within the building is controlled by climate control systems (RANDALL; JACOT, 2003; TAN; PANDA, 2011) and also because the indoor light (spectrum and irradiance) presents a huge variation in the same building (RANDALL, 2003). These indoor

models are based on empirical data measured under controlled environmental conditions. However, the model evaluation and the description of the test setup are very limited. Furthermore, the impact of test environmental conditions on the I-V characteristic of the PVSC device has not been discussed.

In the operation of a PVSC, its I-V characteristic differs from the datasheet curve because the real (or test) environmental conditions differ from the STC conditions (i.e., $G = 1 \times 10^3 \text{ W/m}^2$ with AM1.5g spectrum at 25°C). For example, a PVSC that receives high irradiation levels experiences a temperature rise, which in turn causes the reduction of the available electrical power (SIAW; CHONG, 2012). However, the temperature effects are neglected in indoor PVSC modeling because the temperature is regulated (TAN; PANDA, 2011) and the temperature rise produced by the incident irradiation is low (RANDALL; JACOT, 2003). Recently, in (MINNAERT; VEELAERT, 2014), the authors studied the influence of varying spectral irradiance on the indoor PVSC, and they analyzed the typical indoor light sources and the PVSC technologies for determining which illuminants are relevant for indoor PVSC characterization. Additionally, in (LI et al., 2015), the authors experimentally verified that for a fixed illuminance value, the amount of electric energy available on the PVSC terminals changes with the illuminant type. Furthermore, the white LED (Light-Emitting Diode) spectrum generates the lowest available electric power on the PVSC terminals, when it is compared with the typical irradiance produced by fluorescent (FL) and halogen (HA) lamps (MINNAERT; VEELAERT, 2014; LI et al., 2015).

In the next sections of this chapter, we use the gray box modeling concept to model PVSC devices operating in indoor environments. We will use a well-known circuit model of the PVSC (1D&2R circuit based on the physics phenomena) and a mathematical model (based on fitting techniques) to adjust the model to the measured data. This approach allows us to model a commercial indoor PVSC using an e-PVSC model that reproduces its worst-case scenario as a harvester. The extracted model achieves a mean absolute percentage error (MAPE) of 4.85% for illuminance ranging from 177 to $33.3 \times 10^3 \text{ lm/m}^2$. Furthermore, when the proposed model is compared with the SoA presented in Section 3.2, it is found to be the only model that covers from A to I illuminance categories suggested by the Illuminating Engineering Society of North America (IESNA) for indoor lighting. Furthermore, its model parameters are analytic nonlinear functions of the illuminance, which decreases the model complexity and has a low impact on the model accuracy.

3.2 STATE-OF-THE-ART OF THE INDOOR PVSC MODELING

Considering the modeling approach that is used to capture the environmental conditions on the model, the e-PVSC model can be categorized as small-signal or large-signal. An e-PVSC model that uses small-signal modeling for both L_v (or G) and T is useful when the PVSC supports little changes in the environmental conditions; for example, an indoor-static device near to a known illuminant type. On the other hand, the large-signal modeling for L_v counterpart can be applied when the PVSC is installed on a device that experiences large changes on the environmental conditions; for example, when the wearer of an on-body sensor node walks inside a building. Adopting the proposed categorization, the SoA of indoor PVSC modeling will be discussed next.

3.2.0.1 Small-signal modeling on both L_v (or G) and T .

In (TOH et al., 2014), the authors considered the environmental conditions as constants in the modeling process, consequently the WBAN node was designed to operate under $L_v = 320 \text{ lm/m}^2$ at room temperature. A more realistic PVSC model using small-signal modeling was presented in (YU et al., 2014), which is based on the 1D&2R circuit and uses close math expressions to calculate the circuit components from the environmental conditions using only one single measurement (i.e., $L_v = 200 \text{ lm/m}^2$ at room temperature). The current error reported was of 1.05% at MPP. However, the model's evaluation and the description of their test setup are very limited.

3.2.0.2 Large-signal modeling for L_v (or G) and small-signal modeling for T

In indoor environments, a common modeling approach reproduces the empirical data for several L_v (or G) levels at room temperature using the 1D&2R model. For example, in (BENAVIDES; CHAPMAN, 2008), three I-V curves for 70, 112, and 193 W/m^2 at room temperature were measured. The model parameters (i.e., a database composed of sets of circuits values) of the e-PVSC models were estimated using these curves. The experimental setup was based on a halogen illuminant and a forced-air cooling system. Following the same modeling approach but

using fluorescent lamps in (TAN; PANDA, 2011), five different lighting conditions from 380 to 1010 lm/m^2 were tested. In both papers, the procedures used to extract the model's parameters were not reported, neither was the illuminant impact on the modeling discussed, and the illuminance was chosen as model input. (BRUNELLI et al., 2009) use a customized setup based on a halogen light source and six levels of light intensity, and solve the model parameter estimation problem using explicit equations. The thermal impact of the illuminant in the model was analyzed; however, the electrical impact on the harvested energy was not discussed. All these works only reported a qualitative evaluation of the model, based on a graphic comparison between predicted and measured I-V curves. Moreover, using the discrete level approach for L_v (or G), the behaviors in the intermediate light conditions are ignored, and the only way to increase the model accuracy is to increase the lighting levels; however, this also increases the model's complexity. The 2-diodes / 2-resistors circuit model (2D&2R Figure19(c)) was reported as useful when the environmental conditions are characterized by low-irradiance values (CHAN; PHANG, 1987). Recently, in (SAVANTH et al., 2015) an e-PVSC model based on the 2D&2R circuit and a database with several solution sets ranging from 100 to 2500 lm/m^2 was proposed. They solved the parameter estimation problem using the numerical solution of nonlinear equations and reported a custom low-cost setup based on embedded systems. However, they do not clearly describe the test conditions, such as the illuminant type. The reported e-PVSC model achieves moderate accuracy and the thermal impact of the illuminant on the model was not discussed.

Finally, in (MASOUDINEJAD et al., 2015) two e-PVSC models based on 1D&2R and 2D&2R circuits were compared. A nonlinear optimization problem to extract the parameters of both models was proposed. The experimental setup achieved a $G < 1 \text{ W/m}^2$ using fluorescent and halogen lamps. They proposed the use of regression techniques to generalize its model; however, they were unable to find an analytical expression. Further, the optimization solver that is used to solve the model parameters estimation problem was originally developed for STC conditions; therefore, the extraction process added some error at low-irradiance values. Furthermore, only a qualitative evaluation of the model is reported. In contrast to (CHAN; PHANG, 1987), they found that the 1D&2R model can fit the measured data better than the 2D&2R.

3.3 THEORETICAL FRAMEWORK

3.3.1 1D&2R circuit as PVSC model

The 1D&2R circuit can be used to model a real PVSC device (VILLALVA; GAZOLI; FILHO, 2009), its I–V relationship is given by:

$$I = I_{pv} - \underbrace{I_0 \left[\exp \left(\frac{V + IR_{SS}}{n\phi_t} \right) - 1 \right]}_{I_D} - \frac{V + IR_{SS}}{R_{SP}}; \quad (3.1)$$

where I_{pv} models the photovoltaic current generated by the incident light. The Shockley diode equation (i.e., I_D) represents the PVSC behavior without incident light, where I_0 is the saturation current of the diode, ϕ_t is the thermal voltage (given by $k_B T / q_e$; where q_e is the electron charge, k_B is the Boltzmann constant, T is the temperature in K), and n is the diode ideality constant. The contact resistance between the semiconductor and electrodes is modeled by R_{SS} , and R_{SP} models the leakage current of the p–n junction (JORDEHI, 2016). I_{pv} is given by (CHONG et al., 2016):

$$I_{pv} = A_e \int_{\lambda_1}^{\lambda_2} G_\lambda(\lambda) \cdot R_\lambda(\lambda) d\lambda = A_e \int_{\lambda_1}^{\lambda_2} G_\lambda(\lambda) \cdot \left[\frac{q \cdot \lambda}{c_s \cdot h_P} \eta_\lambda(\lambda) \right] d\lambda; \quad (3.2)$$

where λ is the wavelength of the incident electromagnetic wave (i.e., the light), λ_1 and λ_2 are the spectral limits of G_λ , A_e is the active area of the PVSC, R_λ is the PVSC responsivity, η_λ is the external quantum efficiency, h_P is Planck's constant, and c_s is the speed of the electromagnetic wave. Furthermore, G and L_v are given by:

$$G = \frac{\phi_e}{A_R} = \int_{\lambda_1}^{\lambda_2} G_\lambda(\lambda) d\lambda; \quad (3.3)$$

$$L_v = \frac{\phi_v}{A_R} = k_m \int_{\lambda_1}^{\lambda_2} G_\lambda(\lambda) \cdot V_\lambda(\lambda) d\lambda; \quad (3.4)$$

where ϕ_e and ϕ_v are the radiant power and the luminous radiant power respectively, A_R is the corresponding area (m^2), V_λ is the luminosity

function, and k_m (683.022 lm/W) is the maximum spectral luminous efficacy.

3.3.2 PVSC as an indoor harvester

The PVSC can be modeled using the power EPS concept that was proposed in (FAJARDO; SOUSA, Florianopolis, Brasil. 2016), and discussed in Section 2.3.2. The PVSC is characterized by a limited power and infinite energy, and supplies its maximum available power (i.e., its P_{avs}) to a load, at a specific operating point known as MPP (i.e., $P_{avs} = P_{mp}$), which can be tracked using an electronic converter that optimizes the matching between the power EPS and its load (FAJARDO; SOUSA, 2016b). The MPP point, the MPP region (i.e., typical operation region), and the so-called remarkable points were highlighted in the I-V curve of a generic PVSC that is plotted in Figure19(b). These points correspond to the following conditions: short circuit ($0, I_{sc}$), voltage and current at MPP (V_{mp}, I_{mp}), and open circuit ($V_{oc}, 0$). Using the PVSC model discussed in section 3.3.1, the current and voltage at MPP can be calculated numerically from equations (3.5) and (3.6) that were developed in Section F.2. We solve this equation set using the solve command implemented in MATLAB®.

$$I_{mp} = I_{pv} - I_0 \cdot \left[e^{\left(\frac{V_{mp} + R_{SS} I_{mp}}{n \phi_t} \right)} - 1 \right] - \left(\frac{V_{mp} + R_{SS} I_{mp}}{R_{SP}} \right); \quad (3.5)$$

$$\frac{I_{mp}}{V_{mp}} = \frac{\frac{I_0 R_{SP}}{n \phi_t} e^{\frac{V_{mp} + I_{mp} R_{SS}}{n \phi_t}} + 1}{(R_{SS} + R_{SP}) \left(\frac{I_0 R_{SS}}{n \phi_t} e^{\frac{V_{mp} + I_{mp} R_{SS}}{n \phi_t}} + 1 \right)}. \quad (3.6)$$

3.3.3 Indoor spectrum mismatch

The conventional PVSC models predict the I-V curves of the PVSC device from the environmental conditions, which are both spectral G_λ and T . The G_λ is totally characterized by both its spectrum or normalized spectral distribution (\hat{G}_λ) and its total power density or irradiance (i.e., G). Generally, outdoor e-PVSC models assume the spectrum of the incident light as the standard (i.e., 1.5AMg), neglecting the mismatch between this standard and the real spectrum. This approach is useful because in many practical outdoor applications the

spectrum mismatch is low. However, this modeling approach produces a large prediction error in indoors applications because of the large mismatch between the indoor and 1.5AMg spectrum.

The illumination of an indoor space is planned by considering the human tasks that will be conducted within it, according to the values proposed by an illumination standard (RICHTMAN, 2015). Furthermore, architects design the indoor space with both sunlight and illuminants. Consequently, the indoor G_λ depends on both location and illuminants in the room (RANDALL; JACOT, 2003; LI et al., 2015). The task of finding the typical indoor spectrum is very hard or impossible. However, in (MINNAERT; VEELAERT, 2014), the authors classify the indoor light sources into four groups according to their effect on the harvested power. They conclude that a full indoor PVSC characterization must be done under at least one illuminant of each group. The illuminant group which produces the least harvested power (P_{mp} in Figure19(b)), is composed of: cool white fluorescent lamp, narrow tri-band fluorescent lamp, standard high pressure sodium lamp, and typical standard commercial cool and warm LED. This group is the most interesting for harvesting applications because we can estimate the minimum power that the PVSC can supply (assuming MPP operation) at an arbitrary combination of sunlight and illuminants. Furthermore, if the PVSC is measured under the spectrum produced by one illuminant of the group of interest, then the measured P_{mp} is a good estimation of the payload power constraint.

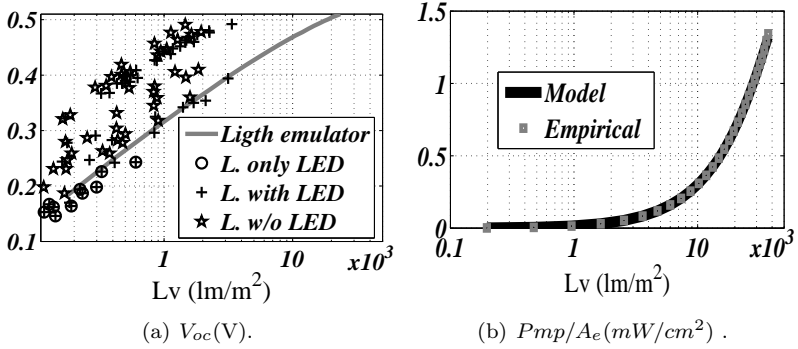
In this study, we measured the power generated by the PVSC using the V_{oc} as an estimator. From 3.1, at open circuit condition ($I = 0$) and neglecting the leakage current ($R_{SP}^{-1} = 0$), we found an expression for the open circuit voltage $V_{oc} = \phi_t \ln(I_{pv}/I_0)$, which shows that V_{oc} can be used to estimate the I_{pv} that is produced by the incident G_λ captured and converted by the PVSC device. In Figure20(a) we compare the V_{oc} that is produced by the PVSC (as modeled in Section 3.5) under controlled LED light with 100 samples of the V_{oc} generated by the same PVSC under uncontrolled indoor environment conditions. As we expected, the electrical response of the PVSC under the G_λ produced by a warm LED illuminant is a reasonable estimation of the worst response of the PVSC as a harvester.

3.3.4 PVSC modeling based on illuminance

The typical outdoor e-PVSC model uses G and T as inputs, and the light spectrum is assumed as to be a 1.5AMg spectrum. This modeling approach reduces the model's complexity and simultaneously simplifies its experimental setup because the researcher can use a pyrometer (calibrated at STC conditions) instead of a spectroradiometer. However, the same modeling approach cannot be used directly to model indoor PVSC because of the huge spectrum mismatch. Therefore, we propose a methodology that can be used to accurately predict the electrical response of an indoor PVSC operating in our extraction test setup. This methodology uses L_v and T , and assumes the spectrum of the incident light as the standard spectrum of an incandescent lamp, neglecting the spectrum mismatch between the light produced by the warm LED and the incandescent lamps. This modeling approach reduces the model complexity and simultaneously simplifies the experimental setup because the researcher can use a low-cost lux meter (which is calibrated under incandescent lamp spectrum) instead of a spectroradiometer. In addition, the warm LED lamp produces a G_λ that is concentrated in the visible spectrum; hence, illuminance can be chosen instead of irradiance.

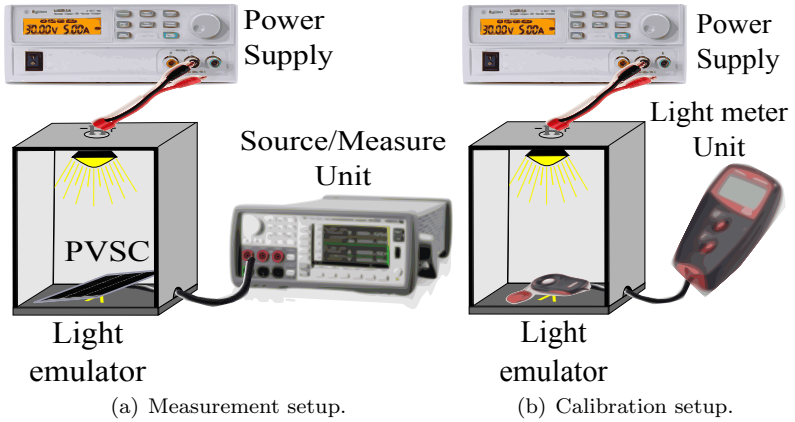
The radiometric (W/m², irradiance) units are more common than the photometric counterpart (lux, illuminance) in the modeling of photovoltaic solar cells. However, the irradiation from artificial light sources is commonly expressed in photometric units rather than radiometric units, representing a measure of the light intensity as perceived by the human eye (LI et al., 2015; ROSSI; PONTECORVO; BROWN, 2015). For example, a 500 lm/m² indoor corresponds to the average illuminance in an office, which is very similar to the intuitive understanding that 1 kW/m² (at STC conditions) corresponds to the irradiance of the incident sunlight on a clear day. Furthermore, a model with illuminance as an input instead of irradiance is more useful for harvesting applications because the engineer can estimate the payload power constraint based on the indoor MPP power density (P_{mp}/A_e) and rated illuminance of the indoor environment. For example, if four KXOB22-12X1L devices are available and the payload will operate in an office (500 lm/m²), then we could use the P_{mp}/A_e calculated in Section 3.5 and plotted in Figure 20(b) to calculate the maximum power that the payload could consume: $P_{max} = NA_e P_{mp}/A_e = 4 \cdot 1.54 \text{ cm}^2 \cdot 5.41 \mu\text{W}/\text{cm}^2 = 33.33 \mu\text{W}$.

Figure 20 – Selected experimental results of the characterization of the PVSC under test.



Source: (The author, 2017)

Figure 21 – Experimental setup of the scalar characterization.

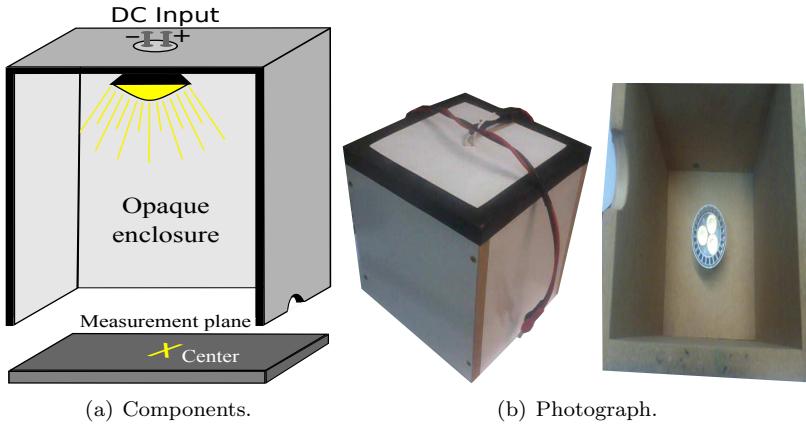


Source: (The author, 2017)

3.4 METHODS AND EXPERIMENTS

We used an experimental setup to recreate the indoor environment and to provide valid measurement data to model the PVSC. This section will describe the test setup and the resulting dataset.

Figure 22 – Indoor lighting emulator.

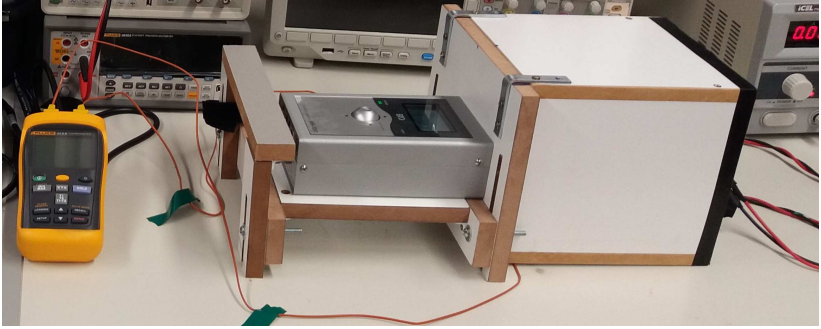


Source: (The author, 2017)

3.4.1 Test Setup

The measurement setup is composed of a power supply (i.e., TP3645A), an indoor light emulator, and a source-measure unit (i.e., B2901A); as shown in Figure 21(a). The light emulator is composed of an opaque enclosure, a light source, and the measurement plane; as illustrated in Figure 22. The voltage-controlled light source modifies the illuminance at the measurement plane, and the opaque enclosure shields the setup from ambient light interference. We implemented a voltage-controlled light source using the on-board LED array of a commercial LED lamp (LP011) and its associated optical elements. The resulting light source operates from 7.5 V to 10.5 V. We measured the illuminance at the center point of the measurement plane and the temperature (near this point) using a lux meter (LX1010BS) and a thermometer (Fluke 54IIB); as shown in Figure 21(b). The measured illuminances were used to characterize the light emulator in Section 3.4.1.1. Moreover, we characterize the light emulator using a spectroradiometer (EKO MS-720) in Section 3.4.1.2. The experimental setup is shown in Figure 23. However, this spectral characterization is optional in the proposed methodology.

Figure 23 – Experimental setup of the spectral characterization.



Source: (The author, 2017)

3.4.1.1 Scalar characterization of the light emulator

Twenty measurements were done using the calibration setup. For each one, the following procedure was made: 1) Mount the light meter into the light emulator on the measurement plane. 2) Set the power supply at the appropriate DC voltage level. 3) Wait for the light measurement to stabilize. The results of 10 trials were processed using fitting techniques, and the relationship between the input DC voltage (v_{idc}) and the illuminance on the center of the measurement plane (L_c) was found:

$$L_c = q_{v1}v_{idc}^8 + q_{v2}v_{idc}^7 + q_{v3}v_{idc}^6 + q_{v4}v_{idc}^5 + q_{v5}v_{idc}^4 + q_{v6}v_{idc}^3 + q_{v7}v_{idc}^2 + q_{v8}v_{idc} + q_{v9} \quad (3.7)$$

The $q_{v1:v9}$ values are summarized in Table 3. The remaining measurements were used to test the calibration and the resulting statistics were a MAPE of 4.32% and a standard deviation (STD) of 5.23%. The maximum calibration error was 26.37 % at 177 lm/m². In addition, during the calibration process we measured the temperature with two thermocouples positioned near to the measurement plane center. The resulting statistics were a mean value of 298,43 K and a STD of 0.77 K. As we expected, the temperature increases with the increase in the input DC voltage. However, we neglect the temperature impact of the light source in the modeling methodology because the measured temperature rise was 1.75 K (less than 2% of the nominal room temperature).

Table 3 – Coefficients of the calibration fitting

Par.	Val	Par.	Val	Par.	Val
q_{v1}	-104	q_{v4}	4324982	q_{v7}	-1571240894
q_{v2}	7562	q_{v5}	-48710417	q_{v8}	4017443081
q_{v3}	-239492	q_{v6}	350334919	q_{v9}	-4483151085

Source: (The author, 2017)

3.4.1.2 Spectral characterization of the light emulator

We use the power supply to sweep v_{idc} from 7.6 to 10.4 V. We measure the G_λ produced by the light emulator ($G_{\lambda_{LED}}$) for each voltage. Some of these measurements are plotted as a function of v_{idc} and λ in Fig 24. As we expected, the $G_{\lambda_{LED}}$ irradiance (G_{LED}) is correlated with v_{idc} . Furthermore, the $G_{\lambda_{LED}}$ spectrum ($\hat{G}_{\lambda_{LED}}$) is almost the same for all the measured data and is concentrated in the visual range (i.e., 400 nm to 700 nm). Moreover, the percentage value of the irradiance concentrated inside this range ($G_{v\%}$) is given by:

$$G_{v\%} = 100 \cdot \frac{\int_{\lambda_4=400nm}^{700nm} G_{\lambda_{LED}}(\lambda) d\lambda}{\int_{\lambda_3=350nm}^{1050nm} G_{\lambda_{LED}}(\lambda) d\lambda} = 100 \cdot \frac{PAR_L}{G_{LED}} \quad (3.8)$$

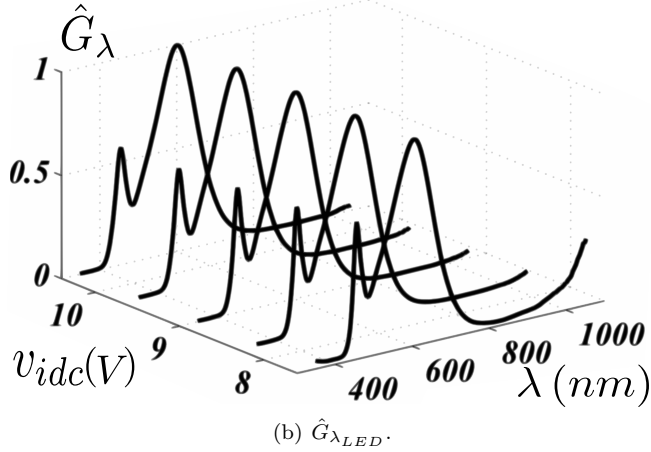
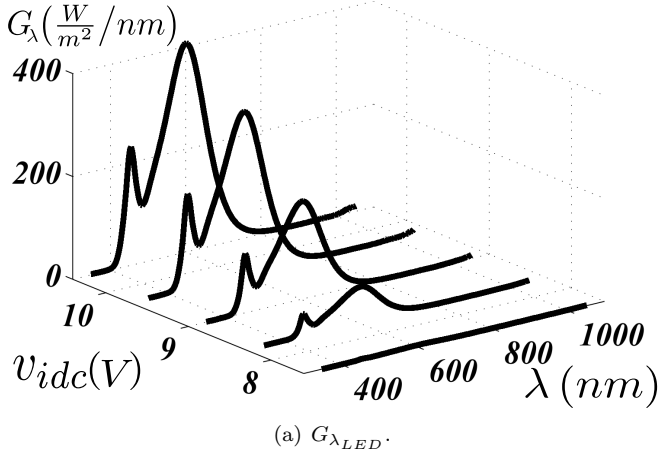
where λ_3 , λ_4 are the wavelength range limits imposed by the spectroradiometer, and PAR_L is the photosynthetically active radiation of the emulator. The resulting statistics of $G_{v\%}$ were mean of 92.01% and STD of 8.68%. Therefore, L_v produced by the light emulator (L_{LED}) is a reasonable estimator of the G_{LED} . Additionally, we quantify the error in the measurement of L_{LED} by the lux meter, which is generated by the mismatch between the spectrum produced by the incandescent

Table 4 – Specifications of the KXOB22-12X1L under AM1.5g.

Area mm x mm	V_{oc} V	I_{sc} mA	V_{mp} V	I_{mp} mA	G $\frac{W}{m^2}$	T $^{\circ}C$
22 x 7	0.63	50	0.5	44.6	1000	25

Source: (Datasheet, 2015)

Figure 24 – Spectral characterization of the light emulator.



Source: (The author, 2017)

lamp and the spectrum produced by our light emulator. The resulting percentage error ($E_{lm\%}$) is given by:

$$E_{lm\%} = \frac{L_{lmL} - L_{spL}}{L_{spL}} = \frac{1}{MF_L} - 1 \quad (3.9)$$

where L_{spL} and L_{lmL} are the illuminance values measured in the light emulator by the spectroradiometer and the lux meter, respectively, and

MF_L is the spectral mismatch correction factor of the lux meter. The resulting statistics were a MAPE of 11.98% and a STD of 7.31%. The resulting statistics of the MF_{LED} were a mean of 1,1169 and a STD of 1.67%. However, these results cannot be generalized for any LED source because the G_λ is not standard. Moreover, we use fitting tools to express G_{LED} as a function of $L_{lm_{LED}}$. The analytic expression that we found is:

$$G_{LED} = (a_{l2w} + b_{l2w}L_{lm}) L_{lm} \quad (3.10)$$

where $a_{l2w} = 3.8 \times 10^{-3}$ and $b_{l2w} = -17.026 \times 10^{-9}$. This function fits the empirical data with a MAPE of 1.43% and STD of 1.58%. In section 3.4.2, we use (3.10) to estimate the reported irradiances from the measured illuminances and, consequently, to estimate the PVSC efficiency. The next section will report on the illuminance that was measured by the lux meter in the scalar calibration and we neglect the spectrum mismatch.

3.4.1.3 Commercial PVSC device

The KXOB22-12X1L was chosen to test the indoor PVSC modeling. This is a silicon monocrystalline PVSC that is fabricated by the IXYS company with a typical efficiency of 22%, as measured at a wafer level and under STC conditions. In addition, it can be used in both indoor and outdoor applications because its percentage external quantum efficiency is greater than 70% from 350 nm to 950nm. The device datasheet (IXYS, 2011) outlines these remarkable points under STC conditions, and are summarized in Table 4.

3.4.1.4 Characterization of the PVSC under test

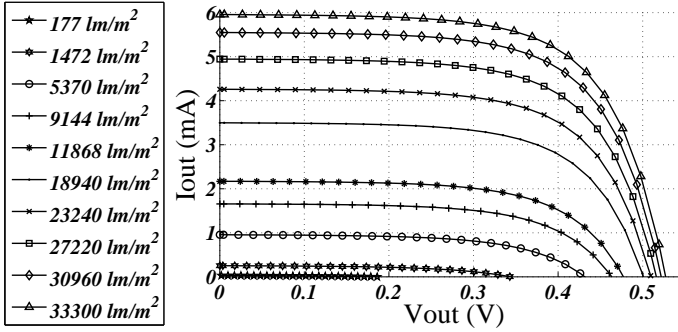
In the measurement process, we extracted the I-V curve of the PVSC for a given illuminance value. We used the source-measure unit to sweep the output voltage (V_{out}) of the PVSC and to measure its output current (I_{out}). We will next detail the experimental procedure: 1) Mount the PVSC into the light emulator on the measurement plane. 2) Adjust the illuminance to the desired value setting using the appropriate DC voltage following equation (3.7). 3) Measure the V_{oc} for the PVSC under test settings using the source-measure unit as a current source of 0 A. 4) Wait for the measurement to stabilize. 5) Set the source-measure unit as a voltage source and as a current meter. 6) Set

a voltage sweep on the source-measure unit using 10 cycles of power line per measurement as the speed option, and a hundred points from 0 V to the measured V_{oc} . 7) Extract the I-V curves with the source-measure unit using the defined settings. 8) Save the extracted I-V curve data and the experimental conditions in the dataset.

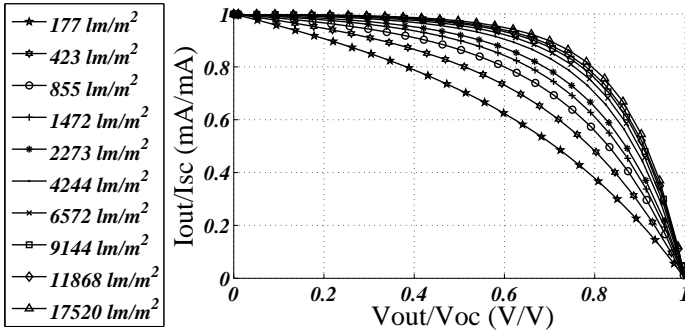
3.4.2 Resulting dataset

The KXOB22-12X1L performance was measured from 177 lm/m^2 to 33.3×10^3 (0.67 W/m^2 to 107 W/m^2) at room temperature and under a warm LED spectrum. For each illuminance, the I-V curve was extracted. These data and the associated test conditions compose the dataset that is analyzed in this chapter. Some of these measured curves are plotted in Figure 25, where V_{out} and I_{out} are the voltage and the current at the output terminals of the PVSC device, and P_{out} is the generated power by the cell. As we expected, both V_{oc} and I_{sc} decrease with the reduction of the incident illuminance because (as discussed in Section 3.3.3) they are related to the incident spectrum intensity and also because (as we measured in Section 3.4.1.2) G_λ is concentrated in the visual range. Although the light emulator does not reach $1 \times 10^3 \text{ W/m}^2$, 107 W/m^2 (33300 lm/m^2) is sufficient and more relevant for our purposes because our setup covers from A to I illuminance categories proposed in (REA, 2000), by the IESNA. The maximum measured power was 2.07 mW at 107 W/m^2 , which corresponds to an approximated cell efficiency of 12.62% . This efficiency reduction (compared with the PVSC datasheet) is partially explained by the huge spectral irradiance mismatch between warm LED and AM 1.5g spectra. To model the PVSC device using this dataset, the following assumptions were made: 1) The incident illuminance on the PVSC under test is uniform and, therefore, it can be measured at the center point of the measurement plane to estimate the incident illuminance in the overall area of the physical device. 2) The temperature throughout the tests remains constant. 3) The positioning error is negligible. 4) The thermal impact of the illuminant on the PVSC behavior is negligible. 5) The illuminance mismatch error is low.

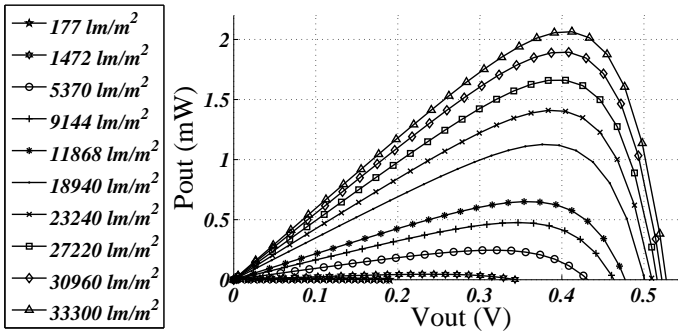
Figure 25 – Empirical dataset of the KXOB22-12X1L.



(a) Measured I-V characteristic.



(b) Normalized measured I-V characteristic.



(c) Measured power characteristic.

Source: (The author, 2016)

3.5 PROPOSED MODELING METHODOLOGY AND STUDY CASE

In this section we discuss the methodology that is used to model the commercial indoor PVSC that is detailed in Section 3.4.1.3. The steps of the methodology are: 1) Measure the PVSC I-V curves under warm LED spectrum, controlled illuminance, and at room temperature. 2) Extract the remarkable points (as detailed in Section 3.4.1.3) of each measured I-V curve. 3) Extract the circuit values of the 1D&2R model (as detailed in Section 3.3.1) for each remarkable point set following the procedure described in Section 3.5.1. 4) We express the circuit values of the 1D&2R model as continuous functions of the illuminance from the discrete values (extracted in Step 3) using fitting tools and the nonlinear functions proposed in Section 3.5.2. We refer to the e-PVSC model that was found using only the first three steps of the proposed methodology as a Not-interpolated (NI) model. If the e-PVSC model is found following all of the steps, then we refer to it as an INterpolated (IN) model.

3.5.1 Extraction of the 1D&2R circuit values

When the PVSC model is based on the 1D&2R circuit, then the measured I-V curve is used to find those values of I_{pv} , I_0 , n , R_{SS} and R_{SP} that fit the model to the empirical data. Many authors have discussed methods to estimate the correct value of the n parameter (HUMADA et al., 2016). However, any value can be chosen to adjust the model and, if necessary, the n value can be modified to improve the model's accuracy (VILLALVA; GAZOLI; FILHO, 2009). Considering silicon cells, the n parameter can be chosen between one and two to simplify the model parameter estimation problem (HUMADA et al., 2016; CUBAS; PINDADO; VICTORIA, 2014). For example, in (CUCÉ; CUCÉ, 2012), the authors use $n = 1.2$ to model monocrystalline devices, whereas they use $n = 1.3$ for polycrystalline cells. In this study, we assumed the parameter n as $n = 1.2$ and we found the remaining model parameters by following the extraction procedure proposed in (CUBAS; PINDADO; VICTORIA, 2014), as summarized in Table 5. These extracted values and the related environmental conditions (saved on a database) are used as the parameters of the NI model.

Table 5 – Parameter extraction steps based on (CUBAS; PINDADO; VICTORIA, 2014).

Solve		Equation
1	n	$1.0 < n < 1.5$
2	R_{SS}	$\frac{(V_{mp}I_{sc} + V_{oc}(I_{mp} - I_{sc}))(V_{mp} - I_{mp}R_{SS})}{n \cdot \phi_t}$ $- (V_{mp}I_{sc} - V_{oc}I_{mp}) = \frac{V_{mp}(2I_{mp} - I_{sc})}{\exp\left(\frac{V_{mp} + I_{mp}R_{SS} + V_{oc}}{n \cdot \phi_t}\right)}$
3	R_{SP}	$R_{SP} = \frac{(V_{mp} - I_{mp}R_{SS})(V_{mp} - R_{SS}(I_{sc} - I_{mp}) - n \cdot \phi_t)}{(V_{mp} - I_{mp}R_{SS})(I_{sc} - I_{mp}) - n \cdot \phi_t I_{mp}}$
4	I_0	$I_0 = \frac{(R_{SS} + R_{SP})I_{sc} - V_{oc}}{R_{SP} \cdot \exp\left(\frac{V_{oc}}{n \cdot \phi_t}\right)}$
5	I_{pv}	$I_{pv} = \frac{(R_{SS} + R_{SP})I_{sc}}{R_{SP}}$

Source: (The author, 2017)

3.5.2 Fitting of the 1D&2R circuit values

We use the NI model parameters and fitting techniques to propose a novel e-PVSC model that is composed of the 1D&2R topology and circuit values given by:

$$n = 1.2; \quad (3.11)$$

$$I_{pv} \cdot 10^3 = p_{i1}L_v^3 + p_{i2}L_v^2 + p_{i3}L_v + p_{i4}; \quad (3.12)$$

$$f_{3dB}(I_0 \cdot 10^{10}) = a_{I_0}L_v^{b_{I_0}} + c_{I_0}; \quad (3.13)$$

$$f_{3dB}(R_{ss}) = a_{R_{ss}}L_v^{b_{R_{ss}}} + c_{R_{ss}}; \quad (3.14)$$

$$f_{3dB}(R_{sp}) = a_{R_{sp}}L_v^{b_{R_{sp}}} + c_{R_{sp}}; \quad (3.15)$$

where a_x , b_x , and c_x are constant values related to x (i.e., $x = R_{sp}$, R_{pp} ou I_0), and $p_{i1:i4}$ are constant values related to the I_{pv} . These 13 constants are used to suite the equations set to the NI model parameters and they are the IN model parameters. The function $f_{3dB}(x)$ was defined as:

$$f_{3dB}(x) = 10\log_{10} (10\log_{10} (10\log_{10} (x))) \quad (3.16)$$

This function set is the result of an exhaustive search of math functions that minimize the percentage error of the fitting of the experimental data. We searched for the “optimal” equation using MATLAB®. We started our quest with the functions integrated on the cftool interface. We then tested all the embedded functions (i.e., Polynomial, Exponential, Fourier, Gaussian, Power, Rational, Sum of Sine, Weibull) and compared them with the perceptual error of the regression. However, the error in the R_{SS} , R_{SS} and I_0 components stayed very high (i.e., 10% considering the overall range of illuminance for the fitting process). Therefore, we test by pre-processing the data using logarithmic functions (i.e., $10 \cdot \log_{10}$ and \ln based expressions) to linearize the fitting problem of these variables. A composition of iterative pre-processing (i.e., $10 \cdot \log_{10}$) and power (i.e., $a \cdot L_v^b + c$) regression was found as the “optimal” (i.e., error less than 10%) solution. However, the reason why this “optimal” equation set produces the lowest fitting error is out of the scope of this present work.

3.5.3 Estimation of the payload power constraint

We can estimate the MPP (i.e., I_{mp} , V_{mp} and P_{mp}) from the circuit component values predicted by the proposed models (IN and NI), and both (3.5) and (3.6). As we discussed in Section 3.3.3, the predicted P_{mp} is a reasonable estimation of the minimum power that the PVSC can supply at an arbitrary illuminance value.

3.5.4 Study Case: KXOB22-12X1L modeling

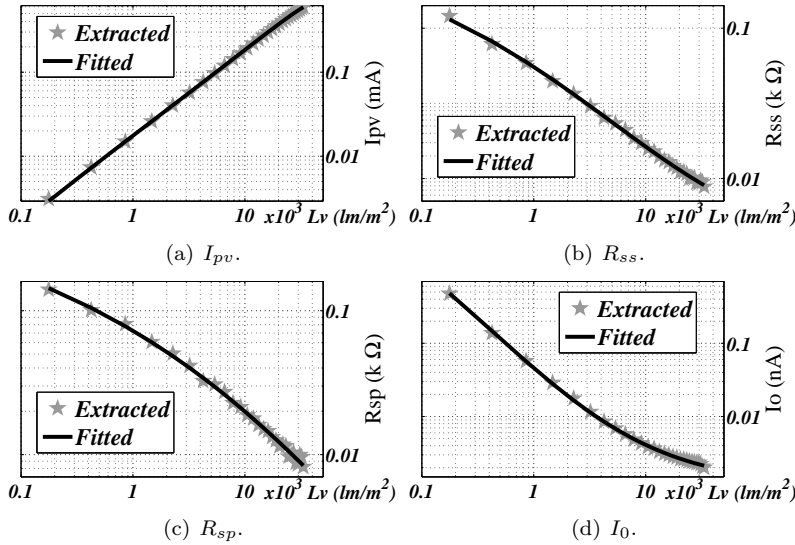
We calculated the parameters of both models (i.e., NI and IN models) using the dataset described in Section 3.4.2, and a customized script written in MATLAB® that implements the methodology presented in Section 3.5. We extracted the IN model parameters from the NI model parameters using the curve fitting tool (cftool); therefore, the

Table 6 – Parameters of IN model of the KXOB22-12X1L.

Par.	R_{ss}	R_{sp}	I_o	Par.	I_{pv}
a	-0.05107651	-0.04469432	-0.12077744	p_{i1}	-3.1147×10^{-14}
b	0.36394392	0.24809839	0.3613418	p_{i2}	1.1176×10^{-9}
c	12.0785002	12.2531266	12.3324676	p_{i3}	0.00017617
				p_{i4}	-0,00195557

Source: (The author, 2017)

Figure 26 – Component values of the circuit model of KXOB22-12X.

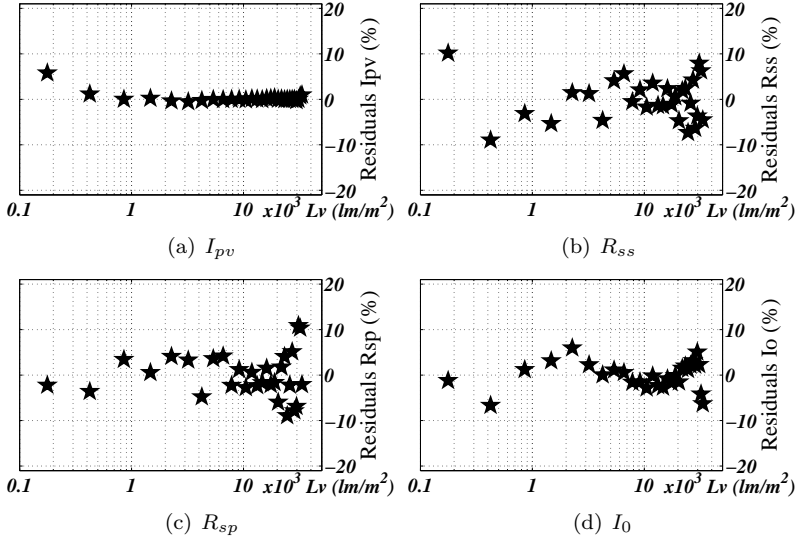


Source: (The author, 2017)

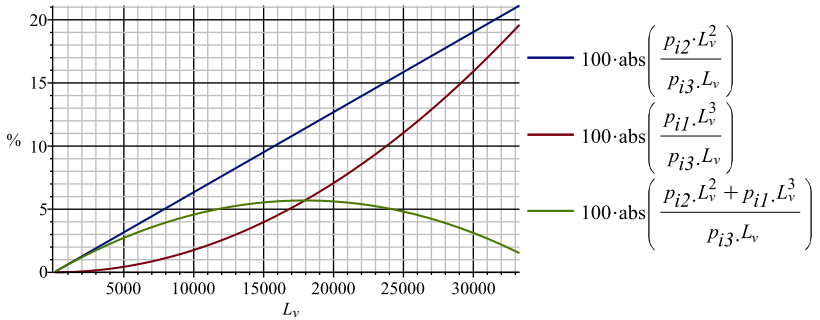
error for all the samples was minimized (in the least squares sense). We summarize the IN model parameters in Table 6. Furthermore, in Figure 26 we compare the component values (continuous functions) that were calculated using (3.11) to (3.15) and the NI model parameters (discrete functions). In Figure 27, we plot the residuals of the fitting process. This figure shows a quasi-random pattern that is always lower than 10.88%, indicating a good fit.

We implemented a script to individually analyze the terms of the fitting I_{pv} equation in Maple[®]. In Figure 28, we plot the linear (i.e., $p_{i3}L_v$), quadratic (i.e., $p_{i2}L_v^2$), and parabolic (i.e., $p_{i1}L_v^3$) terms. As

Figure 27 – Residuals of the fitting process.



Source: (The author, 2017)

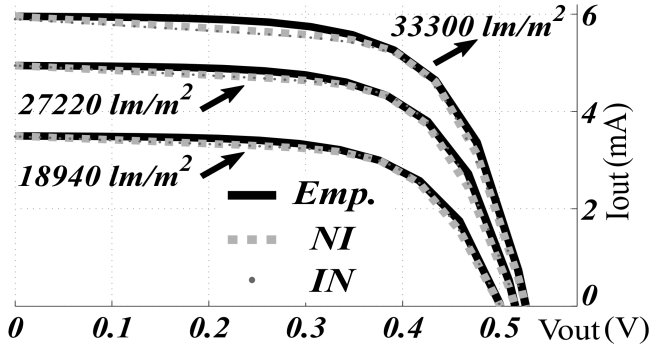
Figure 28 – Comparison of the math terms of the I_{pv} equation.

we show in the figure, the sum of the parabolic and quadratic terms is always less than 6% of the linear term, as is expected because the irradiance spectrum does not depend on the applied input voltage of the indoor emulator.

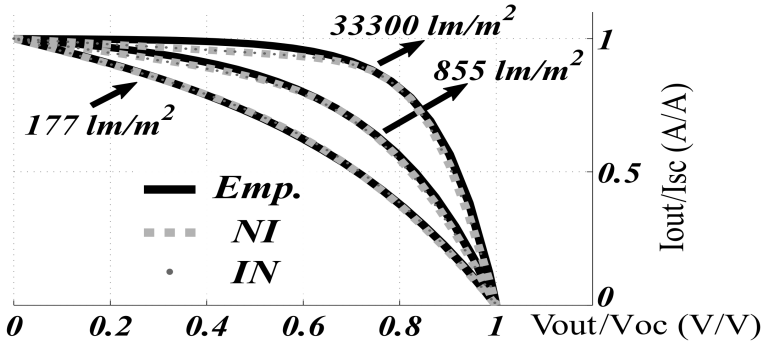
In Figure 29, we compare some of the predicted I-V curves for different levels of illuminance to the empirical data. Additionally, in

Fig 30(a) we plot both the predicted and the empirical values of the minimum power that the PVSC can supply at an arbitrary illuminance value produced by sunlight and/or typical illuminants. By examining the results, it is clear that the models (IN and NI) are similar and can accurately represent the KXOB22-12X1L behavior, especially around the MPP.

Figure 29 – Predicted I-V characteristics of the PVSC under test.



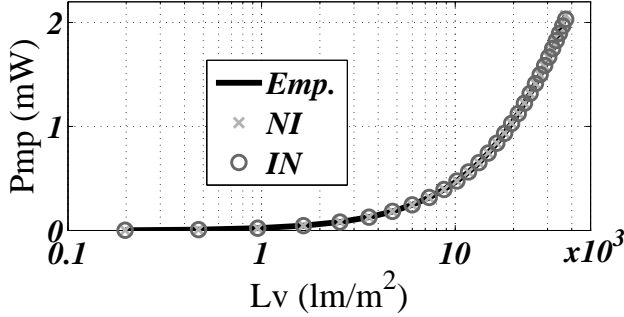
(a) I-V curve.



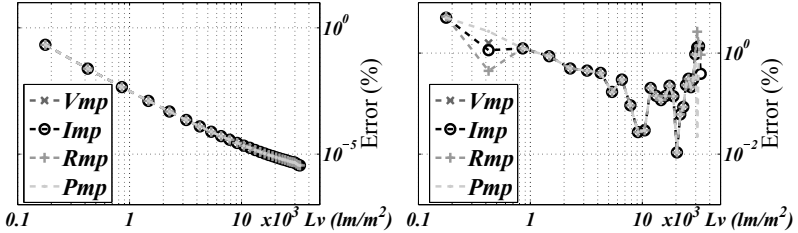
(b) Normalized I-V curve.

Source: (The author, 2017)

We have numerically evaluated the model's accuracy by comparing the empirical and predicted values of the maximum available power of the PVSC (i.e., P_{mp}), the voltage and current at MPP (i.e., V_{mp} , I_{mp}), and the impedance that must be imposed to the PVSC device to extract its maximum value (i.e., $R_{mp} = V_{mp}/I_{mp}$). In Figure 30, we calculate and plot the error involved in the prediction of these

Figure 30 – P_{mp} at the MPP and its error.

(a) Comparison of the predicted and experimental power at MPP.



(b) NI model.

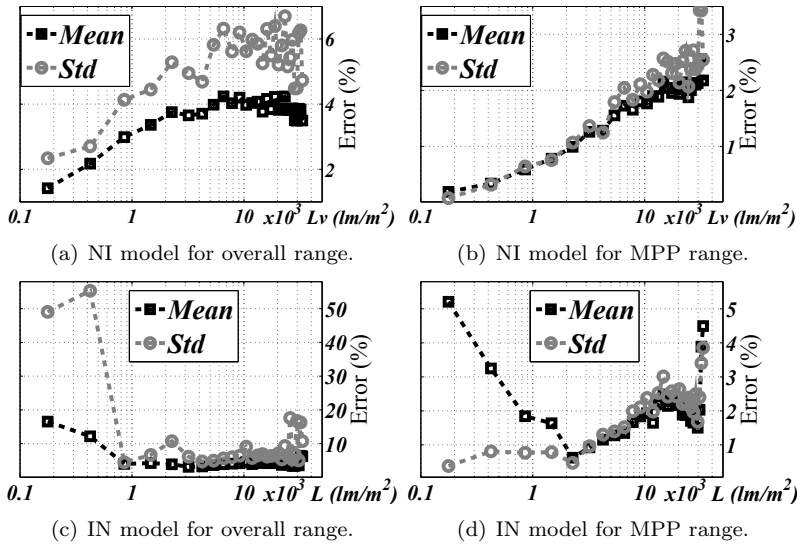
(c) IN model.

Source: (The author, 2017)

variables as a function of the illuminance. We conclude that on both models the error involved is very small (especially for the NI model) for almost the full illuminance range. Furthermore, the IN model had an error larger than the NI but this error is always lower than 5%. For the NI model, this error was higher for low-illuminance values. For the IN model, the error was concentrated near both the limits of the analyzed illuminance range. These were the worst-cases because of the fitting process.

We used the circuit component values that were predicted by the proposed models, the measured voltage and the equation (3.1) to estimate the current of the PVSC. We utilized these predicted currents to evaluate the model error in the overall voltage range (i.e., $0 < V_{in} < V_{oc}$) and for the MPP region (i.e., $0.8V_{mp} < V_{in} < 1.2V_{mp}$). In Figure 31, we calculate and plot the statistics of the absolute error as illuminance functions. By examination of these numbers and considering the overall range, it can be seen that the IN model is less accurate

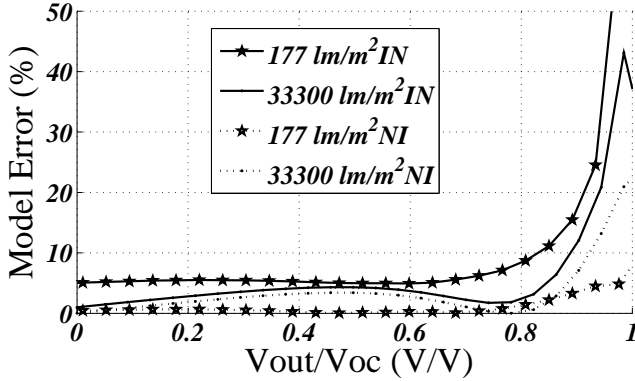
Figure 31 – Statistics of the absolute error of the e-PVSC models.



Source: (The author, 2017)

than the NI model, especially near both the minimum and maximum illuminance values. On the other hand, both models are very similar in the MPP region. Furthermore, the IN model had a mean error larger than the NI model, especially for lower values of illuminance; however, this mean error is lower than 6% for all of the illuminance range. To develop insight into the error distribution, in Figure 32 we plot the worst-cases of the absolute current error as a function of the normalized voltage. We note that the error is concentrated outside the MPP region, and increases near the V_{oc} and for low-illuminance levels. The error near V_{oc} is very high because the empirical current value is near to zero, which means that the percentage error increases hastily. Considering the IN model, the error at low-illuminance levels is high because of the fitting process.

Finally, Table 7 gives the statistics of the absolute current error. We conclude that both models are similar and very accurate in the MPP region. In contrast, in the overall range the impact of the fitting process is small in the mean error; however, it is critical for some samples outside of the MPP region.

Figure 32 – Current error vs V_{out}/V_{oc} of the PVSC under test.

Source: (The author, 2017)

Table 7 – Summary of the predicted error of the models.

Error (%)	IN model		NI model	
	MPP region	Overall range	MPP region	Overall range
MAPE	2.07	4.85	1.74	3.70
Stand. dev.	2.34	16.16	2.23	5.4

Source: (The author, 2017)

3.6 DISCUSSION AND FUTURE WORK

In this chapter, We presented only one study case as a proof of concept of the model methodology. We found a function that can be used to fit the experimental data of a solar cell to the analytical model. However, more study cases must be analyzed and explored to validate our approach. Besides that, the search of functions that can be used for PVSC arrays is out of the scope of this work.

In Table 8, we have summarized the proposed models that were discussed in Section 3.5.4 and the SoA that was discussed in Section 3.1. A comparison of the proposed models and the references that report a quantitative evaluation shows that the current error of the NI model is the lowest. Contrary to the previously reported test conditions, our test considers a large irradiance variation that covers from A to I illuminance categories suggested by the IESNA (RICHMEN, 2015).

Table 8 – SoA of the models for indoor PVSCs

Test Conditions						
Ref	Illum. type	Temp. control	Method	L_v or G Range	T Method	Range
(BENAVIDES; CHAPMAN, 2008)	HA	Yes	Est.	70-193 W/m^2	Cont.	30-40 °C
(TAN; PANDA, 2011)	FL	No	Mea.	380-1010 lm/m^2	Est.	295 K
(BRUNELLI et al., 2009)	HA	No	Not R.	10-100 W/m^2	Est.	27.5-40.2 °C
(YU et al., 2014)	Not R.	Not R.	Not R.	160-530 lm/m^2	Not R.	297 K
(SAVANTH et al., 2015)	Not R.	No	Mea.	100-2500 lm/m^2	Mea.	14-24 °C
(MASOUDINEJAD et al., 2015)	FL&HA	Yes	Mea.	0.01- 0.6 W/m^2	Cont.	298 K
This Work (NI).	LED	No	Mea.	177-33300 lm/m^2	Est.	298 K
This Work (IN)	LED	No	Mea.	177-33300 lm/m^2	Est.	298 K
Est.=Estimated, Mea.=Measured, Not R.=Not reported, Cont.=Controlled.						
Parameters Estimation Problem						
Ref	Circuit Topology	Implemented solution				
(BENAVIDES; CHAPMAN, 2008)	1D&2R	Not Reported				
(TAN; PANDA, 2011)	1D&2R	Not Reported				
(BRUNELLI et al., 2009)	1D&2R	Numerical solution at operation point and empirical EE.				
(YU et al., 2014)	1D&2R	Not reported solution at operation point and empirical EE.				
(SAVANTH et al., 2015)	2D&2R	Iterative solution of non-linear equations				
(MASOUDINEJAD et al., 2015)	1/2 D&2R	Solving a optimization problem by numerical iterative technique				
This Work (NI).	1D&2R	Numerical solution and assuming n value.				
This Work (IN)	1D&2R	Numerical solution and assuming n value, and fitting techniques .				
EE= Explicit Equations, 1/2 D&2R= 1D&2R and 2D&2R.						
Reported Extended Model						
Ref	Environment model inputs			Parameters calculation	Model accuracy	Model error
	L_v or G	level	T			
(BENAVIDES; CHAPMAN, 2008)	Discrete G	5	Continuous	Database	Low	Not R.
(TAN; PANDA, 2011)	Discrete L_v	3	Continuous	Database	Medium	Not R.
(BRUNELLI et al., 2009)	Discrete G	6	Continuous	OP+EE	Low	Not R.
(YU et al., 2014)	Discrete G	5	Continuous	OP+EE	Medium	1.05%@maxMPP
(SAVANTH et al., 2015)	Discrete L_v	4	Continuous	Database	Low	10%@maxMPP
(MASOUDINEJAD et al., 2015)	Discrete L_v	Not. R.	Continuous	Database	Medium	Not R.
This Work (NI)	Discrete L_v	29	Continuous	Database	High	1.74%@MMPPR
This Work (IN)	Continuous L_v	NA	Continuous	EE	High	2.07%@MMPPR
Not R.=Not reported, NA= it does not apply, OP=Model Parameters at Operating Point. MMPPR=current MAPE at MPP Region, maxMPP=maximum power error at MPP.						

Source: (The author, 2017)

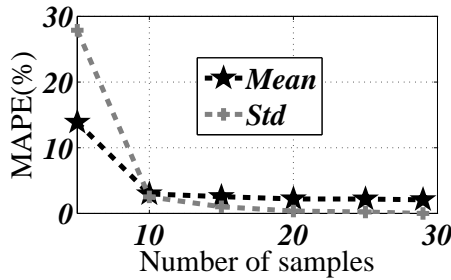
Furthermore, our methodology uses a LED lamp as illuminant and illuminance as environment input; therefore, the model reproduces the worst-case performance of a harvester based on indoor PVSCs. Finally, our model captures with analytical expressions the impact of the illu-

minance on the PVSC behavior and, therefore, the model complexity decreases, with a low impact on the model's accuracy.

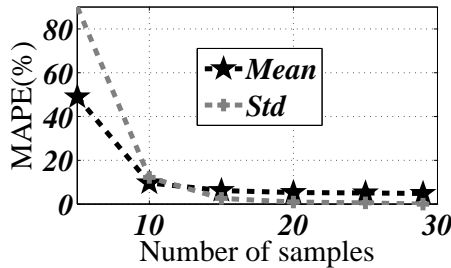
In the proposed methodology, the model is the result of a fitting process. To analyze the impact of the number of the samples used on the interpolation, the MAPE of the IN model was computed using less samples than were available. Using a random selection process, groups of 5, 10, 15, 20, and 25 selected levels were chosen. Then, the interpolation process detailed in Section 3.5 was calculated for each group. As shown in Figure 33, the MAPE increases as the number of samples decreases. Furthermore, when the number of samples is higher than 10, the increase in the MAPE variation is lower than 1%.

In Figure 31(b) the mean error increases with the increase in illuminance, this trend is partially explained by the impact of the temperature on the measured data, which is neglected in our modeling approach. To develop insight into the impact of temperature in our

Figure 33 – MAPE of the IN model Vs N. of samples.

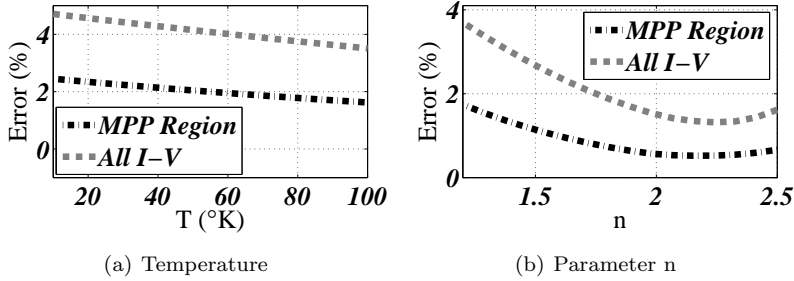


(a) MPP Region.



(b) Overall range.

Source: (The author, 2017)

Figure 34 – Variation of the NI MAPE with respect to the T and n .

Source: (The author, 2017)

models, in Figure 34(a) we have calculated and plotted the MAPE of the NI model as a function of the temperature. In our experimental setup, the temperature was an uncontrolled variable. Hence, as we expected, the error decreases with an increasing in temperature. However, this difference is lower than 1% for the analyzed temperature range. Therefore, the thermal impact produced by the illuminant on the PVSC device only partially explains the increase of the mean of the model at high illuminance level; hence, some other physical phenomena, such as low-internal isolation of the opaque enclosure could be affecting the results. In addition, in Figure 31(d) the STD of the current error increases with a decrease in illuminance, and the higher calibration error of the light source occurs in the low-illuminance region. Therefore, our test setup needs to be improved to increase the accuracy of the extracting models in the overall voltage range.

In the proposed methodology, we assumed that the parameter n was a fixed technology parameter to simplify the method. However, it could be used to optimize the resulting MAPE. For example, in the analyzed study case, the MAPE error of the NI model was computed by assuming that n was in a range from 1.2 to 2.5; as shown in Figure 34(b). Hence, if we had set n as 2.2, then the impact of this optimization would be significant (from 2.07% to 0.52%). However, the reason why this “optimal” value differs from the reported value for monocrystalline silicon PVSCs is out of the scope of this work.

In previous experimental studies of indoor PVSC that have considered small-signal modeling of illuminance, the authors have found a constant relationship (i.e., $V_{mp}/V_{oc} = k_V$) between the V_{mp} and the V_{oc} (LU; RAGHUNATHAN; ROY, 2010a). However, in our case study, which

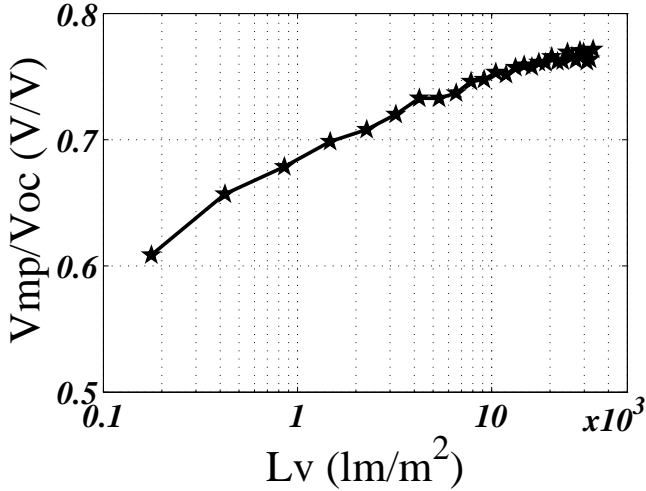


Figure 35 – Measured normalized V_{mp} .

uses large-signal modeling on illuminance, the relationship is approximately linear in the semi-log plot; as shown in Figure 35. Therefore, for our case study, a fractional open circuit voltage technique, such as the MPP tracking method, is unable to track the system at MPP for the full indoor illuminance range. The generalization of this result requires us to analyze more case studies.

3.7 CONCLUSIONS AND CONTRIBUTIONS

In this chapter, we present the synthesis of a novel model of indoor PVSC devices. This model is based on the 1D&2R and the extraction parameters proposed in (CUBAS; PINDADO; VICTORIA, 2014). However, as the main contribution, we propose a change in the actual indoor model paradigm using illuminance (instead of irradiance) and fitting tools to propose an e-PVSC 1D&2R circuit model with parameters expressed as nonlinear analytic functions of the illuminance, decreasing the model complexity with a low impact in the model's accuracy. The irradiance (W/m^2) is more common than illuminance (lm) in the modeling of photovoltaic solar cells. We could use the radiometric units instead of the photometric counterpart. However, we chose the photometric units because these units are directly related to the indoor

conditions. For example, a 500 lm/m^2 in indoor corresponds to the normal illuminance in an office, very similar to the intuitive understanding that 1 W/m^2 (at STC conditions) corresponds to the irradiance of the incident sunlight on a clear day.

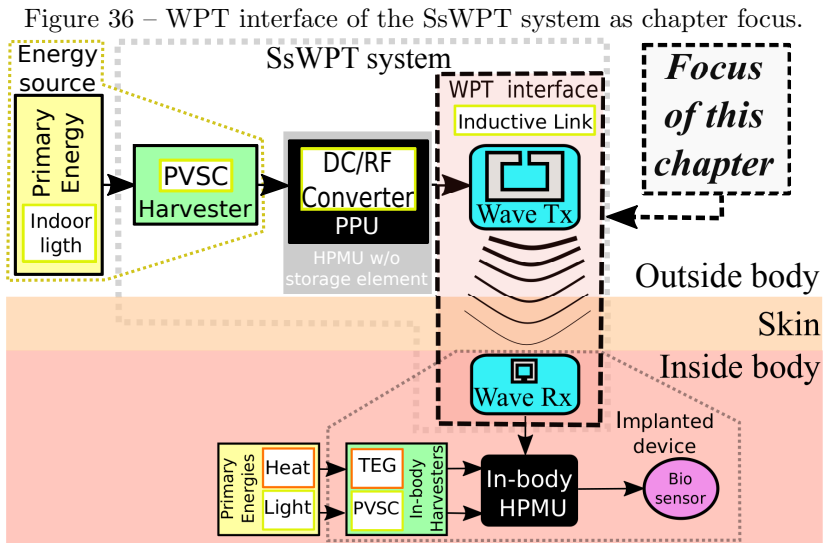
This model is advantageous in harvesting applications because it predicts the power constraint imposed by the indoor PVSC device to the payload. Furthermore, this model accurately predicts the operation of the indoor PVSC under the proposed test conditions (i.e., warm LED spectrum, illuminance from 177 to $33.3 \times 10^3 \text{ lm/m}^2$, and room temperature). To summarize, the synthesized model achieves a MAPE of 4.85% for the overall I–V curve and 2.07% considering only the MPP region. When the proposed model is compared with the SoA, it is the only model that covers from A to I illuminance categories suggested by the IESNA for indoor lighting.

As minor contributions developed in this chapter, we have found that for warm LED light the open circuit voltage and the voltage at the MPP do not have a constant relationship.

4 ON THE MODELING OF PLANAR SQUARE ONE-TURN INDUCTORS FOR WIRELESS POWER TRANSFER APPLICATIONS

In this chapter, we present a lumped circuit model of Planar Square One-turn Inductors (PSOIs), which we extend to model an inductive link that is based on this type of inductor. Also in this chapter, we evaluate the performance of the inductor and link models using full-wave EM simulation and experimental results. As we show in this chapter, the presented link model can be used to understand the link optimization problem from the physical point of view. Furthermore, in Chapter 5, we use this link model instead of EM simulation to maximize the power transfer efficiency of an SsWPT system that is composed of an indoor PVSC, a DC/RF converter, and an inductive link that is based on PSOI devices. We summarize in Figure 36 the focus of this chapter.

We organize the rest of this chapter as follows. In Section 4.1, we discuss the context of planar inductor modeling for WPT applications using a brief and balanced review of the pertinent published literature. In Section 4.2, we introduce the geometry and frequency response of

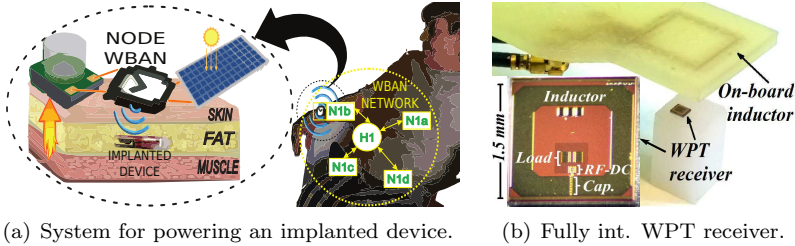


Source: (The author, 2017)

the PSOI devices and we analyze a previously reported link that uses the model presented in this chapter to develop an insight into the inductive links that are based on PSOIs. Section 4.3 focuses on some of the theoretical fundamentals of inductor modeling for WPT applications. Section 4.4 describes the specific procedures that were used in the modeling of the PSOI device. We extend the inductor model to model the link. We evaluate the inductor and the link models using full-wave EM simulations and experimental characterization in Section 4.5. In Section 4.6 we describe the main results of this chapter and we also make a number of recommendations for future modeling and characterization of planar inductors for WTP applications. Finally, in Section 4.7 we highlight the conclusions and the contributions of this chapter.

4.1 INTRODUCTION

Figure 37 – Examples of asymmetrical inductive links.



(a) System for powering an implanted device.

(b) Fully int. WPT receiver.

Source: ((a) The author, 2014; (b) Taken from (CABRERA; SOUSA, 2016))

There is currently increasing interest in providing energy autonomy to electronic devices for implementing concepts such as the Internet of Things (WHITMORE; AGARWAL; XU, 2014), and Wireless Body Area Networks (MOVASSAGHI; ABOLHASAN; LIPMAN, 2013; FAJARDO; SOUSA, 2016d). In healthcare applications, autonomous implants have been proposed thanks to innovations in design, materials, and circuits (HANNAN et al., 2014). The most suitable solution to continuously power an implanted device is a WPT system that is composed of an external energy source and a resonance-based inductive link (HANNAN et al., 2014; AMAR; KOUKI; CAO, 2015); as illustrated in Figure 37(a). A unique characteristic of miniaturized implants is the limited surface of the receiver (R_x), which restricts the magnetic flux in the R_x coil.

To circumvent this constraint, the geometry of the transmitter(Tx) coil can be properly designed to provide the coupling coefficient (k_{IL}) that optimizes the link efficiency. This type of inductive link with individually designed coils is asymmetric (KIOURTI; NIKITA, 2017; ZARGHAM; GULAK, 2015; CABRERA; SOUSA, 2016). CMOS implants are commonly based on asymmetrical inductive links with an Rx coil attached to the application chip through wire bonding (KIOURTI; NIKITA, 2017). However, fully integrated WPT receivers, such as the one illustrated in Figure 37(b), have recently been explored using square planar coils (ZARGHAM; GULAK, 2015; CABRERA; SOUSA, 2016).

In (ZARGHAM; GULAK, 2015), an iterative optimization process assisted by full-wave EM simulation was used to maximize the efficiency of a link based on a $2 \times 2.18 \text{ mm}^2$ on-chip WPT receiver fabricated in standard $0.13 \text{ }\mu\text{m}$ CMOS technology. The authors report a measured efficiency of 1.42%, and propose a FoM, achieving a link FoM of 160. In (CABRERA; SOUSA, 2016), an intensive full-wave EM simulation work was carried out to determine the design space of a link based on a $2 \times 1.5 \text{ mm}^2$ on-chip WPT receiver fabricated in $0.18 \text{ }\mu\text{m}$ CMOS technology. The authors report a link efficiency of 0.93% and a FoM of 276. We note that this FoM is a numerical quantity that is calculated using the WPT receiver area, the distance (d_{IL}) between Rx and transmitter (Tx) coils, and the link efficiency. Generally, the “fully integrated” link optimization process starts by fixing the receiver area (i.e., chip area), and the distance between the chip and the external unit (i.e., d_{IL}). Next, the designer determines both the optimum operation frequency and the associated geometric values of the coils, using link efficiency as the main design goal (HANNAN et al., 2014).

The optimization problem formulation involves several variables, such as load matching, coil geometries, and operating frequency (HANNAN et al., 2014; ZARGHAM; GULAK, 2015; CABRERA; SOUSA, 2016). It is solved using full-wave EM simulations and, consequently, demands excessive time and resources (ZARGHAM; GULAK, 2015). However, the designer can maximize the EM coupling level of the link (A) instead of the link efficiency (CABRERA; SOUSA, 2016), thereby simplifying the problem formulation in asymmetrical links (CABRERA; SOUSA, 2014, 2016). This factor is a generalization of the well-known kQ factor (which is used in symmetrical links (OHIRA, 2017)) and it is directly related to the efficiency. Furthermore, as we show in Section 4.3.2, the

link efficiency can be expressed as a function of A :

$$\frac{1}{\eta_{IL}} = \left(\sqrt{\frac{1}{A}} + \sqrt{1 + \frac{1}{A}} \right)^2 ; \quad (4.1)$$

where $A = k_{IL}^2 Q_1 Q_2$ and $Q_{1(2)}$ is the quality factor of the $Tx(Rx)$ coil. In (CABRERA; SOUSA, 2016), the authors partially maximize the A factor using a link based on PSOI devices and solve the resulting optimization problem with full-wave EM simulations. As far as we are aware, this reported link has the best performance (i.e., FoM of 276).

The PSOI is suitable for links with fully integrated receivers for the following reasons:

- The planar geometry can be laid in one or several integrated circuit metal layers (ZARGHAM; GULAK, 2015; CABRERA; SOUSA, 2016).
- The one-turn coil partially maximizes the A factor because the number of turns (considering planar inductors) decreases both the k_{IL} coefficient and the inductor quality factor (CABRERA; SOUSA, 2016).
- The square shape of the receiver coil efficiently uses the area available in the chip and in the receiver coil it maximizes the k_{IL} (assuming that there is a square coil in the receiver) (ZARGHAM; GULAK, 2015; CABRERA; SOUSA, 2016).

In the optimized asymmetrical links reported in (CABRERA; SOUSA, 2014, 2016), the Tx and Rx PSOI operates near and far below Self-Resonance Frequency (SRF), respectively. We emphasize that the conventional planar inductor models cannot be used directly to optimize the Tx PSOI geometry because these models underestimate the inductor quality factor near the SRF (DOLDAN; GINES; RUEDA, 2013; O., 1998), and/or because the relation between the model circuit components and the inductor quality factor is not analyzed.

The quality factor could be used as functional starting point for high-performance RF system design. However, ambiguous expressions of the quality factor appear in the literature. For example, in (OHIRA, 2016), the author review some of the typical definitions used in RF circuits, which are not equivalents. This is the reason why circuit designers can become confused about how to exploit the Q concept to create or optimize a circuit topology or parameter. Probably the most

fundamental definition for Q factor in both physics and engineering context is given by (O., 1998):

$$Q_{E_{\max}} = 2\pi \frac{W_{\max}}{W_{\text{diss}}} \quad (4.2)$$

where W_{\max} is the maximum total stored electric and magnetic energy in the system, and W_{diss} is the dissipated energy per cycle. However, an experimental measure of the Q based on this definition is complex or impossible. In the conventional modeling approach, the inductor Q is defined as $Q_a = \text{Im}\{Z_e\}/\text{Re}\{Z_e\}$; where Q_a is the apparent inductor quality factor, which corresponds to the inductor Q only when the coil can be modeled as a lossy inductor without parasitic capacitance (as we discussed in Section 4.3.1.3). This definition is useful in several practical circuits because the inductor operates at a frequency that is much less than its SRF, and hence the estimation error (i.e., $E_Q = \{Q - Q_a\}/Q$) is negligible (DOLDAN; GINES; RUEDA, 2013; O., 1998). However, the Tx coil of a link based on PSOI devices operates near its SRF and, consequently, this error impacts significantly on the predicted values of A and η values (as we analyze in Section 4.2.2).

In (CABRERA; FEITOZA; SOUSA, 2015), the authors propose a scalable lumped model to model onboard PSOI devices, which estimates the inductor Q instead of the “apparent” Q (i.e., Q_a). Furthermore, the estimated quality factor is involved in the mutual coupling between inductors, which is useful when estimating the A factor. These authors extracted the model parameters using an iterative process that involves physically oriented simplifications, circuit analysis, and algebraic manipulations. This model is used in (CABRERA; SOUSA, 2014) to optimize an asymmetric link that is composed of two onboard PSOIs that are fabricated on FR-4 substrate. These authors solve the optimization problem using geometric programming instead of full-wave EM simulation, which is used only in the final test before the link prototyping. Indeed, the development of PSOI electric models is required to simplify the link optimization by avoiding the need for hard simulation work in all of the optimization process.

After the careful design of the link, the experimental characterization of the inductors and their coupling allows us to estimate their performance in the WPT system. Moreover, it can also be used to validate inductor and link models, and to optimize the coil geometry of the inductors (O., 1998). Recently, in (OHIRA, 2017), the authors study the WPT systems as a two-port black box and derive a general expression for the KQ factor from the impedance parameters. Although this ap-

proach is useful when measuring the ability to transfer the power of the system, it cannot be used to assess the contribution of the inductors. The experimental characterization of the PSOI inductors in an efficient link is challenging for several reasons (CABRERA; SOUSA, 2014, 2016):

- The inductors operate at high-frequency bands (i.e., HF, UHF, and VHF).
- The input impedance of the inductors significantly differs from the characteristic impedance of the instrument and cabling (i.e., $Z_0 = 50\Omega$).
- The receiver coil is fully integrated.
- The transmitter coil operates near its SRF, and it has a high Q value.

Recently, in (CABRERA; SOUSA, 2015) the authors propose an accurate contactless method that can be used to measure the Q_a of fully integrated inductors while avoiding the use of additional EM structures (e.g., microprobes) that are useful to de-embed or to reduce the parasitics (added by the wired connections). Although this method can be used to characterize the Rx coil because it operates below its SRF, it cannot be used to characterize the Tx coil. As we discussed previously, this coil operates near its SRF and, consequently, the Q differs greatly from the Q_a . Furthermore, this Q characterization can lead to a large error because of the following reasons:

- When a Vector Network Analyzer (VNA) is employed, the Q is estimated from the measured $|S_{11}|$, which approaches 1 for high Q values. Therefore, even a tiny inaccuracy creates a huge error value. For frequencies lower than 3 GHz, this problem is overcome using an impedance or material analyzer and/or special calibration techniques (e.g., the Short-Open-Load-Through standard and low-loss capacitor as the second load) (HARUTA, 2006).
- Measurements near the SRF are influenced by the residual parasitics produced by the interaction between Inductor Under Test (IUT) and test fixture. This fact is typically accepted and the test fixture has been reported with the measured values (HARUTA, 2006).
- The quality of the inductors is commonly estimated from the measured values of its terminal impedance, which can be obtained

with the help of a VNA. This leads to correct results for frequencies well below the device SRF because the Q_a is equal to Q . However, near the SRF, the Q_a is less than Q ; hence, Q is underestimated (DOLDAN; GINES; RUEDA, 2013; O., 1998).

As we discuss in Section 4.2.2, the estimation error produced by this underestimation noticeably impacts the predicted values of A and η values, and it becomes larger as the link asymmetry increases. As far as we know, only two papers have reported extraction techniques to reduce the estimation error of the inductor quality factor (O., 1998; DOLDAN; GINES; RUEDA, 2013). In (O., 1998), the authors use a virtual capacitor to artificially shift the resonance frequency so that the value of Q can be estimated from the 3 dB bandwidth of from the frequency stability factor. This is a clever solution because it enables us to estimate the Q of the device in any frequency, instead of the Q_a , without requiring modifications of the measurement setup. However, this measurement technique produces inaccurate results for high- Q inductors because the VNA measurement of the inductor impedance is very inaccurate when the $|S_{11}|$ approaches 1.

In the next sections, we extend the scalable PSOI model that was proposed in (CABRERA; FEITOZA; SOUSA, 2015; CABRERA; SOUSA, 2014) using a novel parameter extraction methodology, which ensures a very small error in the estimation of the inductor input impedance (Z_e) up to the SRF. The resulting scalable model is analytical, its circuit components have physical meaning, and it can be used for estimating the Q and the A factor. The presented PSOI model shows good agreement with the full-wave EM simulations, a MAPE of less than 7% in both the real and the imaginary parts of the PSOI impedance in a range from 10 MHz to 0.97 SRF MHz. Moreover, for the studied link, the error between the model and the EM simulation is 2.3% and 4.7% for the A_{max} and η_{ILPTE_M} , respectively. In addition, we report a novel method to experimentally characterize high- Q inductors up to their SRF, which is based on the contactless technique that was reported in (CABRERA; SOUSA, 2015). It uses an inductor to sense the IUT EM fields without electric contact. The Q is then calculated from the measured sensor reactance. We apply the proposed method to a Tx coil of a previously published link (CABRERA; SOUSA, 2014). The empirical data are consistent with the scalable model and the full-wave simulation.

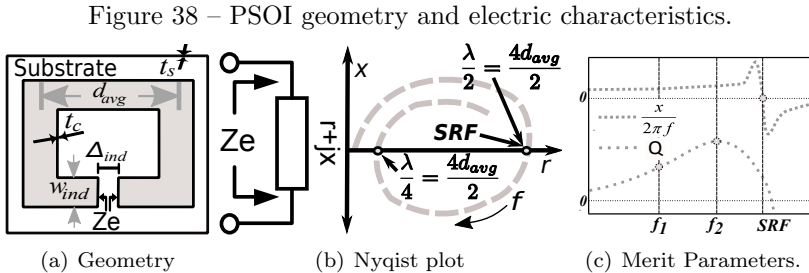
4.2 PLANAR SQUARE ONE-TURN INDUCTOR

4.2.1 Geometry and frequency response

The PSOI is etched onto a substrate by laying out the metal trace, as illustrated in Figure 38(a). The PSOI is defined by its geometric parameters, as follows: the metal thickness (t_c), the average diameter (d_{avg}), the line width (w_{ind}), and the substrate thickness (t_s). However, t_c does not significantly affect the frequency response of the device and, therefore, can be neglected. The PSOI impedance (i.e., $Z_e = r + jx$) varies with the frequency (f); as shown in Fig 38(b). This variation is due to several physical phenomena, such as skin effect, eddy currents, and radiation. Therefore, the PSOI “apparent” inductance (i.e., $L_a = x/2\pi f$) and the inductor Q varies with frequency; as shown in Fig 38(c). The PSOI operates as an ideal inductor from f_1 to f_2 because the inductance value is relatively constant and the Q values are high. On the other hand, in an asymmetric link, the operation frequency is chosen to maximize the A factor. Consequently, the Tx PSOI operates in a frequency range from f_2 to its SRF, and Rx PSOI operates in a range from f_1 to f_2 . Therefore, the PSOI model must be valid from f_1 up to the SRF, with an accurate prediction of the Q and Z_e .

4.2.2 Inductive links based on PSOI devices

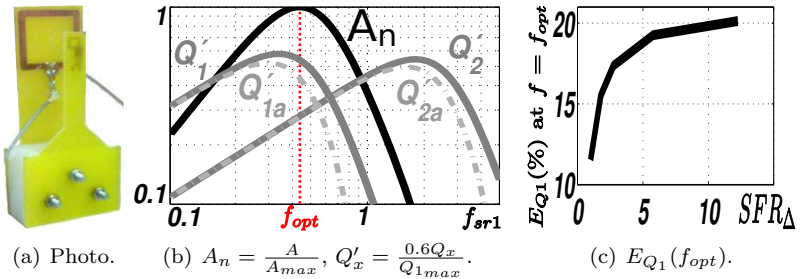
To develop insight into the impact of E_Q , we analyzed the link reported in (CABRERA; SOUSA, 2014) using the model presented in this



Source: (The author, 2017)

chapter. We normalized the frequency to the SRF of the transmitter (i.e., $f_{sr1} = f/SRF_1$) and drew the scaled theoretical curves of this link versus the normalized frequency; as shown in Figure 39(b). In this example, the optimum frequency (f_{opt}) was 393 MHz ($0.44 \cdot SRF_1$), $E_{Q1}(f_{opt})$ was = 19.5%, and $E_{Q2}(f_{opt})$ was 0.6%, the $A(f_{opt})$ was 6.63, the link efficiency was 47%. These errors in the Q produced an under-estimation of the A and η of 19.6% and 7.9%, respectively. In addition, to quantify the relationship between E_Q and the link asymmetry, we studied a link composed of two PSOs fabricated on a standard FR-4 substrate and separated by 15 mm. Moreover, the receiver geometry was specified. We found the theoretical design space using the model proposed in (CABRERA; FEITOZA; SOUSA, 2015) and varying both the average diameter (d_{avg}) and the line width ($W_{ind} = d_{avg}/5$) of the transmitter coil. In the resulting design space, f_{opt} varied from $0.3 SRF_1$ to $0.7 SRF_1$, the $E_{Q2}(f_{opt})$ was negligible and $E_{Q1}(f_{opt})$ was significant. Furthermore, the $E_{Q1}(f_{opt})$ increases as the link asymmetry increases (numerically quantified by $SRF_{\Delta} = SRF_2/SRF_1$) until it reaches a maximum saturated value, where the link operates in the weakly coupled regime. We illustrate this trend in Figure 39(c), where the saturated value of the error was 20%, approximately.

Figure 39 – Results and photograph of the link reported in (CABRERA; SOUSA, 2014).



Source: ((a) Taken from (CABRERA; SOUSA, 2016); (b) and (c) The author, 2017)

4.3 THEORETICAL FRAMEWORK

4.3.1 Lumped circuit inductor models for WPT applications

From a practical point of view, a broadband lumped circuit model for a given inductor structure is desirable because it can be used by multiple designers and at different frequencies. It can also be used to explore the link design space without full-wave EM simulations. Although the inductors are three-dimensional distributed system, they are usually modeled by a two-port equivalent circuit with lumped components (ARVAS, 2012). The component values are commonly extracted by fitting the two-port Y-parameters that are obtained after de-embedding (DOLDAN; GINES; RUEDA, 2013; ARVAS, 2012). Several equivalent circuit topologies to model spiral inductors have been reported, especially for integrated inductors. A survey of the published works on this subject can be found in (ARVAS, 2012). In WPT applications, researchers commonly use the circuits shown in Fig. 40 because its L parameter (i.e., L_p or L_s) relates to the magnetic flux generated by the coil and it can be used to model the WPT dynamics with the theory of coupled inductors.

4.3.1.1 Lumped RL circuit used as an inductor model

The model parameters of the RL circuit, shown in the Fig. 40(a), are the equivalent series inductance (L_s) and the equivalent series resistance R_s), which are related to the impedance of the real inductor by:

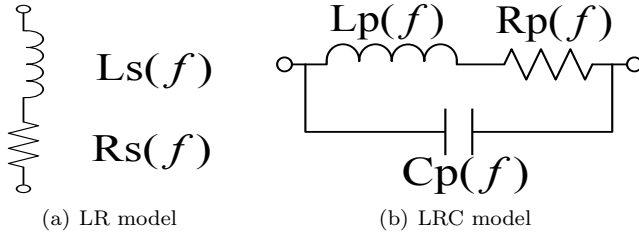
$$L_s = \frac{\text{Im}(Z_e)}{2\pi f} = \frac{x}{2\pi f}; \quad (4.3)$$

$$R_s = \text{Re}(Z_e) = r; \quad (4.4)$$

where, f is the electric frequency. This model is used in resonant WPT systems because the coils, in the majority of practical applications, work at frequencies far below their SRFs. Furthermore, the manufacturers of inductors use this model because its parameters can be extracted directly from the measured impedance or S-parameters of the IUT.

At low frequencies, the L_s of a real inductor is relatively constant. When the operating frequency increases, the parasitic effects (such as parasitic capacitances) start to increase and L_s value turns

Figure 40 – Circuit inductor models for WPT applications.



Source: (The author, 2017)

a function of f . Finally, the real inductor impedance is only real (i.e., $\text{Im}(Z_e(\text{SRF})) = 0$) at the SRF; hence, $L_s(\text{SRF}) = 0$. However, following the physical concept of inductance means that the device does not store energy, which is not true. This model gives incorrect results because of the non-physical meaning of the inductive definition given by (4.3). This modeling approach is useful when the coils operate far below their SRFs. However, it is irrelevant for calculating the design space of asymmetrical inductive links because the transmitter coil typically operates near its SRF.

4.3.1.2 A lumped RLC circuit as an inductor model

The L_p component represents the self-inductance of the wire and also the distributed mutual inductance of the spiral coil. However, near to the SRF, the overall inductance is due to a distributive phenomenon because the current density in the wire becomes nonuniform and, therefore, the current magnitude depends on both the frequency and the position. Similarly, the C_p value stands for the self-capacitance of the wire and the distributed capacitance of the spiral coil. Furthermore, when the inductor operates near to its SRF, the electric field distribution varies as the current changes. Therefore, the capacitance becomes dependent on the frequency and position. The R_p value accounts for the resistance associated to the wire, which is determined by several physical phenomena (e.g., skin effect, current-crowding effects, eddy currents, radiation, etc). For a first-order approach, we can consider L_p and C_p as frequency-independent parameters and concentrate all the frequency-dependent physical phenomena into R_p (RIAÑO et al., 2016).

The RLC circuit is typically employed to model the planar inductors of inductive links (LI; MI, 2015; CABRERA; SOUSA, 2014; RIAÑO et al., 2016). The model's parameters are not directly related to the measured inductor impedance (or S-parameters). Furthermore, these model parameters must be fitted to the measured data and there are some possible solutions that minimize the involved error. To separate inductance and resistance values with physical meaning from the apparent values created by the parasitics capacitance, we proposed in Section 4.4.2.2 to use a physical oriented fitting instead of the traditional approach. However, contrary to the LR model that was discussed in the last section, the RLC model shown in Figure 40(b) allows us to capture the parasitic capacitor of the real inductor. It also separates the resonance phenomenon from the inductance and loss resistance. Therefore, it allows a better understanding of the inductor physics. In the rest of this chapter, we use L , C and R instead of L_p , C_p and R_p .

4.3.1.3 Inductor quality factor

The quality factor (i.e., Q) is used to give an indication of its performance in a circuit. For instance, in matching networks, the Q factor is related to loss; in bandpass filters, it is related to the 3-dB bandwidth; and in oscillators, it is related to the frequency stability and phase noise. Basically, the Q describes the inductor performance as an energy-storage element, which means that it quantifies the relationship between storage and dissipated energy in the device (RAZAVI, 2011). Moreover, accurately estimating of the Q is difficult because of the inaccurate modeling of the distributed nature and the frequency dependence of the involved physics phenomena (O., 1998; RAZAVI, 2011). In addition, some errors are introduced by the extraction of circuit model parameters (e.g., capacitive, resistive and inductive elements) from the measurements (O., 1998).

As we discussed in the introduction, the more general definition of Q factor is given by (O., 1998):

$$Q_{E_{\max}} = 2\pi \frac{W_{\max}}{W_{\text{diss}}}. \quad (4.5)$$

However, in inductor modeling the conventional definition is (O., 1998):

$$Q_{\bar{W}} = 2\pi \frac{(\bar{W}_M - \bar{W}_E)}{W_{\text{diss}}} \quad (4.6)$$

where \bar{W}_M and \bar{W}_E are the average stored magnetic and electrical energies in the inductor. This definition is commonly used because the researcher can easily calculate $Q_{\bar{W}}$ from the measured impedance of the inductor by:

$$Q_{\bar{W}} = \frac{Im(Z_e)}{Re(Z_e)}. \quad (4.7)$$

However the estimation of the $Q_{E_{max}}$ by $Q_{\bar{W}}$ can lead to a large error (O., 1998; DOLDAN; GINES; RUEDA, 2013). At low frequencies, the total energy ($\bar{W}_M - \bar{W}_E$) is dominated by \bar{W}_M and Q_a is close to $Q_{E_{max}}$. However, as frequency is increased, the \bar{W}_E increases, and the total energy decreases, which in turn increases the difference between and $Q_{\bar{W}}$ and $Q_{E_{max}}$. Furthermore, at the SRF the total energy is zero, which means that the $Q_{E_{max}}$ estimated using $Q_{\bar{W}}$ is zero. This result is physically unreasonable. Therefore, the $Q_{\bar{W}}$ is only a good estimator of the $Q_{E_{max}}$ at frequencies well below the SRF.

From the circuit's point of view, when the inductor is modeled using the RL model, its Q factor is given by:

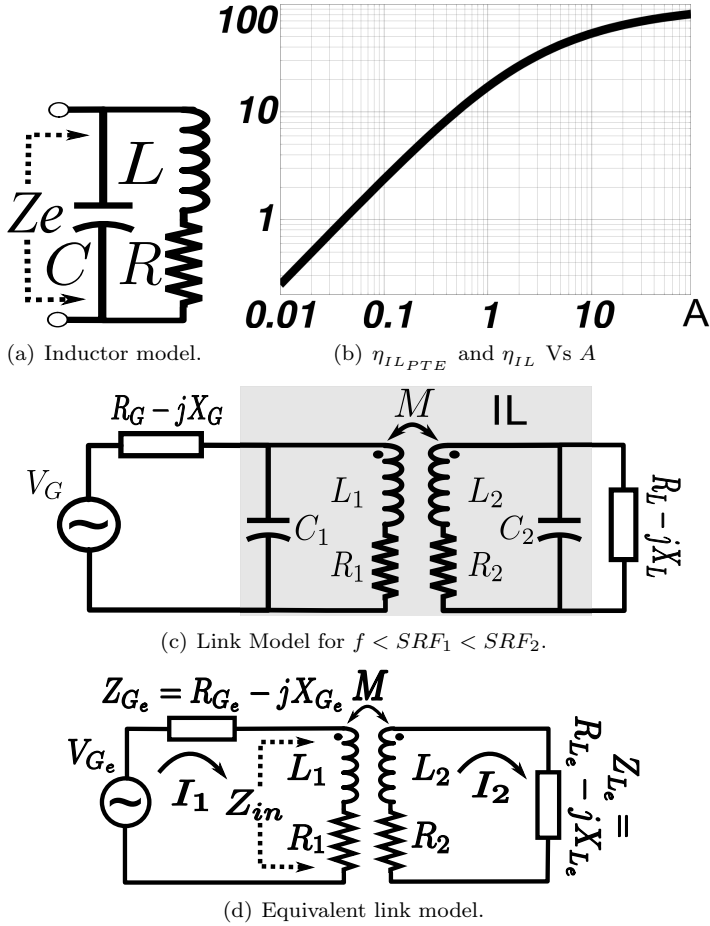
$$Q_s = \frac{\omega L_s}{R_s} = 2\pi \frac{f \cdot L_s}{R_s} = 2\pi \frac{(\bar{W}_M - \bar{W}_E)}{W_{diss}} \quad (4.8)$$

where ω is the electric angular frequency; hence, the Q estimated by this modeling approach is only a good estimator of the quality factor of the real inductor well below its SRF. On the other hand, when the inductor is modeled using the RLC model, its Q factor is given by:

$$Q_p = \frac{\omega L_p}{R_p} = \frac{\omega L}{R} \approx 2\pi \frac{\bar{W}_M}{W_{diss}} = Q_{E_{max}} \quad (4.9)$$

this expression is only a good estimator of the quality factor of the real inductor if the R_p , L_p and C_p parameters accuracy represents the real inductor's EM behaviors.

In summary, the quality factor evaluation as resonant tank (i.e., Q_p) overcomes the drawbacks of the conventional Q definition (i.e., Q_s), avoiding any confusion between the average total and maximum energy of inductor. However, the data sheets normally give the inductor quality factor by considering the conventional definition, and they may contribute to the existing confusion about the inductor's Q definition. In this chapter, the Q_s and Q_p are referred as the “apparent” Q (i.e., Q_a) and Q of the inductor, respectively.

Figure 41 – Circuit models and the A impact in the WPT system

Source: (The author, 2017)

4.3.2 The power transfer effectiveness of the inductive link

We can analyze the WPT system based on inductive link with the aid of Figure 41(c). In this figure, the Tx coil is powered by an arbitrary sinusoidal energy source that is composed of V_G and $Z_G = R_G - jX_G$, and the Rx coil is loaded by an arbitrary impedance that is defined by $Z_L = R_L - jX_L$. Furthermore, both coils are modeled using the

RLC model that was discussed in the previous section. The energy transfer is modeled by the coupling between L_1 and L_2 , where the mutual inductance (M) is given by:

$$M = k_{IL} \sqrt{L_1 L_2}. \quad (4.10)$$

We can calculate the power transfer effectiveness of the link using two FoM, the efficiency (η_{IL}) and power transfer efficiency of the link (η_{ILPTE}), which are given by:

$$\eta_{IL} = \frac{P_{L_{IL}}}{P_{in_{IL}}}; \quad (4.11)$$

$$\eta_{ILPTE} = \frac{P_{L_{IL}}}{P_{avs}}; \quad (4.12)$$

where $P_{in_{IL}}$ is the input power of the link, $P_{L_{IL}}$ is the power consumed by the load, and P_{avs} is the maximum available power of the source. Without loss of generality, we can merge the self-capacitors C_1 and C_2 into the source and the load, respectively, resulting in the link model shown in Figure 41(d). Considering this circuit, we rewrite (4.11) and (4.12) as:

$$\eta_{IL} = \frac{\|I_2\|^2 R_{Le}}{\|I_1\|^2 \text{Re}\{Z_{in}\}}; \quad (4.13)$$

$$\eta_{ILPTE} = \frac{P_{in} \cdot \eta_{IL}}{\|V_{G_e}\|^2 / 8R_{G_e}} = \frac{(\omega M)^2 4R_{G_e} R_{Le}}{(\|Z_{G_e} + Z_{in}\| \cdot \|Z_{Le} + Z_{L2}\|)^2}. \quad (4.14)$$

Before some algebraic manipulation, these expressions can be rewritten as:

$$\eta_{IL} = \frac{\alpha_L - 1}{\frac{Q_2}{A} \beta_L + \alpha_L \left(1 + \frac{\alpha_L}{A}\right)}; \quad (4.15)$$

$$\eta_{ILPTE} = \frac{4(\alpha_G - 1)(\alpha_L - 1)}{\left(\frac{\alpha_G \alpha_L}{\sqrt{A}} + \sqrt{A}\right)^2 + \frac{1}{k_{IL}^4} \left[\beta_G \beta_L (\beta_G \beta_L - 2k_{IL}^2) + \left(\frac{R_1}{R_2} \frac{\beta_G}{Q_2}\right)^2 + \left(\frac{R_2}{R_1} \frac{\beta_L}{Q_1}\right)^2 \right]}; \quad (4.16)$$

where

$$\alpha_L = 1 + \frac{1}{p_L} = 1 + \frac{R_{Le}}{R_2}; \beta_L = 1 - \frac{1}{q_L} = 1 - \frac{X_{Le}}{X_{L2}},$$

$$\alpha_G = 1 + \frac{1}{p_G} = 1 + \frac{R_{G_e}}{R_1}; \beta_G = 1 - \frac{1}{q_G} = 1 - \frac{X_{G_e}}{X_{L1}},$$

and $R_{1(2)}$ is the resistance of the Tx (Rx) coil. Assuming optimum matching conditions (i.e., $\beta_G = \beta_L = 0$ and $\alpha_L = \alpha_G = 1 + \sqrt{1 + A}$), we put (4.16) and (4.15) in the form of (4.1), that is:

$$\frac{1}{\eta_{ILM}} = \frac{1}{\eta_{ILPTE_M}} = \left(\sqrt{\frac{1}{A}} + \sqrt{1 + \frac{1}{A}} \right)^2; \quad (4.17)$$

where η_{ILPTE_M} and η_{ILM} are the maximum values of η_{ILPTE} and η_{IL} respectively.

4.3.3 The relationship between A and the S-parameters of the link

We can model the inductive link as a linear two-port network. Consequently, we represent it by its equivalent S-parameters. In this modeling domain, the power transfer efficiency is directly related to the well-known power gains that are commonly used to design microwaves amplifiers. The η_{ILPTE} is equivalent to the available power gain, and η_{ILPTE_M} is equivalent to the Maximum Available power Gain (MAG), respectively. Therefore, we express η_{ILM} as:

$$\eta_{ILM} = \eta_{ILPTE_M} = MAG = \frac{|s_{21}|}{|s_{12}|} \left(K_{MAG} - \sqrt{K_{MAG}^2 - 1} \right); \quad (4.18)$$

where

$$K_{MAG} = \frac{1 - |s_{11}|^2 - |s_{22}|^2 + |\Delta|^2}{2|s_{12}s_{21}|}; \quad \Delta = s_{11}s_{22} - s_{12}s_{21};$$

where s_{xy} are the S-parameters of the equivalent two-port network of the link. Furthermore, the parameters s_{11} , s_{22} are reflection coefficients, and s_{21} , s_{12} are the transmission coefficients. In addition, we rewrite the (4.17) as:

$$A = 4 \frac{MAG}{(MAG - 1)^2}. \quad (4.19)$$

4.4 MODELING METHODOLOGY

A scalable compact model is a set of empirical relations between the circuit model components and the geometric parameters of the modeled device, which are sufficiently simple and accurate to be incorporated in circuit simulators and to make the simulator results useful to circuit designers (GAO; YU, 2006; GILDENBLAT, 2010). Furthermore, in scalable modeling, the model is adjusted to the empirical data (simulated or experimental) using fitting techniques. However, if the interpolating formulas have physical insight, then the model's predictability increases and the number of testing devices necessary for calibration decreases (GAO; YU, 2006).

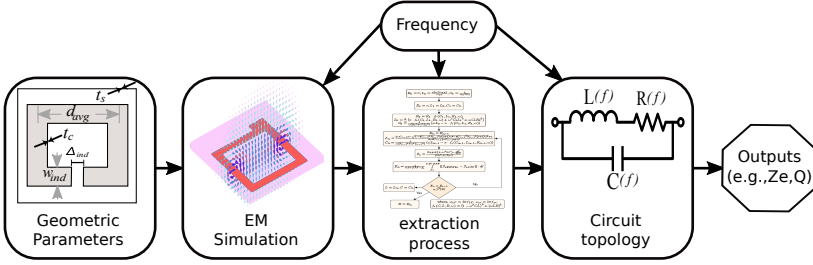
In this subsection, we discuss two levels of modeling approaches, which are: 1) the fixed model of the PSOI, which directly extracts the values of circuit elements from the full-wave simulation data, achieving high accuracy, but no scalability; and, 2) the scalable compact model, in which circuit elements are related to the PSOI geometry (i.e., layout) through a set of formulas with model parameters calibrated upon a few simulated testing devices.

4.4.1 Fixed models of the PSOI

We followed the modeling technique summarized in Figure 42 to synthesize a fixed compact circuit model of the PSOI fabricated on an FR-4 board. We chose 39 devices with d_{avg} varying between 4 mm and 30 mm and w_{ind} varying between 0.3 mm and 4.5 mm. We simulated these devices using the finite element method implemented in Electromagnetic Professional (EMPro®). We simulated each PSOI using 65 frequency points in a range from 10 MHz to SRF, which we estimated from a dedicated high-resolution simulation around the first zero-crossing frequency of x , the imaginary part of Z_e .

We stored the resulting s_{11} and SRF values in a library of CVS (i.e., comma-separated values) files. For each simulated device, we calculated its input impedance (i.e., $Z_e = r + j \cdot x$) from the s_{11} parameter using $Z_e = Z_0 (1 + S_{11}) / (1 - S_{11})$; where Z_0 is the characteristic impedance used in the simulation, which we set in 50Ω . We then extracted the circuit components values from Z_e using a procedure that was optimized to reduce the impedance error. We illustrate the implemented algorithm in Figure 43. This process allows us to extract the values of the L , C and R values at each simulated frequency. The

Figure 42 – Diagram of the fixed modeling techniques.



Source: (The author, 2017)

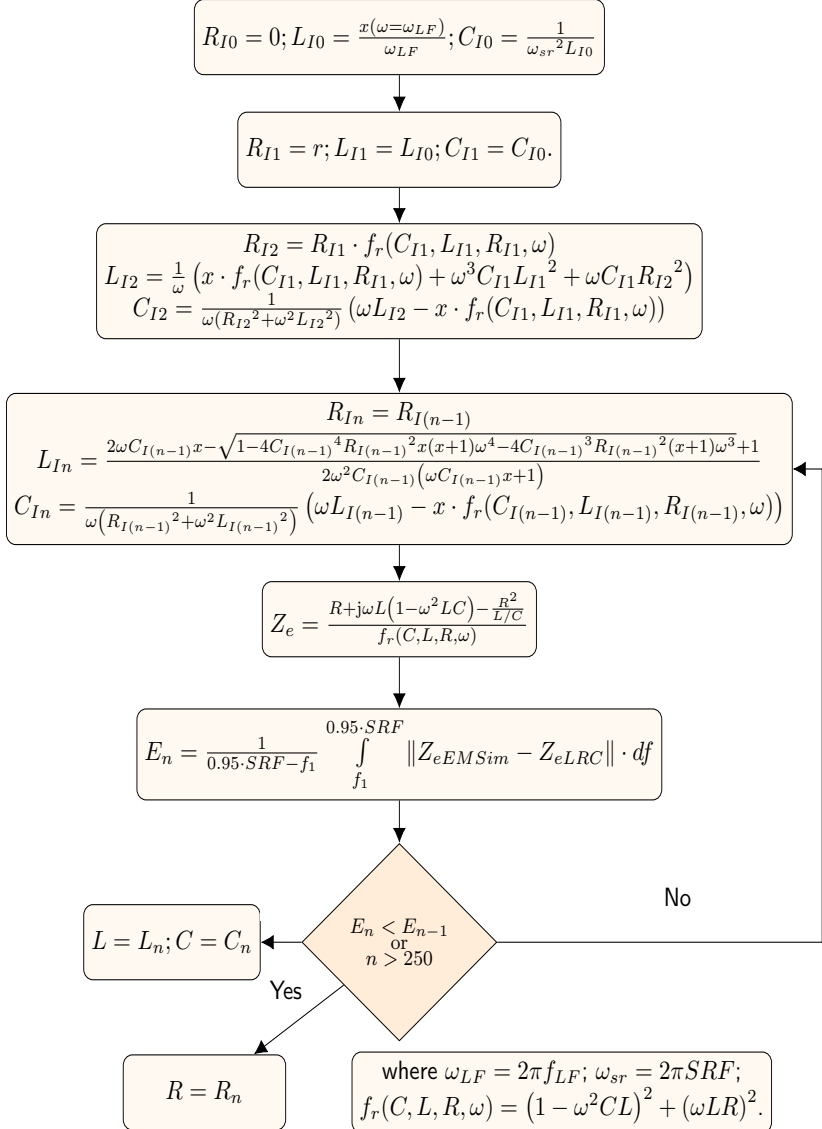
fixed models of the simulated PSOI devices consisted of these values, which are characterized by the absence of non-physical circuit component values (e.g., $R < 0$) and small error in the prediction of Z_e . This error was less than 1% in the range from 10 MHz to 0.8 SRF for all the simulated PSOI devices. For example, in Figure 44, we plotted the fixed model of the PSOI defined by $d_{avg} = 50$ mm, $W_{ind} = 6.2$ mm, $\Delta_{ind} = 0.4$ mm, and $t_c = 35\mu\text{m}$.

Considering all the extracted fixed models, we calculated the maximum percentage change of the components regarding their low-frequency value (Figure 45). As we expected, the L and C are relatively constant until they near the SRF, whereas the R varies strongly with frequency. Therefore, a simple lumped model with constant L and C values (i.e., only R as frequency-dependent parameter) captures the main physics of the device up to 80% of the SRF with small error.

4.4.2 Scalable compact models of the PSOI

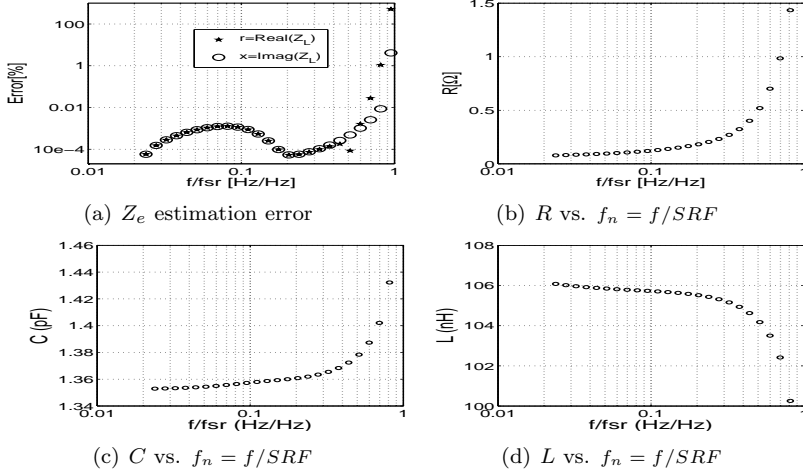
First, we chose the RLC model discussed in Section 4.3.1.2 as the circuit topology for modeling PSOI devices. Second, we found a set of physically oriented equations that describe its circuit components as a function of the geometric parameters of the PSOI devices. Third, we defined some model parameters to fit the scalable model to the simulated empirical data, which we calculated from the full-wave simulation of a representative number of PSOI devices. Finally, we used fitting tools to calculate the model's parameter values and adjust the model to our fabrication process, although the model can be adapted to other fabrication technologies (e.g., other substrates) by fitting the model parameters to arbitrary empirical data. Also, we defined the model's

Figure 43 – Flowchart of the physics-based RLC extraction process.



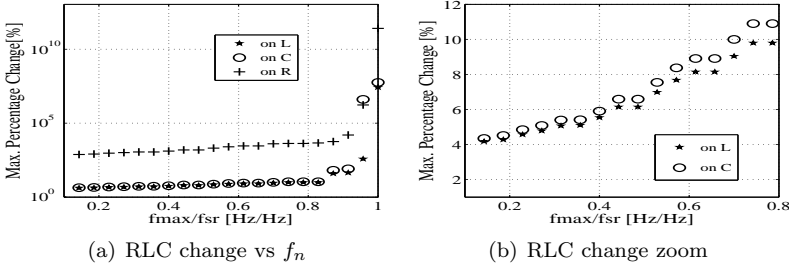
Source: (The author, 2017)

Figure 44 – PSOI example with extracted SRF of 420 MHz.



Source: (The author, 2017)

Figure 45 – Variations of the fixed model components as a function of the normalized frequency.

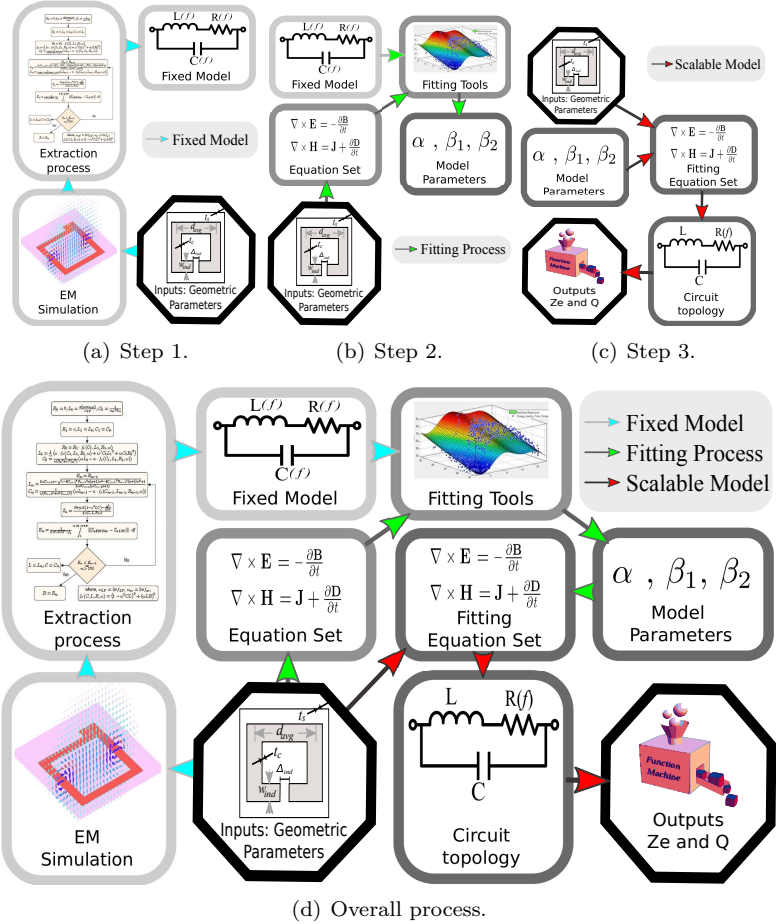


Source: (The author, 2017)

outputs as Z_e and Q .

We followed the modeling technique summarized in Figure 46 to synthesize a compact circuit model of the PSOI, which was fabricated on an FR-4 board. This figure illustrates the modeling flow, which is composed of three processes, the calculation of the fixed model, the fitting of the model parameters and the calculation of the circuit model from the physically oriented equations. The inputs in this modeling flow are the geometric variables of the inductor, which are used to extract

Figure 46 – Diagram of the scalable modeling techniques.



Source: (The author, 2017)

the fixed models (using a significative number of inductors), then we adjust the pre-defined physically oriented equations to the fixed models using the pre-defined model parameters. As the last modeling step, we compute the scalar model using the geometric variables of the inductor and the calculated model parameters for the used technology. Finally, we calculate the model's outputs using analytical expressions based on simple circuit analysis.

4.4.2.1 Set of equations of the compact model

In (CABRERA; SOUSA, 2014), the authors proposed an equation set to estimate the Q of the PSOI, which is given by:

$$L = \frac{2d_{avg}\mu}{\pi} \ln \left(\frac{0.59\pi d_{avg}}{w_{ind}} \right); \quad (4.20)$$

$$R = \underbrace{2\sqrt{\rho\pi\mu\alpha}w_{ind}^{(\beta_1-1)}f^{(\beta_2+0.5)}d_{avg}}_{R_{DC}F_{skin}F_r} + \underbrace{134\sqrt{\varepsilon^3\mu^5}f^4d_{avg}^4}_{R_{rad}}; \quad (4.21)$$

where μ is the magnetic permeability, ε is the electric permittivity, R_{DC} is the PSOI resistance value at DC, R_{rad} is the PSOI radiation resistance, and ρ is the conductor resistivity. The F_{skin} and F_r factors model the current redistribution effects (i.e., roughness, current-crowding, skin and edge effects.), and α , β_1 and β_2 are the model parameters. In (RIAÑO et al., 2016), the authors expanded this equation to estimate both SRF and Z_e of the PSOI. They then used an additional equation to calculate the parallel parasitic capacitor (C) of the PSOI from its geometric parameters, this expression is:

$$C = C_\lambda + C_G; \quad (4.22)$$

$$C_\lambda = \frac{\mu\varepsilon}{L} \left(\frac{4d_{avg}}{\pi} \right)^2,$$

$$C_G = \frac{\varepsilon w_{ind}}{\pi/2} \left[\ln \left(\frac{(d_{avg} + w_{ind})}{\Delta_{ind}^2/2w_{ind}} \right) - \frac{d_{avg} - w_{ind}}{4d_{avg}} \right].$$

where C_λ is the intrinsic capacitance of the coil, and C_G is its geometric capacitance. Finally, using circuit analysis, we can calculate the SRF, Z_e , and the Q from:

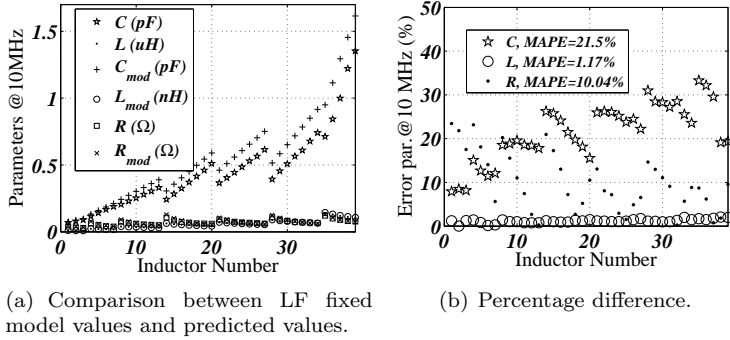
$$SRF^2 = \frac{1}{(2\pi)^2} \left(\frac{1}{CL} + \frac{R^2}{L^2} \right); \quad (4.23)$$

$$Z_e = \frac{R + j\omega L \left[(1 - \omega^2 LC) - \frac{R^2}{L/C} \right]}{(1 - \omega^2 LC)^2 + (\omega LR)^2}; \quad (4.24)$$

$$Q = \frac{\omega L}{R}. \quad (4.25)$$

To numerically quantify the estimation error that was introduced by using the presented equation set, we calculated the difference be-

Figure 47 – Broadband model parameters at minimum frequency



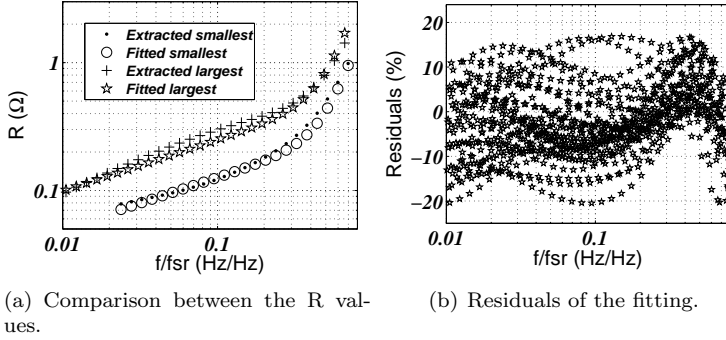
Source: (The author, 2017)

tween the circuit component values (i.e., R , L , C) of the fixed models and the values predicted by the equation set at the lowest simulated frequency (i.e., $f = 10$ MHz), and assuming that $\alpha = 1$, $\beta_1 = 0$ and $\beta_2 = 0$. The results are summarized in Figure 47. From this figure, we concluded that (4.20) accurately models the low-frequency inductance of the coil and the error introduced by using (4.23) is moderate. Moreover, it decreases as the frequency increases and, therefore, the overall error of the required frequency range is acceptable. Finally, the error introduced by (4.21) is moderate. However, it increases as the frequency increases and eventually becomes highly significant. We note that only (4.21) can be adjusted to the fabrication technology; thus, decreasing this error in the scalable model. This approach reduces the complexity of the model with little impact on its accuracy.

4.4.2.2 Adjusting the model's parameters

We fitted the equation (4.21) (in the frequency domain) to the R values of the fixed models (discussed in Section 4.4.1) using the curve fitting toolbox (cftool) of MATrix LABoratory (MATLAB®) software. The resulting model parameters were: $\alpha = 128$, $\beta_1 = 0.3$ and $\beta_2 = -0.1$. The results of the fitting process for both the smallest and the largest PSOI of the library are shown in Figure 48(a). The residuals of the fitting process are plotted in Figure 48(b), which exhibits quasi-random patterns that are always less than 20%, indicating an

Figure 48 – Results of the fitting process.



Source: (The author, 2017)

acceptable fit over the whole frequency range.

4.4.2.3 Extending the scalable model for an inductive link

We used the analytical expression of the mutual inductance (M) proposed in (CABRERA; FEITOZA; SOUSA, 2015) to model the inductive links based on PSOI devices, which is given by:

$$M = \mu \sqrt{\frac{d_{avg1} d_{avg2}}{\pi}} \left[\left(\frac{2}{\gamma} - \gamma \right) K_{\gamma}(\gamma) - \frac{2}{\gamma} E_{\gamma}(\gamma) \right]; \quad (4.26)$$

where $K_{\gamma}(\gamma)$ and $E_{\gamma}(\gamma)$ are the complete elliptic integrals of the first and second kind, respectively, whose argument, γ , is expressed as:

$$\gamma = \sqrt{\frac{4d_{avg1}d_{avg2}}{(d_{avg1} + d_{avg2})^2 + \pi d^2}}.$$

4.5 EVALUATING THE MODEL

4.5.1 Accuracy of the Z_e estimation

4.5.1.1 Simulation and experimental setup

We numerically evaluated the accuracy of the Z_e estimation using full-wave EM simulations of 39 PSOIs with d_{avg} varying between 4 mm and 30 mm, and w_{ind} varying between 0.3 mm and 4.5 mm. We simulated them using the finite element method implemented on EMPro[®]. We also experimentally evaluated the accuracy of the Z_e for low frequencies (i.e., $f_{LF} < f < 0.1f_{sr}$) using three PSOIs fabricated on an FR-4 substrate with surface-mounted U.FL. connectors; which are shown in Figure 49(a) and their geometric values are summarized in Table 9. The experimental setup is shown in Figure 49(b). We developed a custom calibration kit based on the Short-Open-Load-Through standard to perform the calibration and fixture compensation of the VNA (two ports R&S[®] ZVB8); as shown in Figure 49(c). An example of the resulting experimental data is shown in Figure 49(d).

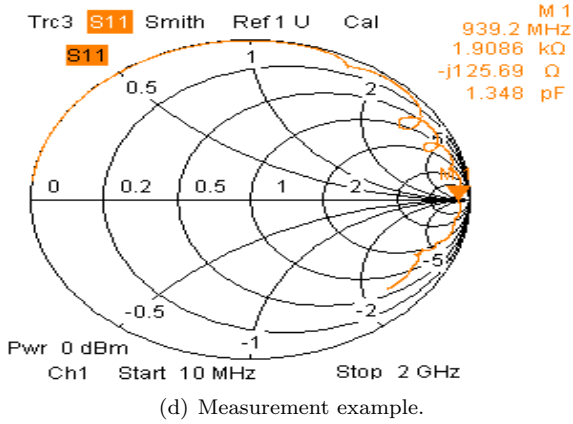
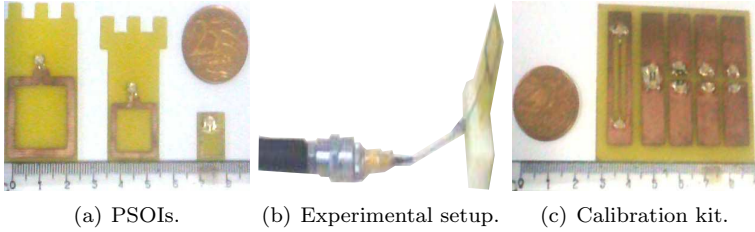
4.5.1.2 Results

We calculated the SRF values using the scalable model and the (4.25), which were both implemented as MATLAB[®] scripts. We compare the simulated and predicted SRF values in Figure 50(a) and the resulting absolute percentual error is plotted in Figure 50(b). We note that the model captures the resonance phenomenon of the PSOI with an error of less than 15% for all of the samples. Moreover, we have calculated the error in the Z_e estimation for all samples, as illustrated in Figure 50. The model predicted the Z_e values with an error of less than 10% for both resistance (r) and reactance (x) of the PSOI, and

Table 9 – Geometric parameters of the implemented PSOIs.

Ind. No.	d_{avg} (mm)	w_{ind} (mm)	Δ_{ind} (mm)	t_c (μ m)
1	22	2.8	0.4	35
2	12	2.0	0.4	35
3	8	0.6	0.4	35

Source: (The author, 2017)

Figure 49 – Experimental evaluation of the PSOI Z_e .

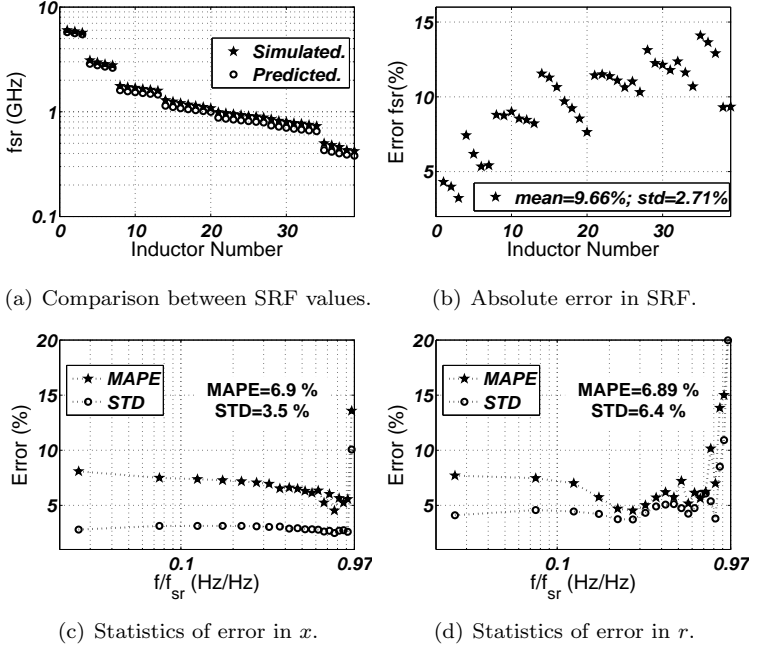
Source: (The author, 2017)

a low STD in a range from 10 MHz to $0.8 \cdot SRF$. Furthermore, considering the error in SRF and Z_e estimation, all the samples, ranging from 10 MHz to $0.97 \cdot SRF$, the MAPE was always less than 10%. We also calculated the experimental data and the predicted values. The empirical error in the estimation of Z_e is shown in Figure 51. The empirical resistance differs from the predicted values. However, the error involved in the prediction of the reactance is low. Finally, the overall error statistics are summarized in Table 10. From the experimental results, we conclude that the MAPEs in the predictions of reactance and resistance are small and moderate, respectively.

4.5.2 Accuracy of the Q estimation

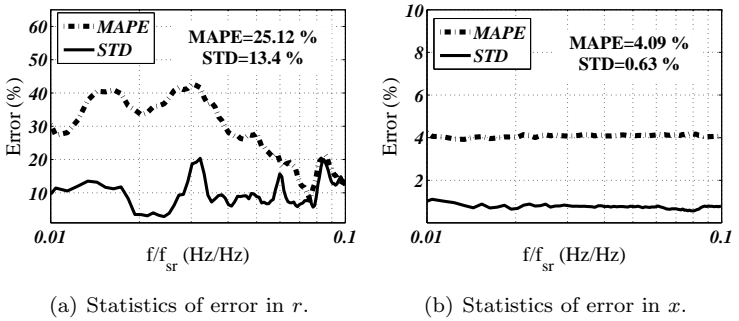
The main FoM of an inductor is its quality factor (Q). Furthermore, the Q characterization is useful when estimating its performance

Figure 50 – Full-wave EM simulations versus scalable model predictions.



Source: (The author, 2017)

Figure 51 – Empirical data versus scalable model predictions.



Source: (The author, 2017)

Table 10 – Summary of model errors.

Error in	Re $\{Z_L\}$ (%)	Im $\{Z_L\}$ (%)	frequency (%)	Range (MHz)
MAPE Sim.	6.89	6.90	9.66	10 to $0.97 \cdot \text{SRF}$
STD Sim.	6.4	3.5	2.71	10 to $0.97 \cdot \text{SRF}$
MAPE Exp.	25.12	4.09	-	10 to $0.1 \cdot \text{SRF}$
STD Exp.	13.4	0.63	-	10 to $0.1 \cdot \text{SRF}$

Source: (The author, 2017)

embedded in a WPT system. When it operates near its SRF, and it has a high Q value, its characterization is challenging, especially because the test instrument must be able to measure a large reactance and a very small resistance at a frequency where it begins to radiate. In this section, we present a novel method that is suitable for characterizing high- Q inductors up to its SRF, which is based on the contactless technique proposed in (CABRERA; SOUSA, 2015). We applied this method to verify the capacity of the presented model to predict the Q of PSOI devices.

4.5.2.1 Measurement methodology

In Figure 52(a), we show the circuit model of the asymmetrical inductive link ($\text{SRF}_\Delta \ll 1$) powered by a VNA and loaded with an external lossy capacitor (C_l and R_l). We modeled the Rx coil as a resonant tank (C , L , and R) and the Tx coil as a lossy inductor (L_S and R_S). The input impedance imposed by the circuit to the VNA in the Rx coil presence is given by (CABRERA; SOUSA, 2015):

$$Z_W = R_s + j\omega L_s + \Delta R + j\Delta X = Z_{WO} + 2\pi f(e + jg); \quad (4.27)$$

where Z_{WO} is the Rx coil absence (Figure 52(b)). We drew the graphs of the functions e and g in Figure 53, in which we normalized the frequencies to the resonance frequency (f_0) of the equivalent resonant circuit composed of the Rx coil and the external load capacitor. Furthermore, Q_R is the Q of this resonant circuit. At f_0 ($\approx 1/\{2\pi\sqrt{L(C+C_l)}\}$), Q_R is given by $1/Q_R = 1/Q_{IUT} + 1/Q_x$; where $Q_x = 1/\omega_0 C_x R_x$, and $Q_{IUT} = \omega_0 L/R$. From this development, we devise the following method for the contactless measurement of the Q_{IUT} :

1. Using the IUT and an inductive sensor, implement an appropriate link that allows the clear visualization of the resonance

phenomenon in the plot of the sensor reactance. That means an enough magnetic coupling and a low sensor interference (i.e., $k > k_{th}$ and SRF of the sensor (SRF_S) $> G_{th} \cdot SRF_{IUT}$ where k_{th} and G_{th} are thresholds that depend on the inductor technology used). For instance, the sensor was prototyped on an FR-4 substrate and designed to guarantee $SRF_1 > 5 \cdot SRF_2$. Also, for the test with the IUT, the sensor was positioned very near to the IUT to guarantee $k > 0.03$.

2. Measure the SRF :

- a) Without load capacitor, measure Z_W and Z_{WO} .
- b) Estimate $e(f)$ from $\text{Re}\{Z_W - Z_{WO}\}/2\pi f$.
- c) Calculate the SRF as the frequency where the maximum of $e(f)$ occurs.

3. Measure the Q_{IUT} at SRF :

- a) Estimate $g(f)$ from $\text{Im}\{Z_W - j\omega L_s\}/2\pi f$; where $L_s = \text{Im}\{Z_W(2\pi SRF)\}/2\pi SRF$.
- b) Evaluate the frequencies where the maximum (f_{p1}) and the minimum (f_{p2}) values of $g(f)$ occur.
- c) Estimate the Q_{IUT} from $\{f_{p2} + f_{p1}\}/\{f_{p2} - f_{p1}\}$.

4. Measure Q_R at $f_0 < SRF$:

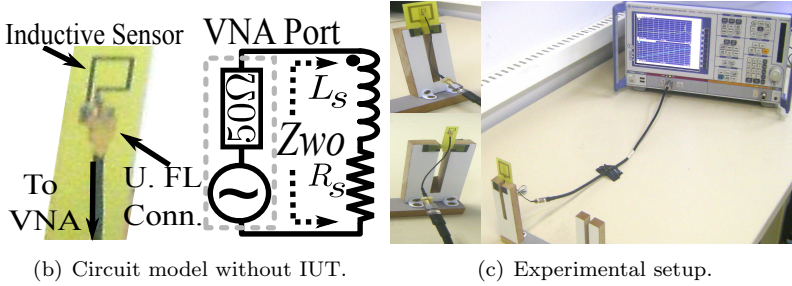
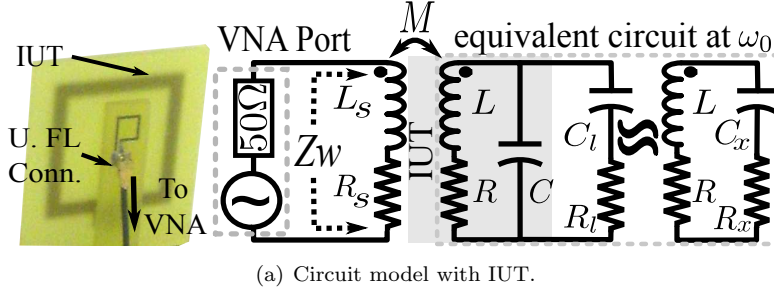
- a) Using a load capacitor, measure Z_W and Z_{WO} , and repeat Step 2b.
- b) Calculate f_0 as the frequency where the maximum of $e(f)$ occurs.
- c) Repeat Step 3a with $L_s = \text{Im}\{Z_W(2\pi f_0)\}/2\pi f_0$, and Steps 3b and 3c.

5. Estimate Q_{IUT} at f_0 from:

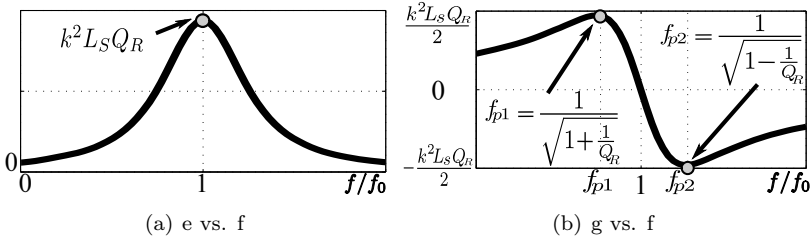
$$\frac{1}{Q} = \frac{1}{Q_R} - \frac{C_l}{C_l + C} \left(\frac{1}{Q_l} \right); \quad (4.28)$$

where Q_l is the Q of the load capacitor, $C^{-1} = 2\pi SRF^2 L$, and $L = 2d_{avg}\mu(\pi)^{-1} \ln\left(0.59\pi d_{avg}(w_{ind})^{-1}\right)$ (CABRERA; FEITOZA; SOUSA, 2015).

Figure 52 – Experimental setup and circuit models.



Source: (The author, 2017)

Figure 53 – Theoretical waveforms of the functions e and g .

Source: (The author, 2017)

4.5.2.2 Simulation and Experimental Setup

We chose the IUT as the transmitter of a previously optimized link (CABRERA; SOUSA, 2014), which is an FR4-board coil that is defined by the following geometric parameters: $d_{avg} = 22$ mm, $w_{ind} = 2.8$ mm, and $\Delta_{ind} = 0.4$ mm. We calculated its theoretical values of Q (Q_{th}

and $Q_{a.th}$) using the model proposed in Section 4.4. Additionally, we evaluated its simulated Q_a ($Q_{a.sim}$) using full-wave simulations. We found the “simulated” Q (Q_{sim}) values from the expression:

$$Q \approx \frac{Q_a}{1 - \left(\frac{f}{SRF}\right)^2}; \quad (4.29)$$

This approximation is valid if $Q \gg 1$ and $f \ll SRF$.

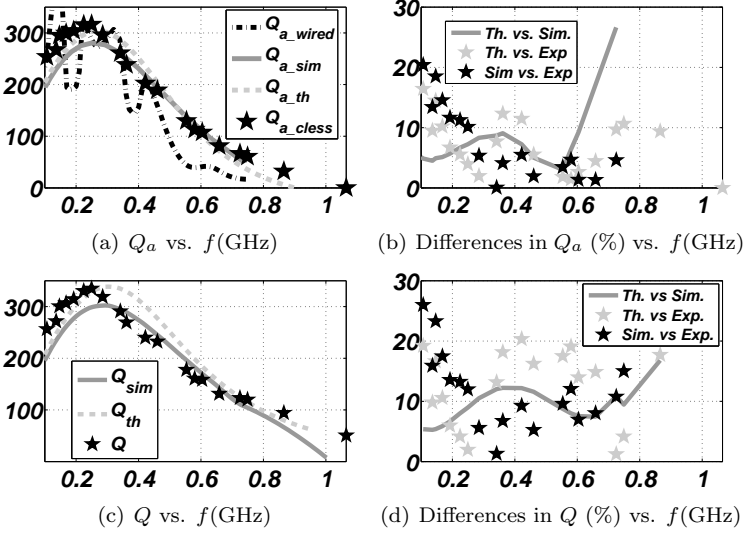
We measured the Q using two approaches. We employed the conventional approach with a wired setup to measure the Q_a and then we applied the method presented in Section 4.5.2.1 with a contactless setup to measure the Q and estimate the Q_a . The wired experimental setup comprised a VNA (R&S® ZVB8), the custom U. FL. calibration kit described in Section 4.5.1.1, and the connectorized IUT. We performed the calibration and fixture compensation of the VNA under non-free-field test conditions and we then measured the differential/balanced input reflection coefficient (s_{dd}). Finally, we calculated Z_e and $Q_{a.wired}$.

The contactless setup was composed of the IUT without connectors, an inductive sensor, and the same VNA and calibration kit of the wired setup. Furthermore, we designed the sensor to guarantee an SRF_Δ less than 0.2, and it was prototyped on an FR-4 substrate and connectorized. Using the same test conditions, calibration and fixture compensation as in the wired setup, we measured the s_{11} parameter in the absence and presence of the receiver, and we calculated Z_{WO} and Z_W . To measure Z_W , we placed the IUT and the sensor in physical contact with each other to ensure a k_{IL} greater than 0.03. From the measured impedances, we estimated the empirical contactless Q (Q_{cless}) by applying the proposed method and using the typical Q_l values reported in the capacitor datasheet. We repeated the experiment 20 times with 19 high-Q capacitors ($Q_l > 1000$) from 0.2 pF to 185 pF. Next, we used the resulting Q_{cless} values and (4.29) to estimate the “empirical” contactless Q_a ($Q_{a.cless}$).

4.5.2.3 Results

We illustrate the resulting Q_a values and their differences in Figure 54(c) and Figure 54(b). The $Q_{a.cless}$ is consistent (deviation $< 20\%$) with $Q_{a.th}$ and $Q_{a.sim}$ values between 0.1 GHz and 0.8 GHz, whereas the contactless counterpart, $Q_{a.wired}$, significantly deviates from the

Figure 54 – Comparison of the experimental data with the simulated and theoretical results.



Source: (The author, 2017)

predicted values. In Figure 54(c) and 54(d), we plotted the IUT Q -values and its associated differences. We note that the maximum difference between Q_R and Q_{cless} is 17% at 0.25 GHz. Both the SRF (1.065GHz) and the maximum Q (334.7) deviate relatively little ($< 12\%$ and $< 10\%$) from the theoretical (0.947 GHz and 338.6) and simulated (1.002GHz and 302.2) values. Additionally, the Q_{cless} had a maximum deviation of 20.3 % and 25.9 % from Q_{th} and Q_{sim} , respectively. Furthermore, between 0.1 GHz and 0.8 GHz the deviation from both Q_{th} and Q_{sim} is less than 20%.

4.5.3 Accuracy of the A estimation

4.5.3.1 Simulation and experimental setup

We evaluated the accuracy estimation of the A factor using a link that was based on two onboard PSOI separated by 15 mm. We summarize the geometric parameters of the coils in Table 11. We sim-

ulated this link using EMPro[®], and calculated η_{ILPTE} and A from the simulated S-parameters using (4.18) and (4.19), respectively. We also carried out S-parameter simulations of this link in ADS[®] using the model presented in Section 4.4, which was implemented using the Z1P_Eqn block (impedance controlled by a frequency-dependent function), as depicted in Figure 55. Finally, we calculated η_{ILPTE} and A from the simulated S-parameters.

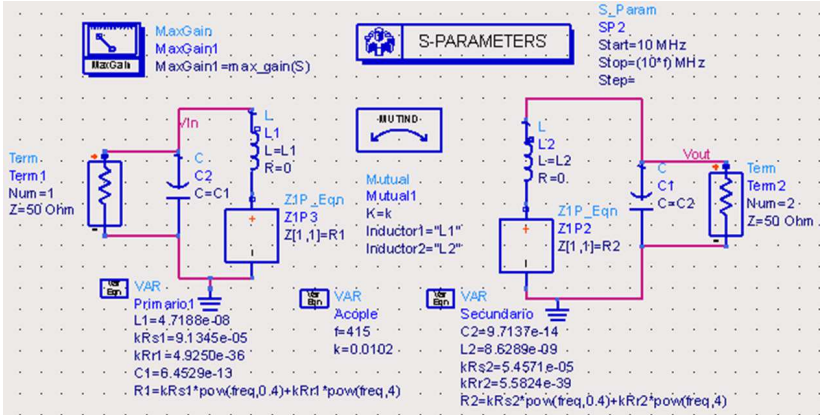
The S-parameters of the link were measured using the experimental setup shown in Figure 56. This setup used external capacitors to partially match the link to the VNA port impedance (i.e., 50 Ω), thereby increasing the accuracy of the measurement. Capacitors C_{R1} and C_{R2} represent the equivalent capacitances of the Tx and Rx coils, respectively. These capacitors are the equivalent between the intrinsic capacitor of the PSOI and an external capacitor. These external components were chosen to resonate with $L_{1(2)}$ at each test frequency. The experiment was repeated 10 times to archive an acceptable resolution near the maximum point of A , with 20 high-Q capacitors with a typical

Table 11 – Geometric parameters of Tx and Rx PSOI.

Ind. No.	d_{avg} (mm)	w_{ind} (mm)	Δ_{ind} (mm)	t_c (μ m)
Tx PSOI	21.8	2.7	0.4	35
Rx PSOI	4	0.5	0.4	35

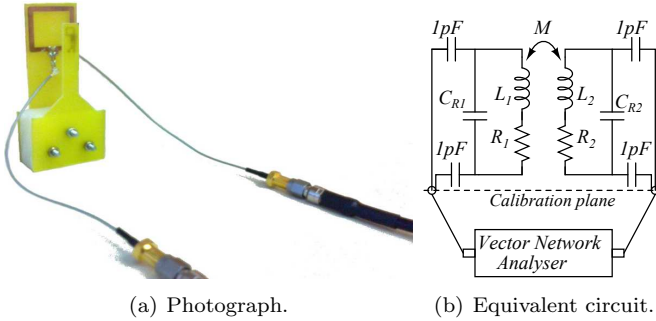
Source: (The author, 2017)

Figure 55 – Link model implemented in ADS.



Source: (Adapted from ADS Software, 2017)

Figure 56 – Empirical setup to measure the S-parameters of the link.



Source: (Taken from (CABRERA; SOUSA, 2014), 2014)

$Q > 1000$ (reported in the device datasheet).

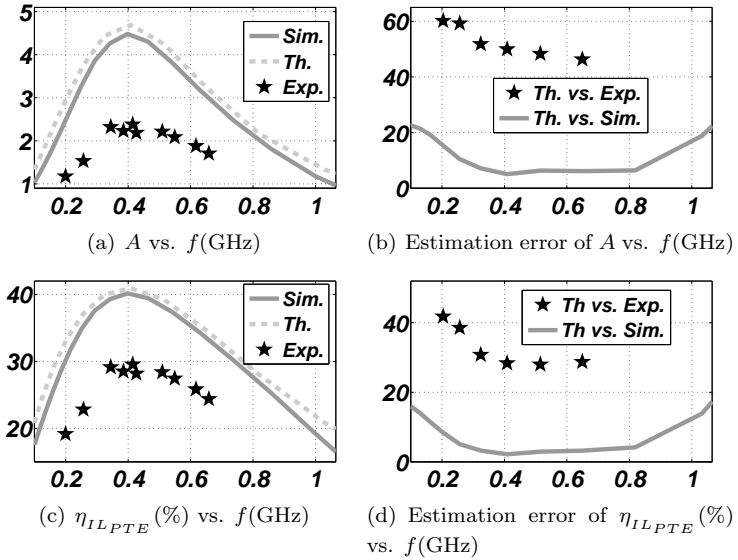
4.5.3.2 Results

We present the resulting values of $\eta_{ILPTEmax}$ (or MAGs) and A in Figure 57. We summarize their maximum values in Table 12. By analyzing the values predicted by the model (theoretical values) and the EM simulation, we note that they are very similar and their differences are lower than 20% throughout almost the whole frequency range. Furthermore, both predictions are consistent with the shape of the graph and the expected optimum frequency, although they differ from the experimental curve in absolute value. In addition, the absolute difference between the maximum values for $\eta_{ILPTEmax}$ and A , comparing the model to the measurements, is 28% and 50%, respectively, and, considering the model and simulations, is 2% and 5%, respectively.

Table 12 – Resulting maximum values of A and $\eta_{ILPTEmax}$

	ADS	EMpro	Experimental
Maximum $\eta_{ILPTEmax}$ (%)	40,9	40	29,1
Maximum A (%)	4.69	4.48	2.38

Source: (The author, 2017)

Figure 57 – Results of A and η_{ILPTE} .

Source: (The author, 2017)

4.6 DISCUSSION AND FUTURE WORK

The presented scalable PSOI model was consistent with the full-wave simulations in the overall test. Thus, it can be used to simplify the optimization process of the link while avoiding the need for full-wave EM simulations. Furthermore, we used the simulation data to fit the presented PSOI model to our fabrication process because of the high ambiguity of the measurement setup and to simplify the analysis of a large number of alternative scenarios under different realistic conditions.

The main experimental challenges that we found were: 1) the interaction between the IUT and the test setup for frequencies near its SRF; 2) the accurate measurement of very low resistance values (1Ω or lower) at high frequencies, and very high values ($1 \text{ k}\Omega$ or higher) at UHF and VHF using a VNA; and, 3) the MAG measurement with a VNA and under extreme mismatching conditions.

As a partial solution for the undesired EM interactions, we used U.F.L. connectors instead of SMA connectors. We prototyped two iden-

tical PSOI devices and connected them with SMA and U.FL. We have plotted the results in Figure 58. We also consider the widely known problem of the asymmetric current density in the coaxial cable, which can load the measurement. Therefore, we measured the differential/balanced input reflection coefficient (S_{dd}) of the PSOIs (with two connectors), whose results are illustrated in Figure 58. However, the test setup is not robust near the inductor SRF because of the interactions between the PSOI, although the test instrument and the test fixture still are significant (especially for the “SMA” PSOIs).

As a partial solution to characterize the Q value of the PSOI without measuring low resistance values, we proposed a method that is suitable for the experimental characterization of high- Q inductors up to its SRF. The proposed Q characterization is less sensitive to the electromagnetic interactions between the test setup and the IUT because it modeled the magnetic coupling between the sensor and the IUT; consequently, it is removed from the measurement. We also eliminated the interactions between the sensor, the VNA and the wired connections from the measured Z_W using the Z_{WO} test. Moreover, the proposed method is less sensitive to the inaccuracies in the s_{11} parameter because the Q is inferred only from the reactance of Ze , avoiding the need for an accurate measurement of the resistance of Ze , which becomes extremely sensitive to the s_{11} parameter for high- Q inductors. Therefore, it reduces the underestimation of the Q value up to the SRF. On the other hand, the model presents three drawbacks: because it modifies the IUT (welding a capacitor), it requires one capacitor and two measurements for each characterization frequency, and it introduces additional losses, although we can remove these losses from the measurements. In Table 13, we make a complete comparison between the proposed method and directly related works of the scholarly literature.

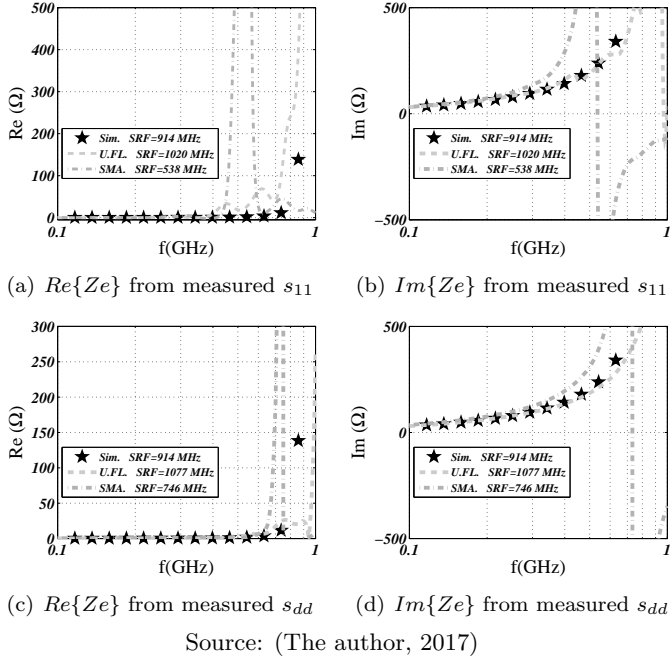
Table 13 – Comparison with the SoA.

Ref.	Q Definition	S_{11} Sensitivity	E_Q Error	Iter.	Text Fixture Sensitivity	Modify the IUT	Additional losses
Conv.	$\frac{Re(Z_e)}{Im(Z_e)}$	High	High		High	No	No
(O., 1998)	$\frac{\frac{\partial Z_e}{\partial \omega}}{Z_e}$	Moderate	Low		Moderate	No	No
(O., 1998)	$-\frac{\frac{\partial Z_e}{\partial \omega}}{Z_e} \bigg _{\omega=\omega_0}$	Moderate	Low		Moderate	No	No
(DOLDAN; GINES; RUEDA, 2013)	$\frac{\frac{\partial Z_e}{\partial \omega}}{Z_e}$	Moderate	Low		Moderate	No	No
This work	$\frac{f_{p2}-f_{p1}}{f_{p2}+f_{p1}}$	Low	Low		Low	yes	yes

Source: (The author, 2017)

We used high- Q capacitors, partially matching conditions, and the MAG concept to increase the measurement accuracy of the link efficiency. However, the discrepancy between simulated and empirical

Figure 58 – Example of parasitics after test fixture compensation.



results is significant. These differences are mainly due to losses in the test setup, which became significant due to the high-quality factor of the PSOI under test. Such parasitic resistances are related to the quality factor of the capacitors, the calibration process and even to the welding of the components.

In summary, the EM-simulated and predicted values are similar under all of the tests. In addition, the experimental results are consistent with the theoretical model and the full-wave simulation. However, the experimental characterization of the model was only partially solved. Furthermore, we cannot experimentally evaluate the ability of the model to predict Z_e because of the low accuracy of the measurement with a VNA under mismatching conditions. Consequently, we must update the test setup. One possible solution that we can explore is to use I-V measurements that are based on an impedance or material analyzer and on special calibration techniques (e.g., a low-loss capacitor as the second load).

4.7 CONCLUSION AND CONTRIBUTIONS

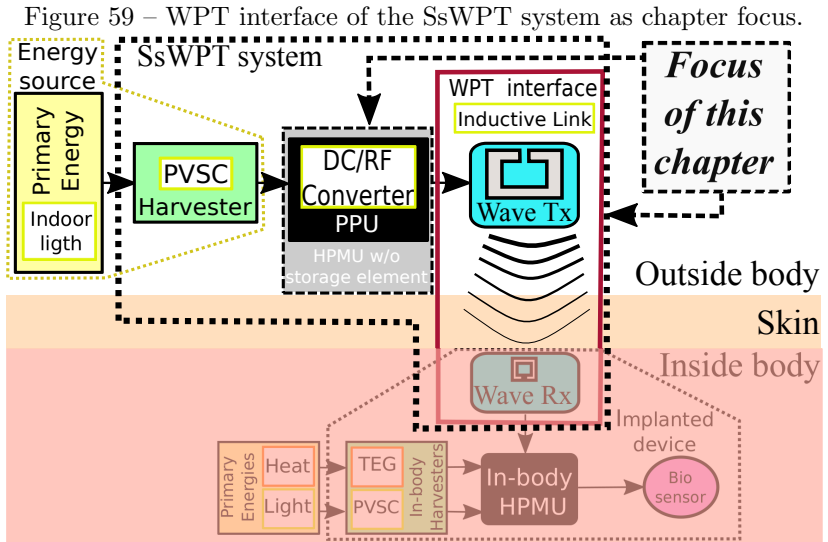
In this chapter, we presented and evaluated a PSOI scalable model, which was validated by full-wave EM simulations and measurements. The resulting lumped model is analytical and its circuit components have physical meaning. This model extends the model proposed in (CABRERA; FEITOZA; SOUSA, 2015; CABRERA; SOUSA, 2014), using a novel parameter extraction process that guarantees a very small error in the inductor input impedance, Z_e , near the SRF. In addition, we reported a novel method for the experimental characterization of high-Q inductors up to its SRF, which is based on the contactless technique presented in (CABRERA; SOUSA, 2015). Moreover, this methodology avoids the use of an anechoic chamber, specialized instruments (e.g., impedance/material analyzer) or special calibration techniques (e.g., a low-loss capacitor as the second load).

As minor contributions developed in this chapter, we found analytical expressions for the η_{IL} , η_{ILPTE} as a function the parameters of the inductor model and the A factor. Furthermore, a simple relationship between this factor and the well-known MAG definition was developed and summarized in an algebraic equation. We found some evidence of a significant iteration between the common SMA connector and the IUT near its SRF. We presented the model proposed in (CABRERA; FEITOZA; SOUSA, 2015; CABRERA; SOUSA, 2014) by using a compressive approach.

5 ON THE MODELING OF SELF-SUSTAINING WPT (SSWPT) SYSTEMS

In this chapter, we propose a design methodology for the SsWPT system that is composed of a harvester as the energy source, a DC/RF converter as PMU, and an inductive link as WPT interface. Furthermore, the energy is processed in the power stage using a PA. We illustrate this system in Figure 59. We applied the proposed methodology in some study cases. In these examples, the resulting SsWPT systems extract the P_{avs} of the harvester and supply this power to its payload with maximum efficiency.

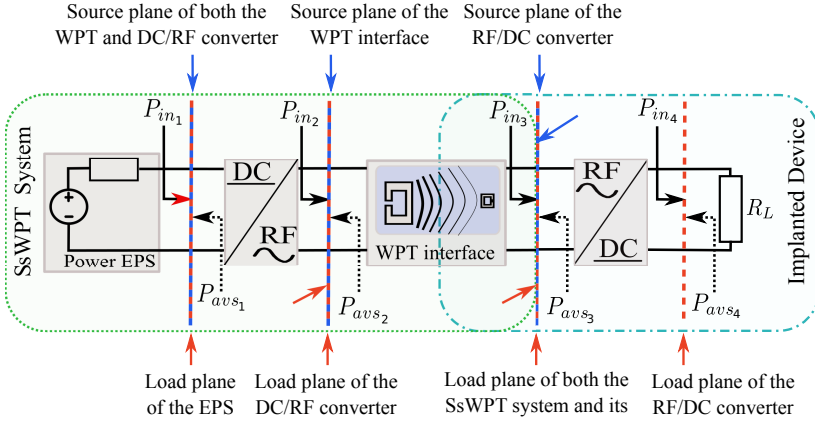
We organize the rest of this chapter as follows. In Section 5.1, we discuss the context of PA and WPT modeling for WPT applications according to references. In Section 5.2, we present some power efficiency definitions for WPT applications that were inspired by the well-known power gain notions used in the conventional microwave theory. In Section 5.3, we describe the specific procedures adopted in the modeling of the PAs, and we present some amplifiers as examples. Furthermore, as a proof of concept, we evaluate a Class-A PA designed



Source: (The author, 2017)

using its impedance port model and the proposed methodology. In Figure 60, we highlight the reference power planes considered in the rest of this chapter. More specifically, in Section 5.4, we propose a design methodology for self-sustaining PA that moves the maximization plane from the EPS load plane to the PA's. In Section 5.5, we extend this method to push further the maximization plane until the load plane of the SsWPT system. In Section 5.6, we describe the main results of this chapter, and we also make some recommendations for the future modeling of SsWPT systems. Finally, in Section 5.7, we outline the conclusions and the contributions of this chapter.

Figure 60 – Power chain of the SsWPT system.



Source: (The author, 2017)

5.1 INTRODUCTION

Recently, harvesting sources and WPT techniques have been used to obtain artificial EM ambient sources to provide energy autonomy to electric devices (NIOTAKI et al., 2014). These WPT systems are so-called SsWPT systems (FAJARDO; SOUSA, 2016b), which conventionally are based on a power EPS, a DC/RF converter (e.g., power oscillator or a PA driven by an oscillator), and a WPT interface (i.e., antenna or inductive link), as shown in Figure 60. For instance, in

(GEORGIADIS; COLLADO, 2013), the authors proposed a SsWPT that was based on a PVSCs, a class-E power oscillator, and monopole antenna as WPT interface.

As discussed in Chapter 2, an EPS that is composed of ambient energy, such as solar, and a harvester (e.g, PVSCs) can be considered as a Power EPS. That means this EPS can supply a high amount of energy (i.e., self-sustaining), but it has a limited power density (i.e., its P_{avs}). In the traditional design approach of self-sustaining devices, the designer reduces the interactions among EPSs, converters and loads to voltage or current specifications between the subsystems. Then he individually optimizes them using these specs as constraints. For example, in (BANDYOPADHYAY; CHANDRAKASAN, 2012), the authors impose an arbitrary voltage specification of 1.9 V as the output of a regulated self-sustaining voltage source, then this EPS was optimized to maximize its efficiency. The autonomous voltage source proposed in (LIU; SANCHEZ-SINENCIO, 2015) to power smart nodes is another example of this design approach. This EPS achieves low-power operation and a high efficiency for the predefined voltage specification of 3.3V. The main drawback of this design technique is that the EPS imposes an arbitrary voltage as a constraint for its load, and this fact limits the full optimization of the power chain. In general, this traditional approach is inadequate because it does not maximize the power delivered to the load since the power chain does not operate at its Maximum Available Efficiency (MAE). In the rest of this chapter, we utilize the term MAE instead of MAG when its numerical value is lower than 1 because of historical and physical reasons. However, the concept remains the same.

The designer can overcome the drawbacks of the conventional approach through the optimization of both the trade-offs and interactions within the subsystems. As an example, in (RUDELL; BHAGAVATULA; WESSON, 2014), the authors proposed a non-regulated voltage between the EPS and PA. The reported regulatorless PA uses an adaptive output matching network to maintain the load power constraint while the supplied voltage decreases. This topology approach increases system efficiency and complexity. As another example, in (GEORGIADIS; COLLADO, 2013), the authors maximize the oscillator efficiency without penalty on the system complexity by using the harmonic balance optimization. However, this technique is limited to a single environmental condition.

From a broad literature review, we conclude that the design of self-sustaining systems without predefined specification of voltage or

current is just in the beginning. For example, only few authors discuss the fact that the DC signal imposed to the DC port of an amplifier can improve its efficiency. Furthermore, in the conventional PA design, the fact that all amplifier is a three-port circuit is ignored. In (MCCUNE, 2016), the authors discuss the impact of the bias point on the PA efficiency, and propose the three-port characterization of an amplifier as a design tool. However, they assume an ideal voltage source as the input of the DC port. Therefore, this characterization cannot be directly applied when a harvester powers the PA.

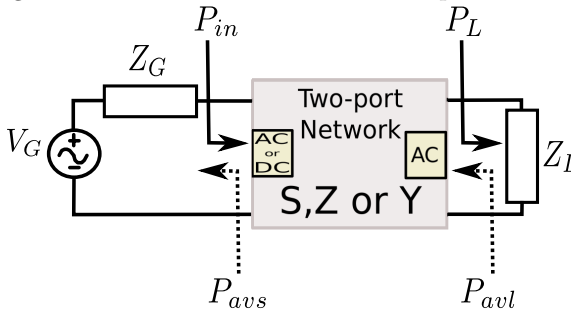
The problem of a limited AC power source loaded by a power chain has been explored in several works about microwave amplifiers (RAZAVI, 2011). On the other hand, limited DC power source loaded by a power chain has been little analyzed. In the next sections of this chapter, we use the power gain definitions of the conventional microwave theory to guide the design process of the power chain when the DC source is limited in power.

5.2 THEORETICAL FRAMEWORK

5.2.1 Gains and efficiencies of the two-port networks

Three widely used definitions for power gains of two-port networks are proposed in the microwave theory, where the input and output ports are AC ports. They are the transducer power gain (G_T), the available power gain (G_A), and the power gain (G_P). These definitions are used only for gain values, which means a number greater than one.

Figure 61 – Power definitions in a two-port network.



Source: (The author, 2017)

When the input port of the network is a DC port, we use the term efficiency instead of gain. This is because they represent very different physical phenomena, which are associated with the gain or loss of energy in the network. Considering the power references shown in Figure 61, these power gains and efficiencies ¹ are given by:

$$\eta_{PTE} = G_T = \frac{\text{Power delivered to the load}}{\text{Power available from the source}} = \frac{P_L}{P_{avs}}; \quad (5.1)$$

$$\eta_{PTE_M} = G_A = \frac{\text{Power available from the network}}{\text{Power available from the source}} = \frac{P_{avl}}{P_{avs}}; \quad (5.2)$$

$$\eta = G_P = \frac{\text{Power delivered to the load}}{\text{Power delivered to the network}} = \frac{P_L}{P_{in}}; \quad (5.3)$$

where η is the efficiency of the network, η_{PTE} is the power transfer efficiency of the network, and η_{PTE_M} is its maximum value. η_{PTE} might be viewed as the most representative FoM of the transfer efficiency of WPT systems because it incorporates the effect of both the payload and source, whereas η_{PTE_M} depends only on the source, and η only on the payload.

5.2.2 Simple power gain expression using equivalent impedances of the system

The input and output equivalent impedances allow us to replace the two-port network by simpler equivalent circuits. As shown in Figure 62, the network and its load can be replaced by the equivalent input impedance (Z_{in}). Also, the source and the network can be replaced by its Thevenin equivalent circuit connected to the output port. In this model, the power transfer efficiency is given by:

$$G_T = \frac{P_L}{P_{avs}} = \frac{P_{in} \cdot \eta}{\|V_{G_{rms}}\|^2 / 4R_G} = 4R_G R_{in} \frac{\|I_{G_{rms}}\|^2}{\|V_{G_{rms}}\|^2} \eta = \eta_{mpAC} \eta; \quad (5.4)$$

where η_{mpAC} is a numerical value that quantifies the effectiveness of the network on the extraction of the P_{avs} from its AC source. In the rest

¹To be consistent with the nomenclature proposed in the microwave theory, these efficiencies must be called transducer power efficiency (η_T), the available power efficiency (η_A), and the power efficiency (η_P). However, we decided to use the names power transfer efficiency and efficiency because they are commonly used in the WPT systems framework.

of this document, we refer to this FoM as the MPP efficiency, which is given by:

$$\eta_{mpAC} = \frac{4R_G R_{in}}{\|Z_G + Z_{in}\|^2}; \quad (5.5)$$

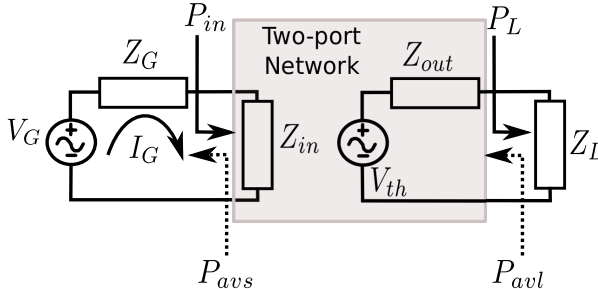
where R_{in} and R_G are the real part of the impedances Z_{in} and Z_G , respectively.

5.2.3 Power-efficiency trade-off in a power EPS

In the system illustrated in Figure 60, the power EPS cannot supply its P_{avs} at its maximum efficiency. Furthermore, in order to decrease its losses, it must deliver less power than its P_{avs} (KONG, 1995). This power-efficiency trade-off (PETO) is present in many circuits and systems, such as portable electronic devices, electric motors, and harvesters. Considering an EPS that can be modeled using the circuit that is shown in Figure 63(a), the PETO can be quantified². In Figure 63(b), we plot this trade-off assuming that $\frac{R_{spp_e}}{R_{sspe}} \gg 1$. According to this figure, the efficiency is maximized if $RL \gg R_{sspe}$. However, satisfying this condition implies a reduction of the power delivered to the load. On the other hand, the load power is maximized if $R_L = R_{sspe}$, which leads to an efficiency of 50%.

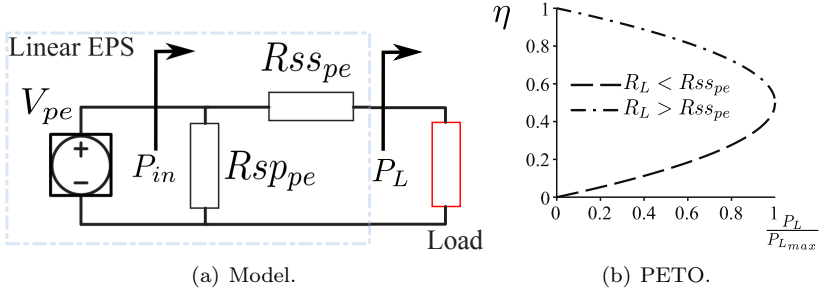
²In the Appendix H, we find an analytic expression to quantify the PETO of a linear EPS. Moreover, this function is validated by an experimental prototype circuit. Also, we use the ideal battery model proposed in Chapter 2, and the PETO expression to analyze the trade-off between the runtime and the power consumed in a generic cell-phone.

Figure 62 – Equivalent circuits of the network with AC energy input.



Source: (The author, 2017)

Figure 63 – Linear EPS model and PETO.



Source: (The author, 2016)

In several cases, the power EPS that are based on harvesters operates at a low efficiency value (i.e., 50% or less) in order to guarantee the extraction of its P_{avs} . In the rest of this chapter, we follow this design goal instead of the maximization of the harvester efficiency.

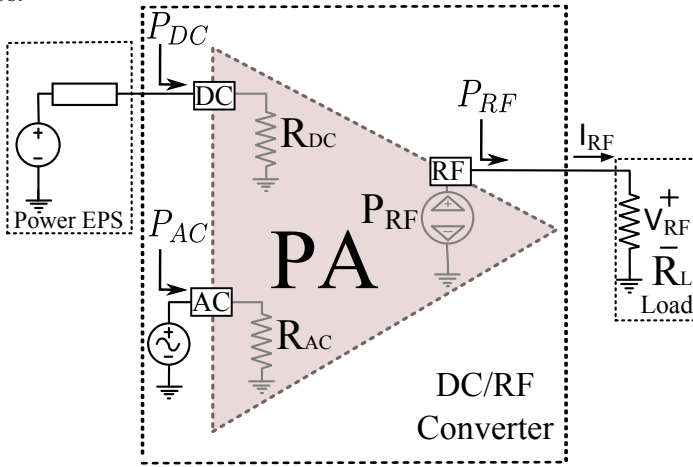
5.3 ON THE PA MODELING FOR WIRELESS POWER TRANSFER APPLICATIONS

5.3.1 PA Modeling using equivalent impedances in its input power ports

In this Section, we analyze a DC/RF converter that is based on an oscillator that drives a PA, as shown in Figure 64. In this converter, the energy flows from the DC and AC sources to the load connected to the RF port. We model this flow process by using equivalent resistances in the DC and AC ports, which are R_{DC} and R_{AC} , respectively. In this modeling approach, some of the power “dissipated” by these equivalent resistances is transferred to the load. This power in the steady state depends only on the external elements connected to the PA. Therefore, we can model the output power of the PA by using a circuit power source (ERICKSON; MAKSIMOVIC, 2001). In Figure 65, we plot the I–V characteristic of a DC power source of 1 W, for example.

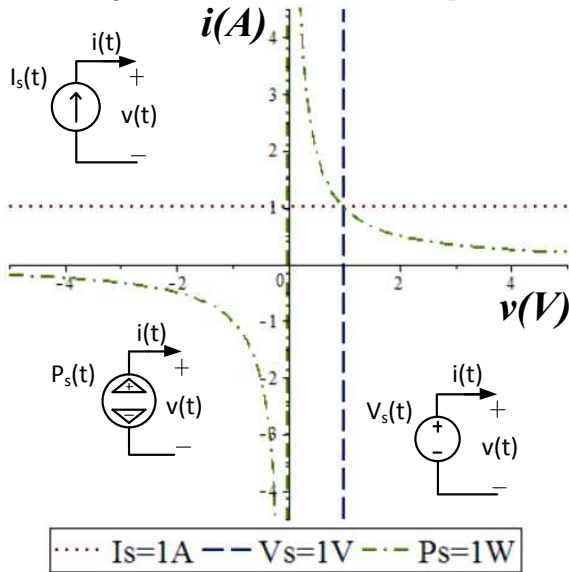
The current (I_{RF}) and the voltage (V_{RF}) in the RF port are

Figure 64 – PA model based in its port resistors and a controlled power source.



Source: (The author, 2017)

Figure 65 – Power source example.



Source: (The author, 2016)

defined by both the load and power source values, and are given by:

$$I_{RF} = I_m \sin(\omega_0 t); \quad (5.6)$$

$$V_{RF} = V_m \sin(\omega_0 t); \quad (5.7)$$

where I_m is the load peak current, V_m is the load peak voltage, and ω_0 is the natural frequency of the resonant load. In addition, the power delivered to the load (P_{RF}), the power supplied by both the DC (P_{DC}) and AC (P_{AC}) sources are given by:

$$P_{RF} = \frac{I_m^2}{2} R_L = \frac{V_m^2}{2R_L} = \frac{I_m \cdot V_m}{2}; \quad (5.8)$$

$$P_{AC} = \frac{\omega_0}{2\pi} \int_0^{2\pi} i_{AC}(t) \cdot v_{AC}(t) dt; \quad (5.9)$$

$$P_{DC} = I_{DC}^2 R_{DC} = \frac{V_{DC}^2}{R_{DC}} = I_{DC} V_{DC}; \quad (5.10)$$

where R_L is the load impedance at resonance, i_{AC} is the current supplied by the AC source, v_{AC} is the voltage provided by the AC source, I_{DC} is the DC current delivered by the EPS, V_{DC} is the voltage supplied by the EPS, and R_{DC} is the impedance imposed by the amplifier in its DC port.

5.3.2 Efficiency of the PA

The fraction of the power “dissipated” by R_{DC} and R_{AC} that is transferred to R_L by P_{RF} is given by:

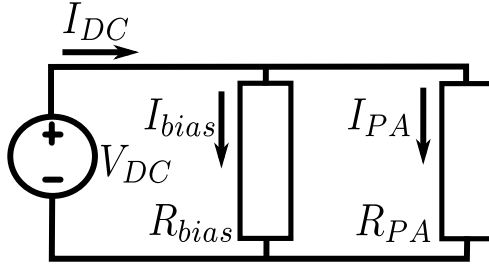
$$P_{RF} = \eta_{PA} \cdot (P_{DC} + P_{AC}); \quad (5.11)$$

where, P_{DC} is supplied by the DC source (V_{DC}), P_{AC} is provided by the AC source (V_{AC}), and η_{PA} is the PA efficiency. If P_{AC} is negligible compared to P_{DC} , then Eq. (5.11) can be rewritten as:

$$\eta_{PA} = \frac{R_L}{2R_{DC}} \left(\frac{I_m}{I_{DC}} \right)^2. \quad (5.12)$$

The power delivered by V_{DC} is consumed by both the bias circuit (or the driver circuit) and the PA power stage as shown in Figure 66. Therefore, I_{DC} is given by Eq. (5.13). By using (5.13), R_{DC} can be

Figure 66 – Equivalent DC circuit of a generic PA.



Source: (The author, 2017)

calculated by Eq. (5.14).

$$I_{DC} = I_{bias} + I_{PA} = \frac{R_{PA} \cdot I_{PA}}{R_{bias}} + I_{PA}; \quad (5.13)$$

$$R_{DC} = \frac{V_{DC}}{I_{DC}} = R_{bias} \parallel R_{PA}; \quad (5.14)$$

where I_{bias} is the DC current of the bias circuit, I_{PA} is the DC current of the PA power stage, R_{bias} is the resistance imposed by the bias circuit to the DC source, and R_{PA} is the resistance imposed by the PA power stage to the DC source. Hence, by using Eq. (5.13) and (5.14), Eq. (5.12) can be rewritten as (5.15).

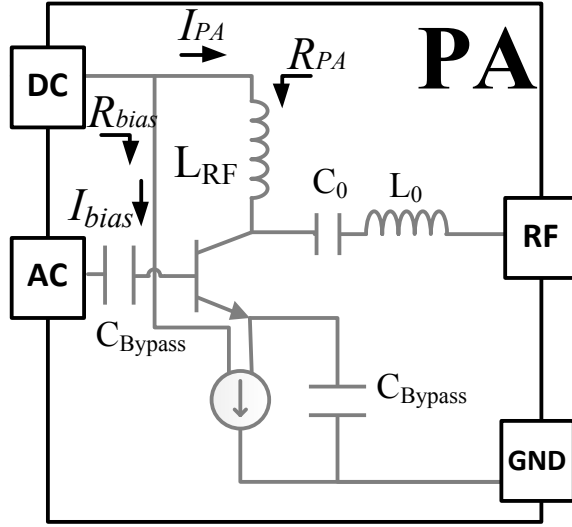
$$\eta_{PA} = \frac{1}{2} \frac{R_L R_{DC}}{R_{PA}^2} \left(\frac{I_m}{I_{PA}} \right)^2 = f_{PA}(r_L); \quad (5.15)$$

where r_L is the load impedance factor of the PA, defined as $r_L = R_{DC}/R_L$, and f_{PA} is a function dependent on the PA topology. The PA efficiency is maximum for an optimum relation between its port impedances (i.e. $r_L = r_{L_{opt}}$). In the next subsections, we discuss some examples of the proposed modeling technique.

5.3.2.1 Example 1: BJT class-A PA

Considering the schematic shown in Figure 67, a negligible energy consumption of the bias circuit (i.e. $R_{DC} \approx R_{PA}$) and Eq. (5.15),

Figure 67 – Class-A PA topology.



Source: (The author, 2016)

η_{PA} can be expressed as:

$$\eta_{PA} \approx \frac{0.5R_L}{R_{PA}} \left(\frac{I_m}{I_{PA}} \right)^2 \approx \frac{0.5R_L}{R_{DC}} \left(\frac{I_m}{I_{DC}} \right)^2. \quad (5.16)$$

Assuming the exponential model of the BJT presented in (CLARKE; HESS, 1971), Eq. (5.16) can be rewritten as:

$$\eta_{PA} = \frac{1}{2r_L} h_i^2 \left(\frac{|v_{ac}|}{\phi_t} \right); \quad (5.17)$$

where $|v_{ac}|$ is the peak voltage value of the sinusoid input signal (V_{AC}) normalized by the thermal voltage (ϕ_t) and the function $h(x)$ is given by:

$$h(x) = 2 \frac{I_{B1}(x)}{I_{B0}(x)}; \quad (5.18)$$

where $I_{B\sigma}(x)$ is the modified Bessel function of the first kind with order σ and argument x . The PA operates as class-A PA until I_m is equal to I_{PA} or V_m is equal to the collector bias voltage (V_C). Therefore, to achieve the class-A operation (i.e., $I_m < I_{PA}$ and $V_m < V_C$), the $|v_{ac}|$

value must be lower than a maximum value given by:

$$|v_{ac}|_{\phi_{tM}} = \begin{cases} h^{-1}(1) \approx 1.16 & r_L > 1; I_m = I_{PA} \\ h^{-1}(r_L) & r_L < 1; V_m = V_C \end{cases}; \quad (5.19)$$

where $h^{-1}(x)$ is the inverse function of $h(x)$. Finally, from Eq. (5.17) and (5.19), the PA efficiency is given by :

$$\eta_{PA} = f_{ABJT}(r_L) = \begin{cases} 0.5 \cdot r_L & r_L < 1; I_m = I_{PA} \\ \frac{1}{2r_L} & r_L \geq 1; V_m = V_C \end{cases}. \quad (5.20)$$

This efficiency is maximum when $r_L = r_{L_{opt}} = 1$ is imposed by design.

5.3.2.2 Example 2: CMOS class-D PA

The class-D schematic is shown in Figure 68, where the (N- or P-type) MOSFET is modeled by an ideal switch with a series resistance (R_{on}). The current I_m is given by Eq. (5.21) when we consider ideal components, a duty cycle of 50%, and resonant load with a high loaded quality factor. The current waveform of the power stage is a rectified sinusoid with a peak value of I_m . Thus its average value (i.e., I_{PA}) is given by (5.22). Furthermore, by using Eq. (5.21) and (5.22), the impedance imposed by the PA power stage (R_{PA}) can be calculated by (5.23). Moreover, the power used to charge and discharge the total gate capacitances of the MOSFETs (C_G), dissipated by the driver, can be modeled by an equivalent resistance (R_{bias}) given by (5.24).

$$I_m = \frac{V_m}{(R_L + R_{on})} = \frac{4V_{DC}}{\pi(R_L + R_{on})}; \quad (5.21)$$

$$I_{PA} = 2I_m/\pi; \quad (5.22)$$

$$R_{PA} = \frac{V_{DC}}{I_{PA}} = \frac{\pi^2}{8}(R_L + R_{on}); \quad (5.23)$$

$$R_{bias} = \frac{V_{DC}^2}{P_{bias}} \approx \frac{V_{DC}^2}{V_{DC}^2 \cdot f \cdot \alpha_G \cdot C_G} = \frac{1}{f \cdot \alpha_G \cdot C_G}; \quad (5.24)$$

where the factor α_G represents the capacitance excess due to the driver, and f is the frequency of the AC input. The product $C_G \cdot R_{on}$ can be considered quasi-constant and is given by the product of two technological parameters (i.e., a_M and b_M) introduced in (STRATAKOS; BRODERSEN; R.SANDERS, Napa . 1994), hence Eq. (5.24) can be rewritten as

(5.25). From Eq. (5.14), (5.23) and (5.25), r_L can be calculated using (5.26).

$$R_{bias} = \frac{R_{on}}{f \cdot \alpha_G \cdot a_M \cdot b_M}; \quad (5.25)$$

$$\frac{1}{r_L} = \frac{R_L}{R_{DC}} = \frac{f \cdot \alpha_G \cdot a_M \cdot b_M}{\frac{R_{on}}{R_L}} + \frac{8}{\pi^2} \frac{1}{\left(1 + \frac{R_{on}}{R_L}\right)}. \quad (5.26)$$

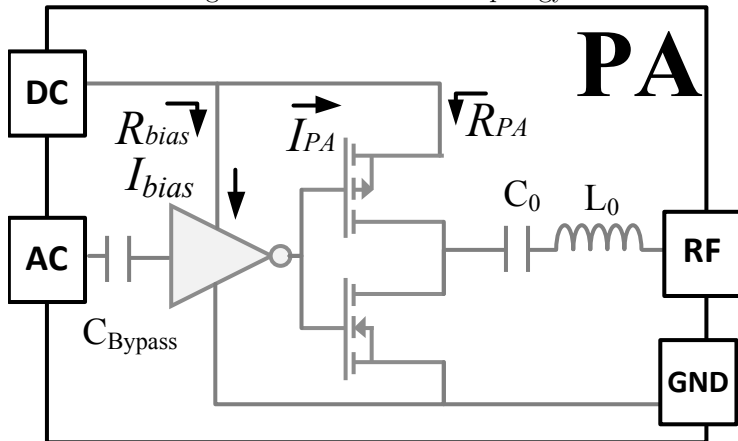
From Eq. (5.15), (5.22) and (5.23), η_{PA} can be calculated by:

$$\frac{1}{\eta_{PA}} = \frac{\pi^2}{8} \cdot \frac{1}{r_L} \cdot \left(1 + \frac{R_{on}}{R_L}\right)^2. \quad (5.27)$$

Using (5.26), Eq. (5.27) can be rewritten as:

$$\eta_{PA} = f_{DCMOS}(r_L) = \frac{1}{(1+l_D(r_L)) \left(1+k_G \left(1+\frac{1}{l_D(r_L)}\right)\right)}; \quad (5.28)$$

Figure 68 – Class-D PA topology.



Source: (The author, 2016)

where $k_G = \frac{\pi^2}{8} \alpha_G \cdot a_M \cdot b_M \cdot f$, and the function $l_D(x)$ is given by:

$$l_D(x) = \frac{1}{2} \left((A_l + B_l)x - 1 \pm \sqrt{1 + (2A_l - 2B_l)x + (A_l + B_l)^2 x^2} \right); \quad (5.29)$$

where $A_l = f \cdot \alpha_G \cdot a_M \cdot b_M$, and $B_l = \frac{8}{\pi^2}$. This efficiency is maximum when Eq. (5.30) is imposed by design. In this case, the maximum value of η_{PA} is given by (5.31).

$$l_D(r_{L_{opt}}) = \sqrt{\frac{k_G}{k_G + 1}} \quad (5.30)$$

$$f_{DCMOS}(r_{L_{opt}}) = \frac{\sqrt{k_G^2 + k_G}}{(k_G + \sqrt{k_G^2 + k_G})(k_G + 1 + \sqrt{k_G^2 + k_G})}. \quad (5.31)$$

5.3.2.3 Example 3: Ideal class-E PA

The class-E PA topology is shown in Figure 69(a), where the transistor is modeled by a switch without on-resistance to alleviate the mathematical difficulties involved in the time-domain analysis of the Class-E PA with finite DC-feed inductance. Also, we find the “optimum” r_L as the one that produces zero-voltage and zero-slope conditions. This approach allows us to obtain an r_L value close to the $r_{L_{opt}}$ that optimizes the PA efficiency. This suboptimal value can be used as the initial point of an iterative CAD optimization process of the PA (FAJARDO; SOUSA, 2016a).

We model the class-E PA using the model reported in (ACAR; ANNEMA; NAUTA, 2007a), which is shown in Figure 69(b). The output current is given by Eq. (5.32). This model is accurate if the AC signal has zero-time transitions, f is close to f_0 , and the series resonant circuit (i.e., L_0 , C_e and R_L) has a high loaded quality factor. Assuming nominal operation (i.e., zero-voltage and zero-slope switching conditions) and this model, the PA currents and voltages are given by the

equations (5.33) to (5.38).

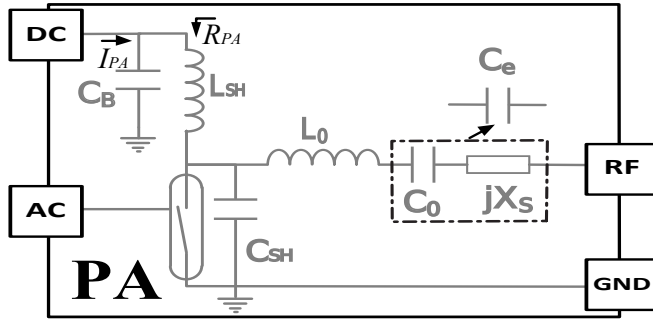
$$i_R(t) = I_P \sin(\omega t + \varphi) = \sqrt{\frac{2P_{out}}{R_L}} \sin(2\pi f t + \varphi); \quad (5.32)$$

$$v_{CSH_{on}}(t) = i_{CSH_{on}}(t) = i_{S_{off}}(t) = 0; \quad (5.33)$$

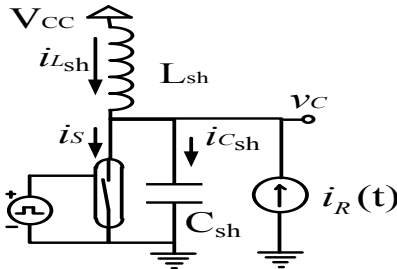
$$i_{LSH_{on}}(t) = \frac{V_{CC}}{L_{SH}} t - I_P \sin(\varphi); \quad (5.34)$$

$$i_{S_{on}}(t) = \frac{V_{CC}}{L_{SH}} t + I_P (\sin(\omega t + \varphi) - \sin(\varphi)); \quad (5.35)$$

Figure 69 – Class-E PA with a finite DC-feed inductance.



(a) Ideal model.



(b) Ideal model with high Q.

Source: (The author, 2016)

$$i_{L_{SH\,off}}(t) = \frac{V_{CC}}{L_{SH}}t - \int_{\frac{2\pi D_{SH}}{\omega}}^t \frac{v_{C_{SH}}(\tau)}{L_{SH}}d\tau - I_P \sin(\varphi); \quad (5.36)$$

$$v_{C_{SH\,off}}(t) = V_{CC} + \frac{C_{SH_1} \cos(q\omega t) + C_{SH_2} \sin(q\omega t)}{-\frac{q^2}{1-q^2}pV_{CC} \cos(\omega t + \varphi)}; \quad (5.37)$$

$$i_{C_{SH\,off}}(t) = \frac{V_{CC}}{L_{SH}}t - \frac{1}{L_{SH}} \int_{\frac{2\pi D_{SH}}{\omega}}^t v_{C_{SH}}(\tau)d\tau; \quad (5.38)$$

$$+ I_P (\sin(\omega t + \varphi) - \sin(\varphi))$$

where X_{on} means that the expression for the respective function X is being taken when the switch is in the ON state ($0 < t < \frac{2\pi D_{SH}}{\omega}$). On the other hand, X_{off} means that the expression for the respective function X is being taken when the switch is in the OFF state ($\frac{2\pi D_{SH}}{\omega} < t < \frac{2\pi}{\omega}$). The factors C_{SH_1} and C_{SH_2} are analytic functions of p , q , φ and V_{CC} , and they are described in (ACAR; ANNEMA; NAUTA, 2007a). The variables p and q are given by (ACAR; ANNEMA; NAUTA, 2007a):

$$q = \frac{1}{\omega \sqrt{L_{SH} C_{SH}}} = \frac{\omega_{SH}}{\omega}; p = \frac{\omega L_{SH} I_P}{V_{CC}} = \frac{Z_{L_{SH}}}{R_{\omega}}; \quad (5.39)$$

where ω_{SH} is the natural frequency of the LC_{SH} network, $Z_{L_{SH}}$ is the impedance of L_{SH} , and R_{ω} is:

$$R_{\omega} = \frac{V_{CC}}{I_P} = \sqrt{\frac{P_{in} R_{DC}}{2P_{out}/R_L}} = \frac{\sqrt{R_L R_{DC}}}{\sqrt{2}}; \quad (5.40)$$

where R_L is the PA load, P_{in} is the power delivered by V_{CC} , P_{out} is the power dissipated by R_L , and R_{DC} is the equivalent resistance that the amplifier imposes to V_{CC} , which can be calculated as (FAJARDO; SOUSA, 2016a):

$$R_{DC} = \frac{V_{DC}}{I_{DC}} = V_{CC} \left/ \frac{\omega}{2\pi} \int_0^{\frac{2\pi}{\omega}} i_s(t) dt \right. = \frac{R_{\omega}}{g}. \quad (5.41)$$

From Eq. (5.41) and (5.40), we find:

$$R_{DC}(q, D_{SH}) = \frac{R_L}{2 \cdot (g(q, D_{SH}))^2}, \quad (5.42)$$

where

$$g(q, D_{SH}) = \left\{ \begin{aligned} & \left(\frac{1 - \cos(2\pi D_{SH})}{2\pi} \right) \cos(\varphi) \\ & + \left(\frac{\sin(2\pi D_{SH})}{2\pi} - D_{SH} \right) \sin(\varphi) + \frac{D_{SH}^2 \pi}{p} \end{aligned} \right\}. \quad (5.43)$$

Therefore, the approximated optimum value of r_L is given by:

$$r_{L_{opt}}(q, D_{SH}) \approx \frac{1}{2 \cdot (g(q, D_{SH}))^2}. \quad (5.44)$$

To develop numerical insight into this optimum value, we plot Eq. (5.44) in Figure 70. We emphasize that Eq. (5.32) to (5.44) can be calculated in terms of V_{CC} , ω , R_L , and P_{out} only if p , q , φ and D_{SH} are known. However, in (ACAR; ANNEMA; NAUTA, 2007a), the authors demonstrated that both φ and p can be solved as analytic functions of both q and D_{SH} ³. Additionally, the peak value of v_C must be less than the breakdown voltage of the switch. In (FAJARDO; SOUSA, 2016c), we proposed Eq. (5.45), which is a simple analytic relation between the DC input voltage and the peak value of v_C . This expression was based on the numerical solution of the analytical equations of the ideal class-E proposed by (ACAR; ANNEMA; NAUTA, 2006, 2007a).

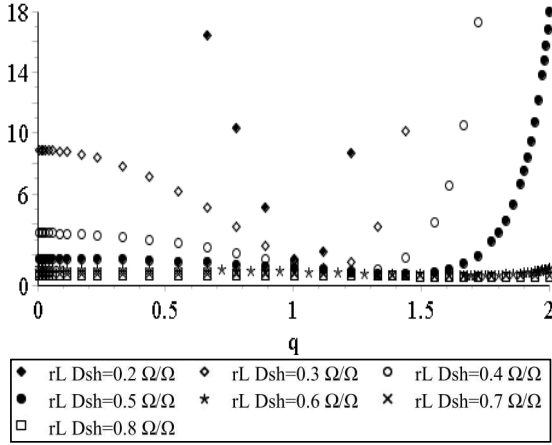
$$V_{c_{max}} \approx V_{CC} \left(\frac{1.83}{1 - D_{SH}} \right). \quad (5.45)$$

5.3.3 Power transfer efficiency of the PA

A PA is a three-port network, as illustrated in Figure 64. However, when P_{AC} is negligible compared to P_{DC} , the PA can be modeled by a two-port network, as shown in Figure 71(a). We analyze the PA using the model proposed in Section 5.3.1, which allows us to replace the PA by two equivalent circuits, as depicted in Figure 71(b). The PA and its load are replaced by its DC resistance (i.e., R_{DC}). Similarly, the source and PA can be replaced by an equivalent power source connected to the output port of the PA. From this equivalent circuit and Eq. (5.4), we find an expression for the power transfer efficiency of the PA:

$$\eta_{PA_{PTE}} = \eta_{mp_{DC}} \eta_{PA}. \quad (5.46)$$

³In Appendix I, we report the Maple code that implements the variables φ and p as functions of q and D_{SH} .

Figure 70 – r_{Lopt} of the ideal class-E amplifier.

Source: (The author, 2017)

where η_{mpDC} is a numerical value that quantifies the effectiveness of the network on the extraction of the P_{avs} from its DC source, and is given by:

$$\eta_{mpDC} = \frac{4 \frac{R_{DC}}{R_G}}{\left(1 + \frac{R_{DC}}{R_G}\right)^2}. \quad (5.47)$$

When the power EPS is non-linear, it can be modeled by an equivalent one using the following relation:

$$V_{G_{dc}} = 2V_{mp}; \quad (5.48)$$

$$R_{G_{dc}} = R_{mp}. \quad (5.49)$$

5.3.4 Maximum power transfer efficiency of the PA

The maximum power transfer efficiency (or available efficiency) of the PA is given by:

$$\eta_{PA_{PTE_M}} = \max \{ \eta_{PA_{PTE}} (R_{G_{DC}}, R_L) \}. \quad (5.50)$$

From Eq. (5.15), (5.46), and (5.50), this efficiency can be rewritten as:

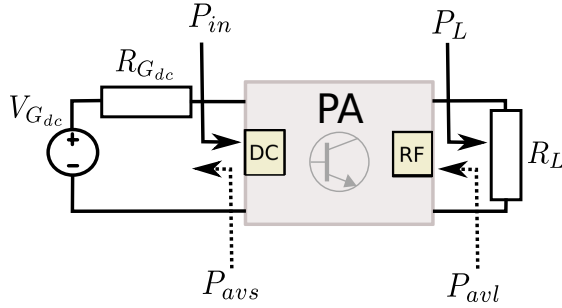
$$\eta_{PA_{PTEM}}(r_L, r_G) = \max \{f_{pm}(r_G) f_{PA}(r_L)\}; \quad (5.51)$$

where r_G is the generator impedance factor of the PA, which was defined as $r_G = \frac{R_{DC}}{R_{GDC}}$. $f_{mp}(x)$ is independent of the PA topology, and is calculated as follows:

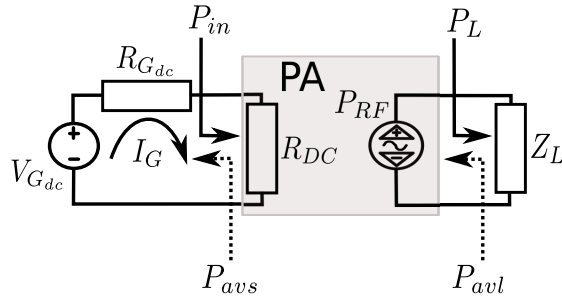
$$f_{pm}(x) = \frac{4x}{(1+x)^2}. \quad (5.52)$$

If there is a solution for the maximization process of (5.51) subject to $r_{G_{opt}} R_{GDC} = r_{L_{opt}} R_L$, then the PA can operate at its MAE, where $r_{G_{opt}}$ and $r_{L_{opt}}$ maximize f_{pm} and f_{PA} , respectively. As a con-

Figure 71 – Energy flow models of the PA.



(a) Power definitions of the PA.



(b) Equivalent circuit model of the PA.

Source: (The author, 2014)

the DC port of the PA, the PA efficiency increases, whereas that of the converter decreases. Therefore, this voltage must be chosen carefully to solve this trade-off. However, for a power EPS based on harvesters, V_{mp} solves this trade-off because the DC/DC converter consumes a high amount of power while in operation. In addition, this methodology

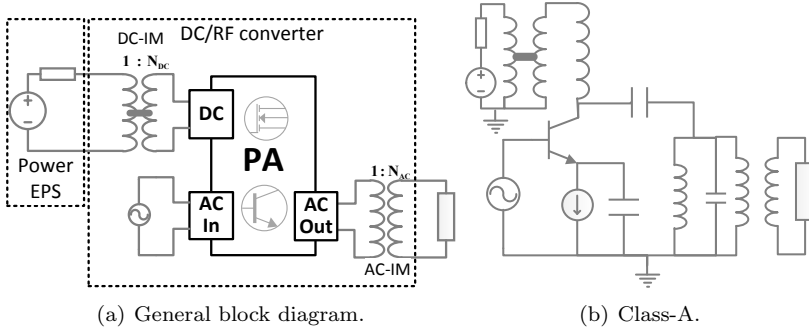
Table 14 – Design methodology for SsPA systems.

Description	Equation or example
1 Find the P_{avs} of the power EPS and its related variables: R_{mp} , V_{mp} and I_{mp} .	Considering a linear EPS: $R_{mp} = R_{sspe}$, $V_{mp} = \frac{V_{pe}}{2}$, $I_{mp} = \frac{V}{R_{sspe}}$
2 Set the voltage across the DC port to V_{mp} or to the voltage of a particular implementation with efficiency constraint (V_{max}). For instance, this limit can be the supply voltage of a particular CMOS technology.	$V_{DCopt} = V_{mp}$ or V_{max} This decision is related to a trade-off between the non modeled losses in the matching network and the ones in the PA.
3 Find the DC current that extracts the P_{avs} of the EPS.	$I_{DCopt} = \frac{P_{avs}}{V_{DCopt}}$
4 Find the impedance of the PA DC port that maximizes the power extracted from the harvester.	$R_{DCopt} = \frac{V_{DCopt}}{I_{DCopt}}$
5 Find the load value that maximizes the PA efficiency.	$R_{Lopt} = \frac{R_{DCopt}}{r_{Lopt}}$
6 Find the specifications of the DC and AC impedance matching networks (DC-IM and AC-IM).	e.g., ideal transformer turn ratios: $N_{DC} = \sqrt{\frac{R_{DCopt}}{R_{mp}}}$ $N_{AC} = \sqrt{\frac{R_L}{R_{Lopt}}}$

Source: (The author, 2017)

finds the optimum R_L (R_{Lopt}) based on the calculated R_{DCopt} and the r_{Lopt} of the PA topology. In particular, Table 15 summarizes the values of r_{Lopt} for the PAs that we analyzed in Section 5.3. Finally, R_{DCopt} is

Figure 73 – SsPA with ideal impedance matching networks.



Source: (The author, 2016)

matched to the power EPS impedance by a DC impedance matching network (DC-IM) and $R_{L_{opt}}$ is matched to the impedance of the real load by an AC network (AC-IM), as illustrated in Figure 73(a).

Table 15 – $r_{L_{opt}}$ for the analyzed Pas.

PA	$r_{L_{opt}}$
BJT Class-A	1
CMOS Class-D	$\frac{\sqrt{(k_G+1)k_G+k_G}}{(A_l+B_l)\sqrt{(k_G+1)k_G+A_l(k_G+1)}}$ $k_G = \frac{\pi^2}{8}\alpha_G \cdot a_M \cdot b_M \cdot f$ $A_l = f \cdot \alpha_G \cdot a_M \cdot b_M \text{ and } B_l = \frac{8}{\pi^2}$
Ideal Class-E	$\frac{1}{2 \left[\left(\frac{1-\cos(2\pi D_{SH})}{2\pi} \right) \cos(\varphi) + \left(\frac{\sin(2\pi D_{SH})}{2\pi} - D_{SH} \right) \sin(\varphi) + \frac{\pi D_{SH}^2}{p} \right]^2}$

Source: (The author, 2017)

We assume impedance matching networks with negligible losses. Therefore, we model them by ideal transformers, as shown Figure 73. Furthermore, the DC-IM implementation can be a DC/DC converter, and the AC-IM implementation can be an L or π network. We present the application of these procedures in Section 5.4.2.

5.4.2 PA study case 1: SsPA based on class-A PA

We designed, simulated and implemented a class-A PA to experimentally verify Eq. (5.20). We show the amplifier topology in Figure 73(b), and summarize the amplifier specifications in Table 16.

We simulated the PA using the harmonic balance simulation technique, which was carried out in the ADS[®] software. Furthermore, we ran two parametric sweeps, one for the input signal (V_{AC}) and the other for R_{PA} . The latter was performed by a fixed current ($I_{PA}=1\text{mA}$) and a V_{DC} sweep. Additionally, we simulated the circuit with and without the output LC tank filter. Moreover, we verified the assumption that P_{AC} was negligible compared to P_{DC} (i.e., $P_{AC} < 8 \mu\text{W}$ for all simulations). Table 17 summarizes the simulation results.

We implemented the PA without the output LC tank, and the FFT processing obtained the fundamental components of the voltage output in the frequency domain. This approach allows us to avoid the influence of the parasitic elements of the LC tank on the results. We show the experimental setup in Figure 74(a). In this setup, we set I_{PA} to 1 mA and R_{PA} with V_{DC} . Also, we increased V_{AC} until the PA operated at the limit of the class-A operation ($I_m = I_{PA}$ or $V_m=V_C$). At this point, we calculated the efficiency from the measured values

Table 16 – PA specifications.

V_{DC}	I_{PA}	f	$R_{L_{opt}}$
1 V	1 mA	100 kHz	1 k Ω

Source: (The author, 2017)

Table 17 – PA simulation results.

R_{PA}	Limit		P_{DC}	P_{DC}	P_L	P_L	η	η
(Ω)	type	$ v_{ac} _{\phi_t}$	w/o.LC	w.LC	w/o.LC	w.LC	w/o.LC	w.LC
			(mW)	(mW)	(mW)	(mW)	(%)	(%)
0.5	$V_m=V_C$	0.530	0.564	0.564	0.138	0.138	24.5	24.5
1.0	$V_m=V_C$	1.181	1.127	1.127	0.545	0.545	48.3	48.2
1.5	$I_m=I_{PA}$	1.180	1.691	1.691	0.545	0.545	32.2	32.1
2.0	$I_m=I_{PA}$	1.180	2.254	2.254	0.545	0.545	24.2	24.1

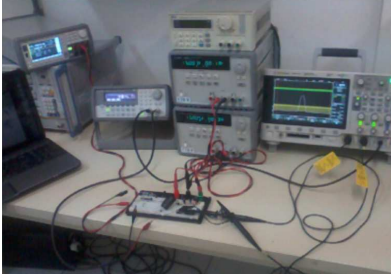
Source: (The author, 2017)

Table 18 – PA experimental results.

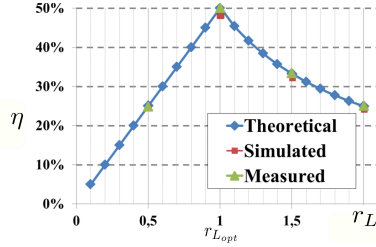
R_{PA} (Ω)	Limit type	$ v_{ac} _{\phi_t}$	LC tank	P_{DC} (mW)	P_L (mW)	η (%)
0.50	$V_m=V_C$	0.679	w/o	0.5002	0.1242	24.8
1.00	$V_m=V_C$	1.516	w/o	1.003	0.5004	50
1.50	$I_m=I_{PA}$	1.516	w/o	1.502	0.5010	33.3
2.00	$I_m=I_{PA}$	1.516	w/o	2.002	0.5010	25

Source: (The author, 2017)

Figure 74 – Implemented class-A PA.



(a) Experimental setup.



(b) Efficiency results.

Source: (The author, 2014)

(i.e., I_{PA} , V_{DC} , and V_m). Then we estimated the voltage operation limit ($V_m = V_C$) using a digital oscilloscope with FFT option. Next, we estimated the current operation limit ($I_m = I_{PA}$) from V_m and the measured load value ($R_L = 997.74 \Omega$). Table 18 summarizes the experimental results. Figure 74(b) shows the predicted efficiency and the simulated and experimental results. Hence, we conclude that Eq. (5.20) is an accurate expression to model the efficiency of this amplifier.

We chose a scenario with the following specifications: a power EPS with $P_{avs} = 1$ mW and $R_{pavs} = 1$ k Ω , a resistive load of $R_L = 1$ k Ω , and an ideal sinusoid input signal with the required amplitude and frequency of 100 kHz. This approach allows us to experimentally verify the proposed methodology without the practical limitations of the commercial harvesters and the matching networks (AC and DC). We utilized the methodology in Table 14 to calculate the specifications of

Table 19 – DC/RF converter specifications.

$V_{DC_{opt}}$	$I_{DC_{opt}}$	$R_{DC_{opt}}$	$R_{L_{opt}}$	M_{DC}	M_{AC}
1V	1mA	1k Ω	1k Ω	1	1

Source: (The author, 2017)

Table 20 – SsPA experimental results.

R_{DC}	P_{EPS}	P_{DC}	P_{RF}	η_{EPS}	η_{PA}	η_{mp}	η_{PTE}
1.001k Ω	2.004mW	1000.3 μ W	500.4 μ W	50%	50%	100%	50%

Source: (The author, 2017)

the PA and the matching networks. Table 19 displays the results. Finally, we calculated the DC/RF converter efficiency from the measured values of the PA, and the EPS efficiency was calculated from its DC current and open-circuit voltage. Table 20 presents the results, which reveals that the designed converter extracts the P_{avs} of the power EPS with the maximum PA efficiency and guarantees the MAE operation of the converter.

5.5 DESIGN FOR MPP OPERATION OF THE SSWPT

An SsWPT system operates at its MAE when the power maximization plane is at the load. The designer can shift the maximization plane from the harvester to the WPT due to the (input, output, and inter-stage) impedance matching networks that simultaneously force the MPP operation of the EPS and the MAE operation of both the PA and inductive link. In the next sections, we propose a design methodology to achieve this goal in the power chain shown in Figure 75.

5.5.1 Optimum frequency of a SsWPT system

In an SsWPT system, the operation frequency affects the efficiency of the PA and the inductive link, as illustrated in Figure 76. We consider three generic links that use the same technology, and operate under the same constraints. At low and intermediate frequencies (LF and IF), the switch-mode PA can operate with an efficiency higher

Figure 75 – SsWPT MAE operation and block diagram.

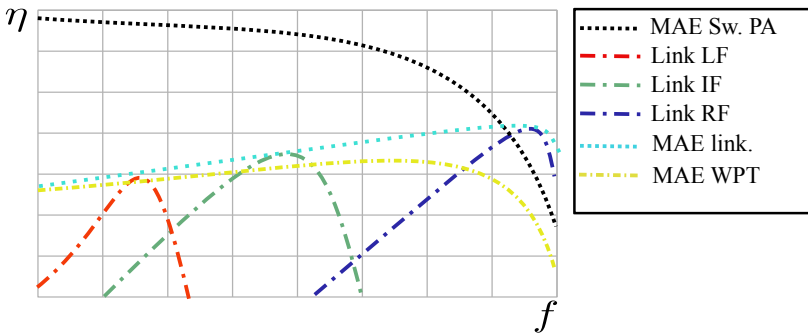
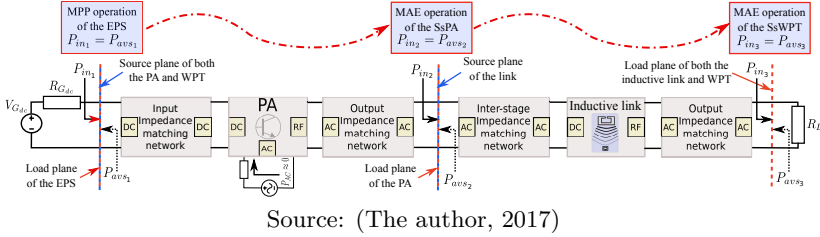


Figure 76 – Efficiency versus frequency.

than that of the inductive link. Thus, the frequency that maximizes the link efficiency is very close to the one that minimizes the losses of the SsWPT power chain.

At RF frequencies, the PA and link efficiencies are comparable to each other, and the former can be lower than latter. Therefore, the optimum frequency might differ significantly from the one that maximizes the link efficiency. Besides, the reliability of the PA switch-mode operation at RF frequency range sometimes is complicated to achieve. Therefore, how can we know if this operation is possible?. In (MCCUNE, 2015b), the authors answer this question using the transistor transition frequency (f_T) as a constraint. Furthermore, they conclude that a PA switch-mode operation is possible as long as the operating frequency remains below 5% of the transistor f_T . Consequently, if the PA switch-mode operation is not possible, then the optimum frequency can be estimated as $f_{opt} = 0.05f_T$.

5.5.2 Design methodology proposed for SsWPT systems

We propose the design methodology outlined in Table 21. This method maximizes the power transfer efficiency of an SsWPT system based on an inductive link and a DC/RF converter. The latter is implemented by an efficient PA, that is, $\eta_{PA} > \eta_{IL}$ at the operation frequency. Also, the methodology assumes the availability of a prototype (or an accurate model) of the inductive link, which must be previously optimized by the designer.

The method sets the operation frequency of the WPT system to the one that maximizes the efficiency of the link. We calculate this optimum frequency (f_{opt}) and the respective optimum load of the system ($R_{L_{opt}}$) from the RLC model of the link (or the S-parameters of the EM structure). Then we design the SsPA system, which feeds the link, so as to operate at f_{opt} by following the methodology presented in Section 5.4.1. In Section 5.5.3, we present an application of this procedure to a study case based on an ideal class-E PA.

The main drawback of the proposed method lies in the fact that it requires accurate knowledge of the PA's r_L . In practice, this accuracy is limited by technological issues. For instance, the r_L of a switched class-E PA implemented by a real transistor differs significantly from the ideal model (perfect switch and lossless components), especially in the RF frequency range, because the transistor usually operates in compression instead of switching (MCCUNE, 2015a). In Table ??, we extend the proposed methodology to the case without the r_L factor or considering a very inaccurate prediction. This method estimates $r_{L_{opt}}$ using an iterative process that guarantees MAE operation of the PA. Then we design the SsWPT system using $r_{L_{opt}}$. In Section 5.5.4, we present an application of this procedure to a study case based on a “real” class-E PA, which comprised an array of heterojunction bipolar transistors (HBT) as the switching device and was simulated using lossy components.

No.	Description	Equations or example
1	Follow step 1 of the methodology for SsWPT systems in Table 21. Then follow steps 1 to 4 of the method for SsPA systems in Table 14.	

Source: (The author, 2017)

No.	Description	Equations or example
2	Find the r_L that maximize both the PA and MPP efficiencies using an iterative process.	For example, class-E PA with $\eta_{PA} < 1$ and $D_{SH} = 0.5$.
2a.	Assume r_L as r_{L_0} (a default or an approximate value), and set the iteration counter to zero ($m_i = 0$).	Initial values: $m_i = 0; \eta_{PA_0} = 0.5; q_{m_i} = 1.4134$ $r_{L_{m_i}} = r_{L_\eta} = \left(\frac{1}{\sqrt{2} \cdot \eta_{PA_{m_i}} g(D_{SH}, q)} \right)^2$
2b.	Calculate: $R_{LPA_{m_i}} = \frac{V_{DC_{opt}}}{r_{L_{m_i}}}$.	$R_{LPA_{m_i}} = R_{DC_{opt}} (\sqrt{2} \cdot \eta_{PA_{m_i}} g(D_{SH}, q))^2$
2c.	Design and optimize the PA using $V_{DC_{opt}}$ as input voltage, and $R_{LPA_{m_i}}$ as load. This process can be performed in any available CAD tools, optimization solvers etc.	We design the inter-stage network to maximize the quality factor of the PA load, which is given by: $Z_{LPA_{m_i}} = R_{LPA_{m_i}} + jX_{LPA_{m_i}}$, where $X_{LPA_{m_i}}$ can be calculated as: $X_{LPA_{m_i}} = X_{CIM} \frac{\left(\frac{X_{CIM}}{1 - Q_{inIL} \frac{X_{CIM}}{R_{inIL}} + Q_{inIL}^2} \right)}{\left(1 + \left(\frac{X_{CIM}}{R_{inIL}} - Q_{inIL} \right)^2 \right)}$ $r_{GIM} = \frac{R_{inIL}}{R_{LPA_{m_i}}}; Q_{inIL} = \left(\frac{X_{inIL}}{R_{inIL}} \right).$ Using $Z_{LPA_{m_i}}$ as input, we calculate the PA components with the set of equations in Section 5.5.3.
2d.	Calculate the resulting $R_{DC_{m_i}}$, and estimate $\eta_{mpDC_{m_i}}$ assuming an equivalent linear EPS.	$R_{DC_{m_i}} = R_{DC_{sim}}$, $\eta_{mpDC} = \frac{4R_{DC_{m_i}}/R_{mp}}{(1 + R_{DC_{m_i}}/R_{mp})^2}.$
2e.	If $\eta_{mpDC_{m_i}} > \eta_{mpDC_{th}}$ (a designer-defined threshold), then jump to step 2h.	If $\eta_{mpDC_{m_i}} > 0.99$, then jump to step 2h.

Source: (The author, 2017)

No.	Description	Equations or example
2f.	If $m_i > m_{ith}$ (an arbitrary threshold), then stop the optimization process without solution.	If $m_i > 5$, then stop the process.
2g.	Set $m_i = m_i + 1$, and recalculate $r_{L_{m_i}} = \frac{R_{DC_{m_i-1}}}{R_{PA_{m_i-1}}}$. Then continue the process from step 2b.	From simulation: $\eta_{L_{PA_{m_i+1}}} = \eta_{PA_{sim}}$ and jump to step 2b.
2h.	Summarize the optimization process results: $r_{L_{opt}} = r_{L_{m_i}}$ and $R_{L_{PA_{m_i}}} = R_{L_{PA_{m_i}}}$.	$r_{L_{opt}} = r_{L_{m_i}}$, $q_{opt} = q_{m_i}$, and $R_{L_{PA_{m_i}}} = R_{L_{PA_{m_i}}}$.
3	Find the specifications and design the (input, output and inter-stage) impedance matching networks, e.g., ideal transformers: $N_{input} = \sqrt{\frac{R_{DC_{opt}}}{R_{mp}}}$, $N_{output} = \sqrt{\frac{R_L}{R_{L_{opt}}}}$, $N_{inter} = \sqrt{\frac{R_{G_{opt}}}{R_{L_{PA_{opt}}}}}$.	We simply use the inter-stage network, which is composed only of a parallel capacitor to maximize the quality factor of the PA load. This capacitor is given by: $C_{IM} = \frac{1}{\omega X_{C_{IM}}}$ $= \frac{(1-r_{G_{IM}})}{\omega R_{in_{IL}} \left(Q_{in_{IL}} + \sqrt{r_{G_{IM}} (1+Q_{in_{IL}}^2)} - 1 \right)}$ <p>The calculated value was adjusted in simulation using the link model of Section J.1.</p>
4	Test the designed WPT with the power EPS to check if it is necessary to increase the DC capacitor filter.	We test the system with an equivalent linear power EPS, $V_{ep} = 2V_{DC_{opt}}$ and $R_{SS_{ep}} = R_{DC_{opt}}$. We also test it with the PVSC model of Section J.2.

Source: (The author, 2017)

Table 21 – Design methodology for SsWPT systems.

No.	Description	Equation or Example
1	Calculate the MAE of the link. Also, find the frequency at which it occurs and the associated optimum loads ($Z_{G(L)_{opt}}$). Use the link model or the measured S-parameters of the link.	Considering the RLC model of the link, the MAE and the impedances are: $\frac{1}{MAE} = \left(\sqrt{\frac{1}{A}} + \sqrt{1 + \frac{1}{A}} \right)^2 = \left(\sqrt{\frac{1}{k\omega^2 \frac{L_1 L_2}{R_1 R_2}}} + \sqrt{1 + \frac{1}{k\omega^2 \frac{L_1 L_2}{R_1 R_2}}} \right)^2$
		$Z_{G(L)_{opt}} = R_{G(L)_{opt}} + j \cdot X_{G(L)_{opt}} = \frac{R_{G(L)_{opt}} \left(\frac{X_{C1(2)}}{R_{G(L)_{opt}}} \right)^2}{\left(\left(\frac{X_{C1(2)} + X_{G(L)_{opt}}}{R_{G(L)_{opt}}} \right)^2 + 1 \right)}$ $+ \frac{X_{G(L)_{opt}} \left(X_{C2(1)} X_{G(L)_{opt}} \left(\frac{1}{R_{G(L)_{opt}}^2} + \frac{1}{X_{G(L)_{opt}}^2} \right) + \left(\frac{X_{C2(1)}}{R_{G(L)_{opt}}} \right)^2 \right)}{\left(\left(\frac{X_{C2(1)} + X_{G(L)_{opt}}}{R_{G(L)_{opt}}} \right)^2 + 1 \right)}$ <p>where, $X_{C1(2)} = \frac{1}{\omega C_{1(2)}}; X_{G(L)_{opt}} = -X_{L1(2)},$ and $R_{G(L)_{opt}} = R_{1(2)} \sqrt{1 + A} = R_{1(2)} \sqrt{1 + k Q_1 Q_2} = R_{1(2)} \sqrt{1 + \omega^2 k \frac{L_1 L_2}{R_1 R_2}}.$ Considering the S-parameters, the MAE and impedances can be found using the well-known equations of the microwave theory, which are implemented in the simulator (e.g., MAG, SmZ1, and SmZ2 in ADS[®]).</p>
2	Follow steps 1 to 5 of the design method for SsPA systems in Table 14.	
3	Find the specifications and design the (input, output and inter-stage) impedance matching networks.	Ideal transformer turn ratios: $N_{input} = \sqrt{\frac{R_{DC_{opt}}}{R_{mp}}}, N_{output} = \sqrt{\frac{R_L}{R_{L_{opt}}}}, N_{inter} = \sqrt{\frac{R_{G_{opt}}}{R_{LPA_{opt}}}}.$
4	Design the PA using the input impedance of the inter-stage matching network as load	$X_{LPA_{opt}} \approx R_{LPA_{opt}} + X_{inIS}$
5	Test the designed WPT system with the power EPS to check if it is necessary to increase the DC capacitor filter.	Linear power EPS : $V_{ep} = 2V_{DC_{opt}} \text{ and } R_{SS_{ep}} = R_{DC_{opt}}$

Source: (The author, 2017)

5.5.3 Study Case 1: SsWPT system based on an ideal class-E PA

Using the proposed methodology when the r_L is available, we designed an SsWPT system composed of an indoor PVSC, an inductive link, and an ideal class-E PA. We performed a harmonic balance simulation of this system in ADS[®] software using the models presented in Chapters 3 and 4⁴, and lossless components, that is, ideal capacitors, inductors, and switches. For the link that was optimized in (CABRERA; SOUSA, 2014), which model was discussed in Section J.1, we calculated the link MAE and the related impedances and frequency using the equations proposed in our methodology. Besides, we performed S-parameter and harmonic balance simulations of this link in ADS[®]. Both results were in agreement, as expected. Then we carried out a DC simulation of the PVSC model that we discussed in Section J.2. From the simulation results, we extract the P_{avs} of the indoor PVSC as a function of the illuminance (i.e., L_V) of the light emulator. Figure 77 displays the simulation setup and the resulting function. Also, by using fitting tools, we found an analytical expression for this function, which is:

$$P_{avs} = M_{p1}L_v^3 + M_{p2}L_v^2 + M_{p3}L_v + M_{p4}; \quad (5.54)$$

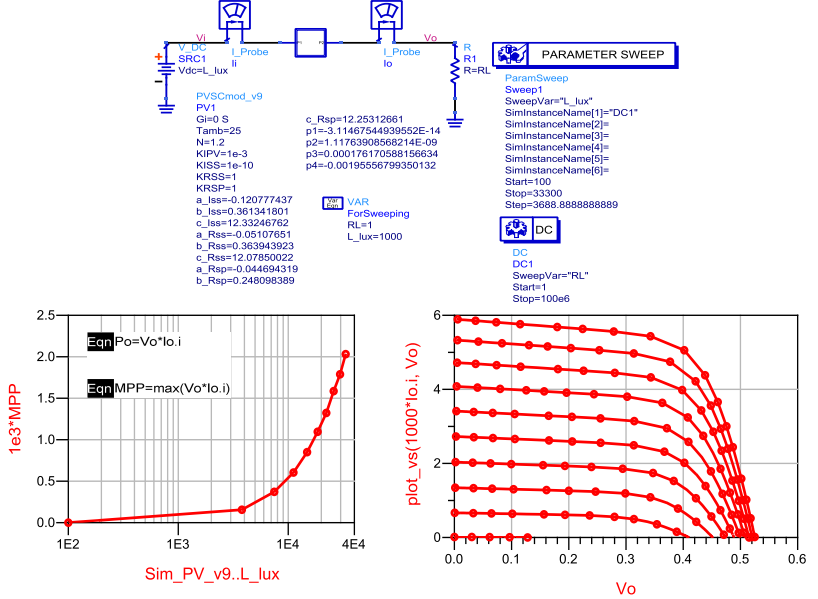
where $M_{p1} = -1.81 \times 10^{-17}$, $M_{p2} = 1.08 \times 10^{-12}$, $M_{p3} = 4.63 \times 10^{-8}$, $M_{p4} = 2.22 \times 10^{-5}$. We verified the accuracy of the fitting process and obtained a root-mean-square error of 1.043×10^{-5} . We used this analytical expression in the rest of the ADS[®] simulations to calculate the η_{PTE} of the systems. Finally, we chose the maximum illuminance (33,300 lux) of the indoor emulator as the nominal environmental condition. Table 23 reports the P_{avs} of the resulting EPS and its related variables.

In this example, the trade-off between the losses in the DC matching network and the PA does not exist. In fact, the ideal class-E PA has 100% of efficiency with any input voltage. Therefore, the $R_{DC_{opt}}$ is the one that maximizes 5.47. Thus, the optimum values of V_{DC} and I_{DC} are V_{mp} and I_{mp} , respectively. To calculate the optimum PA load ($R_{PA_{opt}}$) that maximizes the power transfer efficiency of the SsPA ($\eta_{PTE_{PA}}$), we need to know the $r_{L_{opt}}$ of the PA. Consid-

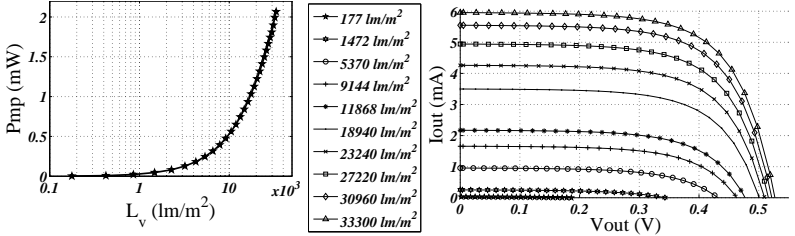
⁴In Appendix J, we summarize the models presented in Chapters 3 and 4 for the indoor PVSC and the inductive link based on PSOI devices. Furthermore, we give the details of its implementation in the ADS[®] software.

Table 23 – Design results of the SsWPT system of study case 1.

Step 1							
f	$Z_{in_{IL}}$	$\frac{X_{in_{IL}}}{\omega}$	$R_{in_{IL}}$	$Z_{L_{IL}}$	$\frac{1}{-X_{L_{IL}} \cdot \omega}$	$R_{L_{IL}}$	MAE
(MHz)	$(\frac{\Omega}{\Omega})$	(nH)	$(\frac{\Omega}{\Omega})$	$(\frac{\Omega}{\Omega})$	(pF)	$(\frac{\Omega}{\Omega})$	(%)
399	1.377+j146.297	58.36	1.377	0.364-j21.747	18.342	364	41.011
Step 2							
f (MHz)	L_v (lux)	R_{mp} (Ω)	I_{mp} (mA)	V_{mp} (mV)	P_{mp} (mW)		
0	33,300	80.1	5.08	407	2.07		
$\eta_{mp_{DC}}$ (%)	$R_{DC_{opt}}$ (Ω)	$I_{DC_{opt}}$ (mA)	$V_{DC_{opt}}$ (mV)	$P_{DC_{opt}}$ mW			
100	80.1	5.08	407	2.07			
$D_{SH}(\%)$	$q\left(\frac{Rad/s}{Rad/s}\right)$	$r_{L_{opt}}$ (Ω/Ω)	$R_{DC_{opt}}$ (Ω)	$R_{PA_{opt}}$ (Ω)			
50	1.4134	0.73353	80.1	109.1			
Step 3							
f (MHz)	$r_{G_{IM}}$	Q_{IL}	C_{IM} (pF)	$Q_{L_{PA}}$	Sim. C_{IM} (pF)	Sim. $Q_{L_{PA}}$	
399	17.19×10^{-3}	104.06	2.419	13.608	2.421	11.89	
Step 4							
f (MHz)	$D_{SH}(\%)$	K_X	K_L	K_C	K_{CB}		
399	50	-0.0039	0.7308	0.6849	1.4617		
$q\left(\frac{Rad/s}{Rad/s}\right)$	C_0 (pF)	Ce(pF)	L_{SH} (nH)	C_{SH} (pF)	C_B (pF)		
1.4134	0.3072	0.3071	31.8335	2.5020	61.6623		

Figure 77 – PVSC I-V characteristic and P_{avs} .

(a) Simulation results.



(b) Measurement results.

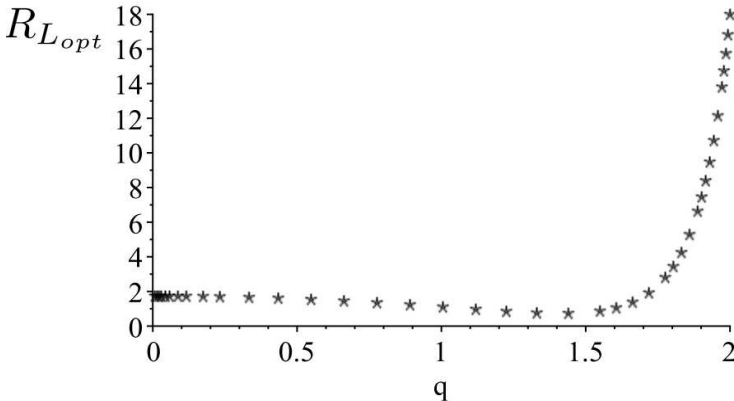
Source: ((a)Adapted from ADS[®] software, 2017; (b) The author, 2017)

ering the ideal Class-E amplifier, there are many possible values. For this example, we set the value of D_{SH} to 0.5 (50%), which is a common choice because it simplifies the design of the RF oscillator and the drive of the PA switch (FAJARDO; SOUSA, 2016c). Figure 78 depicts the respective $r_{L_{opt}}$ as a function of q . We kept the design space of r_L in the range $0 < q < 2$ because low-voltage and high-frequency operation occurs in such interval (ACAR; ANNEMA; NAUTA, 2006). In

addition, we used the mathematical model of Section 5.3.2.3 to generate Figure 78. For the design without an inter-stage network, we needed $r_{L_{\sin IM}} = \frac{R_{DC_{opt}}}{R_{in_{IL}}} = 58.17$, however this value is achieved for q values greater than 2, which correspond to unrealizable components. We chose $q=1.4134$, since this value leads to the minimum L_{SH} that guarantees a switch current always greater than zero and class-E operation. This fact becomes important when the switch is implemented by a unidirectional semiconductor device such as a bipolar junction transistor (BJT). By using $r_{L_{opt}}(0.5, 1.4142)$, we calculated the theoretical optimum value of PA load ($R_{PA_{opt}}$) that maximizes the power transfer efficiency of the SsPA. Moreover, we determined the other values related to this optimum condition. Table 23 summarizes the results.

In this example, the inter-stage impedance matching network must transform the input impedance of the inductive link into $R_{PA_{opt}}$. Furthermore, it must guarantee that the resulting impedance has a high quality factor (for example, $Q_{PAL} > 10$) because the model in Section 5.3.2.3 is accurate only for high- Q loads. Thus, we chose a capacitor in parallel with the link as impedance matching network to maximize the quality factor of the transformed impedance, as shown in Figure 79(b). We calculate this capacitor by the following equation:

Figure 78 – $r_{L_{n_{opt}}}$ for the Class-E PA.



Source: (The author, 2017)

$$C_{IM} = \frac{1}{\omega X_{C_{IM}}} = \frac{(1 - r_{G_{IM}})}{\omega R_{in_{IL}} \left(Q_{in_{IL}} + \sqrt{r_{G_{IM}} (1 + Q_{in_{IL}}^2) - 1} \right)}; \quad (5.55)$$

where

$$r_{G_{IM}} = \frac{R_{in_{IL}}}{R_{LPA_{opt}}}; Q_{in_{IL}} = \left(\frac{X_{in_{IL}}}{R_{in_{IL}}} \right).$$

The resulting quality factor of the transformed impedance is given by:

$$Q_{LPA} = \frac{X_{LPA}}{R_{LPA_{opt}}} = \frac{X_{C_{IM}}}{R_{LPA_{opt}}} \frac{\left(1 - Q_{in_{IL}} \frac{X_{C_{IM}}}{R_{in_{IL}}} + Q_{in_{IL}}^2 \right)}{\left(1 + \left(\frac{X_{C_{IM}}}{R_{in_{IL}}} - Q_{in_{IL}} \right)^2 \right)}. \quad (5.56)$$

We adjusted the capacitor value in the S-parameter simulation. Table 23 presents the calculated and adjusted values.

The class-E PA with a finite DC-feed inductance instead of an RF-choke has been explored in several works (ACAR; ANNEMA; NAUTA, 2007a; SADEGHPOUR; NABAVI, 2014; ACAR; ANNEMA; NAUTA, 2006; FAJARDO; SOUSA, 2016c). This topology is shown in Figure 79(a). To design this PA, we used an expanded version of the class-E design methodology proposed in (ACAR; ANNEMA; NAUTA, 2007a).

We defined q , D_{SH} , Q_{LPA} , $\frac{\Delta V}{V_{CC}}$, R_{LPA} , and ω as input parameters, which can be employed to find the circuit element values (L_{SH} , C_{SH} , C_e , L_0 , C_B) by using a design set of equations. In (ACAR; ANNEMA; NAUTA, 2007a), the authors proposed the following:

$$K_L(D_{SH}, q) = \frac{\omega L_{SH}}{R_{LPA}}; \quad (5.57)$$

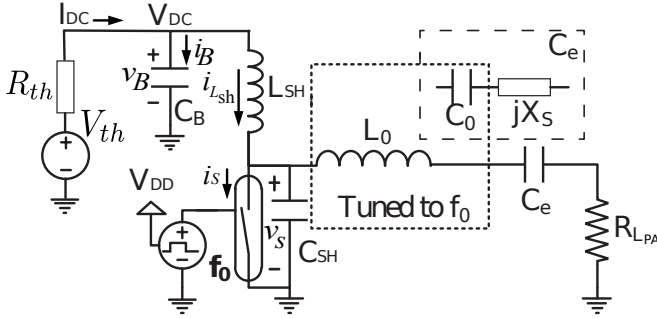
$$K_C(D_{SH}, q) = \omega C_{SH} R_{LPA}; \quad (5.58)$$

$$K_X(D_{SH}, q) = \frac{X_S}{R_{LPA}}. \quad (5.59)$$

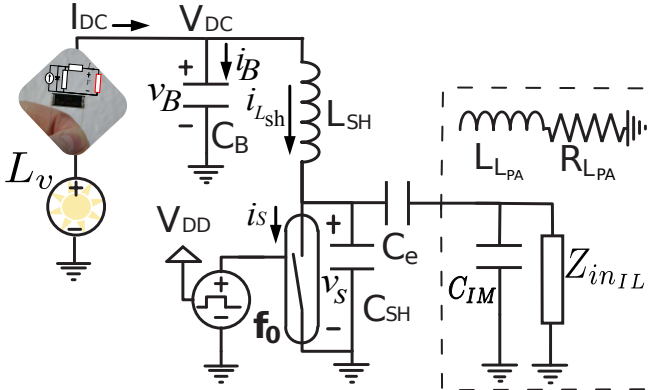
Supposing an ideal switch, we can derive the expression for K_L by assuming that the efficiency of the DC/AC power conversion is 100%. We can easily find the expression for K_C from the definition of q . In order to obtain the analytical expression of K_X , we can use the fundamental quadrature Fourier components of $V_{C_{SH}}(t)$. We implemented this set of equations in the Maple[®] software⁵ according to the model discussed

⁵In Appendix I, we present a tutorial on the implementation of this design set

Figure 79 – Ideal class-E PA with a finite DC-feed inductance.



(a) Powered by a linear power EPS and loaded by a resistance.



(b) Powered by a PVSC and loaded by a link with impedance matching network.

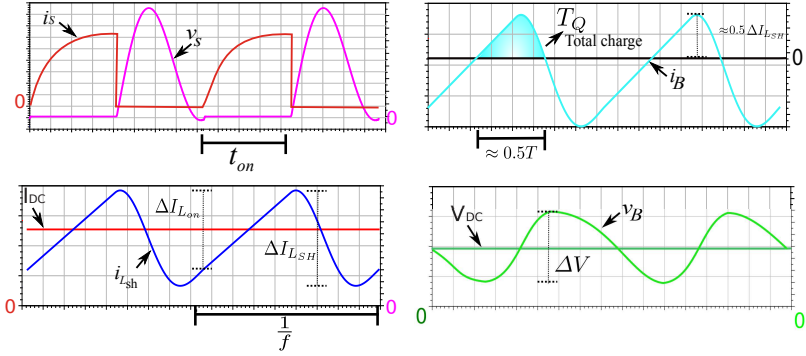
Source: (The author, 2017)

in Section 5.3.2.3.

To calculate the bypass capacitor (C_B), we proposed the “gain” K_{CB} , which is given by:

$$K_{CB}(D_{SH}, q) = \frac{\pi^2}{4\omega} \frac{1}{\left(\frac{\Delta V}{V_{DC}}\right)} \frac{1}{C_B R_{opt}}. \quad (5.60)$$

To find the expression of K_{CB} , we used steady-state and small-ripple approximation (ERICKSON; MAKSIMOVIC, 2001). Considering the cur-

Figure 80 – Approximate waveforms of class-E PA for $D_{SH} = 0.5$.

Source: (The author, 2017)

rent and voltage waveforms in Figure 80, we can estimate the current ripple in L_{SH} by the following expressions:

$$\Delta I_{SH} \approx \Delta I_{on} = \frac{V_{DC}}{L_{SH}} t_{on} = \frac{V_{DC}}{L_{SH}} \frac{D_{SH}}{f} = \frac{2\pi D_{SH} V_{DC}}{\omega L_{sh}} \quad (5.61)$$

where t_{on} is the time in which the switch is in the ON state. Assuming that the signal approaches a triangular wave, we can calculate the total charge approximately by:

$$T_Q = \frac{1}{2} \left(\frac{1}{2f} \right) \left(\frac{\Delta i_{SH}}{2} \right) = \frac{\Delta i_{SH}}{8f}. \quad (5.62)$$

By using Eq. (5.57), (5.61), and (5.62), we found the ripple voltage across C_B as:

$$\Delta V = \frac{1}{C_B} \left(\frac{\pi^2}{4\omega} \frac{V_{DC}}{R_{L_{PA}}} \right) \left(\frac{D_{SH}}{K_L(D_{SH}, q)} \right). \quad (5.63)$$

Finally, from Eq. (5.60) and (5.63), “ K_{CB} ” is given by:

$$K_{CB}(D_{SH}, q) = \frac{K_L(D_{SH}, q)}{D_{SH}}. \quad (5.64)$$

To develop numerical insight into this component design set, we illustrate these “gains” assuming $D_{SH} = 0.5$ in Figure 81(a). From this design set of equations, we can calculate the components of the ampli-

fier as follows:

$$L_{SH} = K_L(D_{SH}, q) \frac{R_{LPA}}{\omega}; \quad (5.65)$$

$$C_{SH} = \frac{K_C(D_{SH}, q)}{\omega R_{LPA}}; \quad (5.66)$$

$$C_e = \frac{1}{(Q_{LPA} - K_X(D_{SH}, q)) \omega R_{LPA}}; \quad (5.67)$$

$$C_B = \frac{\pi^2}{4\omega R_{LPA}} \frac{1}{\left(\frac{\Delta V}{V_{DD}}\right)} \frac{1}{K_{CB}(D_{SH}, q)}. \quad (5.68)$$

$$(5.69)$$

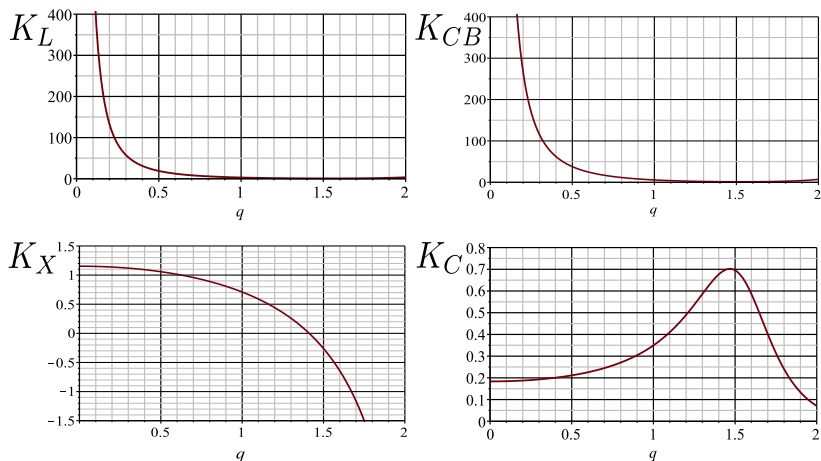
In Table 23, we summarize the design set of this example and the resulting component values. The complete design space is illustrated in Figure 81(b).

Finally, we simulated the SsWPT system as shown in Figure 82. We adjusted C_B to achieve the ripple specification of 10%. The resulting value was 170 pF (instead of the designed value of 61 pF). Table 24 summarizes the simulation results, which indicate that the designed SsWPT system extracts the P_{avs} of the power EPS with a WPT efficiency very close to the WPT MAE. In Figure 82(b), we visualize the simulated waveforms, which confirm class-E PA operation.

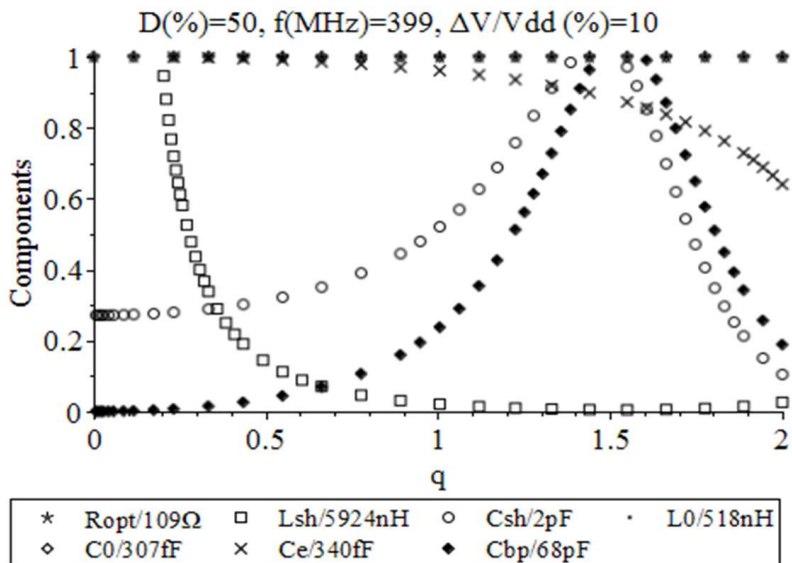
5.5.4 Study Case 2: SsWPT system based on a "real" class-E PA

We chose an array of BFU730F NPN silicon germanium (SiGe) transistors (fabricated by NXP Semiconductors) to implement the switching device because we can optimize this array for low saturation voltage (approximately 140 mV) with an acceptable f_T value (around 7 GHz). For the passive components of the PA and the inter-stage matching network, we used ceramic chip devices, the 0805HP inductors (made by Coilcraft) and the Accu-P capacitors (produced by AVX). To simulate the SsWPT system, we adopted the models presented in Chapters 3 and 4, and the models provided by the manufacturer design kits. We carried out harmonic balance simulations in ADS[®] software.

In this example, we used the same inductive link and power EPS of the previous study case. Thus, there were parameters with the same values. Table 25 displays the results again for clarifying purpose. We

Figure 81 – Component design set and space for $D_{SH} = 0.5$.

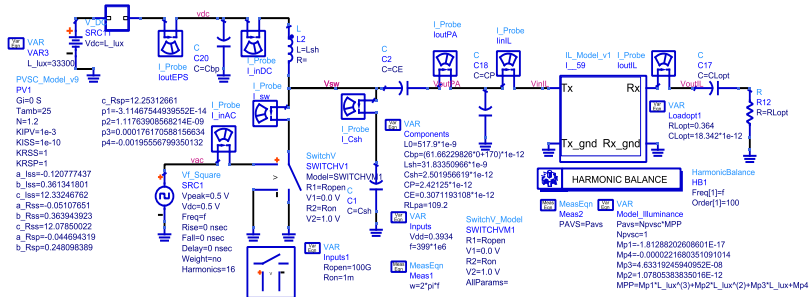
(a) Component design set.



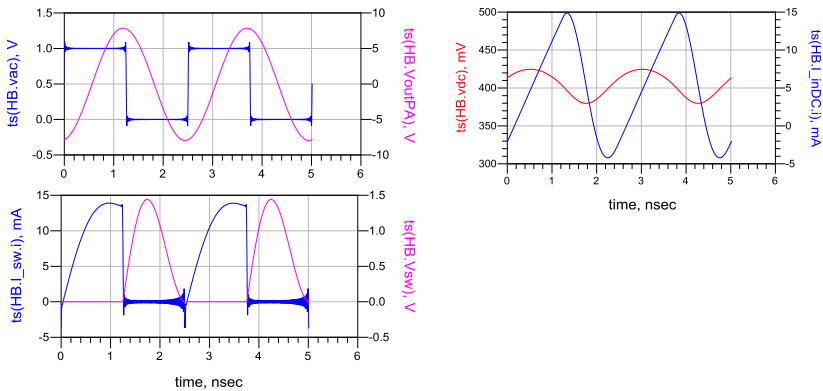
(b) Component design space.

Source: (The author, 2017)

Figure 82 – Simulation setup and PA waveforms for SsWPT system of study case 1.



(a) Simulation setup.



(b) PA waveforms.

Source: (The author, 2017)

Table 24 – Simulation results of study case 1 for $f = 399\text{MHz}$ and $D_{SH} = 50\%$.

Impedances						
EPS load	PA load		Link Z_{in}		Link load	
(Ω)	(Ω)	(nH)	(Ω)	(nH)	(Ω)	(pF)
81.49	109.2	517.9	1.377	58.36	0.364	18.34
Power chain results						
EPS			PA		Link	
P_{avs}	Pout	PinDC	PinAC	Pout	Pin	Pout
(mW)	(mW)	(mW)	(mW)	(mW)	(mW)	(uW)
2.047	2.019	2.019	0	2.016	2.016	827
Efficiencies						
η_{mpp}	η_{PA}	η_{IL}	MAE $_{WPT}$	η_{WPT}	η_{PTEPA}	η_{PTEWPT}
(%)	(%)	(%)	(%)	(%)	(%)	(%)
98.66	99.86	41.01	41.01	40.95	98.52	40.4

use the equivalent inductance of the link as the inductor in the output stage of the class-E PA. Therefore, we performed simultaneously steps 2 and 3 of the methodology in Table ???. First, we found an approximate expression for r_L based on the ideal solution of the class-E PA and η_{PA} . Then we estimated $R_{LPA_{opt}}$ from its expression and the $R_{DC_{opt}}$ calculated in previous steps to maximize η_{mpDC} . Next, we determined the inter-stage matching network from the input impedance of the link ($Z_{in_{IL}}$) and $R_{LPA_{opt}}$.

As in the previous study case, we used a single capacitor to transform the real part of $Z_{in_{IL}}$ ($R_{in_{IL}}$) into $R_{LPA_{opt}}$. We calculated the component design space of the PA from the transformed impedance $Z_{in_{IM}}$, its high-Q load (L_{PA} and R_{PA}) and the design set of equations for the ideal class-E PA. Finally, we evaluated the restrictions on the component values of the design kit that is available for simulation and, depending on the case, kept or changed the default value of q ($q = 1.4134$). Figure 83 shows the resulting design spaces of iterations 1 and 2 of this optimization process. In both iterations, we maintained the default value of q .

The nominal operation of the ideal class-E PA requires zero voltage and zero slope conditions. However, maximum efficiency of a “real” class-E PA occurs out of its nominal operation (SOKAL; MEDI-

Table 25 – Design results of the SsWPT system of study case 2.

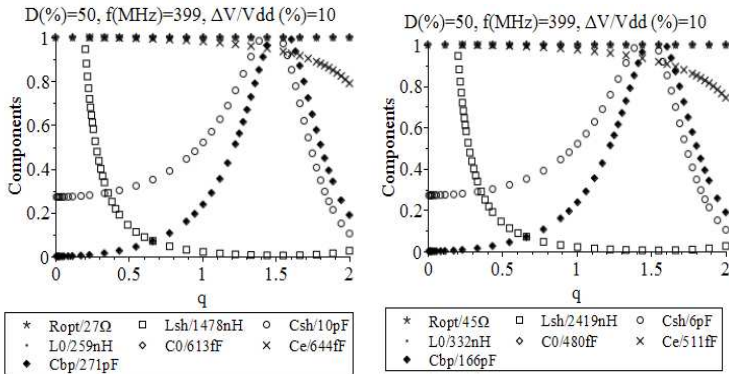
Step 1										
f (MHz)	$Z_{in_{IL}}$ $(\frac{\Omega}{\Omega})$	$\frac{X_{in_{IL}}}{\omega}$ (nH)	$R_{in_{IL}}$ $(\frac{\Omega}{\Omega})$	$Z_{L_{IL}}$ $(\frac{\Omega}{\Omega})$	$\frac{1}{-X_{L_{IL}} \cdot \omega}$ (pF)	$R_{L_{IL}}$ $(\frac{\Omega}{\Omega})$	MAE (%)			
399	1.377+j146.297	58.36	1.377	0.364-j21.747	18.342	364	41.011			
f (MHz)	L_v (lux)	R_{mp} (Ω)	I_{mp} (mA)	V_{mp} (mV)	P_{mp} (mW)					
0	33300	80.1	5.08	407	2.07					
f (MHz)	η_{mpDC} (%)	$R_{DC_{opt}}$ (Ω)	$I_{DC_{opt}}$ (mA)	$V_{DC_{opt}}$ (mV)	$P_{DC_{opt}}$ mW					
0	100	80.1	5.08	407	2.07					
Steps 2 and 3										
D_{SH} (%)	η_{PA} (%)	$r_{L_{\eta}}$ (Ω/Ω)	$r_{L_{opt}}$ (Ω/Ω)	$R_{DC_{opt}}$ (Ω)	$R_{PA_{opt}}$ (Ω)					
50	66.2	1.67	1.66	80.1	48.1					
f (MHz)	$r_{G_{IM}}$	Q_{IL}	C_{IM} (pF)	$Q_{L_{PA}}$	Sim. C_{IM} (pF)	Sim. $Q_{L_{PA}}$				
399	28.62x10 ⁻³	104.6	2.295	13.608	2.248	18.64				
$q^{(*)}$ $\left(\frac{Rad/s}{Rad/s}\right)$	L_{SH} (nH)	Q	C_{SH} (pF)	Q(k)	C_e (fF)	Q(k)	C_{IM} (fF)	Q(k)	C_B (pF)	
1.24	12.36	36	8.4	0.6	500	1.5	2250	1.1	150	
Step 4										
$q^{(*)}$ $\left(\frac{Rad/s}{Rad/s}\right)$	L_{SH} (nH)	Q	C_{SH} (pF)	Q(k)	C_e (fF)	Q(k)	C_{IM} (fF)	Q(k)	C_B (pF)	Q(k)
1.24	12.36	36	8.4	0.6	500	1.5	2250	1.1	321	0.11

Source: (The author, 2017)

ANO, 2013). Therefore, to maximize the PA efficiency, we adopted an optimization process aided by simulation. Figure 84 exhibits the simulation setup and main waveforms. In the same setup, we analyzed both the ideal and the lossy class-E PA. We implemented the ideal amplifier by the switchV component (available in ADS®) with a resistance of 1 m Ω and 100 M Ω in the on and off stages, respectively. The control input of this switch was a pulse-signal source. We used an array of transistors in parallel because there was no transistor optimized for our requirements. Typically, HBT devices are optimized for high-frequency operation (high f_T and $V_{ce_{sat}}$) or low-voltage operation (low f_T and $V_{ce_{sat}}$). In the simulation setup, a single-tone source with an internal impedance of 50 Ω was the input of the transistor array using a driver circuit composed of a resistance of 182 Ω in parallel with a capacitance of 1 pF. The driver design is critical to minimize the transition times in the switching operation of the transistor.

We started the optimization process in each iteration assuming class-E operation. Therefore, we calculated the initial values of the components as the ones used in the design set of the ideal class-E PA. Then we adjusted them to maximize our goals through parametric sweeps of the component values in a predefined order. We proceeded this way because the design kit available in ADS® did not allow optimization algorithms. Tables 26 and 27 summarize the results and goals

Figure 83 – Component design spaces of SsWPT system for study case 2.



Source: (The author, 2017)

Table 26 – Values of circuit elements in the PA optimization.

Name	q (*)	BJT No.	L_{SH} (nH)	Q	C_{SH} (pF)	Q(k)	C_e (fF)	Q(k)	C_{IM} (fF)	Q(k)
$m_i = 0, R_{LPA} = 27.3 \Omega, L_{LPA} = 259 \text{ nF}, Q_{LPA} = 23, \eta_{PA_0} = 50\%$										
Ideal PA	1.41	- -	7.94	-	10.03	-	610	-	2158	-
Ideal PA Opt.	1.41	- -	7.94	-	10.03	-	610	-	2114	-
PA BJT	1.41	1	7.94	-	10.03	-	610	-	2114	-
PA BJT Opt. BJT	1.41	10	7.94	-	10.03	-	610	-	2114	-
PA BJT Opt. C_{SH}	1.56	10	7.94	-	8.20	-	610	-	2114	-
PA L_{SH}	1.37	10	10.28	41	8.20	-	610	-	2114	-
PA L_{SH} Opt. C_{SH}	1.83	10	10.28	41	4.60	-	610	-	2114	-
PA C_e	1.83	10	10.28	41	4.60	-	601	1.4	2114	-
PA C_e Opt. C_{SH}	4.7	10	10.28	41	0.70	-	601	1.4	2114	-
PA C_{SH}	4.7	10	10.28	41	0.70	1.3	601	1.4	2114	-
PA C_{SH} Opt. C_{IM}	4.7	10	10.28	41	0.70	1.3	601	1.4	2118	-
PA C_{IM}	4.7	10	10.28	41	0.70	1.3	601	1.4	2110	0.9
$m_i = 1, R_{LPA} = 44.7 \Omega, L_{LPA} = 325 \text{ nF}, Q_{LPA} = 18.2, \eta_{PA_1} = 65\%$										
Ideal PA	1.41	-	13	-	6.12	-	479	-	2295	-
Ideal PA Opt. C_{IM}	1.41	-	13	-	6.12	-	479	-	2248	-
PA BJT	1.41	1	13	-	6.12	-	479	-	2248	-
PA BJT Opt. BJT	1.41	6	13	-	6.12	-	479	-	2248	-
PA BJT Opt. C_{SH}	1.75	6	13	-	4.0	-	479	-	2248	-
PA L_{SH}	1.79	6	12.36	36	4.0	-	479	-	2248	-
PA L_{SH} Opt. C_{SH}	1.6	6	12.36	36	5.0	-	479	-	2248	-
PA C_e	1.6	6	12.36	36	5.0	-	500	1.5	2248	-
PA C_e Opt. C_{SH}	1.27	6	12.36	36	8.0	-	500	1.5	2248	-
PA C_{SH}	1.24	6	12.36	36	8.4	0.6	500	1.5	2248	-
PA C_{SH} Opt. C_{IM}	1.24	6	12.36	36	8.4	0.6	500	1.5	2241	-
PA C_{IM}	1.24	6	12.36	36	8.4	0.6	500	1.5	2250	1.1

$$*q = \frac{1}{\omega \sqrt{L_{SH} C_{SH}}}$$

Source: (The author, 2017)

of the PA optimization process. In these tables, the identifier *Opt. X* means that the value of component X was optimized by a parametric sweep, and the identifier *PA X* means that the manufacturer model of component X replaced the ideal one. In this example, we needed just one iteration to maximize the PA efficiency. Table 25 shows the component values generated by the optimization process.

Finally, we simulated the WPT system optimized in the previous steps at the nominal illuminance condition (33300 lux) using the PVSC model and its equivalent linear EPS. Figure 85 depicts the respective simulation setups. As expected, all results were very similar.

Table 27 – Performance metrics of the PA optimization.

Name	P_L	R_{DC}	$\eta(\%)$			IL
	(μW)	Ω	MPP	WPT	PA	

$m_i = 0, R_{LPA} = 27.3 \, \Omega, L_{LPA} = 259 \, \text{nF}, Q_{LPA} = 23, \eta_{PA_0} = 50\%.$						
Ideal PA	1381	27	76	24.4	59.4	41
Ideal PA Opt. C_{IM}	3120	20	65	41.0	99.9	41
PA BJT	297	62	98	11.9	29.1	41
PA BJT Opt. BJT	1125	38	87	27.4	66.8	41
PA BJT Opt. C_{SH}	1165	37	86	27.7	67.6	41
PA L_{SH}	1059	37	87	25.6	62.5	41
PA L_{SH} Opt. C_{SH}	1119	37	86	26.5	64.7	41
PA C_e	879	43	91	24.4	59.4	41
PA C_e Opt. C_{SH}	927	44	91	26.1	63.6	41
PA $C_e C_{SH}$	927	43	91	26.1	63.5	41
PA C_{SH} Opt. C_{IM}	1006	40	89	26.0	63.1	41
PA C_{IM}	772	49	94	24.5	64.9	41

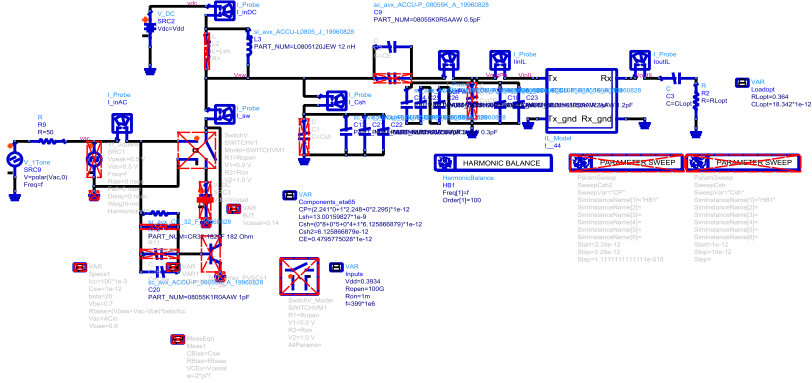
$m_i = 1, R_{LPA} = 44.7 \, \Omega, L_{LPA} = 325 \, \text{nF}, Q_{LPA} = 18.2, \eta_{PA_1} = 65\%.$						
Ideal PA	659	56	97	24.0	58.6	41
Ideal PA Opt.	1895	33.5	99	41.0	99.9	41
PA BJT	338	83.2	100	18.2	44.3	41
PA BJT Opt. BJT	698	60	98	27.2	66.3	41
PA BJT Opt. C_{SH}	739	61	98	29.0	70.8	41
PA L_{SH}	736	59	98	27.9	67.9	41
PA L_{SH} Opt. C_{SH}	713	59	98	27.3	66.7	41
PA C_e	795	52	95	26.6	64.9	41
PA C_e Opt. C_{SH}	674	64	99	27.7	67.7	41
PA C_{SH}	560	75	99	27.2	66.4	41
PA C_{SH} Opt. C_{IM}	661	64	99	27.5	67.1	41
PA C_{IM}	479	81	100	25.1	66.2	41

Source: (The author, 2017)

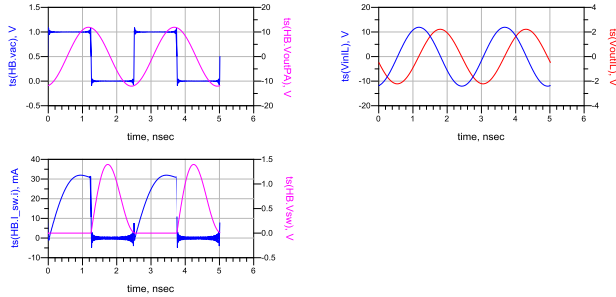
We adjusted the value of C_B to achieve the voltage ripple specification of 10%. Table 25 presents the final components of the designed WPT, and Table 28 outlines the simulation results. We note that the designed PA extracts the P_{avs} of the power EPS with a high drain efficiency. However, the methodology does not guarantee the MAE operation of the converter because the PA efficiency is less than its MAE,

which is 100%.

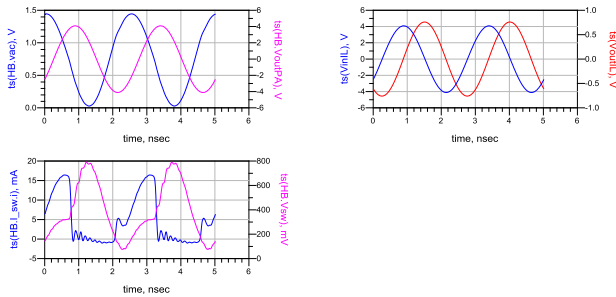
Figure 84 – Simulation setup and waveforms of the SsWPT system for study case 2.



(a) Simulation setup.



(b) Waveforms of ideal class-E PA, $m_i = 1$.



(c) Waveforms of lossy class-E PA, $m_i = 1$.

Source: (The author, 2017)

Table 28 – Simulation results for study case 2, $f = 399$ MHz and $D_{SH} = 50\%$.

Impedancies						
EPS load	PA load		Link Z_{in}		Link load	
(Ω)	(Ω)	(nH)	(Ω)	(nH)	(Ω)	(pF)
81.64	48.91	334.2	1.377	58.36	0.364	18.34
Power chain results						
EPS		PA			Link	
P_{avs}	Pout	PinDC	PinAC	Pout	Pin	Pout
(mW)	(mW)	(mW)	(μ W)	(mW)	(mW)	(μ W)
2.047	2.019	2.019	285	1.255	1.162	477
Efficiencies						
η_{mpp}	η_{PA}	η_{IL}	MAE_{WPT}	η_{WPT}	$\eta_{PTE_{PA}}$	$\eta_{PTE_{WPT}}$
(%)	(%)	(%)	(%)	(%)	(%)	(%)
99.99	64.96	41.01	41.01	24.67	98.52	24.66

Source: (The author, 2017)

ing example that considers a low-power and high-frequency context. In such situation, the assumption that the parasitic losses do not impact frequency optimization is not valid. Besides, this simplification is only accurate in circumstances defined by the absolute value of the operation frequency of the system and the P_{avs} of the harvester. Therefore, we adapted the methodology by using intensive simulation work and an iterative approach. However, we defined the operating frequency as an input of the method that is imposed by the optimization result of the inductive link. Thus, the optimized system is a suboptimal solution (a local maximum instead of the global one). Consequently, we can improve the methodology in a way that involves the operation frequency as an output of the optimization process instead of an input.

With the aim of easing the mathematical analysis, we used an approximate expression of the R_L of the class-E PA with finite DC-feed inductance. However, this simplification depends on intensive simulation work to optimize the lossy class-E PA. In the scholarly literature, the conventional time-domain mathematical analyses of this circuit assume zero switch on-resistance and ideal passive components. Moreover, none takes lossy passive components into account, and only a few analytical approaches consider switch on-resistance (ACAR; ANNEMA;

NAUTA, 2007b). Therefore, there is a modeling hiatus that must be solved to decrease the complexity of methodology proposed here.

We investigated parallel solar cells as the source of the system using the methodology proposed in this chapter. Table 29 highlights the primary results. Maintaining the same link and switch implementation (HBT technology), as we increased the number of PVSC, the energy density of the implanted device increased as well and η_{PTEWPT} decreased. This occurs because the parasitic losses increase as a result of higher current density across the switch and passive components. We also performed tests with series connection of PVSC. As expected, this approach increased the efficiency of the PA but the maximum number of devices is significantly limited by the breakdown voltage of the switch. We simulated an equivalent linear power EPS instead of the PVSC series array due to limitations of the PVSC model implemented in ADS.

Table 29 – Main results of optimized photovoltaic SsWPT systems.

PVSC No.	HJT No.	Efficiencies (%)			Power (mW)		Area (mm ²)		$D_W(\frac{\mu W}{mm^2})$	
		η_{mp}	η_{WPT}	η_{PTEWPT}	P_{avs}	P_{outLL}	Tx	Rx	Tx	Rx
4	15	98.86	21.481	14.741	8.188	1.207	616	30.3	13.29	39.90
2	10	99.01	26.636	18.832	4.094	0.771	308	30.3	13.29	25.49
1	6	99.99	24.67	23.302	2.047	0.477	154	30.3	13.29	15.77

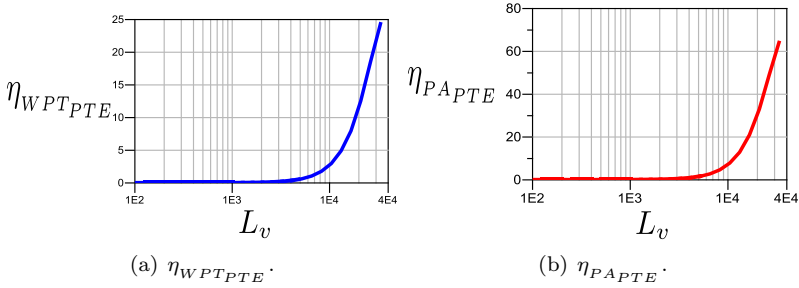
Source: (The author, 2017)

In addition, we evaluated the performance of the WPT system under non-nominal environmental conditions. Figure 86 shows the η_{PTE} of the simulated systems. The designed SsWPT system has an acceptable efficiency (>10%) only for a restricted illumination range ($L_v > 20,000$ lux). Hence, we conclude that the proposed methodology is limited to a fixed environmental condition. To adapt the WPT system to the optimum impedance of the harvester under arbitrary environmental conditions, the R_{DC} of the PA must be a non-linear impedance (an exponential function). This behavior cannot be achieved by a class-E PA because its R_{DC} is approximately a linear resistor.

5.7 CONCLUSION AND CONTRIBUTIONS

In this chapter, we proposed a design methodology for a generic SsPA, and extended it to SsWPT systems. We designed, implemented and measured an SsPA based on a class-A PA. The results demonstrate that the designed PA extracts the maximum available power from the

Figure 86 – Performance metrics of the SsWPT system and SsPA under non-nominal operation.



Source: (Adapted from ADS[®] software, 2017)

source with maximum efficiency. Furthermore, we designed and simulated an SsWPT system composed of a “real” indoor PVSC, class-E PA and inductive link. The simulated SsWPT system achieves a maximum energy density of $39.67 \mu\text{m}/\text{mm}^2$, with an approximate area of the external WPT transmitter and implanted device of 61.6 and 30.6 mm^2 , respectively. As minor contributions developed in this chapter, we presented analytical equations of the impedances for simultaneous impedance matching of the inductive link from its RLC model. We proposed η_{mp} as FoM of the power extracted from the harvester. Also, we adapted concepts of the traditional theory of microwave amplifiers to model the power chain of a generic SsWPT system.

At last, this chapter discussed an open challenge on EPS, energy converters (PAs), and circuits that can take advantage of the use of power specifications instead of predefined voltage or current requirements.

6 CONTRIBUTIONS AND FUTURE WORK

6.1 CONTRIBUTION

One of the RFIC Research Group goals is to research and develop architectures and design methodologies for implanted WBAN nodes with energy autonomy for biomedical applications. In this research work, we focused on the modeling of SsWPT systems. More specifically, we systematically analyzed the different trade-offs, and we proposed a method to maximize the available power of the system. We applied this method to a SsWPT system composed of an indoor PVSC, a class-E PA, and an efficient inductive link. The resulting simulated SsWPT system is compared with some selected references in Table 30. This table shows that the proposed SsWPT system provides the highest power density when considering only the systems powered by ambient energy. Therefore, it can provide energy autonomy to low-power systems with loads as pacemakers, for example.

6.2 SPECIFIC CONTRIBUTIONS

We presented the specific contributions of this work in the final section of each chapter. However, we are going to discuss them briefly in the next paragraph to highlight the main original contributions of our research. that is, the ones that in our opinion will generate a new perspective on the modeling approach of autonomous systems.

In chapter 2, we proposed the Energy Power Source concept that allows us to discuss the SoA of SsWPT systems for WBAN applications. With this concept in mind, we modeled energy carriers, harvesters, and conventional energy sources using a circuit approach to capture the energy flow in the system. Next, in chapter 3, we proposed and validated a novel model of indoor PVSCs for harvesting applications. The main contributions of this modeling approach are the use of illuminance instead of irradiance and the use of worst-case instead of nominal-case. These model choices provided a new perspective on the modeling of PVSC that is more coherent with the indoor environmental conditions and the harvesting applications. In Chapter 4, we discussed and evaluated a lumped circuit model for Planar Square One-turn Inductors. This chapter shows that a lumped model can be used to design the inductive link instead of EM simulation, with low impact on the results

accuracy. However, the main contribution of this chapter is to solve the metrology problem of the experimental characterization of high- Q inductors up to its SRF. Finally, in Chapter 5, we proposed a design methodology to maximize the power transfer efficiency that adapted some concepts of the conventional theory of microwave amplifiers. The main contribution of this chapter is the exploration of a new design paradigm that is based on the power interactions among the subsystems instead of voltage and current ones. This was possible thanks to a novel PA modeling approach that we also proposed in Chapter 5.

6.3 FUTURE WORK

In the discussion section of each chapter, we identified the open challenges that could be used to inspire further research. In this section, We are going to present them briefly in the next paragraphs. In our opinion, them challenges could generate new research topics in the context of the modeling of autonomous systems.

In the PVSC model proposed in chapter 3, there is some error on the measured data that cannot be explained by the influence of the non-regulated temperature. The impact of the low-internal isolation of the opaque enclosure and other physical phenomena that could be affecting the results must be studied further to model the PVSC devices with high accuracy under illuminance lower than 177 lux. We presented only one study as proof of concept of the model methodology. However, more study cases must be analyzed and explored to validate our approach. Besides that, the search of functions that can be used to fit the experimental data to an analytical model is an open challenge that we did not study for PVSC arrays. Also in this chapter, we found that the standard approach that considers as constant the relationship between the V_{mp} and the V_{oc} in PVSC devices does not apply when the illuminance variation is more than a decade. This finding must be confirmed with more study cases.

In chapter 4, we cannot experimentally evaluate the model regarding its capacity of predicting the input impedance of the inductor until its SRF. This metrology problem is related to the inaccuracy of the test setup in RF due to impedance mismatch (i.e., the system does not have an impedance close to the VNA ports impedance, that is 50 Ω). Therefore, some circuit solution could be explored in future research to complete the empirical evaluation of the model.

Chapter 5 discusses the first steps on the modeling for maximiz-

ing the power available of the WPT systems. It is a pioneer research that should be worked further. For instance, the proposed methodology could be upgraded to maximize the performance of the WPT system under the complete range of environmental conditions instead of the non-nominal ones only. This approach requires a dynamic adaptation of the harvester load to the impedance that extracts the P_{avs} . As another example, we designed optimum SsWPT systems that shifted the power maximization plane from the load plane of the harvester to the load plane of the WPT interface. However, this method could be extended (consider the AC/DC converter of the implanted device) to maximize the available power that the power chain can supply to the biosensor. As a final example, an analytical expression of the R_L of the Classe-E PA with finite DC-Feed inductance is not reported in the literature analyzed. This modeling lag must be solved in future works to avoid the use of hard simulation in the optimization process.

6.4 ASSOCIATED PUBLICATIONS

We published articles in conferences and journals that reflect some of the main contributions of this research work. These publications are listed below grouped by the chapter to which they relate.

1. *Chapter 2*:

- (a) A taxonomy for learning, teaching, and assessing wireless body area networks. **Conference:** LASCAS2016.
- (b) Revisiting battery modeling using the energy power supply concept.(FAJARDO; SOUSA, Florianopolis, Brasil. 2016)
Conference: IBERCHIP2016.

2. *Chapter 3*: Simple modeling of photovoltaic solar cells for indoor harvesting applications.(JAIMES; SOUSA, 2017). **Journal:** Solar Energy, the official journal of the international solar energy society.

3. *Chapter 4*: On the characterization of high-Q planar inductors up to its self-resonance frequency for wireless power transfer applications. **Submitted under journal review:** IEEE Microwave and Wireless Components Letters.

4. *Chapter 5*:

- (a) Revisiting the power-efficiency trade-off on a DC voltage source. **Conference:** LASCAS2016.
- (b) Simple expression for estimating the switch peak voltage on the class-E amplifier with finite DC-feed inductance.(FAJARDO; SOUSA, 2016c). **Conference:** LASCAS2016.
- (c) Modeling and design of high-efficiency power amplifiers fed by limited power sources.(FAJARDO; SOUSA, 2016b). SBCCI2016.
- (d) Integrated CMOS class-E power amplifier for self-sustaining wireless power transfer system.(FAJARDO; SOUSA, 2016a). **Conference:** SBCCI2016.

Table 30 – Comparison of in-body harvesting sources uniformly distributed.

References	(GHOVANLOO@ABRERA; ATLURI, 2007)	(SOUSA, 2016)	(LIU et al., 2014)	(GOTO et al., 2001)	This work
	2007	2015	2014	2001	2017
WPT technique	Near-field inductive coupling	EM mid-field	EM far-field	Optical powering	EM mid-field
Type of source	Artificial	Artificial	Artificial	Artificial	Natural
Frequency or wavelength	1 MHz	986 MHz	2.45 GHz	735 nm	399 MHz
Implanted size	10 cm ²	2.25 mm ²	32mm ²	0.6cm ²	30.3cm ²
Distance $T_x - R_x$	10 mm	15 mm	20 cm	10 mm	15 mm
Medium	Air	Air	Liquid skin	Chicken skin	Air
Energy source	External AC	External RF	External Antenna	External Laser	Indoor PVSC (154mm ² @33300lux)
Harvested P	-	0.4 mW	25.1 μ W	-	477 μ W
Harvested D_W	800 μ W/mm ²	180 μ W/mm ²	0.78 μ W/mm ²	10 μ W/mm ²	15.77 μ W/mm ²
Harvester	Inductor	Inductor	Antenna	PVSC	Inductor

References	(VENKATASUBRAMANIAN et al., 2007)	(BEREUTER et al., 2017)	(OZERI; SHMILOVITZ, 2010)
	2007	2017	2010
WPT technique	Thermal	Light	Ultrasonic powering
Type of source	Natural	Natural	Artificial
Frequency or wavelength	-	0-3000 nm	673 kHz
Implanted size	138 mm ²	3.53 cm ²	3.54cm ²
Distance $T_x - R_x$	-	-	5 mm
Medium	-	Skin optical emulator	water
Energy source	Gradient (2 K)	Indoor H.L.	Outdoor H.L.
Harvested P	-	45 μ W	164 μ W
Harvested D_W	10 μ W/mm ²	0.13 μ W/mm ²	0.47 μ W/mm ²
Harvester	TEG	PVSC	PVSC

Source: (The authors, 2017)

APPENDIX A – A brief survey of WBAN

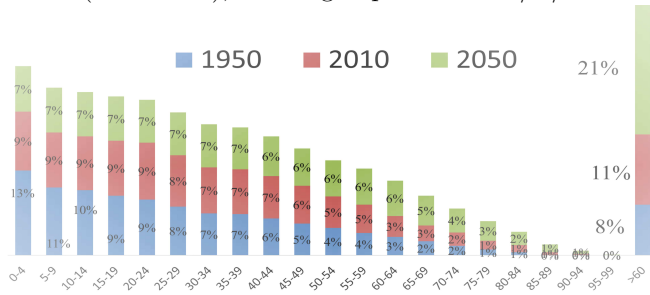
Wireless body area networks (WBANs) have recently gained attention, mainly after the IEEE 802.15.6 standard was proposed. Reviewing the literature, we easily recognize that different authors use different terms for the same concept, or the same term for different concepts. This generates confusion and blocks fair comparisons of different systems. In this appendix, we present an overview of WBANs with a focus on the applications. Moreover, we propose a detailed taxonomy that could help to disambiguate the confusion regarding current WBAN terminology.

A.1 INTRODUCTION

The world's population is growing quickly; from 1950 to 2010 the population increased by around 4,390,405,000 individuals (UNDESA-POPULATION-DIVISION, New York, United Nations Department for Economic and Social Affairs (UN DESA), Working Paper No. ESA/P/WP. 228, 2013). Further, human life expectancy has increased, in the same period: the elderly population (60 years old or older) augmented by about 410,647,596 individuals, representing a change from 8% to 11.1% in their percentage of the population (UNDESA-POPULATION-DIVISION, New York, United Nations Department for Economic and Social Affairs (UN DESA), Working Paper No. ESA/P/WP. 228, 2013). The proportion of the elderly is expected to double over the next four decades, as we can see from Figure 87. It is expected that this increase will overload health-care systems. To face this challenge, new scalable solutions centered on reducing the cost of supporting older adults must be found. On the other hand, millions of people develop chronic or fatal diseases every year, and around 80% of health-care system spending is on chronic condition management (JOVANOVIĆ; MILENKOVIC, 2011). Moreover, as shown in (ORGANIZATION, 2009), most diseases could be prevented if they were detected in their early stages. Therefore, future health-care systems must concentrate efforts on the early detection and prevention of illness. Additionally, there is increasing recognition that remote monitoring should be employed to diminish mortality and the costs of hospitalization and transport (BUI; ZORZI, 2011).

To achieve health-care systems connected at the person-level, at least a network which can be wearable, or implanted in the human body, is needed (MOVASSAGHI et al., 2014). Such networks are commonly referred to as Wireless Body Area Networks (WBANs) (MOVASSAGHI et al., 2014; WANG et al., 2013; IEEE, 2012; BARAKAH; AMMAD-UDDIN,

Figure 87 – World’s age pyramid. Based on (UNDESA-POPULATION-DIVISION, New York, United Nations Department for Economic and Social Affairs (UN DESA), Working Paper No. ESA/P/WP. 228, 2013)



Source: (The author, 2014)

2012; KHAN et al., 2012; DOLATABADI; PRIMAK, 2011; LI; HAMAGUCHI, 2011; LATRÉ et al., 2011). Typically, a WBAN interacts with other wireless technologies (i.e., WSNs, WLAN, WPAN) to provide a complete TI platform for connecting health care services. As an example, (FAJARDO; SOUSA, 2016b) proposed a system concept where a WBAN node transfers energy and receives information from an implanted device. This system is shown in Figure 88. To achieve energy autonomy, the WBAN node harvests energy from the body environment (e.g., solar and thermal). This energy is transferred through an inductive link to the passive implanted device, which answers with the biomedical data. These data could be used to achieve the goal of the specific application. For example, if any abnormalities are found, an alarm can notify the patient or the doctor through email or short message service (SMS) if the gateway of the WBAN node has at least 3G connectivity.

WBANs are expected to cause a dramatic shift in how people behave, in the same way the Internet did. However, technical and social challenges must be faced before a natural adoption (MOVASSAGHI et al., 2014). We are in the “early years” of networks in, on, and around the human body. There are many researchers, companies, professionals, students, and consortiums developing products for this type of network (JOVANOV; MILENKOVIC, 2011; BUI; ZORZI, 2011; MOVASSAGHI et al., 2014; BECHER et al., 2010; CARROLL et al., 2007), because of the wide range of applications (e.g., military, ubiquitous health-care, sport, entertainment, etc.). Since people with different skills and academic background are working on this subject, the information about the topic is sometimes difficult to understand, mainly due to the lack

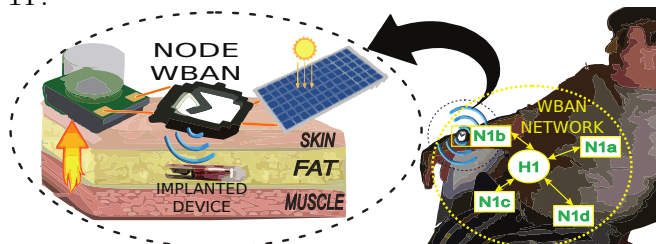
of standardization. It is common to find different terminologies associated with a single subject. As an example, terms as Body sensor Network, Human Body Network, Micro Personal Area Network, Wearable Body Area Network, and Medical Body Sensor Network, are all used as synonymous for Wireless Body Area Network.

The fundamental purpose of this appendix is to analyze the recent literature on WBANs, focusing on applications and network properties, and to achieve a coherent taxonomy for WBANs. Further, we present an intuitive and comprehensive comparison with other wireless networks.

A.2 WBAN FUNDAMENTALS

In the context of the WBAN, the technical requirements, such as data rate, duty cycle per device per time, power consumption, latency, and privacy, are specific for each application (MOVASSAGHI et al., 2014; JUNG; AKBAR; SUNG, 2012). Further, in some applications, the WBAN is only a single piece of the Information Technology (IT) infrastructure, and all the system specifications determine the WBAN requirements (BUI; ZORZI, 2011). In this section, we summarize the applications of WBAN based IT systems as reported in (JOVANOV; MILENKOVIC, 2011; BUI; ZORZI, 2011; MOVASSAGHI et al., 2014; IEEE, 2012; BARAKAH; AMMAD-UDDIN, 2012; LATRÉ et al., 2011; CHEN et al., 2011; FANG et al., 2011; YOO; HOOF, 2010; FALK; MAIER, 2013), then we present an intuitive and comprehensive comparison with other wireless networks used in complex IT systems. Finally, we present a typical communication architecture for IT systems based on the WBAN.

Figure 88 – Self-sustaining implanted device using Energy Harvesting and WTP.



Source: (The author, 2014)

A.2.1 Applications of WBANs

The range of WBAN applications is wide, but the IEEE 802.15.6 standard categorizes them into medical and non-medical. Medical applications of WBANs can be employed for: a) medical treatment, monitoring, and diagnosis; b) prevention of medical accidents; c) remote health/fitness monitoring; d) disability assistance; e) safeguarding of the uninformed (e.g., a WBAN can monitor the level of toxins in the air and warn firefighters or soldiers when a life-threatening level is detected); f) remote control of medical devices; g) telemedicine systems. Non-Medical WBAN applications include a) training schedule of professional athletes; b) consumer electronics; c) advanced human-computer interfaces, such as a neural interface, gaming consoles, and virtual reality; d) personal information sharing (i.e., private or business information can be stored in body sensors for many daily life applications such as shopping and information exchange); e) secure authentication; f) non-medical emergency alert (e.g., emergency detection such as a fire at home).

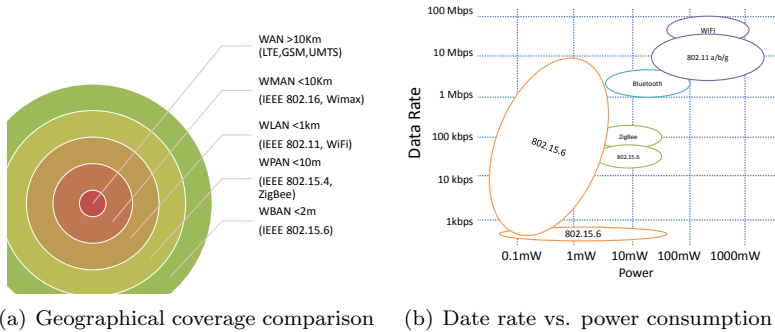
A.2.2 Comparison of a WBAN with other wireless networks

Typically, wireless networks can be categorized based on their geographical coverage, data rate, and power consumption. In Figure 89 the WBAN (IEEE 812.15.6) is compared with other wireless networks, such as Wireless Personal Area Networks (WPAN), Wireless Local Area Networks (WLAN), Wireless Metropolitan Area Networks (WMAN), Wireless Wide Area Networks (WWAN), Zigbee, IEEE 802.15.4, and Bluetooth.

In several works, Wireless Body Area Networks are considered as a particular type of a Wireless Sensor Network (WSN) or a Wireless Sensor and Actuator Network (WSAN), with their own requirements. However, traditional sensor networks do not tackle the specific challenges associated with the interaction between the network and the human body. For example, the implanted sensors have a small form factor resulting in a greater need for energy efficiency. Further, if the data consists of medical information, the reliability of the network must be guaranteed. Other examples are wearable sensor nodes: they can move with respect to each other, e.g., a sensor node placed on the wrist moves relative to a sensor node attached to the hip. Therefore the system requires mobility support. Additionally, the WBAN nodes are

heterogeneous, i.e., they have dissimilar: data rates, power consumptions, and latency (YOO; HOOF, 2010). In brief, although the challenges faced by WBANs are in many ways similar to those presented by WSNs, there are intrinsic differences between them, requiring special attention (LATRÉ et al., 2011). A schematic view of conventional network challenges in WBANs, WSNs and WLANs is presented in Figure 90. It is important to clarify that the illustrated challenges do not involve human compatibility, which is important only in WBAN technologies. The IEEE 802.15.6 overcomes the constraints of the WBAN technologies as its focus is specifically on networking within and around the body (MOVASSAGHI et al., 2014; IEEE, 2012).

Figure 89 – Wireless network comparison.



(a) Geographical coverage comparison (b) Date rate vs. power consumption

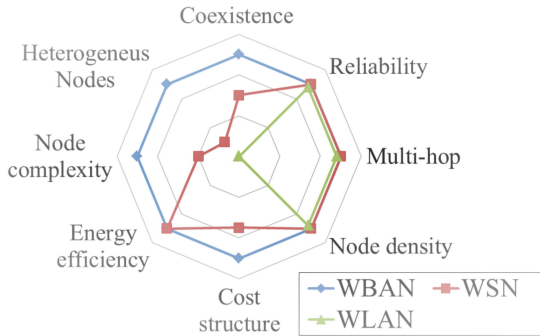
Source: (MOVASSAGHI et al., 2014)

A.2.3 Simplified architecture of a WBAN

A.2.3.1 Isolated WBAN

Unlike WSNs that normally operate as autonomous systems, a WBAN seldom works alone (CHEN et al., 2011). An isolated WBAN is a wireless network composed of different types of nodes. The IEEE 802.15.6 standard considers two possible topologies: one-hop or two-hop star topology with one node in the center of the star (IEEE, 2012). In terms of their functionality, the nodes are classified as coordinator, end, and relay nodes. A coordinator transmits and receives information from and to the end nodes and the relay nodes (sensors and actuators) and handles the interaction with other users (e.g., display or external

Figure 90 – Schematic view of conventional network challenges in WBANs, WSNs and WLANs. Based on (ZASOWSKI, Dept. Elect. Eng, Ph.D. thesis, Federal Institute of Technology (ETH), Zurich, Switzerland, 2007)



Source: (The author, 2014)

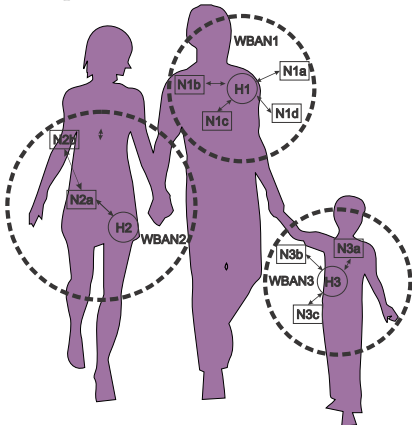
gateway). One difference between the end nodes and the relay nodes is that the relay node may transfer messages to the end nodes or to the coordinator. On the other hand, concerning the implementation, the nodes are classified as: implant node (in body), body surface node (0–2 cm away from the body) and external node (around 2–5 cm away from the body). In Figure 91 some of the possible implementation scenarios of these topologies are shown.

A.2.3.2 IT solution based on WBAN

Figure 92 illustrates the general architecture of a WBAN based health monitoring system. Typically, the generic communication process can be separated into three different tiers, as follows: Intra-WBAN communication (Tier 1), Inter-WBAN communication (Tier 2) and Beyond-WBAN communication (Tier 3) (CHEN et al., 2011). In Tier 1, the internal WBAN communication between nodes takes place (IEEE 812.15.6). The communication going on in Tier 2 is used to interconnect the WBAN with various networks that are easy to access in daily life, such as the Internet and cellular networks. The communication process takes place between the coordinator node of the WBAN and one or more access points (APs). Compared to intra-WBAN communications, wireless technologies for inter-WBAN communication are mature and

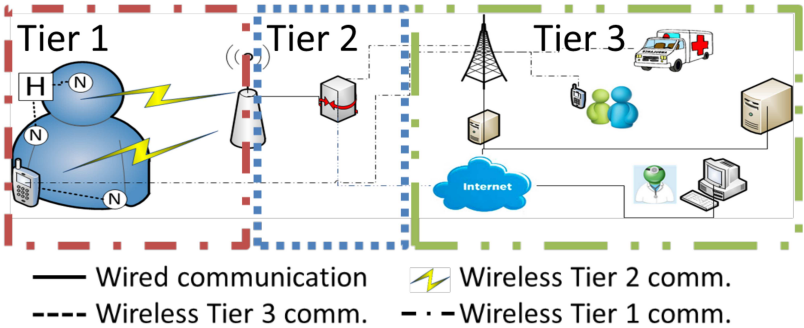
include: WLAN, Bluetooth, Zigbee, cellular, 3G, etc. Tier 3 communications are used to achieve the goal of the specific application and should be adapted to the requirements of user-specific services. For example, if any abnormalities are found based on the up-to-date body signal transmitted to the database, an alarm can notify the patient or the doctor through email or short message service (SMS), therefore in this example we need at least 3G.

Figure 91 – Simplified architecture of an isolated WBAN



Source: (The author, 2013)

Figure 92 – Simplified architecture of a medical TI solution based on WBAN.



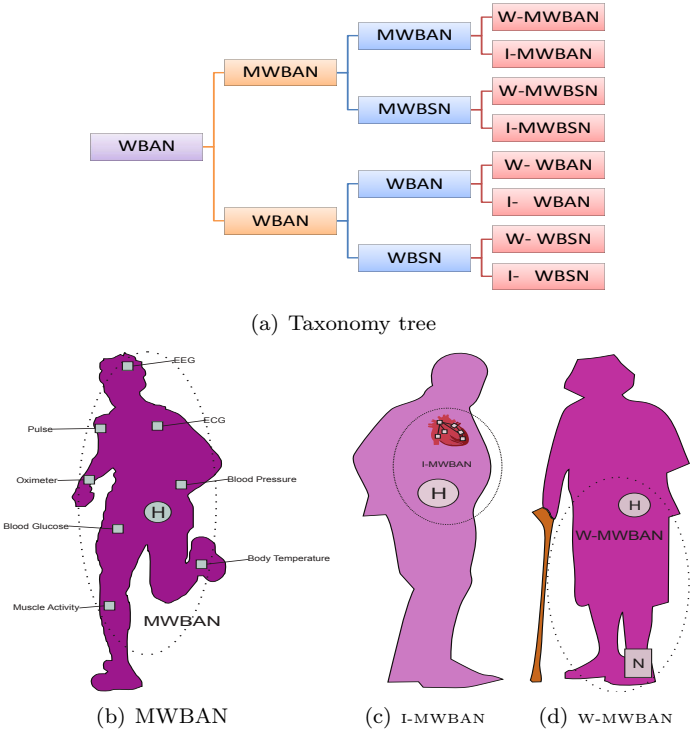
Source: (CHEN et al., 2011)

A.3 A PROPOSED TAXONOMY FOR WBANS

Based on the analyzed literature, we propose some definitions for the most common types of WBAN networks. First, we lay down that a wireless body area network is a wireless network composed of sensor/actuator nodes (N) and hubs (H), which operates in, on, or around the body (but not limited to human bodies), and supports a variety of medical and non-medical applications. This definition is based on (MOVASSAGHI et al., 2014; IEEE, 2012; BARAKAH; AMMAD- UDDIN, 2012; LATRÉ et al., 2011; CHEN et al., 2011; BAE et al., 2011), where BAN and WBAN are used as synonyms. From our point of view, a WBAN is a subcategory of BAN. Additionally, special cases of a WBAN are defined as follows: 1) When all nodes are sensors in a WBAN, the network is called a Wireless Body Sensor Network (WBSN) in agreement with (YANG, 2006; LO; YANG, 2005; LI; TAN, 2010; OTTO; JOVANOVIĆ; MILENKOVIC, 2006; HAO; FOSTER, 2008). 2) When all the nodes (N) and hubs (H) are on the human body, the networks are categorized as wearable (W-WBAN and W-WBSN), as found in (LEONOV, 2011; TUFAIL; ISLAM, 2009). On the other hand, if some N or H are in the human body, the network is referred to as implanted (I-WBAN and I-WBSN), as found in (HAO; FOSTER, 2008; KOHNO et al., 2008; CHUNG; LEE; JUNG, 2008; XING; ZHU, 2009).

WBANs have many applications, but the medical field is perhaps the most important. There are many players working to develop products that will change the medical paradigm of prognosis and treatment. In this scenario, the WBAN must be explored, developed, and implemented in a specific framework (legal, safety, ethics, etc.). The Medical Wireless Body Area Network (MWBAN) is a wireless communication technology designed for electro-monitoring and electro-stimulating the human body wirelessly, through tiny nodes/actuators in, on, or around the body. This definition is based on (FANG et al., 2011; ZHEN; LI; KOHNO, 2007; WANG et al., 2007, 2013). Following the definitions presented in the previous paragraph, it is possible to define Medical Wireless Body Sensor Networks (MWBSN), wearable MBAN (W-MWBAN), wearable MBSN (W-MWBSN), and implanted MBAN (I-MWBSN), but these terms have not been found in the studied literature. The proposed taxonomy tree and some examples are illustrated in Figure 93.

Figure 93 – Proposed WBAN taxonomy.



Source: (The author, 2013)

APPENDIX B – A survey of typical electric loads and associated power demands for WBANs

The harvesters can enable the energy autonomy of the nodes, while imposing constraints on the consumption load. For example, the worst-case scenario for energy harvesting occurs when the individual lies in bed, so that there is practically no mechanical energy to harvest, the light intensity is low, the heat flow is at a minimum because of the blankets, and the metabolic rate is low (mainly elderly). In this scenario, harvesters can deliver an energy supply of approximately 1–10 μW (LEONOV, 2011). As a consequence, an efficiency in terms of the energy load (low power consumption) and efficient energy management are necessary to meet the requirements imposed by the EPS (WANG; CHANDRAKASAN, 2004). In this section, we discuss the energy load efficiency, understood as the lowest consumption with the same functionality, in the context of WBAN nodes.

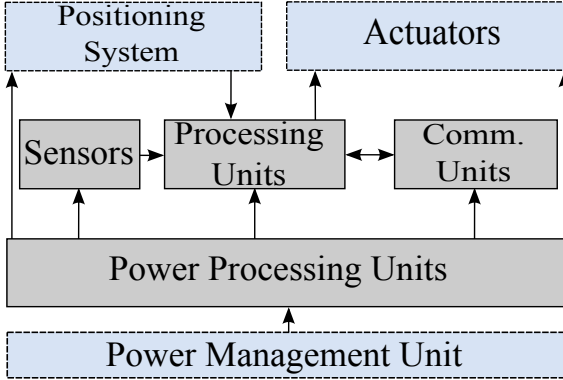
As outlined in the Introduction, in this research framework, there is a wearable WBAN node that collects energy from energy harvesting sources available on the surface of the human body, such as solar and thermal energy, to enable energy autonomy and the connectivity of a miniaturized subcutaneous implantable node. With the aim of studying the relationship between energy consumption and the complexity of the node, we must first understand the main causes of its consumption. For this analysis, in this section, we present three conceptual entities: a communication node, a WPT node (I-WBAN and WPT communication) and a subcutaneous node. Moreover, we present a brief description of the state-of-the-art techniques for W-WBAN node power reduction which do not depend on the application.

B.0.1 Communication node

Figure 94 exhibits a schematic diagram of a general communication sensor node for W-WBAN. The communication unit is often the most energy-hungry element of a sensor node. Commercial transceiver chips typically consume power on the order of 10 to 100 mW for rates of 200–2000 kbps, achieving an energy-per-bit efficiency of 20 to 400 nJ/bit (HUANG MARYAM ASHOUEI, 2009). Considering a system with 10-mW consumption by the node, and an EPS based on a typical battery, with a 1250-mAh capacity and a voltage of 1.5 V, it can only operate continuously for about one week. The need for replacing or recharging the batteries at a very high frequency is usually undesirable for W-WBAN and unacceptable for I-WBAN. For this reason, we seek new ultra-low-power consumption wireless technologies. A good

target performance to achieve autonomy using harvesters is an energy efficiency of 1 nJ/bit at a nominal rate of 200 kbps, which translates to an average energy consumption of 200 μ W (HUANG MARYAM ASHOUEI, 2009).

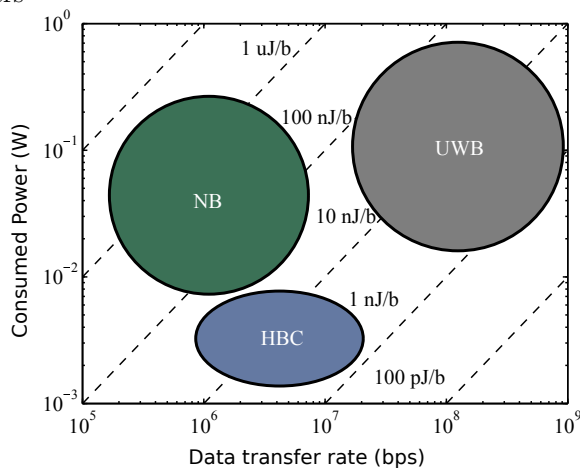
Figure 94 – Typical architecture of a sensor node



Source: (AKYILDIZ et al., 2002)

In 2012, the IEEE 802.15.6 standard (IEEE, 2012) was specified. It tries to provide a low consumption and high reliability solution for WBAN. The protocol indicates the basic requirements for communication between devices on the same network (unified MAC), and for the physical layer, it recommends the operating frequencies, modulation, and transfer rates under certain constraints. The three proposed physical layers are: narrowband (NB), which operates in the 400 MHz, 900 MHz and 2.4 GHz bands; ultra-wideband (UWB), which operates in the 3.1–4.8 GHz and 6.2–10.3 GHz bands; and human body communications (HBC), which operates in the 21 MHz band. The standard does not include the characteristics of the other network layers. A comparison of the consumption, energy efficiency and nominal rates of transceiver circuits for NB, UWB and HBC is shown in Figure 95. To achieve the low energy consumption required to enable energy autonomy, we can use duty cycle techniques, which means the signal is sent only during a fraction of the total transmission time. This technique allows activating the transceivers just at the instant when the signals must be transmitted or received, which reduces the average energy consumption significantly (PENELLA; GASULLA, 2007). For example, (MERCIER et al., 2014) presents the design of an NB transmitter that achieves an average energy consumption of 78 pW and operates at a

Figure 95 – Consumption and transfer rates of NB, UWB and HBC transceivers



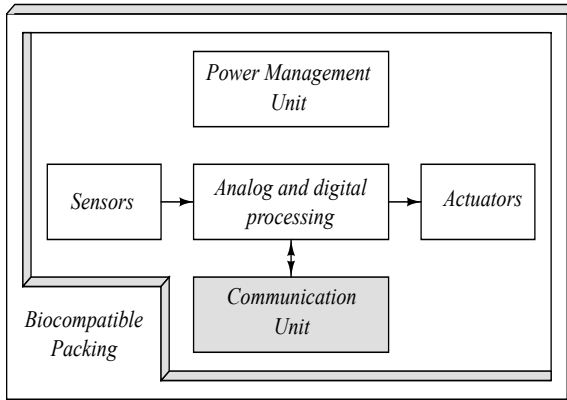
Source: (BAE et al., 2012)

data rate of 1 bps. In this work, the idle consumption of the transmitter is 39.7 pW and in the active mode, the transmitter supports OOK and FSK modulations at 2.4 GHz, consuming 38 pJ/bit at a data rate of 5 Mbps.

B.0.2 Subcutaneous implants

In the development of subcutaneous applications, we must overcome two main problems. The first one is the integration of the biosensors, the electronic instrumentation, and the communication systems to send information through the human skin. The second is to achieve energy autonomy for the implanted device (COLOMER-FARRARONS et al., 2011). In general, we can make a schematic of the electronic implant as shown in Figure 96. Sensors are transducers that convert physical, biological and chemical parameters, such as temperature or pressure or the concentration of some specific type of molecule or ion, into an electrical signal. Analog and digital circuits must then condition and process this signal. This processing module is also responsible for controlling the actuators, for sending data to the communication module, and for the reception. Actuators, in turn, are transducers that inter-

Figure 96 – General composition of a body implant



Source: (CABRERA; SOUSA, 2014)

act with the surrounding environment of the implant. Two examples of actuators are the cardiac tissue stimulator of a pacemaker and an insulin pump. On the other hand, the communication module has the role of sending the measured signals and receiving instructions from devices external to the body. Another important module of the implant supplies energy for the operation of the communication and processing circuits. In many aspects, the implant is a communication node, as described in the previous section, but with the constraints inherent in an implantable device. These are: 1) The smallest possible size, aiming at being non-invasive. 2) A biocompatible package to protect the circuits and electrically insulate the implant from the tissues while keeping open spots to allow interaction between the tissues and transducers (actuators and sensors). 3) Wireless energy autonomy, linking the implant to the outside.

Most current commercial implants use batteries to power the circuits, although such batteries occupy most of the device's volume. Furthermore, batteries store only a limited amount of energy and thus need to be replaced periodically. Each replacement of an implant means a surgical procedure, with risks to the patient's life (GOULD et al., 2006). For these reasons, the node must harvest energy available inside the body to achieve energy autonomy. As examples, (AYAZIAN; HASSIBI, 2011) seeks to use light to power implanted devices using subcutaneous photovoltaic cells, (DETERRE, 2013) uses variations in blood pressure to power pacemakers, and (MERCIER et al., 2014) powers an implantable

node by energy harvested from the endocochlear potential (a battery naturally located in the inner ear of mammals). Another possibility is to generate an artificial energy source in the vicinity of the implant (DARROW et al., 2001). For example, (ZHU; MOHEIMANI; YUCE, 2011) proposes a WPT technique based on ultrasound waves to power implantable biosensors using ultrasound transducers. The simplest WPT method for implants is an energy transfer based on an inductive link (CABRERA; SOUSA, 2014; SAWAN, 2004). Such a method allows alternatives to establish a bidirectional communication between the implanted device and an external interface (base or reader) (HAIDER; ISLAM; ZHANG, 2007). The basic elements of this mechanism are the same as those of RFID tags, where the implanted device acts as a tag. We can find some implantable telemetry circuits based on inductive links in the scholarly literature (MYNY et al., 2008; COLOMER-FARRARONS; MIRIBEL-CATALÀ, 2011).

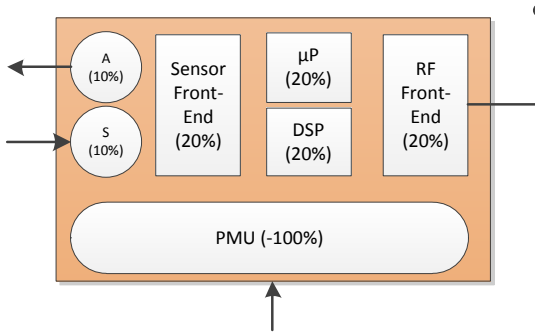
B.0.3 WPT nodes

A WPT node must transmit energy for the operation of the passive implant. By passive, we mean the implant does not have its own energy source. The implant must be able to harvest enough energy from the energy transmitter for its operation, including returning an answer. In this application, we transmit energy and data simultaneously to the implant through an inductive link. Since the implant must have a minimalist operation, the answer is usually obtained from a change of the implant input impedance as a function of the information we wish to send (PINTO et al., 2013; CABRERA; SOUSA, 2014). WPT nodes are currently being researched by the Radio-Frequency Research Group of UFSC. In this architecture, a wearable node (a WPT node) operates as an artificial energy source for the implanted node and, at the same time, allows communication between the node and a W-WBAN.

B.0.4 Techniques of WBAN node power reduction

The energy efficiency of integrated circuits continues to be the determining factor in the size, weight, and cost of WBAN nodes. For all the previously discussed nodes, battery lifetime, energy autonomy, and low cost are critical. In general, in electronic circuit design for WBAN nodes, energy generation and storage technologies are less likely

Figure 97 – Schematic representation of WBAN node



Source: (VULLERS et al., 2010)

to change during the development cycle and are the most limiting elements in the design, considering their size, weight, and cost (ROUNDY et al., 2004). On the other hand, the hardware and software for these technologies is continually changing, and several research efforts are focused on the minimization of electronic circuit consumption using CMOS design techniques (WEI-MING et al., 2007; PIGUET; RENAUDIN; OMNES, 2001; LIANG; CHANG, 2011; PARK et al., 2007; CHEE; RABAEY; NIKNEJAD, 2004) and the management of the efficiency of these circuits (FANG; DUTKIEWICZ, 2009; CHOI; KIM; KIM, 2012; XIE et al., 2006; BAE et al., 2011).

We usually characterize WBAN nodes by their physical dimensions, autonomy, portability, functionality, and building blocks (that is, microcontroller, radio, sensors) as well (VULLERS et al., 2010). A diagram of the distribution of the consumption between the functional blocks of a WBAN node is given in Figure 97, which highlights that the optimization of both analog and digital blocks is important to meet the consumption goals imposed by the application.

In general, we separate the total energy for the operation of a digital circuit into two components: active energy and leakage loss (PE-DRAM, 1996). Scaling the circuit voltage source is one of the most popular methods to decrease consumption. Specifically, the active power for full operation is $C \cdot f_s \cdot V_{DD}^2$. If the voltage is reduced, then the impact on power consumption is quadratic (BURD; BRODERSEN, 2000). However, leakage losses are negligible for high voltages but increase exponentially as V_{DD} decreases (BURD et al., 2000). Typically, close to

the switching threshold voltage, these opposing tendencies give rise to an operating point of minimum energy consumption (CALHOUN; WANG; CHANDRAKASAN, 2005).

In general, for analog circuits, the low power design approach is highly specific to each type of circuit. Nevertheless, it involves, at least, an implementation in low threshold voltage CMOS technology, the operation of CMOS transistors in the weak inversion region, the use of innovative design techniques, new architectures and efficient regulation circuits (WANG; CALHOUN; CHANDRAKASAN, 2006).

Besides circuit techniques, one of the best known solutions to achieve low energy consumption is pulsed operation, which means the system operates at a high power consumption for only a fraction of the total operating time. For example, in a radio front-end, this technique involves turning the RF stage on for only the instants when transmitted signals must be received, and hence significantly reduces the average energy consumption (HUANG MARYAM ASHOUEI, 2009). We also use the pulse operation technique in digital circuits, e.g., low power CPUs process tasks that consume a lot of resources (high current) over short periods of time. This operating mode is more energy efficient than doing tasks that consume a few resources (low current) for a long time (WANG; CHANDRAKASAN, 2005). Additionally, in energy harvesting applications, we can use this technique in the HPMU to guarantee an operation close to the ENO region of the system (COLOMER-FARRARONS et al., 2011).

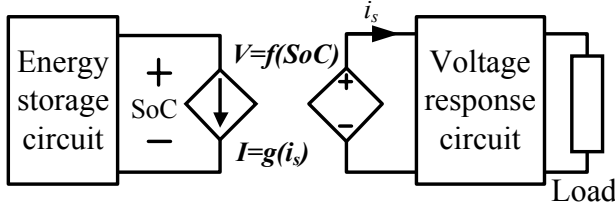
APPENDIX C - Using the EPS concept for modeling batteries

In this appendix, we use the energy power supply concept for proposing a DC voltage source with limited energy storage capacity, which can be used for modeling the energy storage capacity of the batteries, the energy flow process, and the constant voltage output behavior when the battery has stored energy. Further, this circuit source is used for understanding the combined electrical circuit-based battery model, which is commonly used for designing portable electronic devices, hybrid electric vehicles, and smart grid systems. Furthermore, a comprehensive state of the art review of the progress that has been made on this battery model will be presented.

C.1 INTRODUCTION

Energy storage devices have a wide range of applications. Recently, battery technologies have been receiving an enormous amount of attention because of three commercial applications, which have pushed batteries to their limits (NIKDEL et al., 2014). These are portable electronic devices (PEDs), hybrid electric vehicles, and smart grid systems. In the design of PEDs, the trade-off between functionality (i.e., dissipated power) and portability (i.e., battery running time, weight, size) (D'AMBROSIO et al., 2014) must be faced. Typically, device portability is associated with the battery because it is the element least susceptible to change during the development cycle of the product (ERICKSON; MAKSIMOVIC, 2001). Without battery models in hand, circuit designers can neither predict nor optimize either the battery runtime or the circuit performance. To integrate the batteries as energy storage devices into the smart grid, it is important to evaluate their use in the system (RAHIMI-EICHI et al., 2013). This evaluation should be done in terms of cost (e.g., maintenance), lifetime (measured by the charge-discharge cycles and the calendar life of the battery), power delivery (i.e., charge-discharge rate, energy storage level, ramp rate, and charge-discharge efficiency), environmental impact, and safety. This evaluation is much cheaper if it is made by electrical simulation instead of prototyping (WINDARKO; CHOI; CHUNG, 2010). However, the simulation results are dependent on the accuracy of the battery model. The electric vehicle industry uses large battery packs in demanding applications that involve high rates of power charging and discharging, and with long service life (SEAMAN; DAO; MCPHEE, 2014). An accurate and efficient battery model is vital to increase the performance of the driver and its battery and to inform the control systems about its evolution

Figure 98 – Combined electrical-circuit based model.



Source: (The author, 2015)

(RAHIMI-EICHI et al., 2013).

Battery modeling is a broad and complicated field, with no single model capable of meeting the requirements for all applications. Battery models can be classified into physical models, analytical models, and circuit-based models (SEAMAN; DAO; MCPHEE, 2014; NIKDEL et al., 2014). Physical models are mainly used to optimize the physical design aspects of batteries: they capture the fundamental mechanisms of power generation. Analytical models adopt empirical equations (e.g., mathematical fitting of empirical data) to predict system-level behavior, such as battery runtime, efficiency, or capacity. Circuit-based models use a combination of circuit elements (e.g., voltage sources, resistors, and capacitors) to predict the I–V information of the battery. For electrical engineers, these circuit models are more intuitive, useful, and easy to handle, especially when they can be used in circuit simulators (e.g., compatible with spice models) for co-simulation with other circuits.

This appendix is focused on the circuit-based models proposed in (CHEN; RINCON-MORA, 2006), which was referenced as the combined electrical-circuit based model (CECBM) by (NIKDEL et al., 2014; SEAMAN; DAO; MCPHEE, 2014). This model is commonly used for designing portable electronic devices, hybrid electric vehicles, and smart grid systems, because it is capable of accurately predicting the DC voltage response, the runtime, and the transients. Further, it was modified by (ZHANG et al., 2010; KIM; QIAO, 2012; YAO et al., 2013; LAM; BAUER; KELDER, 2011) in order to capture some nonlinear behavior (e.g., the C-rate effect, the state of health (SoH) of the battery). This family of models (illustrated in Figure 98) is based on two separate circuits: the energy storage circuit and the voltage response circuit. These circuits are coupled by a nonlinear relation (i.e., f and g) that models the energy flow process. These models have been used without a comprehensive development about the inspiration of its topology, and the

simple energy flow process that it models. In this appendix, the electric Energy Power Supply (EPS) concept is used, and a DC voltage source with limited energy storage capacity was proposed as the ideal battery model. Further, we use this component for understanding the behavior captured by the reported variations of the CECBM battery models.

Table 31 – EPS taxonomy

EPS Name	P_{avs}	Energy	Example
Ideal EPS	infinite	infinite	Voltage source model
EPS	finite	finite	Electric distribution network
Power EPS	low	high	Solar Energy + PV cell
Energy EPS	high	low	AAA battery

Source: (The author, 2015)

C.2 EPS TAXONOMY

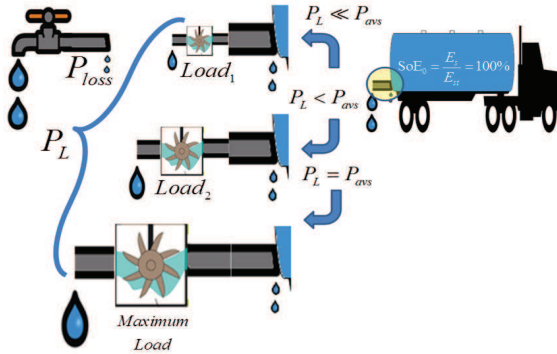
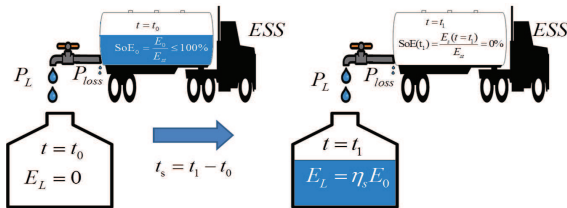
An ideal EPS must supply an infinite amount of energy at the required power load, with a small form factor. On the contrary, any real EPS delivers a limited amount of energy at a limited power, with a specific form factor. This behavior is illustrated in Figure 99, where a real EPS is represented by a water tanker truck, and its related electrical variables are described using the hydraulic analogies summarized in 32. When only one of the imposed constraints is significant for the load, the real EPS operates as a power or energy EPS. For instance, an EPS based on an energy harvester supplies a large amount of energy (i.e., self-sustaining), but at low power (RINCON-MORA, 2013). Additionally, this maximum power value (P_{avs}) can be extracted from the EPS only when the power transfer condition is satisfied. This type of source is referred to as a power EPS. When the EPS is based on energy storage devices (e.g., batteries), it supplies high power for a limited time, because it has a limited energy-storage capacity (E_{st}). This type of source is referred to as an energy EPS. This taxonomy is summarized in Table 31.

Table 32 – Analogies between variables

Hydraulic variables	Unit	Electric variables	Unit
Volume of water	m^3	Electric energy (E)	J
Discharge	$\frac{\text{m}^3}{\text{s}}$	Electric power (P)	W
Volume of water stored in the tank at a particular instant.	m^3	Instantaneous electric energy stored in the EPS (E_s)	J
Tank volume	m^3	Energy storage capacity of the EPS (E_{st})	J
Tank filling percentage	$\frac{\text{m}^3}{\text{m}^3}$	State of energy (SoE) of the EPS	$\frac{J}{J}$
Tank initial filling percentage	$\frac{\text{m}^3}{\text{m}^3}$	initial state-of-energy (SoE_0)	$\frac{J}{J}$
Water tap coming-out discharge (WtD)	$\frac{\text{m}^3}{\text{s}}$	Power dissipated by the load (P_L)	W
Water tank coming-out discharge (WTD)	$\frac{\text{m}^3}{\text{s}}$	Generated power ($P_S = P_L + P_{loss}$)	W
WtD with totally open tap	$\frac{\text{m}^3}{\text{s}}$	Maximum available power of the EPS	W
Relation between WtD and WTD	$\frac{\frac{\text{m}^3}{\text{s}}}{\frac{\text{m}^3}{\text{s}}}$	EPS efficiency $\eta = \frac{P_L}{P_S}$	$\frac{W}{W}$

Source: (The author, 2015)

Figure 99 – Hydraulic analogy of a loaded EPS.

(a) P_{avg} and E_{st} concepts

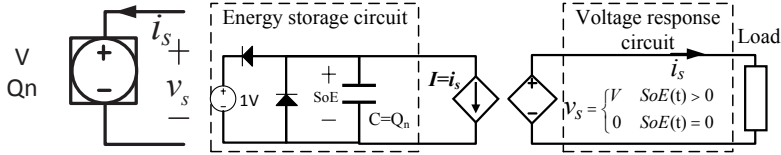
(b) Runtime time concept

Source: (The author, 2015)

C.3 DC VOLTAGE SOURCE WITH LIMITED ENERGY STORAGE CAPACITY

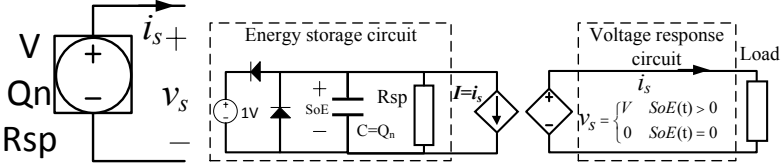
In conventional circuit theory, the voltage source models can supply unlimited energy, therefore a direct battery model is unavailable. However, using the circuit shown in Figure 100(b) for modeling an ideal battery, both its runtime (i.e., the SoE as a function of the load current) and its I–V performance (i.e., output voltage as a function of the SoE) can be captured by the model. Adding three resistors and two capacitors (Figure 101) to the ideal battery model, the following behavior of the real battery can be captured: limited output power, relaxation effect, and internal voltage drop when it is loaded. On the other hand, the self-discharge rate is proportional to the SoE (VERBRUGGE; CONELL, 2002), therefore the energy storage circuit of the ideal battery must be modified to capture the self-discharge effect: this is shown in Figure 100. In the next section, it will be shown how these “ideal” models can be modified for increased accuracy. The tracking of the SoE is modeled by adding nonlinear relations (\mathbf{g} and \mathbf{f}) to describe the energy flow process, as shown in Figure 100(f). Additionally, the component values of the voltage response circuit are modeled as nonlinear functions of the SoE (i.e., more commonly used the \mathbf{SoC}), the discharge current ($\mathbf{I_L}$), the temperature (\mathbf{T}), the charge and discharge time (\mathbf{t}), and the number of discharge–charge cycles (\mathbf{N}).

Figure 100 – DC voltage source with limited energy storage capacity



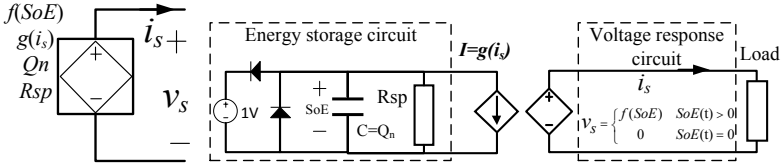
(a) Symbol of (a)

(b) Ideal battery circuit model



(c) Symbol of (d)

(d) Circuit model with self-resistance



(e) Symbol of (f)

(f) Circuit model with nonlinear tracking of SoE

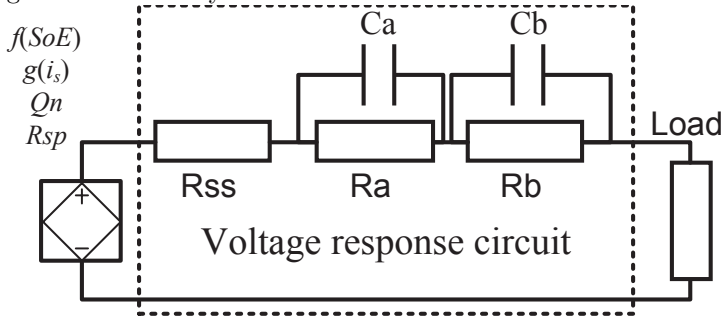
Source: (The author, 2015)

Table 33 – Significant electric battery behaviors

Battery behavior	Description
1) I–V performance (IVP)	I–V performance is the estimation of the battery output voltage for any load.
2) DC–IVP	DC I–V performance is the estimation of the variations in the steady state battery voltage
3) Open circuit voltage (V_{oc})	Is the voltage of battery during equilibrium state when the load is an open circuit
4) Internal resistance on DC–IVP	The internal impedance of the battery, when it increases, the battery’s efficiency decreases and thermal stability is reduced.
5) N on DC–IVP	The DC–IVP changes with N , e.g. The R_{ss} increase when N increase.
6) T on DC–IVP	The DC–IVP changes with the ΔT , e.g., V_{oc} increases when N increases.
7) Transient response	Battery output voltage response when the load current is a rectangular current pulse.
8) State of Health (SoH) tracking	The SoH is a measurement of the ageing of the battery that reflects the general condition of the battery compared with a new battery. The accurate estimation of the SoH by the model is referred to as tracking the SoH .
9) SoC tracking	The SoC is more common than the SoE in the battery literature, but they describe the same energy flow process. The accurate estimation of the SoC by the model is referred to as tracking the SoC .
10) Capacity loss (i.e., storage energy loss)	Changes in the usable capacity (storage energy) can be either a result of irreversible capacity loss or reversible capacity change. Capacity fading depends on many stress factors, such as temperature, C-rate, SoC , and depth of discharge.
11) Capacity fading due to cycle number	Irreversible capacity loss (storage energy) as a result of cell ageing due to cycling.
12) Capacity fading due to time	Irreversible capacity loss (storage energy) as a result of cell ageing due to storage time.
13) Capacity loss due to T	Reversible capacity change as a result of ΔT .
14) C-rate effect (rate capacity effect or current recovery effect)	Reversible capacity change as a result of the C-rate. The current recovery effect is the capacity recovered by discharging at a lower current.
15) Runtime prediction	The period of time during which the battery can operate continually as an energy source for its load (i.e., an output voltage bigger than end-of-discharge voltage).
16) Self-discharge effect	The storage energy (called usable capacity) declines as the storage time (self-discharge) increases.
17) AC response	I–V performance when the load current is an AC current.
18) Charge (Ch) and discharge (dCh)	Typically, a behavior while discharging is not the same as when charging.

Source: (The author, 2015)

Figure 101 – Battery model proposed by (CHEN; RINCON-MORA, 2006) using the ideal battery model



Source: (The author, 2013)

C.4 THE STATE-OF-THE-ART OF THE CECBM MODELS

A brief list of the battery behaviors that can be captured using the CECBM models is presented in Table 33.

In (CHEN; RINCON-MORA, 2006) there was proposed for the first time the CECBM. This model is illustrated using the ideal battery model shown in Figure 101, all component values of the voltage response circuit were proposed as nonlinear functions of the **SoC**. In (ZHANG; CHOW, 2010), the impact of the complexity of the voltage response circuit on the capture of transient response was analyzed. The authors demonstrate that with more than two RC circuits, the battery model gives better accuracy. On the other hand, to improve the basic model with the capture of the C-rate effect, (ZHANG et al., 2010) used a more complex energy balance circuit based on a nonlinear tracking of the **SoC**. This circuit reflects the nonlinear decrease in the battery capacity (i.e., storage energy) when the discharge current increases.

An alternative approach for modeling the C-rate effect was proposed in (KIM; QIAO, 2012). They replace the energy balanced circuit with a mathematical model based on the Kinetic Battery Model (KiBaM); these equations can be interpreted as nonlinear functions of both the charging current and the time. In (ERDINC; VURAL; UZUNOGLU, 2009) there was developed a battery model that captures the capacity fading effects: they propose a capacity correction factor as a nonlinear function of the storage time, temperature, and number of cycles. This factor can also be interpreted as a current correction factor. Recently, in (YAO et al., 2013) there was proposed that the model parameters can

be described as nonlinear functions of the *SOC* and the discharge current. Further, a more complex model was proposed in (LAM; BAUER; KELDER, 2011): they used empirical equations to describe the model parameters as nonlinear functions of the current direction, the state of charge (*SoC*), the temperature, and the C-rate.

A brief comparison of the SoA is summarized in Table 34; it indicates the modeling road-map of the CECBM technique. From the designer’s point of view, the better model is the one that captures the battery behavior of interest accurately with minimum computational complexity and with maximum flexibility and stability. Table 35 summarizes the input variables used for extracting the circuit values of the models. The functions listed in this table ($h(x)$, $p(x1, x2)$, $l(x1, x2)$, $m(x1, x2)$, $q(x1, x2, x3, x4)$) are nonlinear functions that were fitted using the experimental data.

Table 34 – Comparison of the proposed CECBMs

Behavior	Fig.	Fig.	Fig.	2006	2009	2010	2012	2013	2011	2010
Table 33	100(b)	100(d)	101	(CHEN; RINCON- MORA, 2006)	(ERDINC; VU- RAL; UZUNOGLU, 2009)	(ZHANG et al., 2010)	(KIM; QIAO, 2012)	(YAO et al., 2013)	(LAM; BAUER; KELDER, 2011)	(ZHANG; CHOW, 2010)
Item 4	no	yes	yes	yes	yes	yes	yes	yes	yes	yes
Item 5	no	no	no	no	yes	no	no	no	no	no
Item 6	no	no	no	no	yes	no	no	no	yes	no
Item 7	no	no	very lim	lim	lim	lim	lim	lim	lim	yes
Item 9	yes	yes	yes	yes	yes	yes	yes	yes	yes	yes
Item 11	no	no	no	no	yes	no	no	no	no	no
Item 12	no	no	no	no	yes	no	no	no	no	no
Item 13	no	no	no	no	yes	no	no	no	yes	no
Item 14	no	no	no	no	no	yes	yes	yes	yes	no
Item 15	yes	yes	yes	yes	yes	yes	yes	yes	yes	yes
Item 16	no	yes	yes	no	no	no	no	no	no	no
Item 17	no	no	no	no	no	no	no	no	no	no
Item 18	Ch&dCh	Ch&dCh	Ch&dCh	dCh	dCh	dCh	dCh	dCh	Ch&dCh	dCh

Source: (The author, 2015)

Table 35 – Comparison of the dependencies of the circuit values on the analyzed models

Model	Fig.	Fig.	Fig.	2006 (CHEN; RINCON- MORA, 2006)	2009 (ERDINC; VURAL; UZUNOGLU, 2009)	2010 (ZHANG et al., 2010)	2012 (KIM; QIAO, 2012)	2013 (YAO et al., 2013)	2011 (LAM; BAUER; KELDER, 2011)
param.	100(b)	100(d)	101						
Qn	Nominal	Nominal	Nominal	Nominal	Nominal	Nominal	Nominal	Nominal	Nominal
Rsp	infinite	Nominal	Nominal	infinite	infinite	infinite	infinite	infinite	infinite
Rss	0	0	Nominal	$h(SoC)$	$h(SoC)$	$h(SoC)$	$h(SoC)$	$m(SoC, is)$	$q(SOC, T, abs(is), sgn(is))$
Ra, Rb	0	0	Fixed	$h(SoC)$	$h(SoC)$	$h(SoC)$	$h(SoC)$	$m(SoC, is)$	$q(SOC, T, abs(is), sgn(is))$
Ca, Cb	infinite	infinite	Fixed	$h(SoC)$	$h(SoC)$	$h(SoC)$	$h(SoC)$	$m(SoC, is)$	$q(SOC, T, abs(is), sgn(is))$
$g(x)$	$g(is) = is$	$g(is) = is$	$g(is) = is$	$g(is) = is$	$g(is) = is/CF$	$l(is, t)$	$l(is, t)$	$l(abs(is))$	$n(abs(is), sgn(is), T)$
$\frac{f(x)}{sgn(x)}$	$f(SoE) = V$	$f(SoE) = V$	$h(SoE)$	$h(SoE)$	$p(SoE, T)$	$h(SoE)$	$h(SoE)$	$h(SoE)$	$h(SoE)$

Source: (The author, 2015)

APPENDIX D – WBAN harvester as Example of Power and Energy EPS

D.1 WBAN HARVESTER AS POWER EPS EXAMPLE

A thermoelectric generator (TEG) converts heat flow into electrical energy using the Seebeck effect. A TEG is composed of thermopiles electrically in series and thermally in parallel, as illustrated in Figure 102(b). Each thermopile is made of an n-type semiconductor electrically in series with a p-type one. When a temperature difference is applied to the metal plates of the TEG, the heat flows from the warmer side to the colder one. In this process, the thermal gradient allows the movement of free electrons and holes, giving rise to a voltage given by (RAMADASS; CHANDRAKASAN, 2011):

$$V_T = N_T \alpha_t \Delta T_T, \quad (\text{D.1})$$

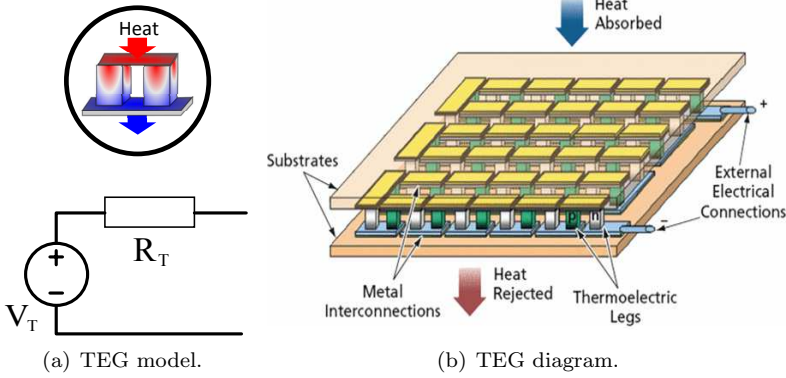
where α_t is the Seebeck coefficient of the thermopile, ΔT_T is the temperature difference between the generator plates, and N_T is the number of thermopiles. Theoretical and experimental analysis shows that the output current of a TEG is linearly proportional to its output voltage (DALOLA et al., 2009). That is because the principal losses are produced by the resistive interconnections inside the generator. Hence, we can model the harvester as a voltage source in series with an approximately constant resistor, as illustrated in Figure 102(a). Human beings generate heat regularly as a secondary effect of the metabolism, which is dissipated to the environment as a thermal flow (LEONOV, 2011). In WBAN applications the TEG is placed in direct contact with the skin to transform this flow into electricity. The human body has a high thermal resistance and thus the heat flow is low. The thermal gradient available at the harvester input (ΔT_{TEG}) can be calculated by (RAMADASS; CHANDRAKASAN, 2011) }:

$$\Delta T_T = \Delta T \frac{\Theta_T}{\Theta_{HB} + \Theta_D + \Theta_T}, \quad (\text{D.2})$$

where ΔT is the thermal gradient between the body and the environment, while Θ_{HB} , Θ_D , and Θ_T are the thermal resistance of the body, of the heat sink, and of the TEG, respectively. For a given temperature difference and according to the theorem of maximum power transfer, the P_{avs} of the TEG is given by :

$$P_{avs} = \frac{V_T^2}{4R_T}, \quad (\text{D.3})$$

Figure 102 – Thermoelectric generator model and diagram.



Source: ((a) The author, 2014; (b) Taken from (RAMADASS; CHANDRAKASAN, 2011))

where R_T is the equivalent series resistance of the TEG. Considering the typical small thermal gradients (from 5 K to 0 K or even less) between the human body and the environment for this application, the load of the TEG must operate with a few millivolts of input voltage to extract a few milliwatts at the output. We note that the HPMU (without storage element) design is feasible only if the power demand of the payload is lower than P_{avs} of the power EPS. In WBAN applications a thermoelectric cooler is also used as a TEG because a commercial cooler is more effective at temperatures closer to room temperature than generator modules, which are optimized for higher temperatures.

D.2 WBAN HARVESTER AS ENERGY EPS EXAMPLE

In this section we add an HPMU with storage element to the power EPS that is composed of the human body and the TEG (e.g., an on-body TEG). Also, we assume that the HPMU is designed to impose a constant electric potential V_y across its terminals whenever the stored energy is greater than a minimum value. In a real HPMU, this value must be higher than 0 because the output PPU needs some input energy to operate and regulate its output voltage. However, we assume this energy threshold to be 0 to simplify the mathematics. Considering this

context, the output voltage of the HPMU can be written as

$$v_P(t) = \begin{cases} V_P & SoE_P(t) > 0 \\ 0 & SoE_P(t) = 0 \end{cases} \quad (D.4)$$

Assuming that the HPMU and payload impose on the power EPS and HPMU a constant electric resistance: R_h , respectively, R_{HL} . The energy flow is given by :

$$SoE_P = \begin{cases} SoE_{0P} - \frac{1}{E_{stP}} \int_0^t \left(\frac{V}{R_{DC}^2} - \frac{V_h}{R_h^2} \right) d\tau & 1 > SoE_{0P} > -\frac{1}{E_{stP}} \int_0^t \left(\frac{V}{R_{DC}^2} - \frac{V_h}{R_h^2} \right) d\tau \\ 0 & SoE_{0P} \leq -\frac{1}{E_{stP}} \int_0^t \left(\frac{V}{R_{DC}^2} - \frac{V_h}{R_h^2} \right) d\tau \end{cases}; \quad (D.5)$$

The electrical behavior described by (D.4) and (D.5) can be represented by the circuit model illustrated in Figure 103(a). In Figure 103(b), we plotted an example of a generic SoE waveform.

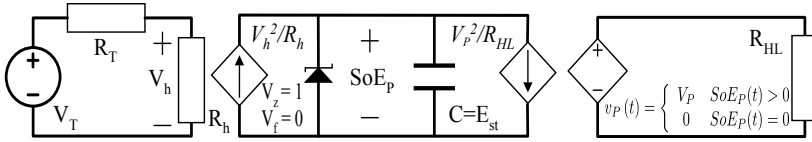
We note that the HPMU design¹ is feasible only if the energy demand of the payload is lower than the maximum available energy of the energy EPS (E_{avs}), given by

$$E_{avs} = E_0 + \int_0^t P_{avs}(\tau) \cdot d\tau. \quad (D.6)$$

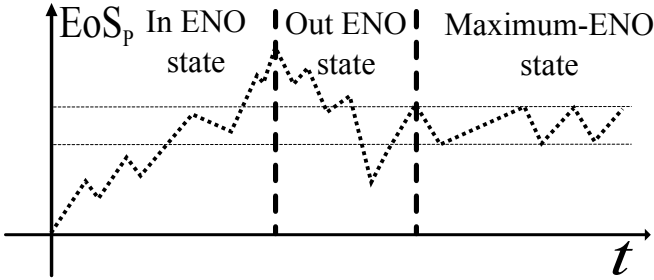
Generally, this condition is forced by the HPMU through an electronic switch, which disconnects the output PPU of the storage element when the stored energy is too low to supply the energy demands of the payload. This switch is shown in Figure 12(a).

¹If the reader is interested in knowing the SoA of the HPMUs for WBAN applications, Appendix E discusses cutting-edge SISO, MISO and MIMO (Multiple-Input Multiple-Output) topologies and describes its functional blocks. This description is focused on the analysis of loss mechanisms and on the proposed models. In addition, we present some techniques used for maximizing the energy extracted from the EPS by the HPMU. Also, we explain techniques for loss reduction at the PPU device level and techniques for miniaturizing inductor-based PPUs.

Figure 103 – Circuit model and SoE of an energy EPS composed of an on-body TEG and its HPMU.



(a) Circuit model of the analyzed energy EPS.



(b) Example of a generic EoS waveform of a generic EPS

Source: (The author, 2017)

APPENDIX E – A survey of power management and processing units for WBAN applications

An HPMU is a PMU designed specifically to manage the energy collected by harvester-based EPSs to deliver the load demands. The harvesters can enable the node to have energy autonomy while imposing constraints on the consumption of the load (HPMU and HPMU load). On the other hand, the node functionalities imply consumption requirements. If the PMU load consumption is lower than the maximum available power of the EPS, an HPMU design is feasible. The design of this system typically encompasses a management of the load imposed by the EPS, and a management system of the energy supplied to the load and storage elements, since the instantaneous power of the EPS and the HPMU loads are different. As we presented in the Introduction, the main figure of merit of this type of system is the capacity of extracting the maximum available power of the EPS with no loss in the processes of extraction, storage, and energy management. In this section, from cutting-edge SISO and MIMO topologies of the HPMU, we describe the functional blocks focusing on the analysis of loss mechanisms and on the models proposed to characterize them. Finally, in this section, we present the state of the art in the techniques for maximizing the energy extracted from the EPS by the PMU, techniques for loss reduction at the PPU device level, and techniques for miniaturizing inductor-based PPUs.

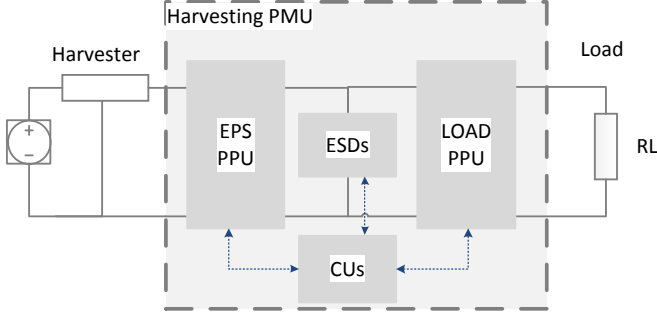
E.1 HPMU ARCHITECTURES

E.1.1 Single-input single-output HPMUs

The architecture of a typical single-input single-output (SISO) EH system (GUILAR et al., 2009; RAMADASS; CHANDRAKASAN, 2011; BANDYOPADHYAY; CHANDRAKASAN, 2012; TAN; PANDA, 2011) consists of a parallel connection between the harvester, load, and, if necessary, an energy storage device (ESD) using two PPUs, as illustrated in Figure 104.

The system is powered by the energy collected from the environment by the harvester. To guarantee the operation of the system, in this architecture, the first converter has the main objective of ensuring the extraction of P_{avs} from the source and thus must present the optimum impedance as the harvester's load, which is necessary for maximum power transfer from the EPS. For a DC EPS (for example, a TEG or PV cells), the PPU is a DC–DC converter; for an AC EPS (for example, a piezoelectric harvester), we use two cascaded convert-

Figure 104 – SISO HPMU architecture



Source: (The authors, 2014)

ers, one being an AC–DC converter (rectifier) and the other a DC–DC converter. For these sources, the first converter turns the energy into a favorable electrical form, while the second one guarantees the maximum energy extraction. In (KWON; RINCON-MORA, 2010), the authors combined these two converters into one switched converter, to increase the efficiency of the PMU. After ensuring the maximum energy extraction, this energy is stored for future use. At the same time, the ESD fixes the output voltage of the PPU EP in a given range of values determined by the control system. The supply voltage of the system load commonly differs from that output voltage, hence a second PPU (LOAD PPU) is necessary to regulate the supply voltage of the system load. For applications of EH in W-WBAN nodes, the harvester is usually small and the collected energy is low. To maximize the energy available for the load, the HPMU must be energy efficient, and thus we need to optimize all units. In a SISO HPMU, we typically use two performance measures: the peak of the harvesting efficiency η_{PMU} and the tracking efficiency η_{MPPT}^{EPS} :

$$\eta_{PMU} = \max \left(\frac{P_L}{P_{in}^{EPS}} \right); \quad (E.1)$$

$$\eta_{MPPT}^{EPS} = \frac{P_{in}^{EPS}}{P_{avs}^{EPS}}, \quad (E.2)$$

where P_L is the power dissipated in the load, P_{in}^{EPS} is the power delivered by the EPS, and P_{avs}^{EPS} is the maximum power available from the source. The value of η_{MPPT}^{EPS} represents the capacity of the

PMU to extract the maximum power available from the EPS and does not have a physical meaning.

E.1.2 Multiple-input–single-output and multiple-input–multiple-output HPMUs

In this section, we present an overview of the architectures proposed for ultra-low-power multiple-input single-output (MISO) and (SISO) EH systems. A MISO EH system is a hybrid system which combines various energy harvesting technologies to increase the available power and reliability of the equivalent EPS (BANDYOPADHYAY; CHANDRAKASAN, 2012). A multiple-input multiple-output (MIMO) EH system is also a hybrid system, but with the capacity to supply energy to several loads (SAGGINI; MATTAVELLI, 2009). In MIMO and MISO HPMUs, we usually use two performance measures: the peak harvesting efficiency and the tracking efficiency:

$$\eta_{PMU} = \max \left(\frac{P_{L1} + \dots + P_{Lm}}{P_{in}^{EPS1} + \dots + P_{in}^{EPSn}} \right); \quad (E.3)$$

$$\eta_{MPPT}^{EPSn} = \frac{P_{in}^{EPSn}}{P_{avs}^{EPSn}}; \quad (E.4)$$

where P_{Lx} is the power dissipated in the x th load of the PMU, P_{in}^{EPSx} is the power delivered by the x th source to the PMU, P_{in}^{EPSx} is the maximum power available from the x th source, and η_{MPPT}^{EPSx} is the tracking efficiency of the x th EPS. The value of this efficiency represents the capacity of the HPMU to extract the maximum power available from the EPS, and does not have a physical meaning.

The first significant publication on low-power multi-harvesting for WBAN was (COLOMER-FARRARONS et al., 2011), which presents and validates a multi-harvesting MISO PMU focused on low voltage (up to 2.5 V) for low-power applications. The system is capable of collecting and managing energy from the sun, light (indoor), vibration (low-voltage piezoelectric) and artificial electromagnetic induction in the licensed band at 13.56 MHz. The total idle power consumption of the system was **160 μ W** and the maximum power harvested from the three sources was 6.4 mW. The figures of merit were not reported, neither can they be calculated from the data in the paper. The architecture proposed is based on PPU multi-EPS with configurable ESDs to allow an individual storage of the energy collected by each

harvester or a single storage unit for all harvested energy. The topology is programmable, that is, it can be as shown in Figure 105 (c) or as depicted in Figure 105 (d). The Load PPU is a CMOS switch that regulates the system output at a predetermined reference through a comparator with hysteresis. The main disadvantage of this HPMU is its low efficiency, because, by employing parallel linear regulators in the EPS PPU, the EPSs cannot deliver their maximum available power. Therefore, the proposed multi-EPS PPU has the performance of a single-input EPS PPU, only decreasing the efficiency of the system assuming non-correlated energy sources. Other examples of MISO PMUs that have low efficiency when the sources are not correlated are those PMUs based on OR-ing connections to emulate a MISO PMU with a single SISO converter. For example, (TAN; PANDA, 2011) proposes a PMU based on this technique with the architecture shown in Figure 105 (a), which harvests solar and thermal energy, avoiding the use of individual PPUs for each energy source. As a consequence, they reduce the losses, the physical dimensions, and the cost. Moreover, the power extracted from the active source (greatest input voltage) is maximized with a low-consumption micro-controlled system, which implements MPPT over a wide range of operating conditions. From the experimental results, the system can harvest 621 mW with a solar radiance 1.010 lux or thermal gradient of 10 K. Another significant publication that presents the OR-ing technique to allow modularity of a multi-harvesting system is (CARLI et al., 2011). In this appendix, a simple, fully analog, multi-storage and multi-source architecture allows harvesting from an arbitrary number of EH sources, protects the system against long periods of energy shortage, and improves reliability. Furthermore, it minimizes the number of components and idle consumption.

To increase the efficiency of the system while keeping the same physical dimensions, researchers have used architectures based on MISO converters, where only one inductor is used to extract energy from the EPS. For example, in (SHI et al., 2011), the authors proposed a MISO PMU based on a MISO boost DC–DC converter (Figure 105 (b)) allows extracting energy from the multi-EPS and operating in such way that the efficiency of energy extraction is multiplexed in time. Furthermore, they also implemented MPPT without current measurement. They made a prototype of two inputs with discrete components and achieved a tracking efficiency greater than 97.5%, although the efficiency of the system cannot be calculated from the data in the paper. The authors of (BANDYOPADHYAY; CHANDRAKASAN, 2012) use both a MISO

PMU based on a DC–DC converter and a multi-storage scheme with no LOAD PPU, as illustrated in Figure 105 (e). In this architecture, the efficiency increases since the losses in the LOAD PPU are decreased, for some values of the load, by up to 100%. The efficiency of the system cannot be calculated from the data in the paper, but the tracking efficiency is high ($>96\%$), and the peak efficiency of the converters is also high ($>58\%$), although they did not report the idle consumption.

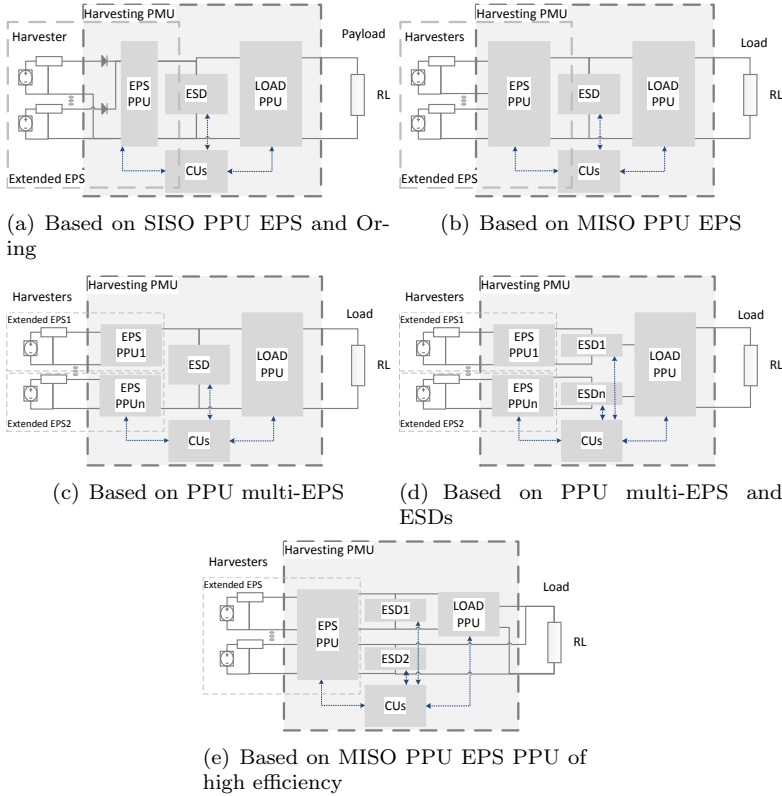
Concerning architectures of MIMO energy management, (SAGGINI; MATTAVELLI, 2009) presents an architecture in an early stage of its development, as illustrated in Figure 106. The authors of that paper propose a multi-harvesting, multi-storage and multi-load system based on a SIMO DC–DC converter which harvests energy from the sources and distributes it to the storage units and the loads. The system is promising, but the authors made only one implementation based on an FPGA with an external supply. Based on this idea, (SHRIVASTAVA et al., 2014) proposes a PMU to capture energy for ultra-low-power systems, which uses only inductors. This PMU collects energy from PV solar cells with input voltage 0.38 V and delivers four regulated output voltages: 3.3 V, 1.5 V, and 1.2 V. They also implement an MPPT circuit, besides over/under-voltage protection for the battery. The system can achieve high efficiency ($>82\%$) at several input and output voltages. The idle consumption is not reported. In (BENAVIDES; CHAPMAN, 2005), the authors implemented a MIMO PMU architecture which integrates the EPS and load PPUs. This approach allows regulating the input power coming from the energy sources and the output voltage as well.

We have not found fully-integrated MISO or SISO systems in the scholarly literature, but they can be implemented using the topologies shown in Figure 105 ((c) and (d)), as a natural expansion of SISO PMUs, although they would have a lower efficiency in the converters and higher idle consumption. New schematics must be developed and researched to achieve miniaturized physical dimensions. In (BANG et al., 2013) the authors present a fully integrated example of this type of system, which can be adapted to various types of harvesters.

E.2 PPUS FOR EH SYSTEMS IN WBAN

A PPU is a unit that provides the specifications of the load voltage and current from an electrical EPS (ERICKSON; MAKSIMOVIC, 2001), which usually involves the process of conversion and a regu-

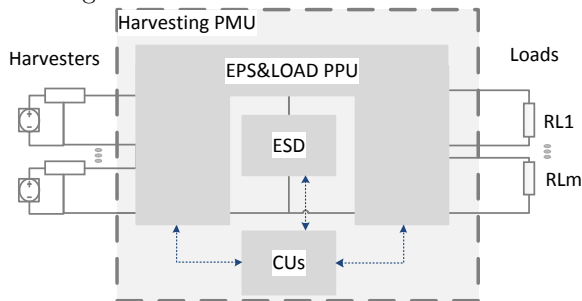
Figure 105 – Architectures of MISO EH



Source: (The author, 2014)

lation of the electrical variables (voltage and current). Considering a low-power PPU for EH systems in WBAN nodes, the electrical requirements of most loads are moderate to low voltage (for example, a continuous voltage of 0.5–2 V), with a demanding consumption (for example, a continual current of 100 μA to 20 mA). Therefore, in this section, we consider only conditioners that supply a continual voltage. This discussion leads to an overview and a comparison between several types of converters. For further details on the modeling, design, and implementation of these converters, we recommend consulting (RINCON-MORA G.N-MORA, 2009; RINCON-MORA, 2013; ERICKSON; MAKSIMOVIC, 2001).

Figure 106 – Architectures of MIMO EH



Source: (The author, 2014)

E.2.1 General comparison between the types of PPU

In Table 36, we present a comparison between the typical types of PPU in EH systems for WBANs concerning some of their limitations. We start the analysis by pointing out that the efficiency of the PPU is considered the most important metric, therefore, switched converters based on inductors are the most interesting because they exhibit lower energy losses. Nevertheless, the difficulty in integrating these converters with CMOS technology is a major drawback, as is, too, the fact that the complexity of the control might decrease the efficiency. However, in switched converters based on capacitors (or charge pumps) and linear regulators, the first-order losses are strongly dependent on the input and output voltage. We can easily integrate these converters, especially the linear regulators, because they need large capacitors on the order of μF . Switched converters allow more flexibility than comparators, linear regulators, or rectifiers, since they can increase or decrease the input voltage. But linear regulators have a faster AC response than switched converters. We note that the AC response is the time of the converter for reacting to perturbations of the input and output.

E.2.2 Types of losses in PPU

We can classify the losses in converters as of first or second order (RINCON-MORA, 2013). The latter are not related to the power consumption of the converters which is necessary for their operation, and do not have a direct relation with the power processing by the

Table 36 – Comparison between low-power PPUs

PPU	Linear	Switched and based on		AC-DC Rectifier
		C	L-C	
Power losses	High	Moderate	Low	Moderate
DC regulation	High	Low	High	Low
AC response (speed)	Fast	Slow	Moderate	Slow
Control	One loop	Open loop	Two loops	Open loops
V_o	$\leq v_{IN}$	$\leq \geq v_{IN}$	$\leq \geq v_{IN}$	$\leq v_{IN}$
Integration	High	Moderate	Low	Moderate

Source: (Based on (RINCON-MORA G.N-MORA, 2009))

converter. The main second-order losses in converters are quiescent losses (P_{qui}) and gate drive losses (P_{GD}). An example of P_{qui} is the consumption of a PPU controller, in which the circuit requires enough quiescent current to guarantee and send a command signal to the PPU. This consumption is independent of the load. However, if the PPU is switched, the EPS must also deliver energy to charge and discharge the intrinsic capacitors of the switches. This consumption is an example of P_{GD} . In PPUs for WBAN, we generate low levels of energy, and the losses make up a substantial part of the output power. For example, if a PPU delivers 100 mW but the PMU dissipates 40 mW in the power processing and consumes 10 mW, the output receives only 50 mW, which is a mere 50% PPU efficiency.

In general, first-order power losses result from the technique the converter uses to process the power, and are associated with parasitic elements of the switches, such as diodes, resistances, inductances, and capacitances. In linear regulators, the main losses of this kind occur because the current supplied by the PPU flows directly from the input to the output through the regulator. Therefore, the PPU dissipates a power greater than the product of the voltage difference across its (input and output) terminals and the output current, as illustrated in Table 37. For switched PPUs based on capacitors, the most significant losses are due to charge redistributions, which occur because of energy losses related to the parallel connections of capacitors with different voltages (MA; BONDADE, 2013). As (RINCON-MORA, 2013) has reported, these losses are dissipated in the interconnections of the switched capacitors and are proportional to the equivalent capacitor

formed by the connected capacitors (C_{EQ}), to the square of the potential difference across the capacitors (ΔV_{SW}^2) and to the switching frequency (f_{SW}). The potential difference across the capacitors of the PPU is the product of the almost linear discharge of the capacitors by supplying current to the load, and thus is proportional to the average input current of the PPU (i_{in}). However, in switched PPU's based on capacitors, the most significant losses are due to conduction in the switches and the losses in the capacitors, which are modeled by the equivalent series resistor of the switch (R_{SW}) and capacitor (R_{ESR}), respectively. These losses are proportional to the rms current through the components, which is proportional to i_{in} , as shown in Table 37.

Table 37 – Comparison between losses in low-power PPU's

PPU	Losses of first order	Losses of second order
Linear	$i_{IN}(v_{IN} - v_O)$	P_{qui}
Switched C	$0.5C_{EQ}\Delta f_{SW}v_{SW}^2$ *	$P_{qui} + P_{GD}$
Switched L-C	$R_{SW}i_{(RMS)}^{2**}; R_{ESR}i_{(RMS)}^{2**}$	$P_{qui} + P_{GD}$

* $\Delta v_{SW} \propto i_{IN(AVG)}$

** $i_{(RMS)} \propto i_{IN(AVG)}$

Source: (Based on (RINCON-MORA, 2013))

Considering the analysis carried out in last paragraphs, summarized in Table 37, switched circuits can dissipate less energy than their linear counterparts, assuming first-order losses. However, all these losses decrease together with the load, so when the load works in idle mode or the CU of the PMU turns it off, the efficiency of the PPU is more sensitive to second-order losses, where the linear converter can be more convenient. In (PANOV; JOVANOVIĆ, 2002) the authors explored PPU's adapted to the load demanded, because the functionality is the key factor in consumer electronics. For example, in inductor-based converters with low loads, the switching losses become higher than the conducting ones. Therefore, in the context of low power consumption, in order to reduce the switching losses, operating the converter at a low switching frequency and in discontinuous current mode is a good choice. Moreover, second-order losses become comparable to those of first-order and hence the control circuits must be designed using low-power techniques. Concerning second-order losses, PPU's based on switched capacitors require more switches than inductor-based PPU's, thus increasing the gate drive losses P_{GD} .

E.2.3 PPU modeling

PPU modeling has been widely studied. The models for the switched PPUs based on inductors have been influenced by (ERICKSON; MAKSIMOVIC, 2001), and those for the switched PPUs based on capacitors, by (MA; BONDADE, 2013).

E.3 STORAGE ELEMENTS

Storage technology plays a key role in the performance of EH systems, so the choice of storage components and recharge technology is of paramount importance. The technologies used in EH for W-WBAN nodes are those of charge storage (batteries and super capacitors).

E.3.1 Available technologies for charge storage

Rechargeable Electrochemical batteries are a common choice for energy storage in W-WBAN nodes. Electrochemical batteries are devices that store chemical energy inside them. This energy is converted into electrical energy by the battery and delivered to the electrical system it supplies. We compare some popular rechargeable technologies in Table 38 by the typical values of some performance measures, such as the energy and power densities, efficiency of discharge (η , the relation between the energy stored in the battery and the energy delivered by it), self-consumption losses (energy dissipated in the battery with no load), nominal voltage, and nominal capacity. For rechargeable batteries, other performance measures are essential (Table 39), such as the maximum number of recharge cycles with no damage to the battery, degradation in nominal capacity after recharge (memory effect), and the technology involved in the recharge. For example, we can directly connect NiMH batteries to an energy source for charging, and the charge is recovered through the DC current that flows through the source and the battery. This type of charging is called trickle charging. On the other hand, other types of batteries, such as LI-ion, need a pulsed current for charging. This type of charging is called pulsed charging. Finally, the efficiency of charging is the relation between the energy delivered to the battery and the energy stored in it during the process of recharge.

Considering Tables 38 and 39, two storage technologies, NiMH

and Li-based, emerge as good candidates for EH nodes. Li-ion batteries have the highest output voltages, energy density, power density, and efficiency of charge–recharge. They also have the lowest self-discharge losses and do not suffer from a memory effect. However, they require pulsed current for charging, which increases system losses by the increase in consumption, a byproduct of the operation of the charge circuit made to achieve this purpose. On the other hand, we can directly recharge NiMH and they do not need complex charging circuits. They have reasonably high values for the number of charge cycles and the densities of energy and power. While they suffer from the memory effect, this effect is reversible if the battery is fully discharged after charged. Even so, the efficiency of their charge–discharge is lower than that of Li-ion batteries. Therefore, both Li-ion and NiMH batteries have pros and cons, and the choice depends on the requirements and constraints of the application.

Alternatively, in ultra-low-power applications, we can use supercapacitors as storage components instead of rechargeable batteries. The main advantages of this charge storage technology are a the high efficiency of its charge–discharge, no memory effect, simple charging circuit, and almost infinite number of cycles. On the other hand, its main disadvantages are its very high self-consumption losses and very low energy density.

E.3.2 Model of batteries as charge storage elements

Researchers around the world have developed a wide variety of battery models of varying degrees of complexity, which capture the battery behavior for specific purposes, such as battery design or the estimation of the performance of the battery in a circuit. We can classify the models as electrochemical, mathematical, and electrical. The latter have an accuracy of approximately 1% to 5%, use a combination of voltage sources, resistors, and capacitors to describe the electrical dynamics of the batteries and to simulate their performance along with the electrical circuits and systems to which they provide energy (JONGERDEN; HAVERKORT, 2009). Based on the models reported in (CHEN; RINCON-MORA, 2006) and (EINHORN et al., 2013), we propose an electrical model that draws upon the concept of practical EPS discussed in Section 2.3.2. In Figure 107, we present this model. In Figure 107(a), the capacitor value (C) refers to the charge storage capacity of

Table 38 – Performance measures: Rechargeable technologies involved in storage capacity and energy supply

Type of Battery	Nom. voltage (V)	Nom. cap. (mAh)	Dens. of E (Wh/kg)	Dens. of P (W/kg)	discharge η (%)	Self-consumption losses (%/month)
SLA	6	1300	26	180	92	20
NiCd	1.2	1100	42	150	90	10
NiMH	1.2	2500	100	250-1k	66	20
Li-ion	3.7	740	165	1800	99.9	<10
Li-pol.	3.7	930	156	3000	99.8	<10
S-cap.	–	–	5	>3000	97	5.9 %/day

Source: (Based on (SUDEVALAYAM; KULKARNI, 2011))

Table 39 – Measures of efficiency: Rechargeable technologies involved in energy recharge capacity

Type of Battery	Efficiency (%)	Memory effect	Technique of charge	Cycles of charge
SLA	70	no	trickle	500-800
NiCd	70	yes	trickle	1500
NiMH	66	yes (reversible)	trickle	1000
Li-ion	99.9	no	pulsed	1200
Li-pol.	99.8	no	pulsed	500-1000
S-cap.	98	no	puls. or trick.	∞

Source: (Based on (SUDEVALAYAM; KULKARNI, 2011))

the battery. This value is given by:

$$C = q_n \cdot K_{c1}(i) \cdot K_{c1}(T); \quad (E.5)$$

where q_n is the nominal battery capacity in Wh, K_{c1} is the correction factor, which is a function of the recharge cycle, and i is the temperature factor, which is a function of the battery operating temperature T . Furthermore, the current-controlled current source (i_s) and the voltage-controlled voltage source (SoE) simultaneously represent the battery lifetime, state of charge (SoC), and the nonlinear relation between the open-circuit voltage (V_{OC}) and SoC . V_{OC} is expressed as:

$$v_s = \begin{cases} f(SoE) & SoE(t) > 0, \\ 0 & SoE(t) = 0. \end{cases} \quad (E.6)$$

The voltage V_{oc} is usually measured in open-circuit conditions for several points of SoC at steady state. In Figure 108, we show a typical discharge curve. Concerning Figure 107(b), we use the self-discharge resistor (R_{spA}) to characterize the self-discharge energy losses. Moreover, through the total internal resistance ($R_{ssA} + R_{scA}$), we model the voltage drop inside the battery. On the other hand, the RC network consisting of R_{scA} and C_{ssA} allows capturing some of the dynamics of the transient response. In (EINHORN et al., 2013), the authors explain that an RC network and the characterization of the model parameters through a linear function offer the best trade-off between parametrization effort and model accuracy. Thus, we can express the model parameters as:

$$R_{ss} = R_{ss0} + k_{R_{ss}} \cdot SoE, \quad (E.7)$$

$$R_{sc} = R_{sc0} + k_{R_{sc}} \cdot SoE, \quad (E.8)$$

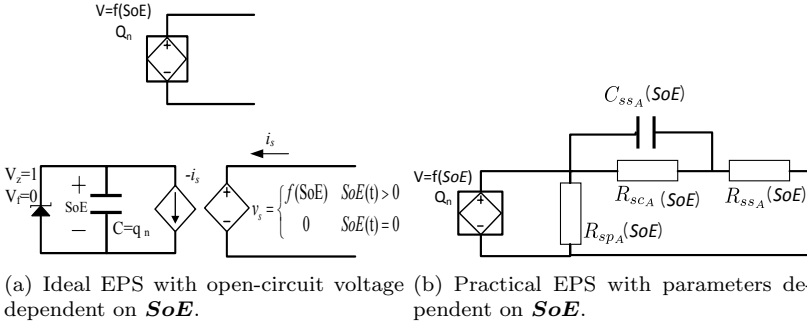
$$R_{sp} = R_{sp0} + k_{R_{sp}} \cdot SoE, \quad (E.9)$$

$$C_{ss} = C_{ss0} + k_{C_{ss}} \cdot SoE. \quad (E.10)$$

E.3.3 Model of supercapacitors as charge storage elements

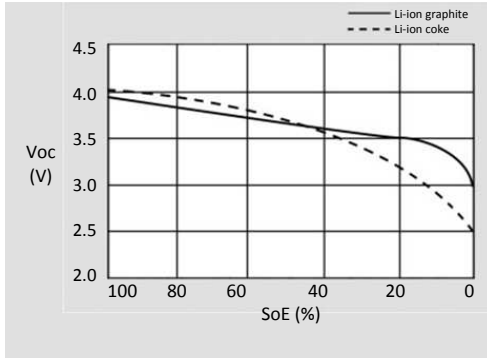
We employ supercapacitors, also known as ultracapacitors or double-layer capacitors, as charge storage units when we request a power density higher than those of batteries. They do not need special load circuits and have a long operational lifetime. The use of super-

Figure 107 – The proposed electrical model of a battery.



Source: (The author, 2014)

Figure 108 – Voltage discharge curve of Li-ion battery.



Source: (Taken from (SUDEVALAYAM; KULKARNI, 2011))

capacitors is common in WSN nodes, although it is less frequent in W-WBAN nodes, which usually resort to integrated capacitors as storage units. There are plenty of integrated capacitor (MOS capacitor) models and studies in the scholarly literature. In the present paper, we adopt the classical model presented in (TSIVIDIS; MCANDREW, 1999; SCHNEIDER; GALUP-MONTORO, 2010). Even though the supercapacitor is often used in nodes of W-WBAN networks when the stored energy is high (SUDEVALAYAM; KULKARNI, 2011), the circuit designers' understanding of its operation is still primitive (WEDDELL et al., 2011).

We portray the supercapacitor models found in the literature in Figure 109. Specifically, the ideal capacitor is portrayed in Fig-

ure 109(a), the simple model in Figure 109(b), the n -branch model in Figure 109(c), and the n -branch model with impedance Z_p in Figure 109(c). The choice of model is markedly dependent on the device charge profile and the complexity of the analysis. For example, in the design of the system, we choose simple models with ideal capacitor with ESR and a leakage resistor. These models are able to explain the short-term behavior of a supercapacitor (JIANG; POLASTRE; CULLER, 2005; JEONG; JIANG; CULLER, 2008), but for very long periods of operation, its behavior is not ideal, exhibiting characteristics such as fall and recovery voltage. In (WEDDELL et al., 2011), the authors use the n -branch model to represent these characteristics and they test it with a pulse consumption, typical in wireless nodes. In (MUSOLINO; PIEGARI; TIRONI, 2013), the authors propose a more complex model, which is valid for a wide range of frequencies and captures all the known phenomena of supercapacitors. Due to its complexity, this model is used for simulation.

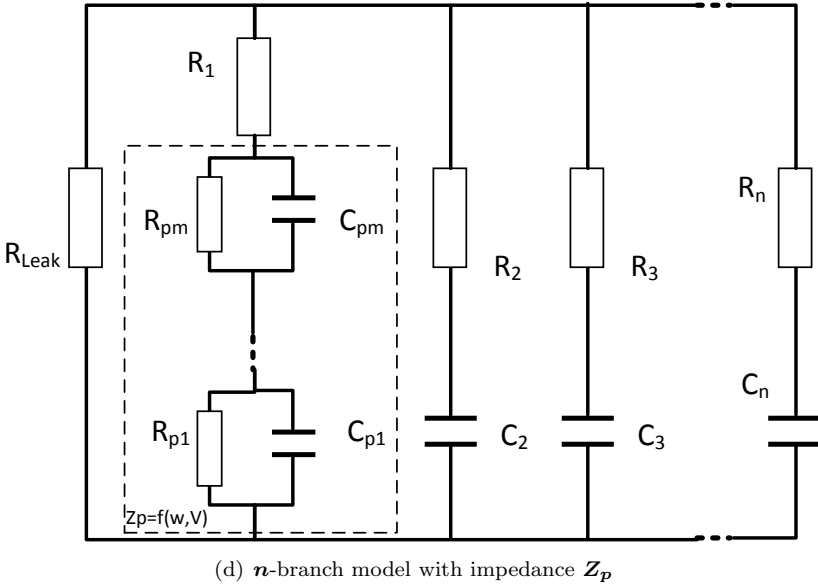
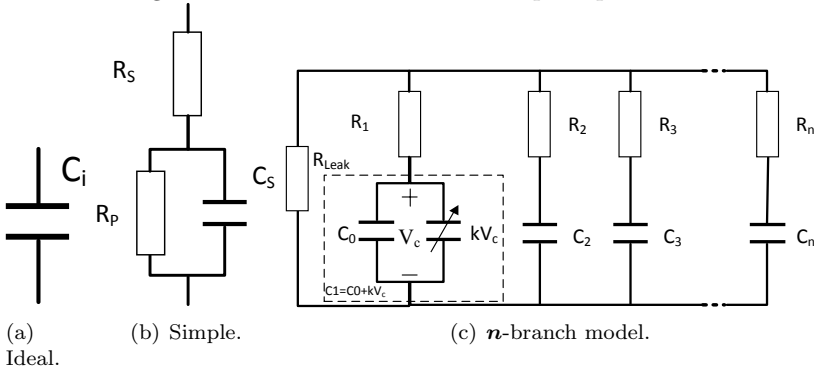
E.4 STORAGE VOLTAGE

In the nodes, where the storage voltage is necessary, the CU monitors the voltage across the storage unit (the voltage shared between EPS, ESDs, and the load) for two reasons: to regulate the voltage (modulation of the load or the sources) or to manage the energy storage devices (ESDs). For example, when an ESD is a rechargeable battery, the SoE of the battery fixes the storage voltage between a minimum and a maximum value to protect the battery and the system. To analyze and design a PPU, we can consider the voltage across the battery as semi-regulated and sometimes constant for a time window that is narrow when compared to the sampling period of the CU. The storage voltage level is a design value that directly affects the system efficiency, especially with respect to the losses in the PPUs and the ESD.

E.4.1 Maximization of the HPMU input power

During normal operation, the PMU must detect the MPP of the EPS for a given environmental condition and provide the optimum load to the harvester so that the collected energy is as high as possible, as mentioned in Section 2.3.2.6. In this section, we discuss some techniques to achieve this goal.

Figure 109 – Electrical model of supercapacitors.



Source: (The author, 2014)

E.4.2 Adaptation of the components during the design stage

In this technique, the EPS output is directly connected to the ESD. Thus, the ESD determines the EPS output voltage and dictates the operating point of the EPS. Following this approach, we can obtain the maximum power extraction through a careful selection of the modules (i.e., EPS and ESD) that allows zero consumption in the MPPT scheme. As we discussed in (RAGHUNATHAN et al., 2005), this method results in a sub-optimal operating point from the power extraction point of view. However, this is better than extracting the maximum available power of the source and consuming a significant part of it in a dedicated MPPT circuit.

E.4.3 MPPT based on the open-circuit voltage of the harvester (FOC–Fractional Open-Circuit Voltage)

This technique draws upon experimental measurements, which show that the harvester output voltage at the MPP (V_{mp}) is linearly proportional to its open-circuit voltage (V_{oc}) (SHAO; TSUI; KI, 2007; LU; RAGHUNATHAN; ROY, 2010b):

$$V_{mp} = k_v \cdot V_{oc}, \quad (\text{E.11})$$

where k_v is a constant that depends on the specific EPS to be used and on the test conditions. For PV cells, k_v is a value between 70% and 90%; for EPSs for which the linear model is valid (e.g., TEG, RF harvesters), k_v is 50% (SHAO; TSUI; KI, 2010). In a typical implementation of the FOC, the EPS PPU momentarily provides an open circuit as a load to the EPS, and during this condition, V_{oc} of the EPS is monitored. From this measurement, we know k_v , and can compute V_{mp} , hence the CU changes the impedance imposed by the EPS PPU as a load to the EPS.

This method is suitable for low-power PMU since it involves a simple control strategy. The disadvantage of this approach is that the EPS is periodically disconnected from the load, which decreases the efficiency of the PMU. Moreover, there is an additional consumption in the multiplexing of the operation at the time (normal and open), and in the operation mode. To overcome these drawbacks, in (BRUNELLI et al., 2008) the authors propose a small additional EPS as a pilot, where they use the open-circuit voltage of the pilot cell instead of the open-circuit

voltage of the main module of the PV cell.

E.4.4 MPPT based on short-circuit current of the harvester (FSC, Fractional Short Circuit Current)

This approach draws upon experimental measurements which show that the harvester output current at the MPP (I_{MPP}) is linearly proportional to its short-circuit current (I_{sc}) (LU; RAGHUNATHAN; ROY, 2010b):

$$I_{MPP} = k_i \cdot I_{sc}. \quad (\text{E.12})$$

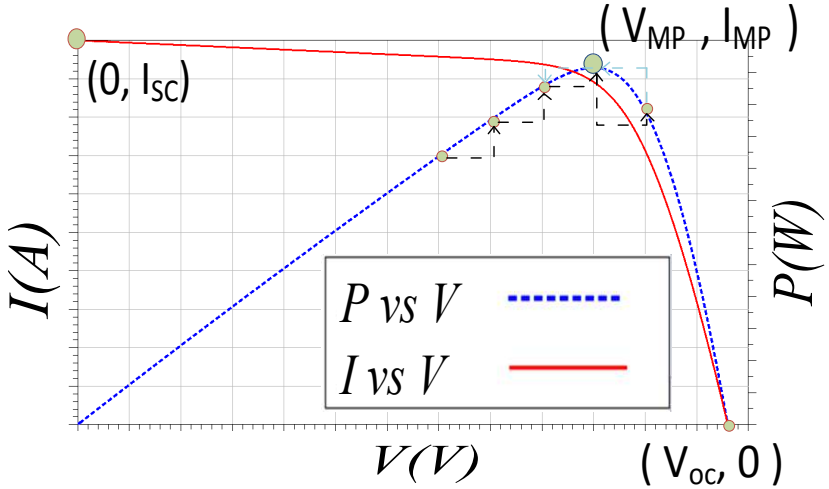
However, the FOC method is usually preferred to this technique, since the implementation of FSC involves measuring the current and causing a short-circuit in the system.

E.4.5 MPPT based on a perturb and observe algorithm (P&O)

This technique draws upon an iterative approach which perturbs the system and measures the error in tracking the MPP. During normal operation of the system, a procedure for tracking the MPP is periodically initiated. This procedure causes a perturbation in the input impedance of the EPS PPU by changing the duty cycle of this PPU (inductor-based PPU), or by changing the switching frequency (capacitor-based PPU). The perturbation in this impedance produces a small change in the EPS output power. If the perturbation increases the power, then another perturbation in the same direction is performed. But if the first perturbation decreases the power, then a second perturbation in the opposite direction is performed. In the equilibrium state, the system oscillates around the MPP of the EPS. This iterative process is depicted in Figure 110. Note that there is a compromise between the dynamic response of the system and the error in the equilibrium state. A large step size of the perturbation corresponds to a fast response to the changes in the energy source, but it also generates a large oscillation around the MPP. A small step size produces a smaller oscillation, but it reduces the speed of the tracking (LU; RAGHUNATHAN; ROY, 2010b).

The main disadvantage of this technique is the power consumption in the iterative control and in the power measurement. The algorithm usually is implemented in software in the CU, although in (BANDYOPADHYAY; CHANDRAKASAN, 2012) the authors use a dedicated digital circuit to run the algorithm. The proposed circuit con-

Figure 110 – Concept of P&O in a PV cell.



Source: (The author, 2014)

sumes little power, and estimates the power without measuring the current, thereby decreasing the additional consumption of the MPPT unit. The P&O algorithm is typically applied to analyze the power supplied by the E-EPS instead of the power supplied by the EPS with the purpose of extracting the available power from the E-EPS (SHAO; TSUI; KI, 2007; LU; RAGHUNATHAN; ROY, 2010b).

E.5 POWER REDUCTION TECHNIQUES IN THE HPMU

In general, the efficiency of PPUs, PMUs, and a PPC is determined by the losses in the power flow path, the consumption necessary for the operation of the system, and the idle consumption. In high power consumption applications (> 100 mW), the losses in the power flow path usually dictate the overall value of the efficiency. On the other hand, in low power consumption applications, reducing all types of losses is important to achieve the goal of high efficiency. In this section, we outline the techniques used in the design of the PPU and the PPC to maximize their efficiency.

E.5.1 Optimum design of the switches

For establishing the size of the MOSFET switches embedded in a PPU, the main objective is to minimize their dissipation losses. To achieve this goal, the designer must reduce simultaneously all the switches' losses, which are conduction losses in the active state (P_{on}), the switching losses due to the device's output capacitance (P_{DS}), and the losses from driving the gate (P_{GD}). We can calculate these losses as follows (RAMADASS, 2009; STRATAKOS; BRODERSEN; SANDERS, 1998; KADIRVEL et al., 2012):

$$P_{GD} = k_{GD} \cdot E_{GD0} \cdot f_s \cdot W; \quad (E.13)$$

$$P_{DS} = k_{DS} \cdot E_{DS0} \cdot f_s \cdot W; \quad (E.14)$$

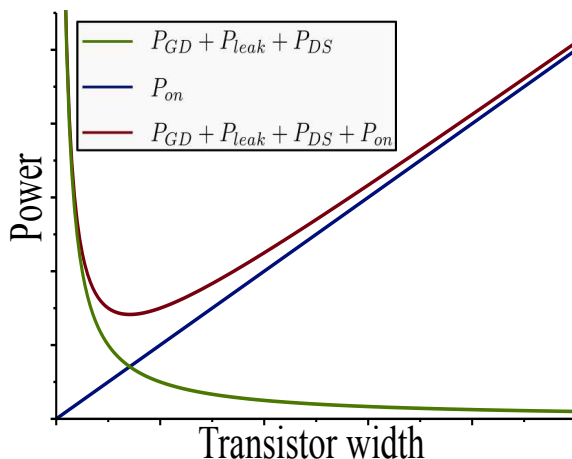
$$P_{on} = k_{on} \cdot I_{rms}^2 \cdot \frac{R_{on0}}{W}; \quad (E.15)$$

where E_{GD0} is the energy (per unit width) necessary to turn the switch on, E_{DS0} is the energy stored (per cycle and unit width) in the parasitic capacitances at the transistor output, f_s is the switching frequency, W is the switch width, I_{rms} is the rms current through the switch, and k_{GD} , k_{DS} , k_{on} are parameters dependent on the technology, the converter topology, and the application (STRATAKOS; BRODERSEN; SANDERS, 1998). Besides these losses, in ultra low-voltage converters we must consider the idle losses in the device (P_{leak}), particularly the losses by the switch's operating in the weak-inversion region (switch off). We can express these losses as (ROY; MUKHOPADHYAY; MAHMOODI-MEIMAND, 2003)

$$P_{leak} = k_{leak} \cdot I_{leak0} \cdot W, \quad (E.16)$$

where I_{leak0} is the idle current per unit width, and k_{leak} is a constant dependent on the technology, the converter topology, and the application. For a given frequency, the optimization of the switch involves minimizing the losses to find the optimum value of W which ensures efficiency maximization by minimizing the losses, as illustrated in Figure111. In optimizing the converter losses, we must consider all the switches together with the conversion frequency to guarantee that the system operates at the global minimum of the system. In (BANDYOPADHYAY et al., 2014), the authors propose the optimization of a boost-type source. As the rms current through the switches changes with time, the optimum value of its width also changes. Based on this

Figure 111 – Losses in the switches as a function of the width.



Source: (The author, 2014)

fact, in (PARAYANDEH et al., 2011), the authors propose a system of maximum efficiency point tracking, where the equivalent width of the integrated switches changes by the combination of switches, depending on the load conditions.

E.5.2 Design of low-power controllers

For low-power converters, the control circuit consumes a significant fraction of the total energy budget. Thus the CU consumption implies a substantial degradation of the system efficiency. The evolution of integrated circuit (IC) manufacturing allows fabricating all circuits with low voltages, hence providing low-power consumption (PATELLA et al., 2003; BANDYOPADHYAY; RAMADASS; CHANDRAKASAN, 2011; WEI; HOROWITZ, 1996). Generally, for the HPMUs of the WBAN nodes, in the active mode the load consumes a high level of power compared to the power available from the EPSs. Hence the load consumes the energy harvested in a time much shorter than the harvest time. Therefore, we must reduce the idle consumption of the controller to decrease the impact of this consumption on the efficiency of the design. In (BANDYOPADHYAY; RAMADASS; CHANDRAKASAN, 2011), the authors adopt the design method known as *power gating* to design digital circuits so that the controllers are capable of operating with low energy consumption

in idle mode. In conjunction, these design techniques help to maximize the global efficiency of the system by reducing the consumption of the PMU's CU.

E.5.3 Soft switching

We can classify the operation of a power converter switch during the transitions between states (from active to open and vice versa) as soft or hard switching. In soft switching, the CU forces the state transitions to occur under favorable conditions of the switch current and voltage. On the other hand, in hard switching, the CU forces the transitions regardless of the conditions of the switch current and voltage. The types of soft switching are zero current switching (ZCS) and zero voltage switching (ZVS) (ERICKSON; MAKSIMOVIC, 2001). In the former, we set the current through the switch to zero before we stop supplying voltage to its gate. In the latter, we set the voltage across the switch to zero before we apply any voltage to its gate. A soft-switching converter performs soft-commutation transitions in one or some of its switches. However, to thoroughly understand the commutation losses, we must examine all the transitions of each switch.

Researchers have much studied soft-switching PPU's and PPC's, which present a reduction in commutation losses (ERICKSON; MAKSIMOVIC, 2001). However, in the context of ultra low-power synchronous converters, only a few works have employed this switching technique due to the high consumption of the switch control logic circuits, such as (BANDYOPADHYAY; CHANDRAKASAN, 2012; RAMADASS; CHANDRAKASAN, 2011; BANDYOPADHYAY et al., 2014), where the authors develop ultra low-power DC-DC converters by using synchronous ZCS DC-DC converters and techniques to minimize the idle consumption.

E.6 HPMU MINIATURIZATION TECHNIQUES

In general, high-efficiency PPU's, PMU's, and PPC draw upon inductors. For MIMO and MISO converters, we can reduce the physical dimensions, although they are not fully integrated. Another possibility is to share inductors between the converters of the conversion system, as proposed in (BANDYOPADHYAY; CHANDRAKASAN, 2012; SHI et al., 2011).

APPENDIX F – MPP examples of linear and non-linear EPS

Table 40 – Specifications of the UT9-28-F2-4040-TA-W6 TEC module.

Width (mm)	Length (mm)	Height (mm)	Area (mm ²)	I_{max} (A)	V_{max} (V)	ΔT_{max} (K)	T_h (K)
40	44	2,8	1760	9,2	36,7	68	300

Source: (Datasheet,2015)

F.1 THE ON-BODY TEG

We chose the UT9-28-F2-4040-TA-W6 (a commercial thermoelectric cooler) to calculate its P_{avs} under typical WBAN environmental conditions. It is a high heat pumping density thermoelectric module fabricated by the Laird Technologies Company. It is assembled with bismuth telluride semiconductor material and thermally conductive aluminum oxide ceramics. The device datasheet provides the information summarized in Table 40. We modeled this thermoelectric cooler as a generator according to the method proposed in (LINEYKIN; BEN-YAAKOV, 2005), where the authors calculate the model parameters of the TEG from the cooler specifications:

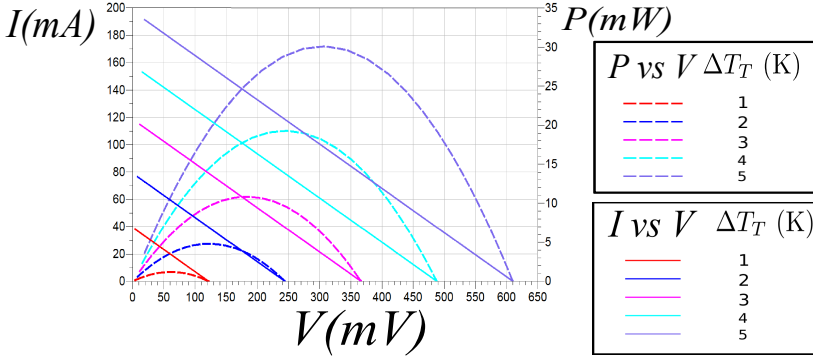
$$R_T = \frac{V_{max} (T_h - \Delta T_{max})}{I_{max} T_h} = R_t N_T \quad (F.1)$$

$$\Theta_T = \frac{\Delta T_{max}}{I_{max} V_{max}} \frac{2T_h}{T_h - \Delta T_{max}} = \frac{\Theta_t}{N_T}; \quad (F.2)$$

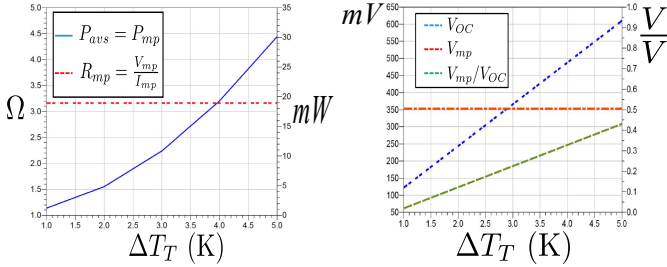
$$\alpha_T = \frac{V_{max}}{T_h} = \alpha_t N_T; \quad (F.3)$$

where R_t and Θ_t are the equivalent electric and thermal resistance of the thermopile, respectively. α_T is the thermal sensitivity of the TEG. The model parameter calculated was: $R_T = 3,08 \Omega$, $\Theta_T = 0,52 \text{ KW}^{-1}$, $\alpha_T = 122,33 \text{ mVK}^{-1}$. We carried out the simulations of the TEG under low-temperature gradients (lower than 5K) in Keysight Advanced Design System (ADS[®]) using the model presented in Section D.1. We plot the results in Figure 112. As we expected, under a fixed temperature difference (i.e., ΔT constant), the TEG output power takes its maximum value if the output voltage is 50 % of the open-circuit voltage (i.e., V_T). This is shown in 113(a) and is corroborated by the direct calculation in Figure 113(c). Furthermore, in Figure 113(b) is presented explicitly that the impedance must be constant and equal to R_T for extracting the P_{avs} of the TEG.

Figure 112 – Simulated results of the UT9-28-F2-4040-TA-W6 device.



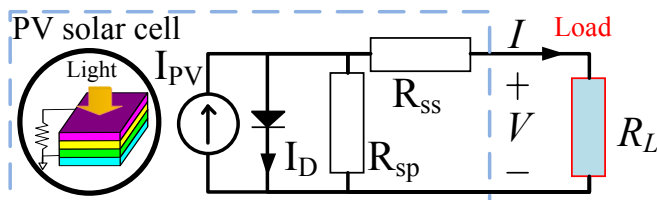
(a) I-V & P-V curves of the commercial device.

(b) Optimum load (R_{mp}) and (c) Relation between open voltage (V_{OC}) and optimum voltage (V_{mp}).

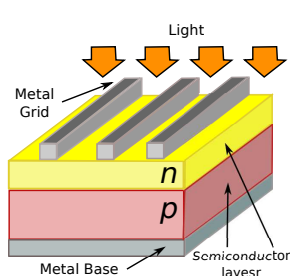
Source: (The author, 2014)

In addition, assuming MPP operation and using both (D.2) and the model, we calculated the harvested energy under typical WBAN environment conditions, which are a thermal density of the human body of $250 \text{ cm}^2 \text{KW}^{-1}$ (LEONOV, 2011), a temperature gradient between the body and environment of 1 K (i.e., $\Delta T = 1$), and a heat dissipator characterized by a thermal resistance of 5 KW^{-1} (i.e., $\Theta_D = 5 \text{ KW}^{-1}$). The results were $\Theta_{HB} = 14.20 \text{ KW}^{-1}$, $\Delta T_T = 0.64 \text{ K}$, $V_T = 77.96 \text{ mV}$, and $P_{avsT} = 492 \text{ uW}$, hence the calculated typical D_W of this TEG was $0.28 \text{ } \mu\text{W mm}^{-2}$.

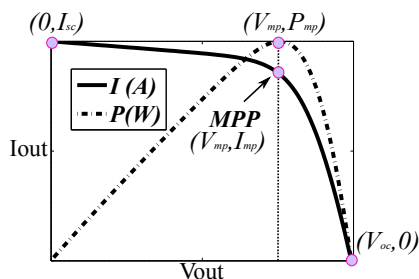
Figure 113 – PVSC model, I-V curve and diagram.



(a) PVSC model based on the 1D&2R circuit.



(b) PVSC Diagram



(c) I-V characteristics of a PVSC.

Source: (The author, 2016)

F.2 AN OUTDOOR PVSC

A photovoltaic system converts solar energy into electricity. The primary device of a photovoltaic system is a PVSC. These cells can be grouped to form panels or matrices (JEONG; JIANG; CULLER, 2008). Photovoltaic devices have nonlinear I-V characteristics with several parameters which are usually adjusted experimentally (RAO; PADMANABHAN, 1973). In essence, PVSCs are semiconductor diodes (p-n junctions) exposed to light (SEDRA; SMITH, 2007). PVSCs are composed of a thin semiconductor layer doped on one of its sides to form a p-n junction, and two electrical connections, a thin metal grid on the semiconductor surface exposed to the sun, and a metal layer on the other side, as illustrated in Figure 113(b). Free charge carriers are generated when the energy of the incident photons is enough to release electrons from covalent bonds. This phenomenon depends fundamentally on the semiconductor material and the wavelength and power of the incident light (VILLALVA; GAZOLI; FILHO, 2009).

Only monocrystalline and polycrystalline silicon cells are com-

mercially available. However, the monocrystalline ones are commonly used in both outdoor and indoor applications because they have a wide spectral sensitivity (300–1100 nm) (IXYS, 2011). The light power (i.e., the irradiance, G , in Wm^{-2}) in the outdoors is much greater than indoors. For example, in offices with lighting from incandescent or halogen lamps, the output power might be around 100 times lower than direct sunlight. In the case of fluorescent lighting, the power might be approximately 200 to 500 times lower due to the limited spectrum of the light source. However, the worst case is LED illumination, where the power might be 500 times lower. There are several models in the scholarly literature to describe the operation of PVSCs (VILLALVA; GAZOLI; FILHO, 2009; MOHAMED; MAHMOUD, 2013; ZHU et al., 2011; CUBAS; PINDADO; VICTORIA, 2014). However, the electrical model shown in Figure 113(a), is the simplest one that captures almost all the dynamics of a PVSC. Its I-V curve is given by (RAUSCHENBACH, 1980)

$$I = I_{pv} - \underbrace{I_0 \left[\exp \left(\frac{V + IR_{SS}}{n\phi_t} \right) - 1 \right]}_{I_D} - \frac{V + IR_{SS}}{R_{SP}}, \quad (\text{F.4})$$

where I_{pv} models the photovoltaic current generated by the incident light. The Shockley diode equation (i.e., I_D) represents the behavior of a PVSC without incident light, where I_0 is the saturation current of the diode, ϕ_t is the thermal voltage (given by $k_B T / q_e$, where q_e is the charge of the electron, k_B is the Boltzmann constant, T is the temperature in K), and n is the ideality constant of the diode. The contact resistance between the semiconductor and the electrodes is modeled by R_{SS} , and R_{SP} models the leakage current of the p-n junction (JORDEHI, 2016). To model a solar panel composed of several cells, we can rewrite (F.4) as (VILLALVA; GAZOLI; FILHO, 2009)

$$I = I_{pv_c} N_p - I_{0_c} N_p \left[\exp \left(\frac{V + R_{SS_e} I}{N_s \phi_t n} \right) - 1 \right] - \frac{V + R_{SS_e} I}{R_{SP_e}}, \quad (\text{F.5})$$

where N_s is the number of series-connected cells, N_p is the number of parallel-connected cells, I_{pv_c} is the current of each parallel cell, I_{0_c} is the saturation current of each parallel cell, R_{SS_e} is the equivalent series resistance of the panel, and R_{SP_e} is the equivalent parallel resistance.

Without loss of generality, and for simplicity of the notation, we will derive an analytical relation for the MPP only for a PVSC instead of for a solar panel. We start from the principle that at each point of

the PVSC's I-V characteristic curve we can calculate the instantaneous electric power by

$$P = IV, \quad (\text{F.6})$$

where I is the electric current and V is the electric voltage. Naturally, the power has a zero value at the open- and short-circuit points. Between these points, there is a maximum power value (P_{mp}), which is the so-called MPP point ($V = V_{mp}, I = I_{mp}$). This behavior is illustrated in Figure 113(c). We can derive the relation between V_{mp} and I_{mp} by taking into account that at the maximum power point the derivate of the power is zero (CUBAS; PINDADO; VICTORIA, 2014):

$$\left(\frac{dP}{dV}\right)|_{[I_{mp}, V_{mp}]} = \left(V \frac{dI}{dV} + I\right)|_{[I_{mp}, V_{mp}]} = 0 \Rightarrow \left(\frac{dI}{dV}\right)|_{[I_{mp}, V_{mp}]} = -\frac{I_{mp}}{V_{mp}}; \quad (\text{F.7})$$

after differentiating (F.4) we find that

$$\frac{dI}{dV} = -\frac{\left(I_o \cdot R_{SP} \cdot e^{\frac{V+I \cdot R_{SS}}{n \cdot \phi_t}} + n \cdot \phi_t\right)}{(R_{SP} + R_{SS}) \left(I_o \cdot \frac{R_{SP} \cdot R_{SS}}{(R_{SP} + R_{SS})} \cdot e^{\frac{V+I \cdot R_{SS}}{n \cdot \phi_t}} + n \cdot \phi_t\right)}. \quad (\text{F.8})$$

From (F.7) and (F.8) we get

$$\frac{I_{mp}}{V_{mp}} = \frac{\left(I_o \cdot R_{SP} \cdot e^{\frac{V_{mp}+I_{mp} \cdot R_{SS}}{n \cdot \phi_t}} + n \cdot \phi_t\right)}{(R_{SP} + R_{SS}) \left(I_o \cdot \frac{R_{SP} \cdot R_{SS}}{(R_{SP} + R_{SS})} \cdot e^{\frac{V_{mp}+I_{mp} \cdot R_{SS}}{n \cdot \phi_t}} + n \cdot \phi_t\right)}. \quad (\text{F.9})$$

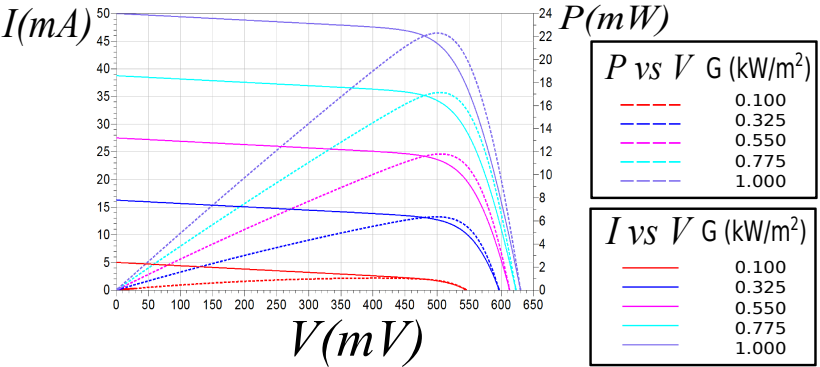
Furthermore, using (F.4), we obtain

$$I_{mp} = I_{pv} - I_o \left[\exp\left(\frac{V_{mp} + R_{SS} I_{mp}}{\phi_t n}\right) - 1 \right] - \frac{V_{mp} + R_{SS} I_{mp}}{R_{SP}}. \quad (\text{F.10})$$

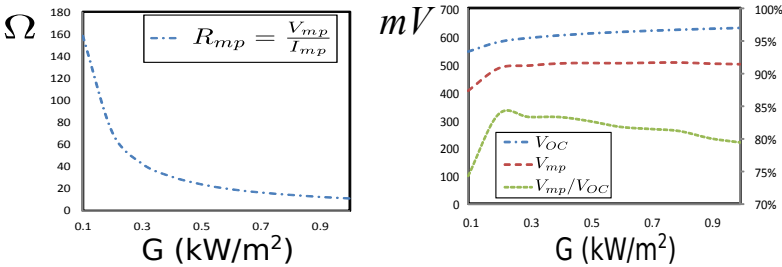
The current and voltage at the MPP can be calculated numerically from (F.10) and (F.9), and using the remarkable points, which are highlighted in Figure 113(c). These points correspond to the following conditions: short circuit ($0, I_{sc}$), voltage and current at MPP (V_{mp}, I_{mp}), and open circuit ($V_{oc}, 0$).

We chose the KXOB22-12X1L (a commercial PVSC) to calculate its P_{avs} under typical outdoor environmental conditions. It is a silicon mono-crystalline PVSC fabricated by the IXYS Company with an typical efficiency of 22% measured at wafer level and under standard outdoor test conditions. The device datasheet (IXYS, 2011) brings the

Figure 114 – Simulated results of the KXOB22-12X1L



(a) I-V and P-V curves of the PVSC.



(b) Optimum load (R_{mp}). (c) Relation between open voltage (V_{OC}) and optimum voltage (V_{mp}).

Source: (The author, 2014)

remarkable points under standard indoors test conditions; the rated values are summarized in Table 41. We modeled this PVSC using the 1D&2R circuit and we extracted the values of the components assuming $n = 1$, following the extraction procedure proposed in (CUBAS;

Table 41 – Specifications of the KXOB22-12X1L under AM1.5g light spectrum.

Area mm x mm	V_{oc} V	I_{sc} mA	V_{mp} V	I_{mp} mA	G $\frac{W}{m^2}$	T °C
22 x 7	0.63	50	0.5	44.6	1000	25

Source: (Datasheet, 2015)

PINDADO; VICTORIA, 2014), detailed in Section 3.5.1. The resulting extracted values were $R_{SS} = 1.21\Omega$, $R_{SP} = 165.2\Omega$, $I_0 = 1.04$ pA, and $I_{pv} = 50.37$ mA. Previous work has shown that the current generated by the incident light is directly proportional to the normal irradiation (G)(VILLALVA; GAZOLI; FILHO, 2009). Hence, adopting a small signal approach in G and assuming a constant temperature, I_{pv} can be calculated as

$$I_{pv} = \frac{I_{pv_{STC}}}{G_{STC}} \cdot G = k_{G_{STC}} \cdot G, \quad (F.11)$$

where $I_{pv_{STC}}$ and G_{STC} are the I_{pv} and G at standard test conditions (STC), respectively, while $K_{G_{STC}}$ is the irradiance sensitivity of the I_{pv} parameter. We used this modeling approach to simulate the PVSC in ADS®. The simulated I-V and P-V characteristic curves of the KXOB22-12X1L are shown in Figure 114(a). In Figure 114(b), we observe that the harvester output impedance must vary to achieve the MPP. Also according to Figure 114(c), the harvester output voltage in the MPP is almost proportional to the open-circuit voltage over a wide range of input radiation. In addition, assuming MPP operation, we calculated the harvested energy under typical outdoor conditions, which are $G = 1 \times 10^3 \text{ Wm}^{-2}$ with AM1.5g spectrum at 25°C. The resulting P_{avs} was 178.4 mW, hence the calculated typical D_W of this PVSC is 148.16 $\mu\text{W mm}^{-2}$.

APPENDIX G – Energy constraints imposed by the harvesting EPSs in WBAN environmental conditions

Table 42 – Power of the most significant harvesters for W-WBAN

Energy type	Ambient power	Harvested D_W			Harvester
Thermal					
Indoor	20	$\frac{mW}{cm^2}$	30	$\frac{\mu W}{cm^2}$	TEG
Outdoor	100	$\frac{mW}{cm^2}$	1	$\frac{mW}{cm^2}$	
EM (Light)					
Indoor	0.1	$\frac{mW}{cm^2}$	10	$\frac{\mu W}{cm^2}$	PVSC array
Outdoor	100	$\frac{mW}{cm^2}$	10	$\frac{mW}{cm^2}$	
Kinetic					
@ 5 Hz	0.5	$\frac{m}{s^2}$	4	$\frac{\mu W}{cm^3}$	Piezoelectric
@ 50 Hz	1	$\frac{m}{s^2}$	4	$\frac{\mu W}{cm^3}$	
EM (RF)					
GSM	4	$\frac{mW}{cm^2}$	1	$\frac{\mu W}{cm^2}$	Rectifying antenna
Wi-Fi	1	$\frac{mW}{cm^2}$	0.25	$\frac{\mu W}{cm^2}$	

Source: Based on (COLOMER-FARRARONS et al., 2013; VULLERS et al., 2010)

G.1 HARVESTING ENERGY CONSTRAINTS IN WEARABLE WBAN APPLICATIONS

When the harvester is on or around the human body, it can harvest energy from three types of primary sources: kinetic from the body's movement, electromagnetic from light or RF waves around the body, and thermal energy from the heat flow of the human body. (LEONOV, 2011). Moreover, they can be considered as uniformly distributed throughout the body because they are present in almost all parts of the body. However, their intensity varies depending on the position of the harvester on or around the body (LEONOV, 2011; COLOMER-FARRARONS et al., 2013; VULLERS et al., 2010). All the ambient sources are uncontrollable and unpredictable, considering their stochastic nature, except for voluntary kinetic energy. (RAMÁREZ, 2014). To increase the robustness of the EPS, some authors have proposed HPMUs fed by several harvesters (BANDYOPADHYAY; CHANDRAKASAN, 2012; COLOMER-FARRARONS et al., 2012), which are so-called hybrid HPMUs.

Table 42 presents some reference values of the reported P_{avs} of on-body EPSs under “typical” environmental conditions when the

harvester is on or around the human body. These values cannot be used for an exhaustive comparison of the harvesters because environmental conditions are reported as typical and they are not standard, and vary significantly from one reference to another. However, these values can be used to gain numerical insight into the energy constraints imposed by the harvester in wearable WBAN applications.

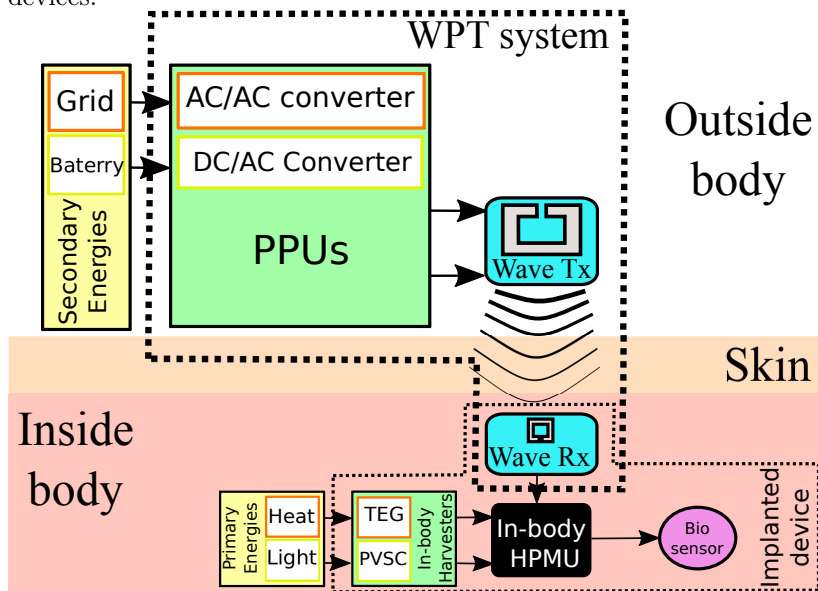
G.2 HARVESTING ENERGY CONSTRAINTS IN IMPLANTED WBAN APPLICATIONS

When the harvester is in the human body, it can harvest energy from many types of primary sources, which are typically located in some organs of the body. For example, in (ZURBUCHEN et al., 2013), the authors implement a harvester that extracts kinetic energy from heart movement. As another example, in (MERCIER et al., 2012), the author developed an implanted device powered by electric energy supplied by a natural battery that is in the inner ear. As a final example, in (RAPOPORT; KEDZIERSKI; SARPESHKAR, 2012), the authors propose an implantable fuel cell that extracts energy from glucose present in the cerebrospinal fluid. Considering their stochastic nature, all the primary sources located in an organ (or constitutive system of the body) are non-controllable but predictable, because the human body maintains its internal conditions (i.e., homeostasis state) by mechanisms of self-regulation (e.g., the metabolism) (RAMÁREZ, 2014).

These conventional in-body harvesters cannot be used for powering subcutaneous implants because the energy that they collect is not uniformly distributed throughout the body. Furthermore, there are only a few natural sources evenly distributed under the human skin (AYAZIAN; HASSIBI, 2011). As an example, in (HAEBERLIN et al., 2014), the authors explored subcutaneous light and PVSCs for powering a cardiac pacemaker, which was tested in vivo in a pig. Thermal energy is another in-body source which is almost uniformly distributed inside the body because there are temperature differences between the inner surface of the skin and the body core. The authors of (VENKATASUBRAMANIAN et al., 2007) develop an optimized TEG for powering implanted pacemakers. Considering their stochastic nature, these natural sources are non-controllable and unpredictable.

Besides the natural harvesting approach, the artificial generation of in-body energy sources has also been proposed and used. In this approach, an external (on-body) unit transfers power to the inside

Figure 115 – Conventional WPT system for powering subcutaneous devices.



Source: (The author, 2017)

of the body, generating an artificial power density that is harvested by the implanted device, as we illustrated in Figure 115. Wireless transfer techniques used are: 1) Near-field inductive coupling (GHOVAN-LOO; ATLURI, 2007; CABRERA; SOUSA, 2014; RAMRAKHYANI; MIRABASI; CHIAO, 2011); 2) EM middle- (ODRISCOLL; POON; MENG, 2009; CABRERA; SOUSA, 2016) and far-field (LIU et al., 2014; FALKENSTEIN; ROBERG; POPOVIC, 2012) links; 3) Optical powering (BEREUTER et al., 2017; GOTO et al., 2001); 4) Ultrasonic powering (ZHU; MOHEIMANI; YUCE, 2011; OZERI; SHMILOVITZ, 2010). In (AGARWAL et al., 2017), the authors present a complete review of these techniques based on their power budgets. Considering their stochastic nature, all of these artificial sources are partially controllable.

Table 43 summarizes the power extracted from the in-body harvesters reported in some selected papers. These values can be used as a reference for the P_{avs} of the in-body EPSs when the harvester is implanted in the dermis. However, they cannot be used for an exhaustive comparison because the test conditions are not reported or are not

Table 43 – Comparison in-body harvesting sources uniformly distributed.

References	(GHOVANLOO; ATLURI, 2007)	(CIABRERA; SOUSA, 2016)	(LIU et al., 2014)	(GOTO et al., 2001)
WPT technique	Near-field inductive coupling	EM mid-field	EM far-field	Optical powering
Type of source	Artificial	Artificial	Artificial	Artificial
Frequency or wavelength	1 MHz	986 MHz	2.45 GHz	735 nm
Implanted size	10 cm ²	2.25 mm ²	32 mm ²	0.6 cm ²
Distance	10 mm	15 mm	20 cm	10 mm
$T_a - R_a$				
Medium	Air	Air	Liquid skin	Chicken skin
Energy source	External AC	External RF	External Antenna	External Laser
Harvested P	-	0.4 mW	25.1 uW	-
Harvested D_W	800 $\mu W/mm^2$	180 $\mu W/mm^2$	0.78 $\mu W/mm^2$	10 $\mu W/mm^2$
Harvester	Inductor	Inductor	Antenna	PVSC

References	(VENKATASUBRAMANIAN et al., 2007)	(BEREUTER et al., 2017)	(OZERI; SHMILOVITZ, 2010)
	2007	2017	2010
WPT technique	Thermal	Ligth	Ultrasonic powering
Type of source	Natural	Natural	Artificial
Frequency or wavelength	-	0-3000nm	673 kHz
Implanted size	138 mm ²	3.53 cm ²	3.54 cm ²
Distance	-	-	5mm
$T_a - R_a$			
Medium	-	Skin optical emulator	water
Energy source	Gradient (2 K)	Indoor H.L.	External ultrasound generator
Harvested P	-	45 uW	100 mW
Harvested D_W	10 $\mu W/mm^2$	0.13 $\mu W/mm^2$	0.28 $\mu W/mm^2$
Harvester	TEG	PVSC	Piezoelectric

Source: (The author, 2017)

equivalent. Yet, these values can be used to gain numerical insight into the energy constraints imposed by the harvester on implanted WBAN applications. The WPT systems based on inductive coupling in near- and mid-field links provide the highest power density. In addition, Table 43 shows that there is a trade-off between the size and the power of the implant. Furthermore, we can miniaturize the implant using a higher operating frequency for the link. However, this size reduction decreases the power that the implant can harvest. The designer resolves this trade-off using systems based on mid-field EM, which achieves a good compromise between power and size.

APPENDIX H – The Power–Efficiency Trade-Off on a linear EPS

When a DC voltage source supplies energy to an electric load, it can operate either for maximum power transfer and low efficiency (50%) or with an acceptable efficiency with less power transferred. In this appendix, an analytic expression is developed to quantify this trade-off. Moreover, this expression is validated by an experimental circuit demonstrator. Finally, we use the ideal battery model and the proposed expression to analyze the trade-off between the runtime and consumed power in a generic cell-phone.

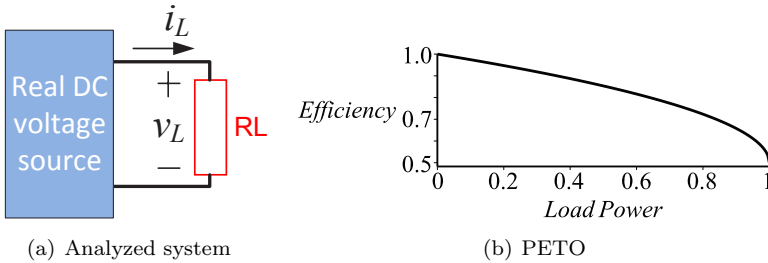
H.1 INTRODUCTION

In the energy flow problem illustrated in Figure 116(a), the DC source cannot operate at maximum efficiency with maximum transfer power. Therefore, to increase its efficiency, less power than the maximum available needs to be supplied (KONG, 1995), as illustrated in the Figure 116(b). This power-efficiency trade-off (PETO) is present in many circuits and systems, such as portable electronic devices and electric motors.

In one of earliest publications about PETO (1978), Edison and his chief assistants researched the design techniques for DC electric generators and determined that a generator with smaller internal resistance than its load is more efficient than a generator with internal resistance equal to its load (STROSS, 2008). Until that moment, the academics believed that the maximum possible efficiency (for any electric energy flow problem) was 50%, reflecting a misunderstanding of the maximum power transfer theorem (MPTT). In (MADI, Dept. Elect. Eng., M.S. thesis, M'Hamed Bougara of Boumerdes Univ., Algeria. 2010), an analytical study of the application of the MTTP to AC and DC voltage sources was made and even though it is still at an early development stage, it contains interesting ideas. For instance, the authors of that paper propose an indirect analytic expression to quantify the PETO for the DC and AC Thevenin equivalent circuit, using an intermediate variable.

Currently, most electronic devices must be portable and must be connected to the Internet (PANG, Dept. Elect. Eng., Ph.D. thesis, Royal Institute of Technology Univ., Stockholm, Sweden. 2013). Typically, device portability is associated with the energy technologies that have been adopted (i.e., battery and DC/DC converters) because they are the element least likely to change during the development cycle of the product (ERICKSON; MAKSIMOVIC, 2001). Currently, there

Figure 116 – Analyzed energy flow problem.



Source: (The author, 2013)

are mainly devices powered by batteries (CHEN; RINCON-MORA, 2006) and more recently by energy harvesters (RINCON-MORA, 2013; MI; ALI; ISLAM, 2013). However, the design of such devices must face a trade-off between functionality (i.e., dissipated power) and portability (i.e., battery running time, weight, size) (D'AMBROSIO et al., 2014). In other words, the engineers need to take the PETO into account to achieve the required specifications and, as a result, an optimum operating point (i.e., optimum load) can be found and then used as a constraint in the electronic design of the system.

In electric circuits textbooks, the PETO is not presented in an integrated approach. Typically, these texts introduce a discussion of each topic involved, without linking them. For example, to calculate the optimum load, the only solved optimization process presented is the MPTT theorem. Probably for that reason, many junior engineers still believe that MTTP solves any energy flow problem (MCLAUGHLIN; KAISER, 2007). On the other hand, many experienced engineers know that the usefulness of the MTTP is limited in practice because it only achieves one optimization criterion (i.e., maximum load power). Likewise, using the conventional circuit theory, the PETO cannot be analyzed directly when the energy comes from batteries. This is because the source models proposed by classic circuit theory represent neither the storage energy capacity of a battery nor the energy extraction process. In (CHEN; RINCON-MORA, 2006), a circuit model that captures the charge extraction process in batteries was proposed. That was extended in (FAJARDO; SOUSA, Florianopolis, Brasil. 2016), which suggested a DC voltage source with limited stored energy capacity to model some kinds of battery behavior.

This appendix presents a direct analytic expression (i.e., the

source efficiency expressed as a function of the normalized load power) for quantifying the PETO on any source that can be modeled using the circuits shown in Figure 118. This analytic expression allows the design engineer to choose an acceptable operating point of source efficiency ($50\% < \eta < 100\%$) and load power (lower than the maximum available power of the source) to design the electronic load.

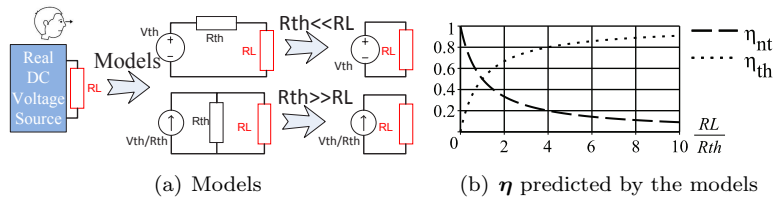
H.2 EFFICIENCY IN A VOLTAGE SOURCE

Electrical circuit models use a combination of circuit elements (i.e., voltage sources, resistors, capacitors, etc.) to model the physical reality of the system. The complexity of the model is determined by the dynamics that the model must predict. This choice defines the variables of interest in the modeling problem. Considering a real DC voltage source that supplies energy to an electrical load (Figure 116(a)), if we define as the behavior of interest only the electric load dynamics, the model must predict at least the current and voltage of the load.

A common technique for modeling a real voltage source is the use of the Norton or Thevenin equivalent circuit as its model (Figure 117(a)). These equivalent circuits predict only the current and voltage performance of the source from the load point of view. Therefore, when this modeling technique was used to predict the real dynamics of sources, a huge error was added to the results. For example, the current and voltage of the load predicted by the Thevenin model are equal to the values predicted by the Norton model. However, the efficiency values predicted by both models are different, as is shown in Figure 117(b); only when the maximum power transfer condition is satisfied ($R_L = R_{th}$) do both models predict the same efficiency. Therefore, without knowledge of the physical laws that govern the internal source behavior, we cannot accurately predict its efficiency.

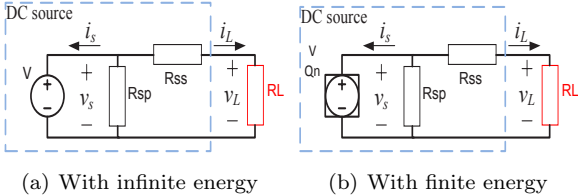
In the next section, the PETO is discussed for any energy source that can be modeled using the circuits shown in Figure 118. In this figure, the circumscribed square (of the voltage source) implies a limited energy of the source. For instance, (FAJARDO; SOUSA, Florianopolis, Brasil. 2016) proposed a battery model based on the circuit presented in Figure 119, which models both the energy restrictions on the batteries and the energy transfer process involved.

Figure 117 – Norton (nt) and Thevening (th)



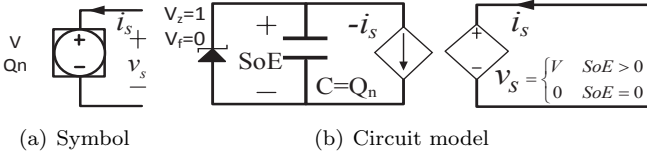
Source: (The author, 2013)

Figure 118 – Real DC voltage source models



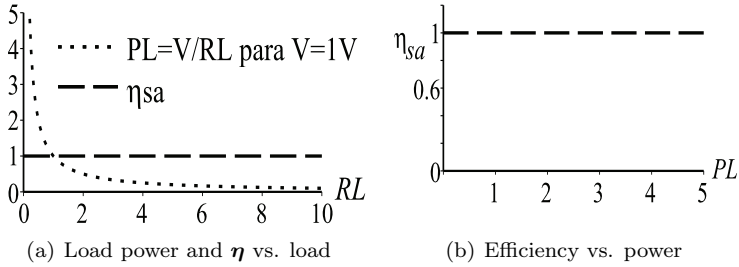
Source: (The author, 2013)

Figure 119 – Ideal battery



Source: (The author, 2013)

Figure 120 – PETO for lossless source



Source: (The author, 2013)

H.3 POWER-EFFICIENCY TRADE-OFF

When a real DC voltage source supplies energy to an electric load, it is impossible to deliver the maximum available power to the load and simultaneously to achieve the maximum source efficiency. Further, when the maximum efficiency is achieved, the power dissipated by the load is less than the maximum available power of the source (P_{avs}). Furthermore, between these two extreme points, we can only increase the load power by decreasing the efficiency, and vice versa. Considering Figure 117, the general expression for the energy consumed by the load (E_c), the energy generated by the source (E_g), and the efficiency (η_s), are given by:

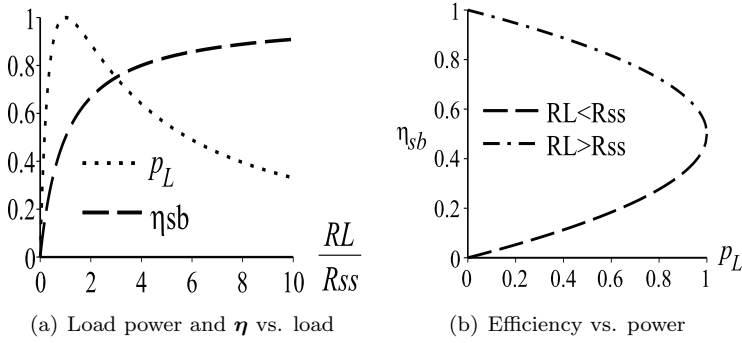
$$E_g = t_s \bar{P}_s = - \int_0^{t_s} (i_s(t) \cdot v_s(t)) \cdot dt; \quad (H.1)$$

$$E_c = t_s \bar{P}_L = \int_0^{t_s} (i_L(t) \cdot v_L(t)) \cdot dt; \quad (H.2)$$

$$\eta_s = \frac{E_L}{E_s} = \frac{\bar{P}_L}{\bar{P}_s}, \quad (H.3)$$

where \bar{P}_L is the mean power dissipated by the load, \bar{P}_s is the mean power generated by the source, and t_s is the runtime of the source. For simplicity in the presentation of concepts, the PETO will be analyzed for a lossless source ($R_{ss} = 0, R_{sp} = \infty$), a source without loss of self-consumption ($R_{sp} = \infty$), and finally the general case.

Figure 121 – PETO for a source w/o loss of self-consumption



Source: (The author, 2013)

H.3.1 PETO for lossless voltage source ($R_{ss} = 0, R_{sp} = \infty$)

Using (H.1), (H.2) and (H.3), the following expressions for the mean dissipated power and the efficiency were obtained:

$$\bar{P}_{L_a} = \frac{V^2}{RL}; \quad (H.4)$$

$$\eta_{sa} = 1. \quad (H.5)$$

For this circuit, the efficiency is 1, and the maximum available power is infinite. Additionally, the efficiency is independent of the load. As a consequence, there is no PETO. The efficiency and the dissipated power regarding resistive load value are shown in Figure120(a). Further, the efficiency versus the load power is shown in Figure120(b).

H.3.2 PETO for voltage source w/o loss of self-consumption ($R_{ss} \neq 0, R_{sp} = \infty$)

Using (H.1), (H.2) and (H.3), expressions for the mean dissipated power (H.6) and the efficiency (H.7) were obtained. When $RL = R_{ss}$, the power dissipated by the load is a maximum (P_{avs}); this power can be calculated by (H.8). Using (H.6) and (H.7), we obtain the

normalized load power (p_L), given by (H.9).

$$\bar{P}_{L_b} = 4P_{avs} \frac{\frac{RL}{R_{ss}}}{\left(1 + \frac{RL}{R_{ss}}\right)^2}; \quad (\text{H.6})$$

$$\eta_{s_b} = \frac{\eta_{s_a}}{1 + \frac{R_{ss}}{RL}}; \quad (\text{H.7})$$

$$P_{avs} = \frac{V^2}{4 \cdot R_{ss}}; \quad (\text{H.8})$$

$$p_L = \frac{\bar{P}_{L_b}}{P_{avs}} = \frac{4 \cdot \frac{RL}{R_{ss}}}{\left(1 + \frac{RL}{R_{ss}}\right)^2}. \quad (\text{H.9})$$

In order to analyze the supplied power and the efficiency of this circuit, we plot them regarding the normalized load (RL/R_{ss}) in Figure 121(a). Considering this figure, it is clear that the efficiency is maximized when the load is much greater than the series resistance of the source ($RL \gg R_{ss}$). However, satisfying this condition implies a reduction of the power delivered to the load. On the other hand, the load power is maximized when the resistive load is equal to the series resistance of the source ($RL = R_{ss}$), which leads to an efficiency of 50%. In order to illustrate this PETO, we plot the efficiency versus power in Figure 121(b). When the resistive load is greater than the series resistance of the source ($RL > R_{ss}$), it is clear that a trade-off occurs, because we can exchange power for efficiency, and vice versa. The load range where the PETO exists, typically, is the load region where we achieve the best compromise between efficiency and power consumption. For this PETO, the limits are 100% of efficiency and 100% of p_L . We cannot reach these limits simultaneously; we can achieve: a p_L of 0% with an efficiency of 100% or a p_L of 100% with an efficiency of 50%. A good compromise of this PETO is p_L of 75% with an efficiency of 75%. In all the operating points of this PETO, the relation between p_L and the efficiency is described by

$$\eta_{s_b} = 1 - \frac{p_L}{\xi}, \quad (\text{H.10})$$

where $\xi = 2(1 + \sqrt{1 - p_L})$ and $RL \geq R_{ss}$.

H.3.3 PETO for general voltage source ($R_{ss} \neq 0, R_{sp} \neq \infty$)

Using (H.1), (H.2) and (H.3), the particular expressions for the mean dissipated power (H.11) and the efficiency (H.7) were obtained. Using (H.11) and (H.12), we obtain the normalized load power (p_L), given by (H.9).

$$\bar{P}_{L_c} = \bar{P}_{L_b}; \quad (H.11)$$

$$\eta_{s_c} = \frac{\eta_{s_b}}{\left(\frac{R_{ss}}{R_{sp}} \left(\frac{RL}{R_{ss}} + 1 \right) + 1 \right)}; \quad (H.12)$$

$$p_L = \frac{\bar{P}_{L_c}}{P_{avs}} = \frac{4 \cdot \frac{RL}{R_{ss}}}{\left(1 + \frac{RL}{R_{ss}} \right)^2}; \quad (H.13)$$

In order to analyze the supplied power and the efficiency of this circuit, we plot both regarding the normalized load (RL/R_{ss}) in Figure 122(a). From the graph, it is clear that the efficiency and the load power are maximized at different values of the load. The P_{avs} is supplied when (H.14) is respected. On the other hand, the maximum efficiency is achieved when (H.15) is satisfied, and its value is given by (H.16). It is important to notice that RL_p is always greater than or equal to RL_η .

$$RL = RL_p = R_{ss}; \quad (H.14)$$

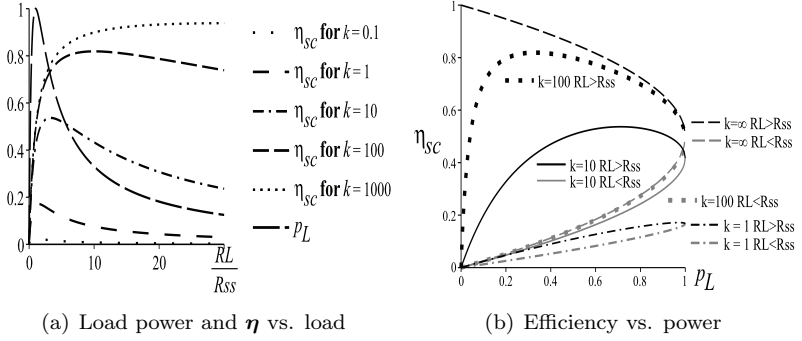
$$RL = RL_\eta = R_{ss} \sqrt{k+1}; \quad (H.15)$$

$$\max \{ \eta_{s_c} \} = \frac{k\sqrt{k+1}}{(1+k+\sqrt{k+1})(k+\sqrt{k+1})}, \quad (H.16)$$

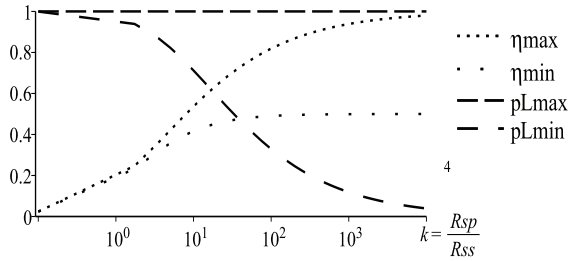
where RL_p is the load value that maximizes the consumed power, RL_η is the load value that maximizes the efficiency, and k is a qualitative measure of the source quality given by $k = \frac{R_{sp}}{R_{ss}}$. A high k means that the power supply is good, i.e., both the self-consumption and the internal conduction losses are low.

When RL is in the PETO range ($RL_p \leq RL \leq RL_\eta$), the load power can increase only if the efficiency decreases. In order to illustrate this, the efficiency versus power graph is plotted in Figure 122(b). In the extreme points of PETO, we can achieve the highest p_L with the lowest efficiency, or vice versa. These limits can be calculated as a function of k , and are plotted in Figure 123. In this source, the

Figure 122 – PETO for the voltage source



Source: (The author, 2013)

Figure 123 – η and load power boundaries vs. k 

Source: (The author, 2013)

relation between p_L and the efficiency is described by

$$\eta_{sc} = \frac{1 - \frac{p_L}{\xi}}{1 + \frac{\xi}{k \cdot p_L}} \quad (\text{H.17})$$

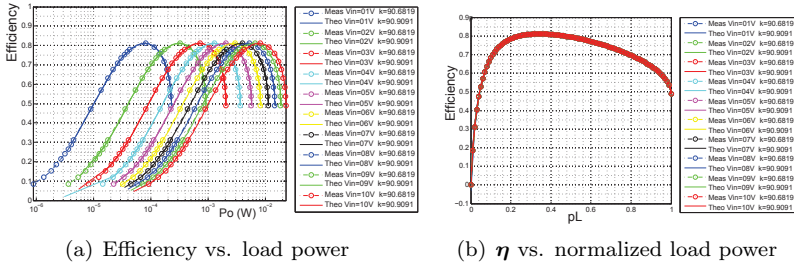
where $R_{ss}\sqrt{k+1} \geq RL \geq R_{ss}$ and $\xi = 2(1 + \sqrt{1 - p_L})$.

H.4 EXPERIMENTAL VERIFICATION

The analytic function proposed, (H.17), was tested with an experimental setup. The implemented system is to demonstrate the validity of the analytic function rather than target a specific application.

Considering Figure 116(a), the real DC source ($k = 90$) was emulated using a power supply ($1 \text{ V} < V < 10 \text{ V}$) and two discrete resistors ($R_{sp} = 100 \text{ k}\Omega$, $R_{ss} = 1.1 \text{ k}\Omega$). The electric load was an adjustable resistor ($100 \text{ m}\Omega < R_L < 10 \text{ M}\Omega$). Using this setup, both the resistive load and the input voltage were swept. The PETO results are plotted in Figure 124, which shows there is a good agreement between the experimental results and the values predicted by (H.17).

Figure 124 – Experimental and theoretical results for PETO on an emulated DC voltage source of $k = 90$

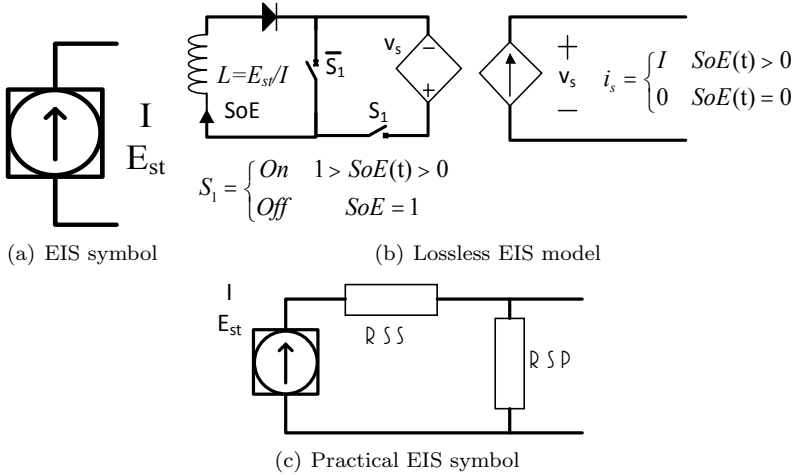


Source: (The author, 2013)

H.5 ENERGY CURRENT SOURCES

As we discussed before, in conventional circuit theory the voltage source models can supply unlimited energy, therefore a direct battery model is unavailable. However, the circuit shown in Figure 118(b) can be used for modeling batteries. Furthermore, this circuit models the battery runtime (i.e., SoE as a function of the load current), its I-V performance (i.e., output voltage as a function of the SoE), its limited power, its energy conversion processing losses, its standby consumption, and self-discharge. This energy source concept can be extended to current sources with limited energy, which can be modeled using the circuit model shown in Figure 125(c).

Figure 125 – Energy current sources



Source: (The author, 2013)

H.6 PETO EXAMPLE: RUNTIME VS. POWER TRADE-OFF IN CELL-PHONE DEVICES

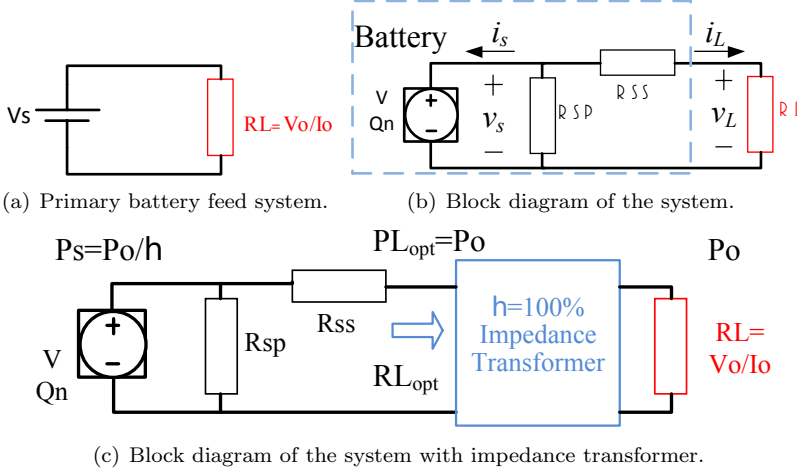
In this section, we analyze the trade-off between the runtime and the consumed power in a generic cell-phone. The proposed problem is presented in Figure 126(a). In this system, a battery feeds a load. In Figure 126(b), the battery was replaced by the Energy voltage source. The generic battery may be specified by its initial State of Charge SoC_0 , its nominal charge storage capacity Q_n , its nominal rated output voltage V , its internal resistant R_{ss} , and its self-discharge resistance R_{sp} . The load is specified by its voltage spec (V_o) and current spec (I_o). In batteries, the concept of SoC (state of the charge) is more commonly used than that of SoE (state of the energy), but both represent the same physical phenomenon.

Q: What is the optimal load impedance?

A: In this power flow problem, an impedance transformer circuit is added (see Figure 126(c)) to the system in order to change the spec of a fixed impedance R_o and fixed power load P_o to a fixed power PL and unknown impedance RL . This addition introduces a new variable into the system design that decouples the design of the load (amplifier, transceiver, etc.) from the design of the power-energy flow. The value

of RL is to be chosen for the particular desired system behavior. This search is called an optimization process, and the value found is the optimum value. The optimum load impedance RL_{opt} is the value of RL that achieves a particular behavior in the system in the “best” way (optimum behavior).

Figure 126 – Battery loaded by a generic load



Source: (The author, 2013)

In this example, we will find the **optimal load impedance** that maximizes the mobile embedded system’s runtime: the system has a fixed power spec and a fixed battery spec. In this context, the optimum load impedance should minimize the power delivered by the battery with a fixed load power, and hence maximize the battery supply time. For a numerical example, we choose a typical cell-phone battery (3.7 V and 1000 mAh) and calculate the PETO for typical cell-phone consumption ($P_o < 5$ W).

Q: Why is this problem related to PETO?

A: Well, the battery runtime t_s can be calculated by (H.18). To maximize t_s the efficiency must be maximized and the load power minimized. However, the load power is P_o , hence we only can maximize the efficiency.

$$t_s = V \cdot SoC_0 \cdot Q_n \frac{\eta}{PL} \quad (H.18)$$

Q: How can one maximize the efficiency if everything in the circuit is known? A: Recall that in this problem, RL is an

unknown: we must find its optimum value for maximizing t_s with a fixed dissipated power P_o .

Q: How do we know that there is an optimal load impedance?

A: For this topology, at least the load power P_o cannot be higher than the value of P_{avs} given by (H.8).

Q: How do we find the optimal load impedance?

A: This is the key point. For algebraic simplicity, we began defining a normalized value of the load power spec (H.19). Next, we find the values of RL that achieve the normalized load power spec: these possible values are found by (H.20). Next, we calculate the efficiency, the highest value of RL maximizes the efficiency (H.21).

$$po = \frac{P_o}{P_{avs}} = 4 \cdot \frac{RL}{R_{ss}} \cdot \left(\frac{RL}{R_{ss}} + 1 \right)^{-2} \quad (H.19)$$

$$RL = R_{ss} \frac{2(1 \pm \sqrt{1 - po}) - po}{po} \quad (H.20)$$

$$RL_{opt} = R_{ss} \frac{2(1 + \sqrt{1 - po}) - po}{po} \quad (H.21)$$

Q: What value of t_s do we achieve by choosing the optimal load impedance?

A: For calculating the maximum t_s . From (H.18) and (H.12) we obtain (H.22). Then, from (H.12) and (H.20) we obtain (H.23). Finally, from (H.22) and (H.23) we find t_s as a function of po .

$$t_s = \frac{Q_n}{\left(\frac{V}{4 \cdot R_{ss}} \right)} \cdot SoC_0 \cdot \frac{\eta(po)}{po} \quad (H.22)$$

$$\eta(po) = \frac{po}{2} \frac{\frac{R_{sp}}{R_{ss}} (2(1 + \sqrt{1 - po}) - po)}{\left(po \frac{R_{sp}}{R_{ss}} + 2(1 + \sqrt{1 - po}) \right) (1 + \sqrt{1 - po})} \quad (H.23)$$

$$t_s = \frac{Q_n \cdot SoC_0}{\left(\frac{V}{2 \cdot R_{ss}} \right)} \frac{\frac{R_{sp}}{R_{ss}} (2(1 + \sqrt{1 - po}) - po)}{\left(po \frac{R_{sp}}{R_{ss}} + 2(1 + \sqrt{1 - po}) \right) (1 + \sqrt{1 - po})} \quad (H.24)$$

Equations (H.21) and (H.24) are valid for all values of po including zero load power. In this special load case ($po = 0$), the optimum value is $RL_{opt} = \infty$, and t_s is limited by the self-discharge resistance (H.25). In the particular case that the load extracts P_{avs} ($po = 1$),

then $\mathbf{RL}_{\text{opt}} = \mathbf{R}_{\text{ss}}$. In this special case, t_s is (H.26).

$$t_s (po = 0) = Q_n \cdot SoC_0 \cdot \left(\frac{V_s}{R_{sp}} \right)^{-1} \quad (\text{H.25})$$

$$t_s (po = 1) = Q_n \cdot SoC_0 \left(\frac{V_s}{2R_{ss} \parallel R_{sp}} \right)^{-1} \quad (\text{H.26})$$

Q: Well, how do all equations answer the problem?

A: Let's try with a numerical example. We choose a typical rechargeable cell Li-Ion (Lithium Ion) battery, with the following specs: nominal capacity of 1000 mAh, nominal voltage 3.7 V, internal resistance of 100 m Ω , 4.795% loss charge in three years, and maximum discharge current of 5 A fully charged. From self-discharge spec, we can calculate a set-discharge resistance using (H.27). Then, we find the optimum value of \mathbf{RL} and its associated battery lifetimes and gains (\mathbf{G}_{MTTP} and \mathbf{G}_{opt}) regarding the lifetime under MPP operation and the other possible value of \mathbf{RL} . The results are summarized in Table H.6. It is important to be explicit about the fact that with the optimization approach, the load power spec is the key factor to achieve the optimum \mathbf{RL} , for example, the optimum \mathbf{RL} value is the same for the open spec load and the short spec load because the load power in both is zero.

In addition, we estimated the consumed power of a typical cell-phone based on the talk times (the officially quoted longest time that a single battery charge will last when you are constantly talking on the phone). The power was estimated based on (H.18) assuming 100% of initial charge and efficiency. The results are presented in Table H.6. From these results, it is clear that the designers of cell-phones must face the trade-off between functionality and runtime because the runtime decreases with an increase in the functionalities of the cell-phone (correlated with consumed power).

$$R_{sp} = \frac{t}{SoC_0 - SoC(t)} \frac{V}{Q_n} \quad (\text{H.27})$$

Q: We began with a current spec I_o and voltage spec V_o , but the load voltage VL and load current IL are different, is this possible?

A: Yes, it is possible. Remember we used an impedance trans-

Table 44 – Estimated Runtime with P_o consumption and optimum RL .

Source Proprieties					Vs (V)	Rss (W)	Rsp (W)	Qn (Ah)	SoC0 (%)	PLmax (W)
					3.7	0.1	20000	1	1	34.2
Load Specs					Optimum Load			Battery Life Gain		
Vo (V)	Io (A)	Po (W)	Ro (W)	po (W/W)	Rlopt (W)	It RLopt (h)	It RLNopt (h)	G_MTP dB (h/h)	G_opt dB (h/h)	
x	0	0	∞	0.00%	∞	5405.4	0.027	37	53	
0	x		0							
5	0.01	0.05	500	0.15%	273.6	72.97	0.027	31	34	
0.01	5		0.002							
5	0.1	0.5	50	1.46%	27.2	7.36	0.0271	21	24	
0.1	5		0.02							
5	1	5	5	14.61%	2.5	0.71	0.028	11	14	
1	5		0.2							
5	4	20	1.25	58.44%	0.46	0.15	0.054	4	7	
4	5		4							
5	6.85	34.2	0.731	100%	0.1	0.05	0.05	0	0	
6.85	5		1.369							

Source: (The author, 2013)

Table 45 – Estimated Runtime with P_o consumption and optimum RL .

Cell phone	Battery Specs			Estimated consumed Power
	Qn (Ah)	It(H)	Vs (V)	Po (W)
Motorola RAZR MAXX	3.3	21.18	3.7	0.576
HTC Vivid	1.62	9.02	3.7	0.665
HTC Rhyme	1.6	8.48	3.7	0.698
Apple iPhone 5	1.44	8.42	3.7	0.633
LG Optimus 3D Max P720	1.52	8.42	3.7	0.668
Sony Ericsson Xperia neo V	1.5	8.41	3.7	0.66
Pantech Burst	1.65	4.46	3.7	1.369
Samsung Galaxy Nexus	1.75	8.2	3.7	0.79

Source: (The author, 2013)

former, a system with 100% efficiency: this device changes the spec impedance Ro in the optimal resistance RL_{opt} . This is illustrated in Fig. 126(c).

Q: How is the impedance transformer implemented? A:

There are many possible implementations. For example, we can use a transformer where the relation between the secondary impedance

(Load) and the impedance referred to the primary winding circuit is governed by a squared turn ratio (n) multiplication factor (H.28).

$$RL = \frac{Ro}{n^2} \quad (\text{H.28})$$

Q: If the source is DC, how can one implement the impedance transformer?

A: There are some possible implementations. For example, a switched DC/DC converter works like a “DC transformer.” For this type of converter, it is possible to find a converter topology turn ratio (M) as a function of the switch control signal duty cycle D . This concept is illustrated in Figures 127 and 128. The relation between the load and RL can be calculated by

$$RL = \frac{Ro}{M^2(D)} \quad (\text{H.29})$$

Figure 127 – Block Diagram of the system with DC transformer model for switched DC/DC converter.

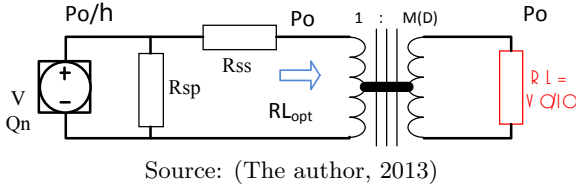
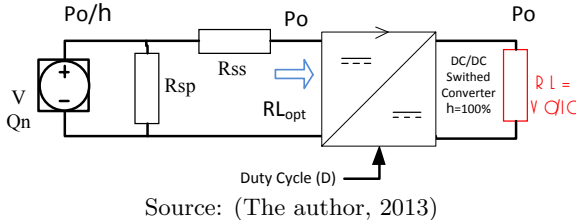


Figure 128 – Block Diagram of the system with DC/DC converter.



Q: Can we build the system without the impedance transformer?

A: If you are in a design step and you may choose the load, the

current and the voltage, you can design the load with the optimum specs ($\mathbf{V_o} = \mathbf{VL}; \mathbf{I_o} = \mathbf{IL}$). The these values can be obtained from (H.30) and (H.31).

$$V_L = V \left(\frac{RL_{\text{opt}}}{R_{ss}} \right) \left(1 + \frac{RL_{\text{opt}}}{R_{ss}} \right)^{-1} \quad (\text{H.30})$$

$$I_L = \frac{V}{R_{ss}} \left(1 + \frac{RL_{\text{opt}}}{R_{ss}} \right)^{-1} \quad (\text{H.31})$$

Assuming the same typical battery as analyzed before, we calculate the optimum voltage and current (Table H.6). From the results, it is clear that for this battery it is not possible to extract the maximum available power, because the optimum current is higher than the maximum discharge current (5 A).

Table 46 – Optimum Voltage and current results.

Source Propierties		Load Specs				
		Po (W)	po (W/W)	RLopt (Ω)	VLopt (V)	ILopt (A)
Vs (V)	3.7	0	0.00%	∞	3.7	0
Rss (Ω)	0.1	0.05	0.15%	273.6	3.699	0.014
Rsp (Ω)	20000	0.5	1.46%	27.2	3.686	0.136
Qn (Ah)	1	5	14.61%	2.5	3.558	1.423
SoC0 (%)	1	20	58.44%	0.46	3.039	6.607
PLmax (W)	34.2	34.2	100.00%	0.1	1.85	18.5

Source: (The author, 2013)

Q: What could happen if the optimum current is bigger than the maximum discharge current battery spec ($IL_{\text{opt}} > I_{\text{max}}$)?

A: You do not design with this optimum value: the battery might explode. In this case, the optimum impedance does not exist. The maximum delivered power is limited by the maximum discharge current battery, given by

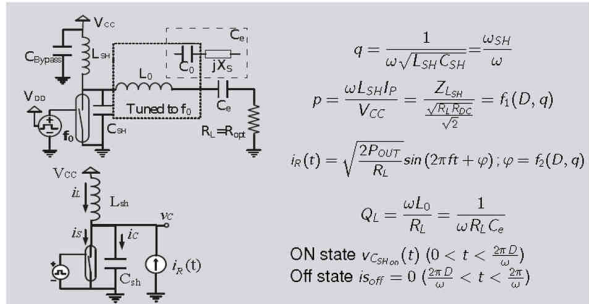
$$P_{O_{\text{max}}} = I_{\text{max}} \cdot V \left(1 - \frac{I_{\text{max}}}{\frac{V}{R_{ss}}} \right) \quad (\text{H.32})$$

Q: What is the maximum power we can deliver with this battery?

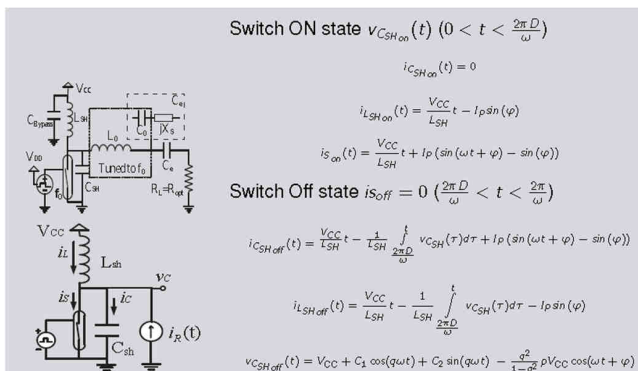
A: The maximum delivered power from (H.32) is 16 W.

APPENDIX I – Tutorial of implementation of the ideal class-E model in Maple

Class-E Model (1/2)



Class-E Model (2/2)



Implementing the model in Maple (1/5)

- 1 step: Define $\varphi=f_1(D,q)$, $\rho=f_2(D,q)$.
- 2 Step: Define the $C1/VCC=f_3(D,q)$, $C2/VCC=f_4(D,q)$.
- 3 step: Define $I_{dc}/I_{ac}=g_x(D,q)$.

$$g_x(D,q) = \frac{I_0}{I_p} = \frac{1}{\frac{2\pi}{\omega} I_p} \int_0^{\frac{2\pi}{\omega}} i_x(t) dt = \frac{\omega}{2\pi} \int_0^{\frac{2\pi}{\omega}} \left(\frac{V_{DD}}{I_p L} t + \sin(\omega t + \varphi) - \sin(\varphi) \right) dt$$

$$= \left(\frac{1 - \cos(2\pi D)}{2\pi} \right) \cos(\varphi) + \left(\frac{\sin(2\pi D)}{2\pi} - D \right) \sin(\varphi) + \frac{D^2 \pi}{p}$$

Implementing the model in Maple (2/5)

- 4 step: Calculate the components Design Set.

$$K_L(D,q) = \omega L / R = ??$$

$$K_C(D,q) = \omega C R = ??$$

$$K_P(D,q) = P_{out} / V_{DD}^2 = ??$$

$$K_x(D,q) = X / R = \omega L / R = -\frac{1}{\omega C R}$$

K	RF-choke [9]	Parallel-Circuit [24]	Even Harmonic Resonant [25]
$K_L = \omega L / R$	$\rightarrow \infty$	0.732	3.534
$K_C = \omega C R$	0.1836	0.685	0.071
$K_P = P_{out} R / V_{DD}^2$	0.5768	1.365	0.056
$K_X = X / R$	1.152	0	-4.903

$$K_L(D,q) = \frac{p(D,q)}{2g_x(D,q)}$$

$$K_C(D,q) = \frac{2 \cdot g_x(D,q)}{q^2 p(D,q)}$$

$$K_P(D,q) = 2 \cdot (g_x(D,q))^2$$

$$V_R = \frac{1}{\pi} \int_0^{2\pi/\omega} (V_C(t) \sin(\omega t + \varphi)) dt$$

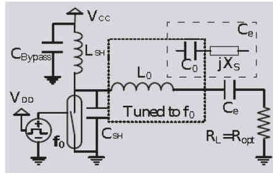
$$V_X = \frac{1}{\pi} \int_0^{2\pi/\omega} (V_C(t) \cos(\omega t + \varphi)) dt$$

$$K_X(q, d) = \frac{V_X}{V_R} = \frac{x_1 + x_2 + x_3 + x_4}{y_1 + y_2 + y_3 + y_4}$$

Implementing the model in Maple (3/5)

- 4 step: Calculate the Components Design Space (Inputs:VDD,Pin,η, Q₀).

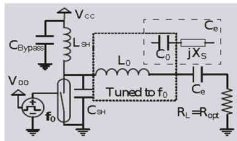
$$\begin{aligned}
 K_p(D, q) &= P_{out} R / V_{DD}^2 \quad \Rightarrow \quad R_{opt} = K_p(D, q) \frac{V_{DD}^2}{P_{out}} = K_p(D, q) \frac{V_{DD}^2}{\eta P_{in}} \\
 K_L(D, q) &= \omega L / R \quad \Rightarrow \quad L_{SH} = K_L(D, q) \frac{R_{opt}}{\omega} = K_L(D, q) K_p(D, q) \frac{V_{DD}^2}{\omega \eta P_{in}} \\
 K_C(D, q) &= \omega C R \quad \Rightarrow \quad C_{SH} = \frac{K_C(D, q)}{\omega R_{opt}} = \frac{K_C(D, q)}{K_p(D, q)} \frac{\eta P_{in}}{\omega V_{DD}^2}
 \end{aligned}$$



$$C_{ypass} = \frac{D}{\frac{\Delta V}{V_{DD}} \frac{4}{\pi} \omega L_{sh}} = \frac{\pi^2 D}{4 \omega K_L(D, q) K_p(D, q)} \frac{1}{\frac{\Delta V}{V_{DD}} \frac{1}{\eta P_{in}}}$$

Implementing the model in Maple (4/5)

- 5 step: Calculate the Components Design Space 1 (Inputs:VDD,Pin,η, Q₀).



$$Q_0 = \frac{\omega_0 L_0}{R} \quad \Rightarrow \quad L_0 = \frac{Q_0}{\omega_0} R = K_p(D, q) \frac{Q_0}{\omega_0} \frac{V_{DD}^2}{\eta P_{in}}$$

$$\frac{1}{\sqrt{L_0 C_0}} = \omega_0 \quad \Rightarrow \quad C_0 = \frac{1}{\omega_0^2 L_0}$$

$$\frac{1}{j\omega C_e} = \frac{1}{j\omega C_0} + jX_s$$

$$\frac{1}{j\omega C_e} = \frac{1}{j\omega C_0} + jK_X(D, q) R$$

$$\frac{1}{C_e} = \frac{1}{C_0} - \omega K_X(D, q) R$$

$$\frac{1}{C_e} = \frac{1 - \omega C_0 K_X(D, q) R}{C_0}$$

$$C_e = \frac{C_0}{1 - \omega C_0 K_X(D, q) R}$$

$$\begin{aligned}
 C_e &= \frac{1}{\frac{1}{C_0} - \omega K_X(D, q) R} \\
 &= \frac{1}{\frac{1}{C_0} - \omega K_X(D, q) K_p(D, q) \frac{V_{DD}^2}{\eta P_{in}}}
 \end{aligned}$$

Implementing the model in Maple (5/5)

- 6 step: Plot the design space using \mathbf{p} as parametric value, and identify the involved trade offs. Define the feasible values of Q with parametric sweeps of the inputs (i.e., VDD, Pin, η, Q_0).

Maple code

You can copy and paste the code.

1. Step Define $\varphi=f_1(D,q)$.

[illegible]

1. Step Define $\rho = f_2(D, q)$.

[illegible]

$K_L(D, q) = \omega L / R$
 $K_C(D, q) = \omega C R$
 $K_P(D, q) = P_{out} R / V_{DD}^2$
 $K_X(D, q) = X / R$

$D = 0.5$

Maximize Gain-Power product

$\omega \cdot P_{OUT} = K_P \cdot K_C \frac{V_{DD}^2}{C_L \cdot R_{opt}^2}$
 $q = 1.442$

$K_L(D, q) = K_L(0.5, 1.442) = 0.6891331864$
 $K_C(D, q) = K_C(0.5, 1.442) = 0.6978567995$
 $K_P(D, q) = K_P(0.5, 1.442) = 1.355039931$
 $K_X(D, q) = K_X(0.5, 1.442) = -0.082383568$
 $p(D, q) = p(0.5, 1.442) = 1.134473117$
 $\phi(D, q) = \phi(0.5, 1.442) = 0.3443797582$
 $g_s(D, q) = g_s(0.5, 1.442) = 0.8231160098$
 $\frac{V_{max}}{V_{DD}}(D, q) = \frac{V_{max}}{V_{DD}}(0.5, 1.442) = 3.651105630$

$K_L(q) = 44.93q^2 - 94.32q + 52.48$
 $K_C(q) = 0.426q^2 - 0.370q + 0.3$
 $K_P(q) = 0.74q^2 - 0.6q + 0.76$
 $K_X(q) = -0.73q^2 + 0.411q + 1.03$

$K_L(q) = 8.085q^2 - 24.53q + 19.23$
 $K_C(q) = -6.07q^3 + 25.93q^2 - 31.071q + 12.48$
 $K_P(q) = -11.90q^3 + 42.753q^2 - 49.63q + 19.70$
 $K_X(q) = -2.9q^3 + 8.8q^2 - 10.2q + 5.02$

Maximize Output-Power

$K_P = \frac{P_{OUT} R_{opt}}{V_{DD}^2}$
 $q = 1.412$

$K_L(D, q) = K_L(0.5, 1.412) = 0.7331560105$
 $K_C(D, q) = K_C(0.5, 1.412) = 0.6841230247$
 $K_P(D, q) = K_P(0.5, 1.412) = 1.363243774$
 $K_X(D, q) = K_X(0.5, 1.412) = -0.00017162645$
 $p(D, q) = p(0.5, 1.412) = 1.210593001$
 $\phi(D, q) = \phi(0.5, 1.412) = 0.2639596324$
 $g_s(D, q) = g_s(0.5, 1.412) = 0.8256039530$
 $\frac{V_{max}}{V_{DD}}(D, q) = \frac{V_{max}}{V_{DD}}(0.5, 1.412) = 3.646760289$

4 step: Calculate the Design Space set.

$$KL=f6(D,q), KC=f7(D,q), KP=f8(D,q).$$

$q1 := 1.442;$		$q1 := 1.412;$	
$CUT1 := 0.5;$		$CUT1 := 0.5;$	
$simpIntf(P(q1, CUT1))$	1.134473117	$simpIntf(P(q1, CUT1))$	1.210593001
$simpIntf(Phi(q1, CUT1))$	0.3443797582	$simpIntf(Phi(q1, CUT1))$	0.2639596324
$simpIntf(gp(CUT1, q1))$	0.8231160098	$simpIntf(gp(CUT1, q1))$	0.8256039530
$simpIntf(C1_YDD(CUT1, q1))$	2.674062883	$simpIntf(C1_YDD(CUT1, q1))$	2.610615846
$simpIntf(C2_YDD(CUT1, q1))$	-1.567715637	$simpIntf(C2_YDD(CUT1, q1))$	-2.138459016
$simpIntf(KL(CUT1, q1))$	0.6891331864	$simpIntf(KL(CUT1, q1))$	0.7331560105
$simpIntf(KC(CUT1, q1))$	0.6978567995	$simpIntf(KC(CUT1, q1))$	0.6841230247
$simpIntf(KP(CUT1, q1))$	1.355039931	$simpIntf(KP(CUT1, q1))$	1.363243774
$simpIntf(KCX(CUT1, q1))$	-0.08238356847	$simpIntf(KCX(CUT1, q1))$	-0.00017162639

5 step: Calculate the Components Design Space (Inputs:VDD,Pin, η , Q0,D).

Inputs:

- Dsp := .5: VDDsp := .5: Pinsp := .10973: effsp := 1: Q0sp := 32.13: fsp := 0.99e9: $\omega_{sp} := \text{evalf}(2 * \text{Pi} * \text{fsp})$: DeltaV_VDD := .1:

Functions:

- Ropt := (q)-> KP(Dsp, q2)*VDDsp^2/(Pinsp*effsp):
- Lsh := (q)-> KL(Dsp, q)*Ropt(q)/ ω_{sp} :
- Csh := (q)-> KC(Dsp, q)/(ω_{sp} *Ropt(q)):
- L0 := (q)-> Q0sp*Ropt(q)/ ω_{sp} :
- C0 := (q)-> 1/(ω_{sp} *L0(q)):
- Ce := (q)-> 1/(1/C0(q)- ω_{sp} *KX2(Dsp, q)*Ropt(q)):
- Cbpass := (q)-> (1/4)*Pi^2*Dsp*Pinsp*effsp/(ω_{sp} *KL(Dsp, q)*KP(Dsp, q)*DeltaV_VDD*VDDsp^2):

5 step: check the implementation

```

> Dsp := 0.5 : VDDsp := 0.5 : Pinsp := 109.73e-3 : effsp := 1 : Q0sp := 32.13 : fsp := 0.99e9 :  $\omega_{sp} := \text{evalf}(2 * \text{Pi} * \text{fsp})$  : q2
:= 0.9 :
> Ropt := (q) ->  $\left( \frac{KP(Dsp, q^2) * VDDsp^2}{Pinsp * effsp} \right)$  :
> evalf(Ropt(q2))
1.800501974 (1)
> Lsh := (q) ->  $\left( \frac{KL(Dsp, q) * Ropt(q)}{\omega_{sp}} \right)$  :
> evalf(Lsh(q2))
1.213578832 10^-8 (2)
> Csh := (q) ->  $\left( \frac{KC(Dsp, q)}{\omega_{sp} * Ropt(q)} \right)$  :
> evalf(Csh(q2))
2.629159069 10^-11 (3)
> L0 := (q) ->  $\left( \frac{Q0sp * Ropt(q)}{\omega_{sp}} \right)$  :
> evalf(L0(q2))
9.610053326 10^-8 (4)
> C0 := (q) ->  $\left( \frac{1}{\omega_{sp}^2 * L0(q)} \right)$  :
> evalf(C0(q2))
2.689329875 10^-12 (5)
> Ce := (q) ->  $\left( \frac{1}{\frac{1}{C0(q)} - \omega_{sp} * KC(Dsp, q) * Ropt(q)} \right)$  :
> evalf(Ce(q2))
2.758761513 10^-12 (6)

```

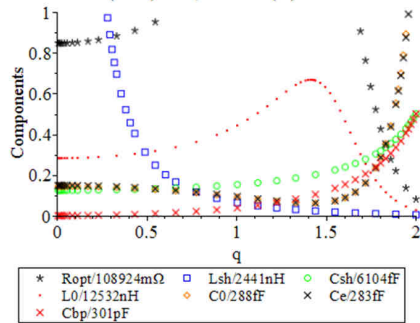
[illegible]

6 step: Plot the components design space

S1 := asterisk:	C1 := black:
C2 := black:	
S3 := circle:	C3 := black:
C4 := black:	
C5 := black:	
C6 := black:	
S6 := point:	C6 := black:

6 step: Plot the components design space

$D(\%)=50$, $V_{dd}(V)=0.4$, $P_{in}(mW)=2$, $\eta(\%)=50$, $Q_0=100$,
 $f(MHz)=415$, $\Delta V/V_{dd}(\%)=10$



APPENDIX J – ADS® models of the link and the indoor PVSC device

J.1 ADS[®] MODEL OF THE INDUCTIVE LINK

We use the link optimized in (CABRERA; SOUSA, 2014) as the WPT interface of the SsWPT examples simulated in Chapter 5. A photograph of this link is shown in Figure 129(a). We summarize the geometric parameters of the link in Table 47. We use the model presented in Section 4.4.2.3 that extends the inductor model discussed in Section 4.4. The model topology is shown in Figure 129(b), and the related equations and parameters are summarized in Tables 48 and 49. We implement this model in the ADS[®] software package with the Z1P.Eqn block (i.e., an impedance controlled by a frequency-dependent function block) and ideal components, as depicted in Figure 129(c).

Table 47 – Geometric parameters of the Link PSOI.

Ind. No.	d_{avg} (mm)	w_{ind} (mm)	Δ_{ind} (mm)	t_c (μm)
Tx PSOI	21.8	2.7	0.4	35
Rx PSOI	4	0.5	0.4	35
d_I	15 mm	Inductor center is aligned, and the inductors are oriented in parallel.		

Source: (The author, 2016)

Table 48 – Summary of the inductive link model.

Component	Equation
$L_{1,2}$	$\frac{2d_{avg1,2}\mu}{\pi} \ln\left(\frac{0.59\pi d_{avg1,2}}{w_{ind1,2}}\right)$
$R_{1,2}$	$2\sqrt{\rho\pi\mu\alpha}w_{ind1,2}^{(\beta_1-1)}f^{(\beta_2+0.5)}d_{avg1,2} + 134\sqrt{\varepsilon^3\mu^5}f^4d_{avg1,2}^4$
$C_{1,2}$	$\frac{\mu\varepsilon}{L}\left(\frac{4d_{avg1,2}}{\pi}\right)^2 + \frac{\varepsilon w_{ind1,2}}{\pi/2} \left[\ln\left(\frac{(d_{avg1,2}+w_{ind1,2})}{\Delta_{ind1,2}^2/2w_{ind1,2}}\right) - \frac{d_{avg1,2}-w_{ind1,2}}{4d_{avg1,2}} \right]$
M	$\mu\sqrt{\frac{d_{avg1}d_{avg2}}{\pi}} \left[\left(\frac{2}{\gamma} - \gamma\right) K_\gamma(\gamma) - \frac{2}{\gamma} E_\gamma(\gamma) \right]$
k_{IL}	$\frac{\mu\sqrt{\frac{d_{avg1}d_{avg2}}{\pi}} \left[\left(\frac{2}{\gamma} - \gamma\right) K_\gamma(\gamma) - \frac{2}{\gamma} E_\gamma(\gamma) \right]}{\sqrt{L_1 L_2}}$
γ	$\sqrt{\frac{4d_{avg1}d_{avg2}}{(d_{avg1}+d_{avg2})^2+\pi(d_{IL})^2}}$

$$\alpha = 128, \beta_1 = 0.3, \beta_2 = -0.1, \mu = \mu_0, \text{ and } \varepsilon = \frac{\varepsilon_{FR4} \varepsilon_0}{2}.$$

Source: (The author, 2016)

Table 49 – Summary of the inductive link model parameters.

Component	Value	Component	Value
L_1	4.718837313922318e-08	L_2	8.628923793429965e-09
C_1	6.452946374341737e-13	C_2	9.713655226140523e-14
$k_{R_{r_1}}$	4.924975464633023e-36	$k_{R_{r_2}}$	5.582362852837703e-39
$k_{R_{s_1}}$	9.134523886887490e-05	$k_{R_{s_2}}$	5.457139370446988e-05
R_1	$k_{R_{s_1}} f^{0.4} + k_{R_{r_1}} f^4$	R_2	$k_{R_{s_2}} f^{0.4} + k_{R_{r_2}} f^4$
M	2.062536619463439e-10	k_{IL}	0.010221293258566

Source: (The author, 2016)

J.2 ADS® MODEL OF THE PVSC INSIDE AN INDOOR LIGHT EMULATOR

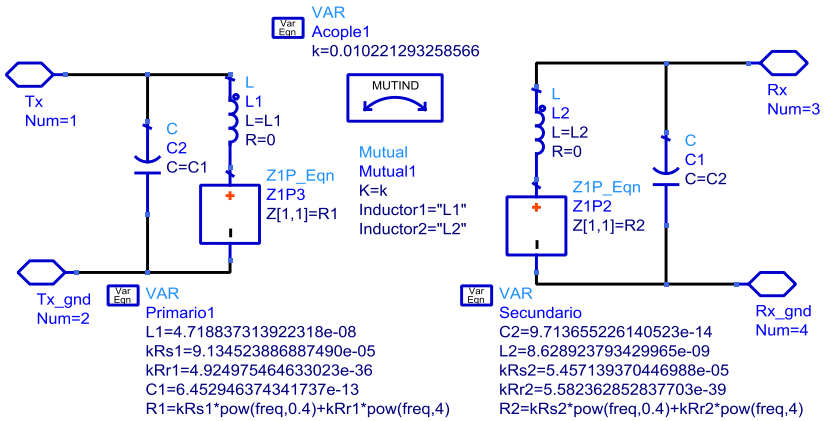
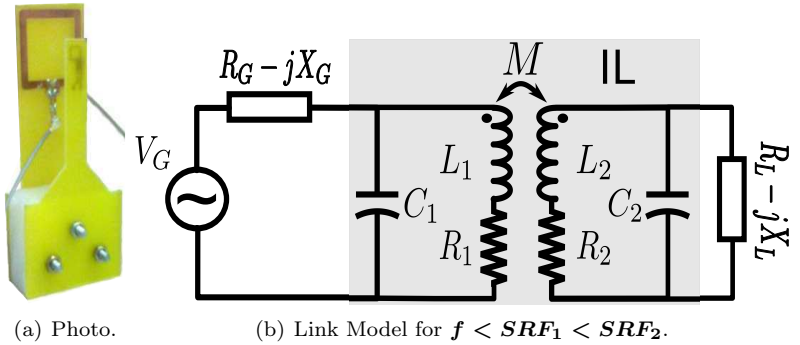
We use a PVSC that operates inside of an indoor light emulator as the energy source of the SsWPT examples simulated in Chapter 5. The experimental setup that we use to verify the model is shown in Figure 130(a). We use the KXOB22-12X1L device, a silicon monocrystalline PVSC that is fabricated by the IXYS Company. The device’s datasheet outlines its remarkable points under STC conditions, and we summarize them in Table 50. The specific environmental conditions inside the indoor emulator are warm LED spectrum, illuminance from 177 to 33.3x10³ lm/m², and room temperature. They were discussed in depth in Chapter 3. The model topology is shown in Figure 130(b), and its equations and parameters are summarized in Tables 51 and 52. We implemented this model in the ADS® software package using the SDD component, as we depict in Figure 130(c). This ADS® block is an equation-based component that allows us to custom define the non-linear model of the PVSC, because it is defined by specifying equations that relate the port currents, port voltages, and their derivatives.

Table 50 – Specifications of the KXOB22-12X1L under AM1.5g.

Area	V_{oc}	I_{sc}	V_{mp}	I_{mp}	G	T
mm x mm	V	mA	V	mA	$\frac{W}{m^2}$	$^{\circ}C$
22 x 7	0.63	50	0.5	44.6	1000	25

Source: (The author, 2016)

Figure 129 – Photograph and model of the link optimized in (CABRERA; SOUSA, 2014).



Source: ((a) Taken from (CABRERA; SOUSA, 2014); (b) The author, 2017; (c) Adapted from ADS[®] Software, 2017)

Table 51 – Summary of PVSC model equations.

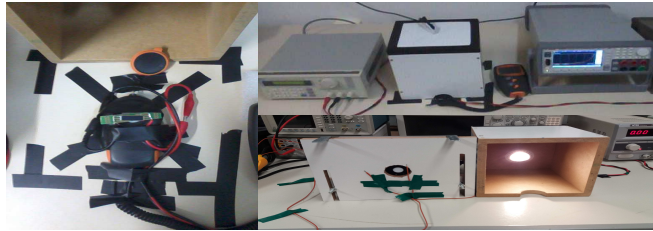
Component	Equation
I_D	$I_0 (e^{V_D/n\phi_t} - 1); \quad n = 1.2; \quad I_0 = \frac{f^{-1}_{3dB} \left(a_{I_0} L_v^{b_{I_0}} + c_{I_0} \right)}{10^{10}}$
I_{pv}	$\frac{p_{i1} L_v^3 + p_{i2} L_v^2 + p_{i3} L_v + p_{i4}}{10^3}$
R_{ss}	$f^{-1}_{3dB} \left(a_{R_{ss}} L_v^{b_{R_{ss}}} + c_{R_{ss}} \right)$
R_{sp}	$f^{-1}_{3dB} \left(a_{R_{sp}} L_v^{b_{R_{sp}}} + c_{R_{sp}} \right)$
$f_{3dB}(x) = 10 \log_{10} (10 \log_{10} (10 \log_{10} (x)))$;	
$f^{-1}_{3dB}(x) = 10^{0.1 \left(10^{0.1 \left(10^{0.1 \cdot x} \right)} \right)}$	
Source: (The author, 2016)	

Table 52 – Model parameters of the PVSC (i.e., KXOB22-12X1L).

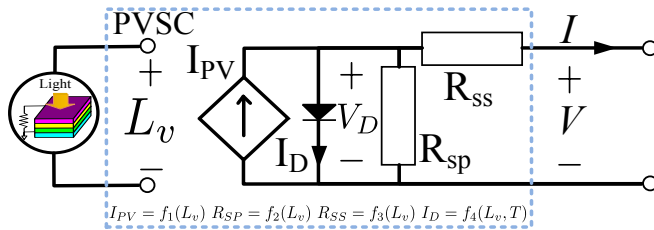
Par.	$Y = R_{ss}$	$Y = R_{sp}$	$Y = I_o$	Par.	I _{pv}
a_Y	-0.05107651	-0.04469432	-0.12077744	p_{i1}	-3.1147x10 ⁻¹⁴
b_Y	0.36394392	0.24809839	0.3613418	p_{i2}	1.1176x10 ⁻⁹
c_Y	12.0785002	12.2531266	12.3324676	p_{i3}	0.00017617
				p_{i4}	-0.00195557

Source: (The author, 2016)

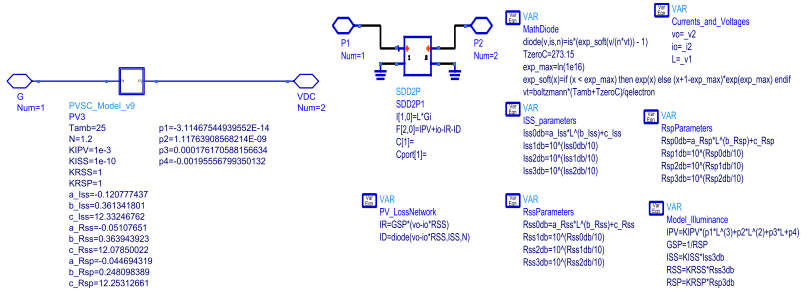
Figure 130 – PVSC model and experimental setup.



(a) Setup.



(b) Circuit Model.

(c) ADS[®] Model.

Source: ((a) and (b) The author, 2017; (c) Adapted from ADS[®] Software, 2017)

REFERENCES

ACAR, M.; ANNEMA, A.; NAUTA, B. Generalized design equations for class-e power amplifiers with finite DC feed inductance. In: **36th European Microwave Conf.** [S.l.: s.n.], 2006. p. 1308–1311. Cited in page(s):

ACAR, M.; ANNEMA, A.; NAUTA, B. Analytical design equations for class-e power amplifiers. **IEEE Trans. Circuits Syst. I, Reg. Papers**, v. 54, n. 12, p. 2706–2717, dez. 2007. ISSN 1549-8328. Cited in page(s):

ACAR, M.; ANNEMA, A.; NAUTA, B. Analytical design equations for class-e power amplifiers with finite DC-feed inductance and switch on-resistance. In: **IEEE Int. Symp. Circuits Systems**. [S.l.: s.n.], 2007. p. 2818–2821. Cited in page(s):

AGARWAL, K. et al. Wireless power transfer strategies for implantable bioelectronics: Methodological review. **IEEE Reviews Biomed. Eng.**, PP, n. 99, p. 1–1, 2017. ISSN 1937-3333. Cited in page(s):

AKYILDIZ, I. F. et al. A survey on sensor networks. **IEEE Comm. Mag.**, IEEE, v. 40, n. 8, p. 102–114, 2002. Cited in page(s):

AMAR, A. B.; KOUKI, A. B.; CAO, H. Power approaches for implantable medical devices. **Sensors**, v. 15, n. 11, p. 28889–28914, 2015. Cited in page(s):

ARVAS, S. Spiral inductor model extraction: A survey of the field. In: **IEEE Wireless Microwave Tech. Conf. (WAMICON)**. [S.l.: s.n.], 2012. p. 1–7. Cited in page(s):

AYAZIAN, S.; HASSIBI, A. Delivering optical power to subcutaneous implanted devices. In: IEEE. **IEEE Ann. Int. Conf. Eng. Medicine and Biology Soc. (EMBC)**. [S.l.], 2011. p. 2874–2877. Cited in page(s):

BAE, J. et al. The signal transmission mechanism on the surface of human body for body channel communication. **IEEE Trans. Microwave Theory Techn.**, IEEE, v. 60, n. 3, p. 582–593, 2012. Cited in page(s):

BAE, J. N. et al. Efficient interference cancellation scheme for wireless body area network. **IEEE J. Commun. and Networks**, v. 13, n. 2, p. 167–174, 2011. Cited in page(s):

BANDYOPADHYAY, S.; CHANDRAKASAN, A. P. Platform architecture for solar, thermal, and vibration energy combining with mppt and single inductor. **IEEE J. Solid-State Circuits**, v. 47, n. 9, p. 2199–2215, 2012. Cited in page(s):

BANDYOPADHYAY, S. et al. 23.2 a 1.1nw energy harvesting system with 544pw quiescent power for next-generation implants. In: **IEEE Int. Solid-State Circuits Conf. Dig. Tech. Papers (ISSCC)**. [S.l.: s.n.], 2014. p. 396–397. ISSN 0193-6530. Cited in page(s):

BANDYOPADHYAY, S.; RAMADASS, Y.; CHANDRAKASAN, A. 20a to 100ma dc-dc converter with 2.8 to 4.2v battery supply for portable applications in 45nm cmos. In: **IEEE Int. Solid-State Circuits Conf. Dig. Tech. Papers (ISSCC)**. [S.l.: s.n.], 2011. p. 386–388. ISSN 0193-6530. Cited in page(s):

BANG, S. et al. A fully integrated switched-capacitor based pmu with adaptive energy harvesting technique for ultra-low power sensing applications. In: **IEEE Int. Symp. Circuits and Syst. (ISCAS)**. [S.l.: s.n.], 2013. p. 709–712. ISSN 0271-4302. Cited in page(s):

BARAKAH, D. M.; AMMAD-UDDIN, M. A survey of challenges and applications of wireless body area network (wban) and role of a virtual doctor server in existing architecture. In: **3th Int. Conf. Intelligent Syst. Modelling Simulation**. [S.l.: s.n.], 2012. p. 214–219. Cited in page(s):

BECHER, K. et al. Design and realization of a wireless sensor gateway for health monitoring. In: **Ann. Int. Conf. IEEE Eng. Medicine Biology Soc.** [S.l.: s.n.], 2010. p. 374–377. ISBN 1557-170X. Cited in page(s):

BENAVIDES, N.; CHAPMAN, P. Power budgeting of a multiple-input buck-boost converter. **IEEE Trans. Power Electron.**, v. 20, n. 6, p. 1303–1309, Nov 2005. ISSN 0885-8993. Cited in page(s):

BENAVIDES, N.; CHAPMAN, P. Modeling the effect of voltage ripple on the power output of photovoltaic modules. **IEEE Trans. Ind. Electron.**, v. 55, n. 7, p. 2638–2643, July 2008. Cited in page(s):

BEREUTER, L. et al. Energy harvesting by subcutaneous solar cells: A long-term study on achievable energy output. **Annals of biomedical engineering**, Springer, v. 45, n. 5, p. 1172–1180, 2017. Cited in page(s):

BHASKARAN, M.; SRIRAM, S.; INIEWSKI, K. **Energy Harvesting with Functional Materials and Microsystems**. [S.l.]: CRC Press, 2013. Cited in page(s):

BRUNELLI, D. et al. An efficient solar energy harvester for wireless sensor nodes. In: **Des. Autom. Test Europe Conf. Exhibition (DATE)**. [S.l.: s.n.], 2008. p. 104–109. Cited in page(s):

BRUNELLI, D. et al. Photovoltaic scavenging systems: Modeling and optimization. **Microelectronics Journal**, v. 40, n. 9, p. 1337 – 1344, 2009. Cited in page(s):

BUI, N.; ZORZI, M. Health care applications: a solution based on the internet of things. In: **Proc. of the 4th Int. Symp. Appl. Sciences Biomed. Commun. Technologies**. [S.l.]: ACM, 2011. p. 131. Cited in page(s):

BURD, T. D.; BRODERSEN, R. W. Design issues for dynamic voltage scaling. In: **IEEE. Proc. Int. Symp. Low Power Electron. Design (ISLPED)**. [S.l.], 2000. p. 9–14. Cited in page(s):

BURD, T. D. et al. A dynamic voltage scaled microprocessor system. **IEEE J. Solid-State Circuits.**, IEEE, v. 35, n. 11, p. 1571–1580, 2000. Cited in page(s):

CABRERA, F. L.; FEITOZA, R. S.; SOUSA, F. R. de. Extending the inductor operating frequency for optimally-coupled wireless power transfer systems. In: **IEEE MTT-S Int. Microw. and Optoelectron. Conf.(IMOC)**. [S.l.: s.n.], 2015. p. 1–5. Cited in page(s):

CABRERA, F. L.; SOUSA, F. R. de. Optimal design of energy efficient inductive links for powering implanted devices. In: **IEEE Topical Conf. Biomed. Wireless Tech. Netw. Sensing Syst. (BioWireless)**. [S.l.: s.n.], 2014. p. 37–39. Cited in page(s):

CABRERA, F. L.; SOUSA, F. R. de. Contactless characterization of a cmos integrated lc resonator for wireless power transferring. **IEEE Microwave Wireless Components Lett.**, v. 25, n. 7, p. 475–477, July 2015. ISSN 1531-1309. Cited in page(s):

CABRERA, F. L.; SOUSA, F. R. de. Achieving optimal efficiency in energy transfer to a cmos fully integrated wireless power receiver. **IEEE Trans. Microw. Theory Tech.**, v. 64, n. 11, p. 3703–3713, 2016. Cited in page(s):

CALHOUN, B.; WANG, A.; CHANDRAKASAN, A. Modeling and sizing for minimum energy operation in subthreshold circuits. **IEEE J. Solid-State Circuits**, v. 40, n. 9, p. 1778–1786, Sept 2005. ISSN 0018-9200. Cited in page(s):

CARLI, D. et al. An effective multi-source energy harvester for low power applications. In: **IEEE. Des. Autom. Test Europe Conf. Exhibition (DATE)**. [S.l.], 2011. p. 1–6. Cited in page(s):

CARROLL, R. et al. Continua: An interoperable personal healthcare ecosystem. **IEEE Pervasive Computing**, v. 6, n. 4, p. 90–94, 2007. Cited in page(s):

CHAN, D. S. H.; PHANG, J. C. H. Analytical methods for the extraction of solar-cell single- and double-diode model parameters from i-v characteristics. **IEEE Trans. Electron Devices**, v. 34, n. 2, p. 286–293, Feb 1987. Cited in page(s):

CHEE, Y. H.; RABAEY, J.; NIKNEJAD, A. M. A class a/b low power amplifier for wireless sensor networks. In: **Proc. Int. Symp. Circuits Systems (ISCAS)**. [S.l.: s.n.], 2004. v. 4, p. IV–409–12 Vol.4. ID: 2. Cited in page(s):

CHEN, M. et al. Body area networks: A survey. **J. Mobile Networks Applicat.**, v. 16, n. 2, p. 171–193, 2011. Cited in page(s):

CHEN, M.; RINCON-MORA, G. A. Accurate electrical battery model capable of predicting runtime and iv performance. **Energy conversion, iee transactions on**, v. 21, n. 2, p. 504–511, 2006. Cited in page(s):

CHOI, Y. H.; KIM, Y. H.; KIM, J. Y. Novel transmission algorithm of uwb signals for wban applications. In: **IEEE Int. Conf. Consumer Electron. (ICCE)**. [S.l.: s.n.], 2012. p. 374–375. ISBN 2158-3994. ID: 1. Cited in page(s):

CHONG, K.-K. et al. Comprehensive method for analyzing the power conversion efficiency of organic solar cells under different spectral irradiances considering both photonic and electrical characteristics. **Applied Energy**, v. 180, p. 516 – 523, 2016. Cited in page(s):

CHUNG, W.-Y.; LEE, Y.-D.; JUNG, S.-J. A wireless sensor network compatible wearable u-healthcare monitoring system using integrated ecg, accelerometer and spo2. In: **30th Ann. Int. Conf. IEEE Eng. Medicine Biology Soc.** [S.l.: s.n.], 2008. p. 1529–1532. ISBN 1557-170X. Cited in page(s):

CIULLA, G. et al. A comparison of different one-diode models for the representation of the characteristic of a pv cell. **Renew. Sustain. Energy Rev.**, v. 32, p. 684 – 696, 2014. Cited in page(s):

CLARKE, K. K.; HESS, D. T. **Communication circuits: analysis and design.** [S.l.]: New York: Addison-Wesley Reading, 1971. Cited in page(s):

COLOMER-FARRARONS et al. **A CMOS Self-Powered Front-End Architecture for Subcutaneous Event-Detector Devices.** [S.l.]: Springer, 2011. Cited in page(s):

COLOMER-FARRARONS, J. et al. A proof-of-concept of a multi-harvesting power source in a low-voltage cmos technology. In: IEEE. **IEEE Int. Conf. on Green Computing Comm. (GreenCom).** [S.l.], 2012. p. 655–659. Cited in page(s):

COLOMER-FARRARONS, J. et al. A multiharvested self-powered system in a low-voltage low-power technology. **IEEE Trans. Ind. Electron.**, v. 58, n. 9, p. 4250–4263, Sept 2011. ISSN 0278-0046. Cited in page(s):

COLOMER-FARRARONS, J.; MIRIBEL-CATALÀ, P. L. Cmos front-end architecture for in-vivo biomedical subcutaneous detection devices. In: **A CMOS Self-Powered Front-End Architecture for Subcutaneous Event-Detector Devices.** [S.l.]: Springer, 2011. p. 133–153. Cited in page(s):

COLOMER-FARRARONS, J. et al. Low-power energy harvesting solutions for biomedical devices. In: C (Ed.). **Energy Harvesting with Functional Materials and Microsystems.** [S.l.]: CRC Press, 2013. p. 31. Cited in page(s):

CUBAS, J.; PINDADO, S.; MANUEL, C. de. Explicit expressions for solar panel equivalent circuit parameters based on analytical formulation and the lambert w-function. **Energies**, v. 7, n. 7, p. 4098–4115, 2014. Cited in page(s):

CUBAS, J.; PINDADO, S.; VICTORIA, M. On the analytical approach for modeling photovoltaic systems behavior. **J. Pow. Sou.**, v. 247, p. 467–474, 2014. Cited in page(s):

CUCE, P. M.; CUCE, E. A novel model of photovoltaic modules for parameter estimation and thermodynamic assessment. **Int. J. Low-Carbon Technol.**, v. 7, n. 2, p. 159–165, 2012. Cited in page(s):

DALOLA, S. et al. Characterization of thermoelectric modules for powering autonomous sensors. **IEEE Trans. Instrum. Meas.**, v. 58, n. 1, p. 99–107, 2009. ID: 1. Cited in page(s):

D'AMBROSIO, S. et al. Mobile phone batteries draining: Is green web browsing the solution? In: **2014 Int. Green Computing Conf. (IGCC)**. [S.l.: s.n.], 2014. p. 1–10. Cited in page(s):

DARROW, C. B. et al. **Implantable medical sensor system**. 2001. US Patent 6,201,980. Cited in page(s):

DETERRE, M. **Toward an energy harvester for leadless pacemakers**. Tese (Doutorado) — Universite Paris Sud-Paris XI, 2013. Cited in page(s):

DOLATABADI, E.; PRIMAK, S. Ubiquitous wban-based electrocardiogram monitoring system. In: **13th IEEE Int. Conf. e-Health Networking Applicat. Services**. [S.l.]: IEEE, 2011. p. 110–113. Cited in page(s):

DOLDAN, R.; GINES, A. J.; RUEDA, A. Inductor characterization in rf lc-vcos. In: **IEEE 4th Latin Amer. Symp. Circuits Syst.** [S.l.: s.n.], 2013. p. 1–4. Cited in page(s):

DORF, R. C.; SVOBODA, J. A. **Introduction to electric circuits**. [S.l.]: John Wiley & Sons, 2010. Cited in page(s):

EINHORN, M. et al. Comparison, selection, and parameterization of electrical battery models for automotive applications. **IEEE Trans. Power Electron.**, v. 28, n. 3, p. 1429–1437, 2013. ID: 1. Cited in page(s):

ERDINC, O.; VURAL, B.; UZUNOGLU, M. A dynamic lithium-ion battery model considering the effects of temperature and capacity fading. In: **2009 Int. Conf. Clean Electrical Power**. [S.l.: s.n.], 2009. p. 383–386. Cited in page(s):

ERICKSON, R. W.; MAKSIMOVIC, D. **Fundamentals of power electronics**. [S.l.]: Springer, 2001. Cited in page(s):

ESRAM, T.; CHAPMAN, P. L. Comparison of photovoltaic array maximum power point tracking techniques. **IEEE Trans. Energy Conversion.**, v. 22, n. 2, p. 439–449, 2007. ID: 1. Cited in page(s):

FAFOUTIS, X.; DRAGONI, N. Odmac: An on-demand mac protocol for energy harvesting - wireless sensor networks. In: **Proc. 8th ACM Symp. Performance Evaluation Wireless Ad Hoc Sensor Ubiquitous Networks**. New York, NY, USA: ACM, 2011. (PE-WASUN '11), p. 49–56. ISBN 978-1-4503-0900-4. Cited in page(s):

FAJARDO, A.; SOUSA, F. R. de. Integrated cmos class-e power amplifier for self-sustaining wireless power transfer system. In: **29th Symp. Integr. Circuits Syst. Des. (SBCCI)**. [S.l.: s.n.], 2016. p. 1–6. Cited in page(s):

FAJARDO, A.; SOUSA, F. Rangel de. Modeling and design of high-efficiency power amplifiers fed by limited power sources. In: **29th Symp. Integr. Circuits Syst. Des. (SBCCI)**. [S.l.: s.n.], 2016. p. 1–6. Cited in page(s):

FAJARDO, A.; SOUSA, F. Rangel de. Simple expression for estimating the switch peak voltage on the class-e amplifier with finite dc-feed inductance. In: **Proc. IEEE 7th Latin American Symp. Circuits Syst. (LASCAS)**. [S.l.: s.n.], 2016. Cited in page(s):

FAJARDO, A.; SOUSA, F. Rangel de. A taxonomy for learning, teaching, and assessing wireless body area networks. In: **Proc. IEEE 7th Latin American Symp. Circuits Syst. (LASCAS)**. [S.l.: s.n.], 2016. p. 179–182. Cited in page(s):

FAJARDO, A.; SOUSA, F. Rangel de. Ideal energy power source model and its implications on battery modeling. In: **Proc. 22th IBERCHIP Workshop**. [S.l.: s.n.], Florianopolis, Brasil. 2016. p. 19–25. Cited in page(s):

FALK, T.; MAIER, M. Context awareness in wbans: a survey on medical and non-medical applications. **IEEE Wireless Commun.**, v. 20, n. 4, 2013. Cited in page(s):

FALKENSTEIN, E.; ROBERG, M.; POPOVIC, Z. Low-power wireless power delivery. **IEEE Trans. Microw. Theory Tech.**,

v. 60, n. 7, p. 2277–2286, July 2012. ISSN 0018-9480. Cited in page(s):

FANG, G.; DUTKIEWICZ, E. Bodymac: Energy efficient tdma-based mac protocol for wireless body area networks. In: **9th Int. Symp. Comm. Inform. Techn. (ISCIT)**. [S.l.: s.n.], 2009. p. 1455–1459. ID: 1. Cited in page(s):

FANG, G. et al. Medical body area networks: Opportunities, challenges and practices. In: **11th Int. Symp. on Commun. Inform. Technologies**. [S.l.: s.n.], 2011. p. 562–567. Cited in page(s):

GAO, W.; YU, Z. Scalable compact circuit model and synthesis for rf cmos spiral inductors. **IEEE Trans. Microwave Theory Techniques**, v. 54, n. 3, p. 1055–1064, 2006. Cited in page(s):

GEORGIADIS, A.; COLLADO, A. Solar powered class-e active antenna oscillator for wireless power transmission. In: **IEEE Radio Wireless Symp. (RWS)**. [S.l.: s.n.], 2013. p. 40–42. Cited in page(s):

GHOVANLOO, M.; ATLURI, S. A wide-band power-efficient inductive wireless link for implantable microelectronic devices using multiple carriers. **IEEE Trans. Circuits Syst. I, Reg. Papers**, v. 54, n. 10, p. 2211–2221, Oct 2007. ISSN 1549-8328. Cited in page(s):

GILDENBLAT, G. **Compact modeling: principles, techniques and applications**. [S.l.]: Springer Science & Business Media, 2010. Cited in page(s):

GOTO, K. et al. Near-infrared light transcutaneous telemetry system having an implantable transmitter driven by external laser irradiation. **Review of Scientific instruments**, AIP, v. 72, n. 7, p. 3079–3085, 2001. Cited in page(s):

GOULD, P. A. et al. Complications associated with implantable cardioverter-defibrillator replacement in response to device advisories. **J. American Medical Association (JAMA)**, American Medical Association, v. 295, n. 16, p. 1907–1911, 2006. Cited in page(s):

GUILAR, N. et al. An energy-aware multiple-input power supply with charge recovery for energy harvesting applications. In: **IEEE Int.**

Solid-State Circuits Conf. Dig. Tech. Papers (ISSCC). [S.l.: s.n.], 2009. p. 298–299,299a. Cited in page(s):

HAEBERLIN, A. et al. Successful pacing using a batteryless sunlight-powered pacemaker. **Europace**, Oxford University Press, v. 16, n. 10, p. 1534–1539, 2014. Cited in page(s):

HAIDER, M.; ISLAM, S.; ZHANG, M. A low-power processing unit for in vivo monitoring and transmission of sensor signals. **Sensors & Transducers J.**, v. 84, n. 10, p. 1625–1632, 2007. Cited in page(s):

HANNAN, M. A. et al. Energy harvesting for the implantable biomedical devices: issues and challenges. **Biomed. Eng. OnLine**, v. 13, n. 1, p. 79, 2014. Cited in page(s):

HAO, Y.; FOSTER, R. Wireless body sensor networks for health-monitoring applications. **Physiological Measurement**, v. 29, n. 11, 2008. Cited in page(s):

HARUTA, H. **The impedance measurement handbook: a guide to measurement technology and techniques.** [S.l.: Agilent Technologies, 2006. Cited in page(s):

HUANG MARYAM ASHOUEI, F. Y. L. Ultra-low power sensor design for wireless body area networks: Challenges, potential solutions, and applications. **Int. J.Digital Content Techn. Applicat. (JDCTA)**, v. 3, n. 3, p. 136–148, 2009. Cited in page(s):

HUMADA, A. M. et al. Solar cell parameters extraction based on single and double-diode models: A review. **Renew. Sustain. Energy Rev.**, v. 56, p. 494 – 509, 2016. ISSN 1364-0321. Cited in page(s):

IEEE. **IEEE standard for local and metropolitan area networks part 15.6: Wireless body area networks.** [S.l.: IEEE, 2012. Cited in page(s):

IXYS. **IXYS preliminary KXOB22-12X1. Accessed: 2015-09-30.** 906-5 Iui-dong, Yeongtong-Gu, Suwon, Gyeonggi-Do (Korea), 2011. Disponível em: <<http://ixapps.ixys.com/DataSheet/20110302-KXOB22-12X1-DATA-SHEET.pdf>>. Cited in page(s):

JAIMES, A. F.; SOUSA, F. R. de. Revisiting the power-efficiency trade-off on a dc voltage source. In: **Proc. IEEE 7th Latin**

American Symp. Circuits Syst. (LASCAS). [S.l.: s.n.], 2016. p. 323–326. Cited in page(s):

JAIMES, A. F.; SOUSA, F. R. de. Simple modeling of photovoltaic solar cells for indoor harvesting applications. **Solar Energy**, v. 157, n. Supplement C, p. 792 – 802, 2017. ISSN 0038-092X. Cited in page(s):

JEONG, J.; JIANG, X.; CULLER, D. Design and analysis of micro-solar power systems for wireless sensor networks. In: **5th Int. Conf. Networked Sensing Syst. (INSS)**. [S.l.: s.n.], 2008. p. 181–188. Cited in page(s):

JIANG, X.; POLASTRE, J.; CULLER, D. Perpetual environmentally powered sensor networks. In: **4th Int. Symp. Inform. Process. Sensor Networks (IPSN)**. [S.l.: s.n.], 2005. p. 463–468. Cited in page(s):

JONGERDEN, M. R.; HAVERKORT, B. R. Which battery model to use? **IET Software**, v. 3, n. 6, p. 445–457, 2009. ID: 1. Cited in page(s):

JORDEHL, A. R. Parameter estimation of solar photovoltaic cells: A review. **Renew. Sustain. Energy Rev.**, v. 61, p. 354 – 371, 2016. Cited in page(s):

JOVANOVIĆ, E.; MILENKOVIC, A. Body area networks for ubiquitous healthcare applications: opportunities and challenges. **J. Medical Syst.**, v. 35, n. 5, p. 1245–1254, 2011. Cited in page(s):

JUNG, B. H.; AKBAR, R. U.; SUNG, D. K. Throughput, energy consumption, and energy efficiency of IEEE 802.15.6 body area network (BAN) MAC protocol. In: **IEEE 23rd Int. Symp. Personal Indoor Mobile Radio Comm.** [S.l.: s.n.], 2012. p. 584–589. ISBN 2166-9570. Cited in page(s):

KADIRVEL, K. et al. A 330nm energy-harvesting charger with battery management for solar and thermoelectric energy harvesting. In: **IEEE Int. Solid-State Circuits Conf. Dig. Tech. Papers (ISSCC)**. [S.l.], 2012. p. 106–108. Cited in page(s):

KANSAL, A. et al. Power management in energy harvesting sensor networks. **ACM Trans. Embedded Computing Syst. (TECS)**, ACM, v. 6, n. 4, p. 32, 2007. Cited in page(s):

KANSAL, A. et al. On sensor network lifetime and data distortion. In: **IEEE. Proc. Int. Symp. Inform. Theory (ISIT)**. [S.l.], 2005. p. 6–10. Cited in page(s):

KHAN, J. Y. et al. Wireless body area network (wban) design techniques and performance evaluation. **J. Medical Syst.**, p. 1–17, 2012. Cited in page(s):

KIM, T.; QIAO, W. A hybrid battery model capable of capturing dynamic circuit characteristics and nonlinear capacity effects. In: **2012 IEEE Power Energy Soc. General Meeting**. [S.l.: s.n.], 2012. p. 1–1. ISSN 1944-9925. Cited in page(s):

KIOURTI, A.; NIKITA, K. S. A review of in-body biotelemetry devices: Implantables, ingestibles, and injectables. **IEEE Trans. Biomed. Eng.**, v. 64, n. 7, p. 1422–1430, July 2017. Cited in page(s):

KOHNO, R. et al. R&d and standardization of body area network (ban) for medical healthcare. In: **IEEE Int. Conf. Ultra-Wideband**. [S.l.: s.n.], 2008. v. 3, p. 5–8. Cited in page(s):

KONG, C. S. A general maximum power transfer theorem. **IEEE Trans. Edu.**, v. 38, n. 3, p. 296–298, 1995. Cited in page(s):

KWON, D.; RINCON-MORA, G. A 2um bicmos rectifier-free ac: Dc piezoelectric energy harvester-charger ic. **IEEE Trans. Biomed. Circuits Syst.**, v. 4, n. 6, p. 400–409, Dec 2010. ISSN 1932-4545. Cited in page(s):

LAM, L.; BAUER, P.; KELDER, E. A practical circuit-based model for li-ion battery cells in electric vehicle applications. In: **2011 IEEE 33rd Int. Telecommun. Energy Conf. (INTELEC)**. [S.l.: s.n.], 2011. p. 1–9. ISSN 2158-5210. Cited in page(s):

LATRÉ, B. et al. A survey on wireless body area networks. **Springer Wireless Networks**, Springer-Verlag New York, Inc., v. 17, n. 1, p. 1–18, 2011. Cited in page(s):

LEONOV, V. Energy harvesting for self-powered wearable devices. In: **Wearable Monitoring Syst.** [S.l.]: New York: Springer, 2011. p. 27–49. Cited in page(s):

LI, C. et al. Energy management system architecture for new energy power supply system of islands. In: **IEEE PES Innovative Smart**

Grid Techn. (ISGT). [S.l.: s.n.], 2012. p. 1–8. ID: 1. Cited in page(s):

LI, H.; TAN, J. Heartbeat-driven medium-access control for body sensor networks. **IEEE Trans. Inf. Technol. Biomed.**, v. 14, n. 1, p. 44–51, 2010. Cited in page(s):

LI, H.-B.; HAMAGUCHI, K. A prototype ban for medical and healthcare monitoring based on high band uwb. In: **14th Int. Symp. Wireless Personal Multimedia Comm.** [S.l.: s.n.], 2011. p. 1–5. ISBN 1347-6890. Cited in page(s):

LI, S.; MI, C. C. Wireless power transfer for electric vehicle applications. **IEEE J. Emerging Select. Topics Power Electron.**, v. 3, n. 1, p. 4–17, March 2015. ISSN 2168-6777. Cited in page(s):

LI, S.; PANDHARIPANDE, A. Networked illumination control with distributed light-harvesting wireless sensors. **IEEE Sensors J.**, v. 15, n. 3, p. 1662–1669, March 2015. ISSN 1530-437X. Cited in page(s):

LI, Y. et al. The effect of the type of illumination on the energy harvesting performance of solar cells. **Solar Energy**, v. 111, p. 21 – 29, 2015. Cited in page(s):

LIANG, K.-H.; CHANG, H.-Y. 0.5–6 ghz low-voltage low-power mixer using a modified cascode topology in 0.18 μm cmos technology. **IET Microwaves Antennas & Propagation**, IET, v. 5, n. 2, p. 167–174, 2011. Cited in page(s):

LINEYKIN, S.; BEN-YAAKOV, S. Analysis of thermoelectric coolers by a spice-compatible equivalent-circuit model. **IEEE Power Electron. Lett.**, v. 3, n. 2, p. 63–66, June 2005. ISSN 1540-7985. Cited in page(s):

LIU, C. et al. Design and safety considerations of an implantable rectenna for far-field wireless power transfer. **IEEE Trans. Antennas Propag.**, v. 62, n. 11, p. 5798–5806, Nov 2014. ISSN 0018-926X. Cited in page(s):

LIU, X.; SANCHEZ-SINENCIO, E. An 86 % efficiency 12 uw self-sustaining pv energy harvesting system with hysteresis regulation and time-domain mppt for iot smart nodes. **IEEE J. Solid-State Circuits**, v. 50, n. 6, p. 1424–1437, June 2015. ISSN 0018-9200. Cited in page(s):

LO, B.; YANG, G.-Z. Key technical challenges and current implementations of body sensor networks. In: **Proc. 2nd Int. Workshop Body Sensor Networks**. [S.l.: s.n.], 2005. Cited in page(s):

LU, C.; RAGHUNATHAN, V.; ROY, K. Maximum power point considerations in micro-scale solar energy harvesting systems. In: **IEEE. Proc. IEEE Int. Symp. Circuits Syst. (ISCAS)**. [S.l.], 2010. p. 273–276. Cited in page(s):

LU, C.; RAGHUNATHAN, V.; ROY, K. Maximum power point considerations in micro-scale solar energy harvesting systems. In: **IEEE. IEEE Int. Symp. Circuits and Syst. (ISCAS)**. [S.l.], 2010. p. 273–276. Cited in page(s):

MA, D.; BONDADE, R. Reconfigurable switched-capacitor power converters. In: **Reconfigurable Switched-Capacitor Power Converters**. [S.l.]: Springer, 2013. p. 71–110. Cited in page(s):

MADI, S. Analytical study of the application of the maximum power transfer theorem to electrical circuits and systems. Dept. Elect. Elect. Eng. M.S. thesis, M'Hamed Bougara of Boumerdes Univ., Algeria. 2010. Cited in page(s):

MASOUDINEJAD, M. et al. A gray box modeling of a photovoltaic cell under low illumination in materials handling application. In: **3rd Int. Renew. Sust. Energy Conf. (IRSEC)**. [S.l.: s.n.], 2015. p. 1–6. Cited in page(s):

MCCUNE, E. Fundamentals of switching rf power amplifiers. **IEEE Microwave and Wireless Compo. Lett.**, v. 25, n. 12, p. 838–840, Dec 2015. ISSN 1531-1309. Cited in page(s):

MCCUNE, E. A technical foundation for rf cmos power amplifiers: Part 1: Key power amplifier issues. **IEEE Solid-State Circuits Mag.**, v. 7, n. 3, p. 81–85, Summer 2015. ISSN 1943-0582. Cited in page(s):

MCCUNE, E. A technical foundation for rf cmos power amplifiers: Part 3: Power amplifier 3-port characteristics. **IEEE Solid-State Circuits Mag.**, v. 8, n. 1, p. 44–50, winter 2016. ISSN 1943-0582. Cited in page(s):

MCLAUGHLIN, J. C.; KAISER, K. L. Deglorifying the maximum power transfer theorem and factors in impedance selection. **IEEE Trans. Edu.**, v. 50, n. 3, p. 251–255, 2007. Cited in page(s):

MERCIER, P. et al. A sub-nw 2.4 ghz transmitter for low data-rate sensing applications. **IEEE J. Solid-State Circuits**, v. 49, n. 7, p. 1463–1474, July 2014. Cited in page(s):

MERCIER, P. P. et al. Energy extraction from the biologic battery in the inner ear. **Nature biotechnology**, Nature Publishing Group, v. 30, n. 12, p. 1240–1243, 2012. Cited in page(s):

MI, M. L. S.; ALI, S. H. M.; ISLAM, M. S. A novel architecture of maximum power point tracking for ultra-low-power based hybrid energy harvester in ubiquitous devices: A review. **American Journal of Applied Sciences**, v. 10, n. 10, p. 1240, 2013. Cited in page(s):

MINNAERT, B.; VEELAERT, P. A proposal for typical artificial light sources for the characterization of indoor photovoltaic applications. **Energies**, v. 7, n. 3, p. 1500–1516, 2014. Cited in page(s):

MOHAMED, H.; MAHMOUD, S. Temperature dependence in modeling photovoltaic arrays. In: **IEEE 20th Int. Conf. Electron. Circuits Syst. (ICECS)**. [S.l.: s.n.], 2013. p. 747–750. Cited in page(s):

MOVASSAGHI, S.; ABOLHASAN, M.; LIPMAN, J. Wireless body area networks: a survey. **IEEE Comm. Surv. Tut.**, p. 1–29, 2013. Cited in page(s):

MOVASSAGHI, S. et al. Wireless body area networks: A survey. **IEEE J. Comm. Surveys & Tutorials**, v. 16, n. 3, p. 1658–1686, 2014. Cited in page(s):

MUSOLINO, V.; PIEGARI, L.; TIRONI, E. New full-frequency-range supercapacitor model with easy identification procedure. **IEEE Trans. Ind. Electron.**, v. 60, n. 1, p. 112–120, Jan 2013. ISSN 0278-0046. Cited in page(s):

MYNY, K. et al. An inductively-coupled 64b organic rfid tag operating at 13.56 mhz with a data rate of 787b/s. In: **IEEE. Dig. Technical Papers IEEE Int. Solid-State Circuits Conf. (ISSCC)**. [S.l.], 2008. p. 290–614. Cited in page(s):

NAGAYOSHI, H.; KAJIKAWA, T.; SUGIYAMA, T. Comparison of maximum power point control methods for thermoelectric power generator. In: **IEEE. 21th Int. Conf. Thermoelectrics Proc. (ICT)**. [S.l.], 2002. p. 450–453. Cited in page(s):

NIKDEL, M. et al. Various battery models for various simulation studies and applications. **Renewable Sustainable Energy Reviews**, Elsevier, v. 32, p. 477–485, 2014. Cited in page(s):

NIOTAKI, K. et al. Solar/electromagnetic energy harvesting and wireless power transmission. **IEEE Proc.**, v. 102, n. 11, p. 1712–1722, nov. 2014. ISSN 0018-9219. Cited in page(s):

O., K. Estimation methods for quality factors of inductors fabricated in silicon integrated circuit process technologies. **IEEE J. Solid-State Circuits**, v. 33, n. 8, p. 1249–1252, Aug 1998. ISSN 0018-9200. Cited in page(s):

ODRISCOLL, S.; POON, A. S. Y.; MENG, T. H. A mm-sized implantable power receiver with adaptive link compensation. In: **2009 IEEE Int. Solid-State Circuits Conf.** [S.l.: s.n.], 2009. p. 294–295, 295a. ISSN 0193-6530. Cited in page(s):

OHIRA, T. What in the world is q? [[distinguished microwave lecture. **IEEE Microwave Mag.**, v. 17, n. 6, p. 42–49, June 2016. Cited in page(s):

OHIRA, T. The kq product as viewed by an analog circuit engineer. **IEEE Circuits Syst. Mag.**, v. 17, n. 1, p. 27–32, 2017. Cited in page(s):

ORGANIZATION, W. H. **Global health risks: mortality and burden of disease attributable to selected major risks**. [S.l.]: Geneva, Switzerland: WHO Press, 2009. Cited in page(s):

OTTO, C. A.; JOVANOV, E.; MILENKOVIC, A. A wban-based system for health monitoring at home. In: **3rd IEEE/EMBS Int. Summer School Medical Devices Biosensors**. [S.l.: s.n.], 2006. p. 20–23. Cited in page(s):

OZERI, S.; SHMILOVITZ, D. Ultrasonic transcutaneous energy transfer for powering implanted devices. **Elsevier Ultrasonics**, Elsevier, v. 50, n. 6, p. 556–566, 2010. Cited in page(s):

PANG, Z. Technologies and architectures of the internet-of-things (iot) for health and well-being. Dept. Elect. Eng, Ph.D. thesis, Royal Institute of Technology Univ., Stockholm, Sweden. 2013. Cited in page(s):

PANOV, Y.; JOVANOVIĆ, M. Adaptive off-time control for variable-frequency, soft-switched flyback converter at light loads. **IEEE Trans. Power Electron.**, v. 17, n. 4, p. 596–603, Jul 2002. ISSN 0885-8993. Cited in page(s):

PARAYANDEH, A. et al. A 10 mhz mixed-signal cpm controlled dc-dc converter ic with novel gate swing circuit and instantaneous efficiency optimization. In: **IEEE Energy Convers. Cong. Exp. (ECCE)**. [S.l.: s.n.], 2011. p. 1229–1235. Cited in page(s):

PARK, M. et al. Low power consumptive mixed mode mmic power amplifier module for wcdma handset applications. In: **European Microwave Conf.** [S.l.: s.n.], 2007. p. 1287–1290. ID: 1. Cited in page(s):

PATELLA, B. et al. High-frequency digital pwm controller ic for dc-dc converters. **IEEE Trans. Power Electron.**, v. 18, n. 1, p. 438–446, Jan 2003. ISSN 0885-8993. Cited in page(s):

PEDRAM, M. Power minimization in ic design: principles and applications. **ACM Trans. Design Automation of Electron. Syst. (TODAES)**, ACM, v. 1, n. 1, p. 3–56, 1996. Cited in page(s):

PENELLA, M. T.; GASULLA, M. A review of commercial energy harvesters for autonomous sensors. In: **IEEE Tech. Conf. Proc. Instrum. Meas. (IMTC)**. [S.l.: s.n.], 2007. p. 1–5. ISBN 1091-5281. ID: 1. Cited in page(s):

PIGUET, C.; RENAUDIN, M.; OMNES, T. J. F. Special session on low-power systems on chips (socs). In: **Proc. Conf. Exhibition Design Automation Test Europe**. [S.l.: s.n.], 2001. p. 488–494. ISBN 1530-1591. ID: 1. Cited in page(s):

PINTO, R. L. O. et al. Efficiency modeling of class-e power oscillators for wireless energy transfer. In: **IEEE Int. Instrumentation Measurement Techn. Conf. (I2MTC)**, [S.l.: s.n.], 2013. p. 271–275. ISBN 1091-5281. ID: 1. Cited in page(s):

PRIYA, S.; INMAN, D. J. **Energy harvesting technologies**. [S.l.: Springer, 2009. Cited in page(s):

PSARROS, G. N.; BATZELIS, E. I.; PAPATHANASSIOU, S. A. Partial shading analysis of multistring pv arrays and derivation of simplified mpp expressions. **IEEE Trans. Sus. Energy**, v. 6, n. 2, p. 499–508, April 2015. Cited in page(s):

RAGHUNATHAN, V. et al. Design considerations for solar energy harvesting wireless embedded systems. In: **4th Int. Symp. Inform. Process. Sensor Networks (IPSN)**. [S.l.: s.n.], 2005. p. 457–462. Cited in page(s):

RAHIMI-EICHI, H. et al. Battery management system: An overview of its application in the smart grid and electric vehicles. **IEEE Ind. Electron. Mag.**, v. 7, n. 2, p. 4–16, June 2013. ISSN 1932-4529. Cited in page(s):

RAMADASS, Y.; CHANDRAKASAN, A. A battery-less thermoelectric energy harvesting interface circuit with 35 mv startup voltage. **IEEE J. Solid-State Circuits**, v. 46, n. 1, p. 333–341, Jan 2011. ISSN 0018-9200. Cited in page(s):

RAMADASS, Y. K. **Energy processing circuits for low-power applications**. Tese (Doutorado) — Massachusetts Institute of Technology, 2009. Cited in page(s):

RAMRAKHANI, A. K.; MIRABBASI, S.; CHIAO, M. Design and optimization of resonance-based efficient wireless power delivery systems for biomedical implants. **IEEE Trans. Biomed. Circuits Syst.**, v. 5, n. 1, p. 48–63, Feb 2011. ISSN 1932-4545. Cited in page(s):

RAMÁREZ, E. A. I. **Energy Harvesting-Aware Resource Management for Wireless Body Area Networks**. Tese (Doutorado) — University Barcelona Electronic Department, 2014. Disponível em: <<http://hdl.handle.net/2445/55325>>. Cited in page(s):

RANDALL, J.; JACOT, J. Is am1. 5 applicable in practice? modelling eight photovoltaic materials with respect to light intensity and two spectra. **Renewable Energy**, v. 28, n. 12, p. 1851–1864, 2003. Cited in page(s):

RANDALL, J. F. **On the use of photovoltaic ambient energy sources for powering indoor electronic devices**. Tese (Doutorado) — Swiss Federal Institute of Technology in Lausanne, 2003. Cited in page(s):

RAO, A. B.; PADMANABHAN, G. A method for estimating the optimum load resistance of a silicon solar cell used in terrestrial power applications. **Solar Energy**, v. 15, n. 2, p. 171–177, 1973. Cited in page(s):

RAPOPORT, B. I.; KEDZIERSKI, J. T.; SARPESHKAR, R. A glucose fuel cell for implantable brain-machine interfaces. **PLoS One**, Public Library of Science, v. 7, n. 6, p. e38436, 2012. Cited in page(s):

RAUSCHENBACH, H. S. Solar cell array design handbook-the principles and technology of photovoltaic energy conversion. **NASA STI/Recon Techn. Report A**, v. 80, p. 34847, 1980. Cited in page(s):

RAZAVI, B. **RF microelectronics**. Second. [S.l.]: Prentice Hall New Jersey, 2011. Cited in page(s):

REA, M. S. **The IESNA lighting handbook: reference & application**. 9 edition. ed. [S.l.]: Illuminating engineering society of north america, 2000. Cited in page(s):

RIÑÑO, F. L. C. et al. **Contribuições à otimização da eficiência na transferência de energia sem-fio para dispositivos eletrônicos miniaturizados**. Tese (Doutorado) — Universidad Federal de Santa Catarina, 2016. Cited in page(s):

RICHTMAN, E. E. **Requirements for lighting levels**. Accessed: **2015-09-30**. 1090 Vermont Avenue, NW, Suite 700 — Washington, DC, 2015. Disponível em: <http://www.wbdg.org/pdfs/usace_lightinglevels.pdf>. Cited in page(s):

RINCON-MORA, G. A. Powering microsystems with ambient energy. In: **Energy harvesting with functional materials and microsystems**. [S.l.]: CRC Press, 2013. p. 1–30. Cited in page(s):

RINCON-MORA G.N-MORA, G. A. Harvesting microelectronic circuits. In: **Energy Harvesting Technologies**. [S.l.]: Springer, 2009. p. 287–321. Cited in page(s):

ROSSI, F. D.; PONTECORVO, T.; BROWN, T. M. Characterization of photovoltaic devices for indoor light harvesting and customization of flexible dye solar cells to deliver superior efficiency under artificial lighting. **Applied Energy**, v. 156, n. Supplement C, p. 413 – 422,

2015. ISSN 0306-2619. Disponível em:

<<http://www.sciencedirect.com/science/article/pii/S0306261915008600>>.

Cited in page(s):

ROUNDY, S. et al. Power sources for wireless sensor networks. In: **Wireless sensor networks**. [S.l.]: Springer, 2004. p. 1–17. Cited in page(s):

ROY, K.; MUKHOPADHYAY, S.; MAHMOODI-MEIMAND, H. Leakage current mechanisms and leakage reduction techniques in deep-submicrometer cmos circuits. **IEEE Proc.**, IEEE, v. 91, n. 2, p. 305–327, 2003. Cited in page(s):

RUDELL, J. C.; BHAGAVATULA, V.; WESSON, W. C. Future integrated sensor radios for long-haul communication. **IEEE Comm. Mag.**, v. 52, n. 4, p. 101–109, 2014. ID: 1. Cited in page(s):

SADEGHPOUR, R.; NABAVI, A. Design procedure of quasi-class-e power amplifier for low-breakdown-voltage devices. **Circuits and Systems I: Regular Papers, IEEE Transactions on**, v. 61, n. 5, p. 1416–1428, May 2014. ISSN 1549-8328. Cited in page(s):

SAGGINI, S.; MATTARELLI, P. Power management in multi-source multi-load energy harvesting systems. In: **13th European Conf. Power Electron. Applicat. (EPE)**. [S.l.: s.n.], 2009. p. 1–10. Cited in page(s):

SAVANTH, A. et al. Photovoltaic cells for micro-scale wireless sensor nodes: Measurement and modeling to assist system design. In: **Proc. 3rd Int. Workshop Energy Harves. Energy Neutral Sensing Syst.** [S.l.: s.n.], 2015. p. 15–20. Cited in page(s):

SAWAN, M. Wireless smart implants dedicated to multichannel monitoring and microstimulation. In: **Proc. IEEE/ACS Int. Conf. Pervasive Services (ICPS)**. [S.l.: s.n.], 2004. p. 21–26. Cited in page(s):

SCHNEIDER, M. C.; GALUP-MONTORO, C. **CMOS analog design using all-region MOSFET modeling**. [S.l.]: Cambridge University Press, 2010. Cited in page(s):

SEAMAN, A.; DAO, T.-S.; MCPHEE, J. A survey of mathematics-based equivalent-circuit and electrochemical battery models for hybrid and electric vehicle simulation. **J. Power Sources**, Elsevier, v. 256, p. 410–423, 2014. Cited in page(s):

SEDRA, A. S.; SMITH, K. C. **Microelectronic Circuits Revised Edition**. [S.l.]: Oxford University Press, Inc., 2007. Cited in page(s):

SHAO, H.; TSUI, C. ying; KI, W.-H. A micro power management system and maximum output power control for solar energy harvesting applications. In: **ACM/IEEE Int. Symp.Low-Power Electron. Des. (ISLPED)**. [S.l.: s.n.], 2007. p. 298–303. Cited in page(s):

SHAO, H.; TSUI, C. ying; KI, W.-H. Maximizing the harvested energy for micro-power applications through efficient mppt and pmu design. In: **15th Asia South Pacific Des. Autom. Conf. (ASP-DAC)**. [S.l.: s.n.], 2010. p. 75–80. Cited in page(s):

SHI, C. et al. A multiple-input boost converter for low-power energy harvesting. **IEEE Trans. Circuits Syst. II, Exp. Briefs**, v. 58, n. 12, p. 827–831, Dec 2011. ISSN 1549-7747. Cited in page(s):

SHRIVASTAVA, A. et al. A 1.2 uw simo energy harvesting and power management unit with constant peak inductor current control achieving 83-92across wide input and output voltages. In: **Symp. VLSI Circuits Dig. Tech. Papers**. [S.l.: s.n.], 2014. p. 1–2. Cited in page(s):

SI AW, F. L.; CHONG, K. K. Temperature effects on the performance of dense array concentrator photovoltaic system. In: **2012 IEEE Conf. Sustainable Utilization Develop. Eng. Technol.** [S.l.: s.n.], 2012. p. 140–144. Cited in page(s):

SOKAL, N.; MEDIANO, A. Redefining the optimum RF class-e switch-voltage waveform, to correct a long-used incorrect waveform. In: **IEEE MTT-S Int. Microwave Symp. Dig.** [S.l.: s.n.], 2013. p. 1–3. ISSN 0149-645X. Cited in page(s):

STRATAKOS, A.; BRODERSEN, R. W.; SANDERS, S. High-efficiency low-voltage DC-dc conversion for portable applications. In: **Proc. Int. Workshop Low-Power Design**. [S.l.: s.n.], Napa . 1994. p. 21–27. Cited in page(s):

STRATAKOS, A. J.; BRODERSEN, R. W.; SANDERS, S. R. **High-efficiency low-voltage DC-DC conversion for portable applications**. Tese (Doutorado) — Electrical Engineering and Computer Sciences)–University of California, Berkeley, 1998. Cited in page(s):

STROSS, R. E. **The wizard of menlo park: how thomas alva edison invented the modern world**. [S.l.]: New York: Three Rivers Press (CA), 2008. Cited in page(s):

SUDEVALAYAM, S.; KULKARNI, P. Energy harvesting sensor nodes: Survey and implications. **IEEE Comm. Surveys & Tutorials**, IEEE, v. 13, n. 3, p. 443–461, 2011. Cited in page(s):

TAN, Y.; PANDA, S. Energy harvesting from hybrid indoor ambient light and thermal energy sources for enhanced performance of wireless sensor nodes. **IEEE Trans. Ind. Electron.**, v. 58, n. 9, p. 4424–4435, Sept 2011. Cited in page(s):

TOH, W. Y. et al. Autonomous wearable sensor nodes with flexible energy harvesting. **IEEE Sensors J.**, v. 14, n. 7, p. 2299–2306, July 2014. ISSN 1530-437X. Cited in page(s):

TSIVIDIS, Y.; MCANDREW, C. **Operation and Modeling of the MOS Transistor**. [S.l.]: Oxford University Press New York, 1999. Cited in page(s):

TUFAIL, F.; ISLAM, M. Wearable wireless body area networks. In: **Int. Conf. Inform. Manage. Eng.** [S.l.: s.n.], 2009. p. 656–660. Cited in page(s):

UNDESA-POPULATION-DIVISION. World population prospects: The 2012 revision. New York, United Nations Department for Economic and Social Affairs (UN DESA), Working Paper No. ESA/P/WP. 228, 2013. Cited in page(s):

VENKATASUBRAMANIAN, R. et al. Energy harvesting for electronics with thermoelectric devices using nanoscale materials. In: **2007 IEEE Int. Electron. Devices Meeting**. [S.l.: s.n.], 2007. p. 367–370. ISSN 0163-1918. Cited in page(s):

VERBRUGGE, M. W.; CONELL, R. S. Electrochemical and thermal characterization of battery modules commensurate with electric vehicle integration. **J. Electrochemical Soc.**, The Electrochemical Society, v. 149, n. 1, p. A45–A53, 2002. Cited in page(s):

VIGORITO, C. M.; GANESAN, D.; BARTO, A. G. Adaptive control of duty cycling in energy-harvesting wireless sensor networks. In: **IEEE. 4th Ann. IEEE Comm. Soc. Conf. Sensor Mesh AdHoc Comm. Networks (SECON)**. [S.l.], 2007. p. 21–30. Cited in page(s):

VILLALVA, M.; GAZOLI, J.; FILHO, E. Comprehensive approach to modeling and simulation of photovoltaic arrays. **IEEE Trans. Power Electron.**, v. 24, n. 5, p. 1198–1208, May 2009. Cited in page(s):

VULLERS, R. et al. Energy harvesting for autonomous wireless sensor networks. **IEEE Solid-State Circuits Mag.**, v. 2, n. 2, p. 29–38, Spring 2010. ISSN 1943-0582. Cited in page(s):

WANG, A.; CALHOUN, B. H.; CHANDRAKASAN, A. P. **Sub-threshold design for ultra low-power systems**. [S.l.]: Springer, 2006. Cited in page(s):

WANG, A.; CHANDRAKASAN, A. A 180mv fft processor using subthreshold circuit techniques. In: **IEEE Int. Dig. Tech. Papers Solid-State Circuits Conf. (ISSCC)**. [S.l.: s.n.], 2004. p. 292–529 Vol.1. ISSN 0193-6530. Cited in page(s):

WANG, A.; CHANDRAKASAN, A. A 180-mv subthreshold fft processor using a minimum energy design methodology. **IEEE J. Solid-State Circuits**, IEEE, v. 40, n. 1, p. 310–319, 2005. Cited in page(s):

WANG, C. C. et al. A low-power 2.45 ghz zigbee transceiver for wearable personal medical devices in wpan. In: **Dig. of Tech. Paper Int. Conf. Consumer Electronics**. [S.l.: s.n.], 2007. p. 1–2. Cited in page(s):

WANG, D. et al. Emerging spectrum regulation for medical body area network. In: **IEEE Int. Conf. Body Sensor Networks**. [S.l.: s.n.], 2013. p. 1–6. ISBN 2325-1425. Cited in page(s):

WEDDELL, A. S. et al. Accurate supercapacitor modeling for energy harvesting wireless sensor nodes. **IEEE Trans. Circuits Syst. II, Exp. Briefs**, IEEE, v. 58, n. 12, p. 911–915, 2011. Cited in page(s):

WEI, G.-Y.; HOROWITZ, M. A low power switching power supply for self-clocked systems. In: **Int. Symp. Low-power Electron. Des.** [S.l.: s.n.], 1996. p. 313–317. Cited in page(s):

WEI-MING, Y. et al. The design of 3.6ghz 4.2ghz low noise amplifier. In: **Int. Symp. Microwave Antenna Propagation and EMC Tech. Wireless Comm.** [S.l.: s.n.], 2007. p. 458–461. ID: 1. Cited in page(s):

WHITMORE, A.; AGARWAL, A.; XU, L. The internet of things, a survey of topics and trends. **Inform. Syst. Frontiers**, v. 17, n. 2, p. 261–274, 2014. ISSN 1572-9419. Cited in page(s):

WINDARKO, N.; CHOI, J.; CHUNG, G.-B. Improvement of electrical modeling of nimh battery for application of microgrid system. In: **2010 IEEE Energy Conversion Congr. Expo. (ECCE)**. [S.l.: s.n.], 2010. p. 4243–4248. Cited in page(s):

WONG, C.-W.; CHONG, K.-K. Solar flux distribution study of non-imaging dish concentrator using linear array of triple-junction solar cells scanning technique. **Solar Energy**, v. 125, p. 86 – 98, 2016. Cited in page(s):

XIE, X. et al. A low-power digital ic design inside the wireless endoscopic capsule. **IEEE J. Solid-State Circuits**, v. 41, n. 11, p. 2390–2400, 2006. ID: 1. Cited in page(s):

XING, J.; ZHU, Y. A survey on body area network. In: **5th Int. Conf. Wireless Comm. Networking Mobile Computing**. [S.l.: s.n.], 2009. p. 1–4. Cited in page(s):

YANG, G.-Z. (Ed.). **Body sensor networks**. [S.l.]: New York: Springer Verlag, 2006. Cited in page(s):

YAO, L. W. et al. Modeling of lithium-ion battery using matlab/simulink. In: **39th Ann. Conf. IEEE Ind. Electronics Soc. (IECON)**. [S.l.: s.n.], 2013. p. 1729–1734. ISSN 1553-572X. Cited in page(s):

YOO, H. J.; HOOFF, C. V. (Ed.). **Bio-Medical CMOS ICs**. 1. ed. [S.l.]: New York: Springer, 2010. Cited in page(s):

YU, H. et al. A hybrid indoor ambient light and vibration energy harvester for wireless sensor nodes. **Sensors**, v. 14, n. 5, p. 8740, 2014. Cited in page(s):

ZARGHAM, M.; GULAK, P. G. Fully integrated on-chip coil in 0.13 um cmos for wireless power transfer through biological media. **IEEE Trans. Biomed. Circuits Syst.**, v. 9, n. 2, p. 259–271, April 2015. Cited in page(s):

ZASOWSKI, T. A system concept for ultra wideband (uwb) body area networks. Dept. Elect. Eng, Ph.D. thesis, Federal Institute of Technology (ETH), Zurich, Switzerland, 2007. Cited in page(s):

ZEGAOUI, A. et al. Universal transistor-based hardware simulator for real time simulation of photovoltaic generators. **Solar Energy**, v. 134, p. 193 – 201, 2016. Cited in page(s):

ZHANG, H.; CHOW, M.-Y. Comprehensive dynamic battery modeling for phev applications. In: **2010 IEEE Power Energy Soc. General Meeting**, [S.l.: s.n.], 2010. p. 1–6. ISSN 1944-9925. Cited in page(s):

ZHANG, J. et al. An enhanced circuit-based model for single-cell battery. In: **2010 25th Ann. IEEE Appl. Power Electron. Conf. Expo. (APEC)**. [S.l.: s.n.], 2010. p. 672–675. ISSN 1048-2334. Cited in page(s):

ZHANG, S.; SEYEDI, A. A markovian model for harvested power from human motion. In: **Proc. 8th Int. Conf. Body Area Networks**. ICST, Brussels, Belgium, Belgium: ICST (Institute for Computer Sciences, Social-Informatics and Telecommunications Engineering), 2013. (BodyNets '13), p. 383–389. ISBN 978-1-936968-89-3. Disponível em: <<http://dx.doi.org/10.4108/icst.bodynets.2013.253912>>. Cited in page(s):

ZHEN, B.; LI, H.-B.; KOHNO, R. Ieee body area networks for medical applications. In: **4th Int. Symp. Wireless Comm. Syst.** [S.l.: s.n.], 2007. p. 327–331. Cited in page(s):

ZHU, X.-G. et al. Sensitivity analysis and more accurate solution of photovoltaic solar cell parameters. **Solar Energy**, Elsevier, v. 85, n. 2, p. 393–403, 2011. Cited in page(s):

ZHU, Y.; MOHEIMANI, S.; YUCE, M. R. A 2-dof mems ultrasonic energy harvester. **IEEE Sensors J.**, IEEE, v. 11, n. 1, p. 155–161, 2011. Cited in page(s):

ZURBUCHEN, A. et al. Energy harvesting from the beating heart by a mass imbalance oscillation generator. **Annals Biomed. Eng.**, Springer, v. 41, n. 1, p. 131–141, 2013. Cited in page(s):